

PhD Thesis

Modeling and Control of Reluctance Actuators

É. Ramírez Laboreo



PhD Thesis

Modeling and Control of Reluctance Actuators

Édgar Ramírez Laboreo
Supervisor: Carlos Sagüés Blázquez

October 2019



Universidad Zaragoza

PhD Thesis

Modeling and Control of Reluctance Actuators

Édgar Ramírez Laboreo

PhD Program in Systems Engineering and Computer Science
Universidad de Zaragoza

October 2019

Supervisor

Carlos Sagüés Blázquez Universidad de Zaragoza, Spain

Examiners

Jesús Acero Acero	Universidad de Zaragoza, Spain
David Paesa García	BSH Home Appliances Spain
Maurice Roes	Eindhoven University of Technology, The Netherlands
Jorge Duarte	Eindhoven University of Technology, The Netherlands
Diego Puyal Puente	BSH Home Appliances Spain

International reviewers

Nilles Vrijsen	Prodrive Technologies, The Netherlands
Johannes Reuter	Hochschule Konstanz, Germany
Elena Lomonova	Eindhoven University of Technology, The Netherlands
Gianluca Palli	University of Bologna, Italy
Paolo Mercorelli	Leuphana University of Lueneburg, Germany

This research has been partially funded by the following agencies/companies:

- Ministerio de Economía y Competitividad, Gobierno de España - European Union (Projects RTC-2014-1847-6 and RTC-2017-5965-6).
- Ministerio de Educación, Cultura y Deporte, Gobierno de España (PhD Scholarship FPU14/04171).
- Aragón Government - European Regional Development Fund (Projects T04 and T45_17R, Grupo de Investigación “Robótica, Percepción y Tiempo Real”).
- BSH Home Appliances Spain.

This is a modified version of the original document submitted for revision and defended at the Universidad de Zaragoza on October 18, 2019. Date of the current version: February 3, 2021.

Copyright © 2019 by Édgar Ramírez Laboreo. All rights reserved.

Resumen

Modelado y Control de Actuadores de Reluctancia

Los actuadores de reluctancia son dispositivos que se caracterizan por una elevada densidad de fuerza, buena eficiencia, gran tolerancia frente a fallos y un coste reducido. Estas características hacen que estén siendo considerados como una alternativa muy prometedora frente a otro tipo de actuadores electromagnéticos en ciertas aplicaciones que requieren gran velocidad y precisión. Por otro lado, los actuadores de reluctancia también son la solución ideal para algunos dispositivos electromecánicos que requieren unas prestaciones modestas, lo cual es debido principalmente a que son compactos, tienen un bajo coste y consumen relativamente poco. En concreto, los relés electromecánicos y las válvulas de solenoide son dispositivos cuya operación está basada en la fuerza creada por un pequeño actuador de reluctancia.

A pesar de sus ventajas, los actuadores de reluctancia son sistemas complejos cuya dinámica es no lineal. Una de sus características más distintivas es que la fuerza magnética que provoca el movimiento es siempre de atracción y, además, depende fuertemente de la posición de la armadura. Básicamente, el comportamiento de esta fuerza es lo que explica que dispositivos como los relés y las electroválvulas sufran fuertes impactos y desgaste cada vez que son activados. Adicionalmente, algunos fenómenos electromagnéticos como la histéresis magnética o las corrientes inducidas hacen que el modelado dinámico de los actuadores de reluctancia sea bastante complejo. El trabajo realizado en esta tesis doctoral está enfocado en estudiar las posibilidades que ofrecen estos actuadores y, en concreto, en analizar el comportamiento dinámico y proponer algoritmos de estimación y control para relés electromecánicos y válvulas de solenoide.

El primer objetivo de la investigación es el desarrollo de modelos dinámicos para actuadores de reluctancia, es decir, modelos de orden reducido que puedan ser utilizados para realizar simulaciones transitorias lo más precisas posibles con un bajo coste computacional. Para ello, lo primero que se ha estudiado es el comportamiento electromagnético de estos sistemas. El método de modelado más usado en la tesis es el de los circuitos magnéticos equivalentes (MEC, por sus siglas en inglés). No obstante, también se han realizado algunas simulaciones con modelos de elementos finitos, en concreto para validar

las aproximaciones del método MEC o para calcular la reluctancia del entrehierro. Se han estudiado los principales fenómenos electromagnéticos que aparecen en los actuadores de reluctancia, lo que ha llevado a la obtención de expresiones analíticas para modelar la dispersión de flujo, las corrientes inducidas y la saturación e histéresis magnéticas. Por otra parte, la expresión de la fuerza magnética que produce el movimiento se ha obtenido mediante un balance energético del sistema.

El movimiento de la armadura también se ha estudiado en la tesis. Dado que los actuadores de reluctancia tienen generalmente un recorrido físicamente acotado, se han propuesto dos técnicas diferentes que permiten modelar los límites del movimiento y los rebotes de la armadura. Una vez estudiado el movimiento, el modelo mecánico se ha combinado con las ecuaciones electromagnéticas para poder analizar el comportamiento dinámico del actuador en su conjunto. Se han desarrollado cinco modelos dinámicos distintos, desde el más sencillo posible hasta uno que incluye todos los fenómenos electromagnéticos citados con anterioridad, y posteriormente se han comparado teniendo en cuenta su precisión y coste computacional.

Las medidas experimentales son fundamentales a la hora de analizar y caracterizar cualquier sistema dinámico. Por ello, otro de los objetivos de la tesis ha sido la evaluación de distintas técnicas de medida que pudieran ayudar a mejorar la comprensión sobre el comportamiento dinámico de los actuadores de reluctancia y, en caso de que fuera posible, formar parte de un bucle de control realimentado. En este sentido, se ha intentado grabar el movimiento de uno de los dispositivos estudiados mediante tres instrumentos ópticos distintos. Los resultados indican que, a pesar de que en ciertas situaciones sí sería posible medir la trayectoria del dispositivo durante su movimiento, ninguno de los instrumentos podría aplicarse en la práctica por su baja flexibilidad y alto coste. Por este motivo, también se ha explorado el uso de otras variables que puedan ser medidas mucho más fácilmente.

Otra parte importante de la investigación ha estado centrada en técnicas de estimación. Se han desarrollado dos algoritmos que son capaces de estimar, en tiempo real, el flujo magnético, la resistencia y la inductancia de un actuador dado. Los algoritmos utilizan únicamente medidas de tensión y corriente, lo cual representa una clara ventaja ya que no se necesita utilizar sensores o equipamiento añadido. Las prestaciones de ambos estimadores han sido analizadas mediante simulación y experimentos reales. El problema de estimar la posición de la armadura también se ha abordado en la tesis. En concreto, se ha prestado especial atención en resaltar los efectos que la histéresis magnética produce en la estimación, algo que no había sido estudiado con anterioridad.

Finalmente, se han propuesto distintas técnicas de control para actuadores de reluctancia. En concreto, el objetivo principal es lograr que estos sigan un movimiento con aterrizaje suave, es decir, un movimiento que no dé lugar a impactos o rebotes. Como un primer paso, se han estudiado las propiedades básicas de los sistemas de control, es decir, la estabilidad, controlabilidad y observabilidad. Después se ha explorado la técnica de linealización por realimentación como un posible método para diseñar un bucle de control realimentado para la trayectoria de la armadura. Los resultados obtenidos demuestran que el control por realimentación es capaz de controlar el movimiento con gran precisión, siempre y cuando haya disponibles medidas o estimaciones precisas de la posición en tiempo real. Como esta situación es difícil que se dé en la práctica, se ha estudiado el uso

de técnicas de control óptimo en bucle abierto para aquellos casos en los que la posición de la armadura no se pueda obtener. En particular, se han obtenido distintas soluciones de tiempo óptimo y de energía óptima para un actuador nominal y, posteriormente, se ha analizado su robustez utilizando un método de Montecarlo.

Como alternativa a los métodos clásicos, se ha estudiado la aplicabilidad de los métodos Run-to-Run (R2R) en actuadores de reluctancia. Estas técnicas están diseñadas específicamente para sistemas que realizan un proceso repetitivo y, por lo tanto, son idóneas para dispositivos como los relés y las válvulas. En concreto, los métodos R2R implícitos se basan en la idea de construir una función que evalúe el desempeño del sistema al final de cada repetición. De esta forma, es posible mejorar el comportamiento dinámico del actuador a lo largo de las repeticiones utilizando un algoritmo de búsqueda. Las posibilidades para diseñar un controlador R2R son prácticamente infinitas, así que en la tesis se dan consejos prácticos sobre cómo elegir y parametrizar la señal de entrada, cómo usar las medidas disponibles para evaluar el comportamiento del sistema o cómo comparar distintos algoritmos de búsqueda. Los experimentos realizados demuestran que el algoritmo R2R diseñado es capaz de mejorar enormemente el comportamiento de un relé electromecánico y que, después de unos pocos ciclos, los resultados son incluso mejores que con cualquier estrategia presente en la literatura.

Summary

Modeling and Control of Reluctance Actuators

Reluctance actuators are characterized by having a high force density, good efficiency, high fault tolerance and reduced cost. These features make them a promising alternative to other electromagnetic actuators for high-speed and high-precision applications. In addition, reluctance actuators are also ideal for small switch-type devices that require a modest performance because of their compactness, low cost, reduced mass and low energy dissipation. In particular, electromechanical switches and solenoid valves are devices whose operation is based on the force created by a small reluctance actuator.

Despite their advantages, reluctance actuators are systems with highly nonlinear dynamics. One of their most distinctive features is that the magnetic force that produces the motion is always attractive and varies greatly with the position of the armature. In essence, the nature of this force explains why switch-type devices like relays and valves are subject to strong impacts and wear each time they are operated. In addition to that, electromagnetic phenomena such as magnetic hysteresis and eddy currents make the dynamic modeling of reluctance actuators even more difficult. The work of this thesis aims to investigate the capabilities of reluctance actuators and, in particular, to analyze the dynamic behavior and propose estimation and control algorithms for electromechanical switches and solenoid valves.

The first objective of the investigation is the development of control-oriented dynamical models for reluctance actuators, i.e., low-order models that can be used to perform accurate transient simulations with low computational requirements. For that, the electromagnetic behavior of these systems is firstly studied. The magnetic equivalent circuit (MEC) methodology is selected as the primary modeling technique. Simulations from finite element models are also used for some specific purposes, e.g., to verify the assumptions of the MEC approach or to calculate the reluctance of the air gap. Then, the main electromagnetic phenomena that occur in reluctance actuators are studied. Analytical solutions are obtained to model magnetic saturation, hysteresis, flux fringing and eddy currents, and an energy balance is used to obtain the expression for the magnetic force that produces the motion.

After that, the motion of the armature is incorporated to the analysis. Given that reluctance actuators usually have a limited range of motion, two different techniques are proposed to model the limits of the armature stroke and the bouncing phenomenon. Then, the electromagnetic equations and the mechanical models are combined to describe the overall dynamic behavior of the actuator. Five different dynamical models are presented, ranging from a computationally inexpensive structure to a comprehensive model that includes saturation, hysteresis, eddy currents and flux fringing. The models are compared in terms of accuracy and computational requirements.

Measurements play an important role in the analysis and characterization of dynamical systems. Thus, another objective of this thesis is the evaluation of different measurement methodologies that may improve the understanding of the dynamic behavior of reluctance actuators and, if possible, be used as part of a feedback controller. In this regard, three optical instruments are explored in order to record the motion of switch-type actuators. The results show that, even though in some cases it is possible to measure the position of several components of the device, none of the instruments could be applied in a practical situation due to their low flexibility and high cost. For that reason, other variables that are much more easily obtainable are also explored.

Another significant part of the research is devoted to estimation in reluctance actuators. Two different algorithms are proposed to estimate the magnetic flux, the resistance and the inductance of the device, both of which can be implemented in real time. The algorithms rely only on measurements of the coil voltage and current, which represents a clear advantage because no additional hardware is required. Simulation and experiments are presented to show the performance of the estimators. Furthermore, the estimation of the armature position is also investigated in this work. In particular, special focus is put on highlighting the effects of magnetic hysteresis on the performance of different estimation approaches.

Control strategies are then proposed to achieve soft landing in reluctance actuators, i.e., a controlled motion without impacts or bounces. As a first step, the basic properties of control systems theory—stability, controllability and stability—are investigated for a nominal actuator. Then, feedback linearization is explored as a method to design a trajectory tracking controller for the armature position. The obtained results show that soft landing can be accomplished by means of feedback control provided that accurate measurements or estimates of the position are available. Since this situation is rare in practice, open-loop optimal control is proposed as an alternative technique when the position is not accessible. Different time-optimal and energy-optimal solutions are derived for a nominal actuator and then compared in terms of robustness using a Monte Carlo analysis.

Finally, Run-to-Run (R2R) control is explored as another method that may be used to improve the performance of reluctance actuators. These techniques are specifically designed for systems that perform a repetitive operation and, hence, they are very well suited to being applied to switch-type devices. In particular, implicit R2R methods are based on the idea of building a function that evaluates the performance of the system at the end of each repetition. In this way, the dynamic behavior of the actuator can be gradually improved along the repetitions by conducting a black-box search. Considering that the possibilities to design a R2R controller are almost endless, practical advice is

given on how to select and parameterize the input profile, how to use measurements to evaluate the system performance and how to compare different search algorithms. The performed experiments show that the designed R2R controller is able to improve greatly the behavior of a switch-type device and that, after a few cycles, it outperforms other methodologies in the literature.

Contents

Resumen	i
Summary	v
1 Introduction	1
1.1 Motivation	1
1.2 Literature review	4
1.3 Objectives	7
1.4 Devices under study	8
1.5 Thesis outline	10
1.6 Contributions and publications	12
2 Electromagnetic Modeling	17
2.1 Fundamental laws of electromagnetism	17
2.2 Basics of modeling of reluctance actuators	21
2.3 Modeling methodologies	23
2.3.1 Magnetic equivalent circuits	23
2.3.2 Finite element method	26
2.4 Flux fringing	31
2.5 Magnetic saturation	33
2.6 Magnetic hysteresis	36
2.7 Eddy currents	42
2.8 Magnetic force	46
	ix

3	Dynamical Modeling of Reluctance Actuators	51
3.1	Mechanics	51
3.1.1	Mechanical modeling of one-degree-of-freedom actuators	51
3.1.2	Mechanical models with multiple degrees of freedom	55
3.2	Dynamical models for reluctance actuators	59
3.2.1	Basic dynamical model	59
3.2.2	Dynamical model including saturation	61
3.2.3	Dynamical model including saturation and flux fringing	61
3.2.4	Dynamical model including saturation, flux fringing and eddy currents	63
3.2.5	Dynamical model including saturation, hysteresis, flux fringing and eddy currents	64
3.2.6	Overview of the models	69
4	Measurement and Identification	73
4.1	Measurement	73
4.1.1	Electromagnetic variables	73
4.1.2	Position	78
4.1.3	Acoustic noise	86
4.2	Identification	87
4.2.1	Experimental setup	88
4.2.2	Parameter estimation	89
4.2.3	Validation and analysis	92
5	Control	97
5.1	Control systems properties	97
5.1.1	Stability	97
5.1.2	Controllability	104
5.1.3	Observability	105
5.2	Feedback control	107
5.2.1	Feedback linearization	107
5.2.2	Trajectory tracking controller design	111
5.2.3	Simulation results	112
5.3	Open-loop control	114
5.3.1	Optimal trajectory design	114
5.3.2	Simulation results	118

6	Estimation	125
6.1	Resistance, inductance and flux estimation	125
6.1.1	SEMERA algorithm	126
6.1.2	Integral estimator	133
6.1.3	Simulation results	134
6.1.4	Experimental results	137
6.1.5	Discussion	141
6.2	Position estimation	143
6.2.1	Position estimation via inductance estimation	146
6.2.2	Position estimation via flux linkage estimation	147
6.2.3	Position estimation via current measurements	149
6.2.4	Simulation results and discussion	151
7	Run-to-Run Control	155
7.1	Problem formulation and solution method	155
7.2	Design of the Run-to-Run controller	162
7.2.1	Input definition and output evaluation	162
7.2.2	Search algorithm	166
7.3	Experimental results	169
7.4	Discussion	173
7.4.1	Versatility	173
7.4.2	Convergence	175
8	Conclusions and Future Work	179
8.1	Conclusions	179
8.1.1	Dynamical modeling	180
8.1.2	Measurement	180
8.1.3	Estimation	181
8.1.4	Control	182
8.2	Recommendations for future work	183
	Bibliography	185
	About the author	199

Chapter 1

Introduction

1.1 Motivation

Since the invention of the dc electric motor by Michael Faraday in 1821 [1, 2], based on the works of Ørsted [3] and Ampère [4], electric machines have contributed to major improvements in living standards and industrial productivity and efficiency. This scientific and technical breakthrough was followed ten years later, in 1831, by the discovery of electromagnetic induction by Faraday himself [5] and, independently in America, by Joseph Henry. The advantages of alternating current in long-distance transmission lines led to the invention and development of the alternator, the ac motor and the transformer during the nineteenth century, with the first models being produced in the 1870s and 1880s. Since then, a broad range of electric machines has been invented and improved during the years, e.g., commutators, brushed machines, permanent magnet machines, reluctance machines or electrostatic machines, all of which have advantages and disadvantages depending on the application.

In particular, reluctance machines are characterized by having a high force density, fast response, good efficiency, high fault tolerance and reduced cost. For all these reasons, switched reluctance motors gained great interest in the last decades [6], specially for aerospace applications [7, 8] and for electric and hybrid vehicles [9, 10]. Variable reluctance machines of all kinds were systematically investigated during the 1970s and 1980s, which resulted in the invention of the first linear reluctance actuators [11, 12]. With the advances in electronics, this class of actuators soon became a competitive alternative [13] to other classes of linear electromagnetic actuators, e.g., voice coil or moving magnet actuators [14], and even to pneumatic or hydraulic devices. Indeed, several applications have been proposed in the last two decades for multiphase linear reluctance actuators, e.g., high-speed and high-precision manufacturing machines [15], elevators [16] or compressors [17], and they are also being used for aeronautical [18] or medical [19] purposes.

More specifically, the term reluctance actuator is usually applied to single-coil reluctance machines with a limited range of motion. Basically, a reluctance actuator is an electromagnet, built by wrapping a wire around a ferromagnetic core, together with a

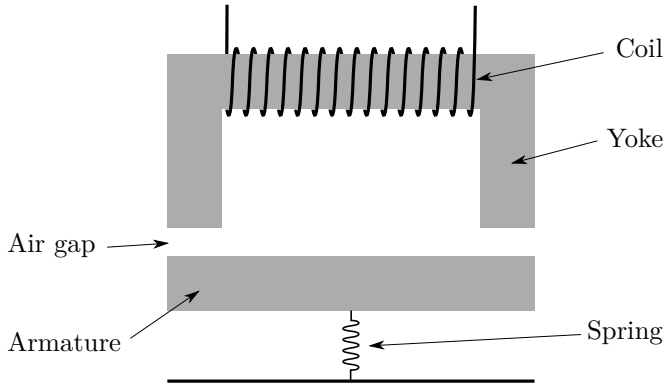


Figure 1.1: Schematic diagram of a C-core reluctance actuator.

moving component commonly known as armature (see Fig. 1.1). When the coil is energized, a magnetic flux starts to flow through the core and creates a magnetic force that pulls the armature towards the yoke. Since the magnetic force is always attractive, the opposing force is usually created by a spring attached to the armature or simply by gravity. More advanced actuators can be designed based on this concept. For instance, latching devices include a permanent magnet so that the armature remains at any of the two boundary positions without needing a continuous supply of power.

The high force density, fast response and efficiency of reluctance actuators make them a good choice for high-precision actuation systems [20, 21]. In this connection, several recent works have been devoted to the design and analysis of reluctance actuators for lithography systems [22–24] or antivibration applications [25], among others. In addition, the absence of permanent magnets in these devices results in high robustness against temperature variations, which is clearly an advantage in harsh environments [26]. On the other hand, reluctance actuators are also ideal for small mass-market devices that require a modest performance [27] because of their compactness, low cost, reduced mass and low energy dissipation. In particular, electromechanical switches and solenoid valves are electromechanical devices whose operation is based on the force created by a small reluctance actuator.

Electromechanical relays and contactors (see Fig. 1.2) are widely used in domestic and industrial applications. Although their basic design comes from the nineteenth century—they were initially designed as amplifiers for telegraph lines—these devices still offer many advantages with respect to solid state switches: They have low energy losses, are able to conduct and block current in both directions, provide electrical isolation between the activation circuit and the power terminals, are generally cheaper and their activation mode is simple. Additionally, whereas semiconductor devices can only provide single-pole single-throw arrangements, relays and contactors with multiple-pole and multiple-throw designs can be easily found in the market and are really useful in some cases. These advantageous features make electromagnetic switches the best choice for several present-day applications, e.g., battery chargers for electric vehicles [28], multiphase electric machines [29], wireless power transfer devices [30], drive-by-wire systems [31], photovoltaic modules [32] or home appliances [33].

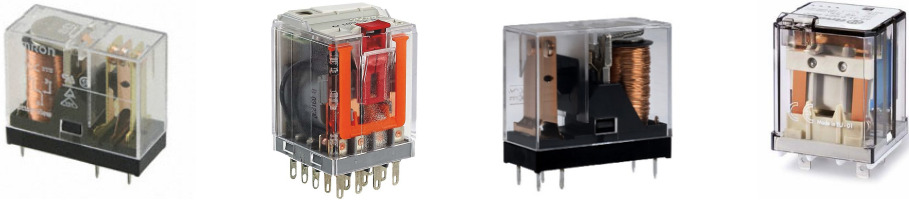


Figure 1.2: Commercial relays.



Figure 1.3: Commercial solenoid valves.

Despite these advantages, electromechanical relays also present some drawbacks related to their operation mode. They are considerably slower than solid-state switches and, since they have moving components, they are continuously subject to wear and their service life is shorter. Additionally, strong impacts are generated in each switching when the movable parts hit the fixed ones, which originates additional wear and an acoustic noise that could be annoying in certain applications. Contact bounce, which is produced when the electrical contacts hit together with an excess of energy, has been studied during the last 50 years [34, 35] and is probably the most known and undesirable problem of electromechanical switches. This phenomenon intensifies the mechanical wear of the contacts, favors the formation of electric arc and increases the probability of contact welding. In short, the apparition of contact bounce leads to an unavoidable reduction in the service life of these devices and the equipment in which they are embedded. As a result, electromechanical switches are sometimes discarded in favor of solid-state switches.

On the other hand, solenoid valves (see Fig. 1.3) are basically plunger-type reluctance actuators that use the motion of the plunger to regulate the flow of a fluid through a hydraulic or pneumatic circuit. These valves are being increasingly utilized because of their low cost, especially in the automotive industry, e.g., in electronic stability control systems [36–38], or in camless engines [39–42]. Nevertheless, the characteristic on-off behavior of this type of actuators poses a significant challenge when it comes to accurate fluid regulation, a problem that could be easily solved with servo or proportional valves [43, 44]. In addition, the impacts that appear during the opening and closing operations of these devices lead to similar problems to those of electromechanical switches, i.e., bounces, acoustic noise and mechanical wear, so there is still research to do until solenoid valves can be regarded as potential substitutes for other more expensive actuators.

The work of this thesis arises from the desire to investigate the capabilities of single-coil reluctance actuators and, in particular, to analyze the dynamic behavior and propose estimation and control algorithms for electromechanical switches and solenoid valves. It

emerges from a collaboration agreement between the University of Zaragoza and BSH Home Appliances Group, a leading company in the manufacturing of household appliances. In order to increase the quality of life of customers and compete in the global market, companies such as BSH are devoting increasing resources in research and development. In this regard, the common objective is to offer more attractive products to customers, either by means of improved or additional functionalities or by reducing the cost of the appliances. Note that, whereas electromechanical relays are currently used in most electric appliances, solenoid valves can be found, either for regulation or safety purposes, in many gas hobs and ovens (see Fig. 1.4). As a consequence, this thesis aims specifically at improving the performance of these mass-market devices by means of control systems techniques. Nevertheless, most of the findings of the research are applicable to any reluctance actuator independently of its use in any given application. In particular, the ultimate objective of the thesis is to design algorithms to achieve soft landing—a controlled motion without impacts or bounces—so that the device can operate silently and has an increased service life.



Figure 1.4: Domestic induction hob (left) and gas hob (right). Electromechanical switches and solenoid valves are currently extensively used in electric and gas appliances.

1.2 Literature review

In order to mitigate the problems and enhance the performance of single-coil reluctance actuators, several research works have been devoted to the modeling and control of these devices. In particular, focusing on electromechanical switches, one of the very first attempts to study the contact bounce phenomenon was made in the 1960s [34]. In that work, an energy analysis and simple spring-mass systems were proposed to model the dynamics of the device. A good review of electrical contacts including the influence of the arc current was made in 1989 [45] and extended three years later [46]. Then, the first works regarding the control of contact bounce were presented in the 1990s [47]. With respect to the modeling, some mechanical and electromagnetic coupled models including contact bounce were already published in 1996 [48, 49] and 1997 [50], but the authors themselves suggested that some aspects should be studied deeply.

On the other hand, the dynamics of solenoid actuators was early studied in the late 1980s [51] and during the 1990s [52–54]. The works by Cheung, Lim and Rahman, [55–58] are of particular relevance for their broad scope, covering the modeling, estimation and

control of this class of devices. Some specific references to solenoid valves from the same years can also be found [59]. Nevertheless, except for a few—possibly out of context—mentions [60], C-core and E-core reluctance actuators were not widely studied until the current millennium [61–65].

The beginning of the century saw an explosion in the number of publications about reluctance actuators in general and, in particular, about electromechanical switches and solenoid valves. Indeed, many proposals have been presented in recent years to predict the dynamic behavior of these devices. The electromagnetic dynamics has been modeled basically by means of two different approaches: analytical parametric models based on the magnetic equivalent circuit (MEC) approach [66], which reduces the complexity at the benefit of faster simulations, or numerical solutions based on the finite element method (FEM), which in general produces more accurate results at the expense of longer simulation times. Several recent MEC-based works can be found. For instance, an electromagnetic model for ac contactors including magnetic saturation is proposed in [67] based on the MEC methodology, and control-oriented models for permanent magnet devices [68, 69] or synchronous machines [70] have been also built using the same approach. On the other hand, FEM models have been proposed, e.g., to calculate the attractive torque of a latching relay [71] or the force of a circuit breaker [72], and they have been also combined with analytical dynamical models using curve fitting methods [73]. Some works combining the two methods can also be found. See, e.g., the research in [74], where a MEC model is improved by using a correction factor calculated from FEM simulations, or [75], where a one-dimensional MEC model and a two-dimensional FEM analysis are compared. Mention should also be made of semi-analytical methods (see, e.g., [76] and references therein).

Despite the extensive literature on the topic, none of the proposals achieve a precise description of the electromagnetic behavior of mass-market devices. On the one hand, FEM models are accurate and allow for considering nonlinear phenomena like magnetic saturation, but some aspects of the actual system—geometry, materials, winding configuration—are usually not revealed by the manufacturer of the device. Besides, FEM models are impractical for real-time implementations due to their high computational requirements. On the other hand, analytical solutions based on the MEC approach can be experimentally fitted to the device, but they usually have less precision because some simplifications are always adopted. In this regard, note that there are several works that consider magnetic saturation [25, 38, 77], but nevertheless only a few including hysteresis [24, 78] or eddy currents [72, 77]. Special mention should be made of [23], which may be considered the most comprehensive work devoted to the electromagnetic modeling of reluctance actuators. However, given that the investigated actuator was designed to work at a specific position, neither the effects of flux fringing nor the motion equations were included in the model.

In this connection, different approaches have been also used to solve the dynamics of the motion. For instance, a mechanical model based on the Euler-Bernoulli theory for beams is proposed to predict the movement of a relay in [79]. A Kelvin-Voigt viscoelastic model is also suggested in the same reference to model the bouncing phenomenon. The beam theory is used in other works [75], but the most widespread approach is the use of mass-spring-damper rigid body models with rectilinear motion and a single degree of freedom [50, 68, 80].

Many other works have focused on finding control strategies to achieve soft landing, i.e., algorithms that force the actuator to reach the final position with zero velocity [81]. One of the first works concerning the control of contact bounce in electromechanical switches [47] was based on the idea of reducing the kinetic energy of the moving contact by timing the coil energization process. Although this early approach was rigid and non self-adaptive to changing conditions, it inspired several subsequent works. For instance, dos Santos Dias de Moraes and Perin [82] proposed a method to detect the beginning of the closing process and modify accordingly the coil energization, and Lin et al. [68] presented an intelligent strategy that adjusts the coil voltage to reduce the magnetic force just before the impact.

Other works have adopted a more control-oriented approach. The underlying idea is that a position controller, together with a well-designed reference path, will permit the device to switch faster, without bounces and without producing any acoustic noise. In this regard, Carse et al. [83] already showed by simulation in 1999 that a simple fuzzy controller could reduce contact bounce in a relay. Several soft-landing and bounce reduction algorithms have been presented since then to increase the service life of solenoid valves and electromagnetic switches [44, 84–86], many of them based on dynamical models.

Designing a feasible trajectory considering input constraints is one of the key points to achieve soft landing. In this connection, some previous works have used optimal control theory [87] to find feasible [88–90], time-optimal [91] or energy-optimal solutions [92]. Then, nonlinear feedback control [93] can be used to follow the designed trajectory assuming that the armature position can be measured [94]. Considering that this situation is rare in practice, many of the proposed controllers [38, 44, 78, 95] rely on a position estimate in order to perform the designed control policy. Indeed, Rahman et al. [58] already used electrical variables in the 1990s to estimate the position of a solenoid actuator. Similar approaches have been used thereafter to control valves [43, 96] and electromechanical switches [97, 98]. It should be noted, however, that the estimation models usually neglect some electromagnetic phenomena, like hysteresis or eddy currents, which have a strong influence on the dynamic behavior of some actuators [22]. A practical approach to increase the robustness of these solutions could be the use of cycle-to-cycle learning-type strategies to adjust the feedback controller [99, 100] or the feedforward signal [85], as has been already done with microelectromechanical systems [101].

In spite of the extensive literature, the soft landing problem in reluctance actuators is still not completely solved. Many of the already presented strategies use open-loop strategies or nonlinear estimators, all of which are strongly dependent on having a good characterization of the system and its parameters. Consequently, if the device is subject to wear or drift, works under changing ambient conditions or simply if some of the parameters have not been properly estimated, the effectiveness of any of these algorithms is considerably reduced.

Finally, it should be highlighted that the research on electromechanical relays and contactors has not been limited to predicting their motion or electromagnetic behavior. See, e.g., the method proposed in [102] to evaluate the erosion of the electrical contacts of a contactor, the FEM-based thermal model of sealed electromagnetic relays in [103], the lifetime statistical analysis under various temperature conditions in [104], the endurance prediction model for ac relays in [105] or the quality analysis presented in [106].

1.3 Objectives

Electromechanical relays and solenoid valves are mass-market devices that use a small short-stroke reluctance actuator to switch between two possible states. Compared to other electromechanical drives, reluctance actuators are advantageous because of their fast response, high force density, low energy dissipation and reduced cost. However, the magnetic force that produces the motion in these actuators is highly nonlinear and increases greatly when the armature approaches the yoke. As a result, the above-mentioned devices are subject to strong impacts and bouncing each time they are activated, which ultimately leads to mechanical wear and, depending on the application, an annoying acoustic noise.

This thesis aims at the development of soft-landing strategies for single-coil reluctance actuators without permanent magnets, in particular for switch-type devices such as solenoid valves and electromechanical relays. In order to achieve that goal, the research work focuses on the following objectives:

- 1. Development of accurate control-oriented dynamical models for reluctance actuators.**

In order to use the models for estimation or control purposes, these should ideally have high accuracy and, at the same time, low computational complexity. Special attention should be paid to the study of the electromagnetic phenomena that occur in these systems—saturation, hysteresis, induced currents and flux fringing—and how to include them in the models. Given that there is usually a tradeoff between model accuracy and complexity, a comparison between models with different levels of detail is also considered of significant importance.

- 2. Evaluation of measurement techniques.**

Measurements play an important role in the analysis and characterization of dynamical systems. One of the objectives of this thesis is to evaluate different measurement methodologies to improve the understanding of the dynamic behavior of reluctance actuators and, if possible, to serve as part of a feedback controller. Considering that the main goal is to design a control strategy to achieve soft landing, the position of the armature is probably the variable with the most interest. Nevertheless, other measurements that could provide useful information about the system performance may also be considered, specially if they are easily obtainable.

- 3. Design and analysis of estimation algorithms.**

Magnetic flux is one of the most relevant variables in a reluctance actuator. Although not straightforwardly, this variable can be measured, e.g., using secondary coils [23] or by means of a Hall sensor [20]. However, these techniques are not applicable to most solenoid valves and electromechanical switches because these are usually encapsulated devices where only the coil terminals are accessible. Thus, this research also aims at the design of flux estimators based only on measurements of the coil voltage and current.

Position estimation is also of major interest when designing a soft-landing controller. Indeed, several research works have addressed the problem using different

approaches [38, 44, 78, 95]. Despite that, the effects of magnetic hysteresis and the robustness of the proposed estimators against parameter uncertainty have never been widely studied.

4. Design and validation of control algorithms.

The ultimate objective of this thesis is the proposal and validation of control strategies to achieve soft landing in reluctance actuators. An analysis of the model equations is first required to study the stability, controllability and observability of the system. The applicability of classical closed-loop and open-loop control techniques should then be evaluated, together with any other control strategy that could be used to achieve the proposed goal.

1.4 Devices under study

Most of the methodologies proposed in this thesis are fully applicable to any reluctance actuator regardless of its design, materials or final purpose. However, as already stated in the motivation section, this research is specially focused on modeling and control of low-cost commercial devices whose movement is driven by a single-coil non-latching reluctance actuator. In particular, electromechanical switches and solenoid valves are the two classes of devices that are considered in the investigation. Two specific devices, each belonging to one of these categories, are used throughout the document to illustrate the modeling, measurement, estimation and control techniques proposed. The main characteristics of these specific devices are described here.

Power relay

The electromechanical switch used in this research is a general purpose dc power relay which features a high electrical insulation between the coil and the contacts (see Fig. 1.5). This is achieved by means of a mechanism with an intermediate plastic part that completely separates the reluctance actuator and the power terminals. It is single-pole and double-throw (SPDT), i.e., the actuator controls a single electrical switch having two possible paths for the current, a normally closed one and a normally open one. Its operating mode is as follows. When the coil is not energized, the movable contact stands still, touching the normally closed contact. If the coil is energized, the armature closes the magnetic circuit and pushes the plastic part. At the same time, the opposite end of this latter component causes the movable contact to touch the normally open contact, thus establishing an electrical connection. This process is commonly known as *making* or *closing*. When the coil is de-energized, the elastic force of a spring makes the relay return to its original position, opening the magnetic circuit and closing the normally closed connection. This second process is generally called *breaking* or *opening*.

This particular model has been selected for various reasons. First, because of its mechanical design, which originates a complex motion that combines both linear and angular paths, therefore making its dynamics more difficult to analyze. As it will be shown, a two-degree-of-freedom mechanism is at least needed to describe the motion of the whole device. Besides, a significant play exists between the components, which causes

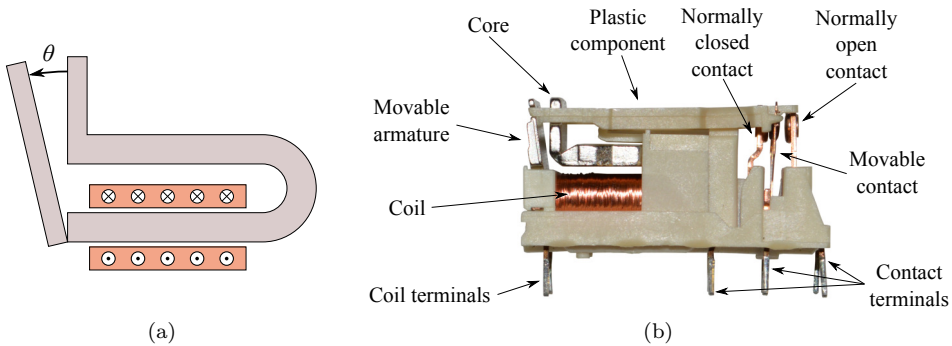


Figure 1.5: Power relay. (a) Schematic diagram of the actuator and (b) actual relay.

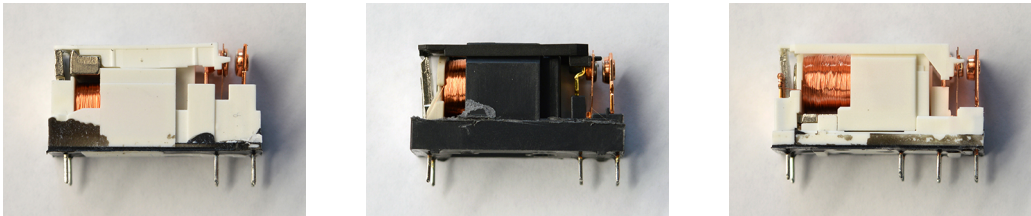


Figure 1.6: Equivalent relays sold by different manufacturers.

the motion of the armature and the movable contact to be decoupled in some stages of the making and breaking operations. Since both components have partially independent motion dynamics, the state-of-the-art estimation and control strategies for the armature are hardly applicable to control the movable contact and reduce the contact bounce in this relay. Additionally, it has a especial industrial interest because similar designs have been adopted by all the main manufacturers (see Fig. 1.6).

Solenoid valve

The second device investigated in this thesis is a commercial solenoid valve (see Fig. 1.7). It is basically a plunger-type actuator, with the coil wrapped around a cylindrical steel core that has a fixed and a movable part (the plunger). The housing, which is also made of the same material, provides a low-reluctance return path for the flux. A helical spring ensures that the mechanism returns to its original position when the coil is de-energized. In particular, this valve is used for safety purposes in domestic gas cookers. It is designed to be placed inside a gas faucet (see Fig. 1.8) and it is used to establish or interrupt the flow of gas. Its operating mode is analogous to that of the relay but, instead of establishing electrical connections, the result of the activation-deactivation cycle is that the gas line switches between being open and closed.

In contrast to the power relay, the motion of this valve is much simpler because there is only one movable component. Indeed, the movement can be described by a one-degree-of-freedom mass-spring-damper system as it will be shown. Despite that, the

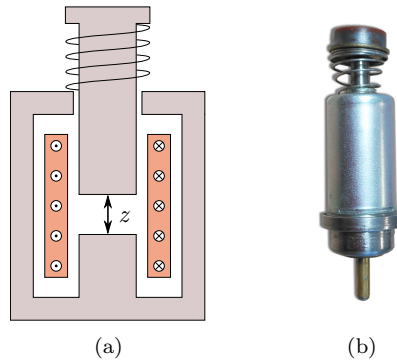


Figure 1.7: Solenoid valve. (a) Schematic diagram of the plunger-type actuator and (b) actual valve.

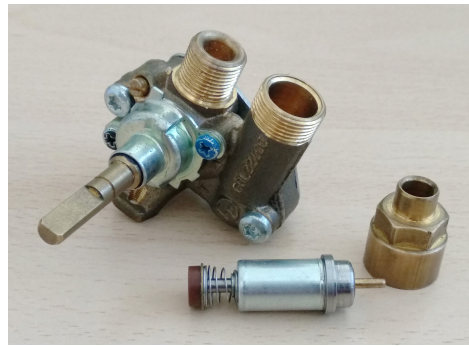


Figure 1.8: Gas faucet and solenoid valve. The valve, which is used for safety purposes, is specifically designed to operate inside the faucet.

material of the core and the housing is completely unknown, which implies an additional challenge in the modeling. For this reason, this device is used in this thesis to show that the electromagnetic properties of an unknown core material can be identified, without disassembling the device, using only measurements of voltage and current.

1.5 Thesis outline

This thesis is devoted to several research topics related to reluctance actuators. The modeling part is firstly addressed and, then, different control and estimation techniques are investigated. Theoretical and practical aspects are discussed all along the document. The contents, which have been divided in eight different chapters including this introduction, are organized as follows.

The electromagnetic modeling of reluctance actuators is investigated in **Chapter 2**. Maxwell's equations and other fundamental relations of electromagnetism are firstly pre-

sented. Then, the basic aspects of the dynamical modeling of reluctance actuators are introduced. The two main modeling methodologies used in the thesis, i.e., the magnetic equivalent circuit approach and the finite element method, are explained with especial emphasis on the approximations adopted. Some theoretical and numerical results are also included. After that, the main electromagnetic phenomena that occur in reluctance actuators are analyzed. Analytical and numerical solutions are proposed to model flux fringing, magnetic saturation, hysteresis and eddy currents. Finally, an energy balance is used to derive an explicit expression for the magnetic force that drives the motion in this class of actuators.

In **Chapter 3**, the motion of the armature is incorporated to the analysis. Considering that most reluctance actuators only move in one direction, a one-degree-of-freedom mass-spring-damper system is proposed to analyze the motion. Two different options are given to include the bouncing phenomenon in the analysis. Besides, a two-degree-of-freedom model is also presented to show how the modeling method can be generalized to more complex devices. Then, the electromagnetic equations and the mechanical models are combined in order to describe the overall dynamic behavior of the system. Five different dynamical models are presented, ranging from the most basic option to a comprehensive model that incorporates all the electromagnetic phenomena studied in the preceding chapter. The main results are summarized for comparison in tables at the end of the chapter.

Chapter 4 focuses on aspects related to measurement and identification. The first part of the chapter explores different measuring methodologies, particularly with regard to the position of the armature and other variables that may be used for analysis, control or estimation purposes. Some measurements are examined and the observed behavior is explained based on the theoretical analysis of the two previous chapters. Then, the second part of the chapter explains how to use some of these measurements to estimate the values of the parameters of the dynamical models. The methodology is illustrated by finding the parameters that best fit to a particular actuator. The results obtained with the five different dynamical models are compared in terms of accuracy and computational requirements.

Once the modeling part is finished, **Chapter 5** is devoted to control in reluctance actuators. Firstly, a stability analysis is used to provide a theoretical explanation for the switching behavior of single-coil actuators, i.e., why these systems are unstable at any position different from the boundaries. The basic properties of control systems theory are also studied to verify that these actuators are controllable and observable. Feedback linearization is then explored as a method to design a trajectory tracking controller for the armature position. Simulation results confirm that soft landing could be achieved via feedback control provided that accurate measurements or estimates of the position are available. Since this situation is rare in practice, open-loop optimal control is proposed as an alternative to achieve soft landing when the position is not accessible. Different time-optimal and energy-optimal solutions are derived for a nominal actuator and compared in terms of robustness using a Monte Carlo analysis.

Estimation in reluctance actuators is tackled in **Chapter 6**. The first part of the chapter focuses on how to estimate the magnetic flux, the resistance and the inductance of a given device using only measurements of voltage and current. Two different algorithms

are proposed to solve the problem and then evaluated by means of simulations and real experiments. On the other hand, the position estimation problem is addressed in the second part of the chapter. Three model-based methodologies are presented and evaluated by simulation in terms of accuracy and robustness, with particular focus on analyzing the effects of magnetic hysteresis.

Chapter 7 explores the applicability of Run-to-Run (R2R) methods to reluctance actuators. These techniques, which are intended for systems that operate in a repetitive manner, make use of offline measurements obtained in previous repetitions to gradually improve the dynamic behavior of the system. The theoretical fundamentals of R2R control are firstly presented and then adapted to the particularities of reluctance actuators. Different options are given to build a R2R controller for this class of systems, in particular with the aim of reducing the bouncing phenomenon and the noise generated during the movement of the device. Results from actual experiments are presented to show the performance of the algorithm and, finally, some additional issues about versatility and convergence are also discussed.

Finally, the main conclusions of the investigation are presented in **Chapter 8**, together with the proposal of new research lines that emerge from the results of this thesis.

1.6 Contributions and publications

As stated, the research project of this thesis emerges from the collaboration agreement between the University of Zaragoza and BSH Home Appliances Group. Whereas the theoretical work has been mainly carried out in the Department of Computer Science and Systems Engineering of the University, most of the experiments have been conducted in the laboratories of the BSH Competence Center for Induction Development, in Montañana, Spain. Additionally, part of the contributions are a result of a three-month stay at the Eindhoven University of Technology in The Netherlands.

The contributions of this thesis can be divided into different categories that correspond approximately to the chapters of the document:

- With regard to the **electromagnetic modeling** of reluctance actuators, the most notorious contribution of this thesis is the proposal of different methodologies to describe, in the time domain, the main electromagnetic phenomena that appear in reluctance actuators. In particular, an explicit dynamical solution of the Preisach model of hysteresis is described in the thesis, which results in much faster computations when compared to implicit solutions. Other contributions of the chapter include the comparison of different functions to model magnetic saturation, an analytical solution for eddy currents in cylindrical cores and a detailed energy balance that is used to obtain the expression for the magnetic force.
- Another major contribution of the research is the proposal of different **dynamical models for reluctance actuators** that consider the dynamics of the movement and the main electromagnetic variables. Five models are analytically described and then compared numerically in terms of accuracy and computational requirements. In particular, this thesis presents the first model in the literature that incorporates

the effects of magnetic saturation and hysteresis, eddy currents, flux fringing and the dynamics of the motion. The use of the explicit solution of the Preisach model of hysteresis has also led to a new class of hybrid dynamical systems whose state not only contains scalar variables, but also sets of constants with varying cardinality.

- This thesis also contributes with practical advice on how to **measure** the position of the armature in reluctance actuators and, more specifically, in commercial devices such as switches and valves. In this regard, three different measuring instruments have been analyzed to highlight the advantages and disadvantages of each technique. According to the author's knowledge, this is also the first research work that suggests the use of noise measurements from a low-cost microphone as a method to improve the performance of a reluctance actuator.
- In the **control** chapter, an in-depth stability analysis is used to explain the switching nature of single-coil reluctance actuators, i.e., why these systems are not stable at any intermediate position between the boundaries. The controllability and observability properties of these actuators are also studied for the first time. In addition, although feedback linearization is a common approach in control systems theory, the application of this technique to achieve soft landing in single-coil switching devices is also an original idea of this research. Finally, the Monte Carlo analysis performed to analyze the robustness of open-loop optimal control is also of special interest because it definitely shows that this could be a practical and cost-effective approach to reduce the impact velocities and increase the service life of switch-type actuators.
- Two **estimation** algorithms are proposed to estimate in real time the magnetic flux, the resistance and the inductance of the actuator. The main benefit of these estimators is that they only use current and voltage measurements. Thus, they can be used to estimate the cited variables in any reluctance actuator without need of specific sensors. Besides, a comparison of three different approaches to estimate the position of the actuator is also presented. Realistic simulations using an accurate model are used to underline the benefits and drawbacks of each method when magnetic hysteresis cannot be neglected.
- Finally, a new strategy based on **Run-to-Run control** has been designed to improve the performance of reluctance actuators. Practical advice is given on how to select the best input profile and how to use measurements to evaluate the behavior of the system. A search algorithm based on direct-search optimization is also proposed. The obtained results, in particular with regard to the reduction of contact bounce, show that the proposed algorithm outperforms other methodologies in the literature. In addition, the suitability of surrogate-based algorithms to R2R control is highlighted and some convergence-related issues are also discussed.

Most of these contributions have been published in high impact journals [107–112] or presented in international peer-reviewed conferences [113–116]. Besides, a patent application [117] has been submitted to protect the Run-to-Run controller designed in this thesis to reduce contact bounce in electromechanical switches. These publications are listed in the following page.

International high-impact journals

E. Ramirez-Laboreo, C. Sagues and S. Llorente, “A New Model of Electromechanical Relays for Predicting the Motion and Electromagnetic Dynamics”, *IEEE Transactions on Industry Applications*, vol. 52, no. 3, pp. 2545-2553, May/Jun. 2016. DOI: [10.1109/TIA.2016.2518120](https://doi.org/10.1109/TIA.2016.2518120).

E. Ramirez-Laboreo, C. Sagues and S. Llorente, “A New Run-to-Run Approach for Reducing Contact Bounce in Electromagnetic Switches”, *IEEE Transactions on Industrial Electronics*, vol. 64, no. 1, pp. 535-543, Jan. 2017. DOI: [10.1109/TIE.2016.2605622](https://doi.org/10.1109/TIE.2016.2605622).

E. Ramirez-Laboreo and C. Sagues, “Reluctance actuator characterization via FEM simulations and experimental tests”, *Mechatronics*, vol. 56, pp. 58-66, Dec. 2018. DOI: [10.1016/j.mechatronics.2018.10.009](https://doi.org/10.1016/j.mechatronics.2018.10.009).

E. Ramirez-Laboreo, E. Moya-Lasheras and C. Sagues, “Real-Time Electromagnetic Estimation for Reluctance Actuators”, *IEEE Transactions on Industrial Electronics*, vol. 66, no. 3, pp. 1952-1961, Mar. 2019. DOI: [10.1109/TIE.2018.2838077](https://doi.org/10.1109/TIE.2018.2838077).

E. Ramirez-Laboreo, M. G. L. Roes and C. Sagues, “Hybrid Dynamical Model for Reluctance Actuators Including Saturation, Hysteresis and Eddy Currents”, *IEEE/ASME Transactions on Mechatronics*, vol. 24, no. 3, pp. 1396-1406, Jun. 2019. DOI: [10.1109/TMECH.2019.2906755](https://doi.org/10.1109/TMECH.2019.2906755).

E. Moya-Lasheras, E. Ramirez-Laboreo and C. Sagues, “Probability-Based Control Design for Soft Landing of Short-Stroke Actuators”, *IEEE Transactions on Control Systems Technology*, in press, 2019. DOI: [10.1109/TCST.2019.2918479](https://doi.org/10.1109/TCST.2019.2918479).

International peer-reviewed conferences

E. Ramirez-Laboreo, C. Sagues and S. Llorente, “A new model of electromechanical relays for predicting the motion and electromagnetic dynamics”, in *IEEE Industry Applications Society Annual Meeting*, Addison, TX, USA, Oct. 2015. DOI: [10.1109/IAS.2015.7356818](https://doi.org/10.1109/IAS.2015.7356818).

E. Moya-Lasheras, C. Sagues, E. Ramirez-Laboreo and S. Llorente, “Nonlinear Bounded State Estimation for Sensorless Control of an Electromagnetic Device”, in *56th IEEE Conference on Decision and Control (CDC)*, Melbourne, Australia, Dec. 2017. DOI: [10.1109/CDC.2017.8264407](https://doi.org/10.1109/CDC.2017.8264407).

E. Moya-Lasheras, E. Ramirez-Laboreo and C. Sagues, “A novel algorithm based on Bayesian optimization for run-to-run control of short-stroke reluctance actuators”, in *2019 European Control Conference (ECC)*, Napoli, Italia, Jun. 2019. DOI: [10.23919/ECC.2019.8795949](https://doi.org/10.23919/ECC.2019.8795949).

E. Ramirez-Laboreo, E. Moya-Lasheras and C. Sagues, “Optimal Open-Loop Control Policies for a Class of Nonlinear Actuators”, in *2019 European Control Conference (ECC)*, Napoli, Italia, Jun. 2019. DOI: [10.23919/ECC.2019.8795785](https://doi.org/10.23919/ECC.2019.8795785).

Patents (Authors in alphabetical order)

D. Anton Falcon, S. Llorente Gil, D. Puyal Puente, E. Ramirez Laboreo and C. Sagues Blazquiz, “A home appliance device and a method for operating a home appliance device”, world patent application [WO 2017/163114](#).

S. Llorente Gil, E. Moya Lasheras, E. Ramirez Laboreo and C. Sagues Blazquiz, “Domestic Appliance Device”, world patent application [WO 2019/106488](#).

J. Ballester Castañer, J. Corral Ricalde, S. Llorente Gil, E. Moya Lasheras, J. S. Ochoa Torres, E. Placer Maruri, E. Ramirez Laboreo, J. Rivera Peman, C. Sagues Blazquiz, D. Serrano Garcia, “Gas Cooking Appliance Device”, world patent application [WO 2019/220247](#).

Chapter 2

Electromagnetic Modeling

The modeling part of this thesis is divided into three chapters that cover different aspects of the dynamical modeling of reluctance actuators. In particular, this first chapter is devoted to the description of several electromagnetic phenomena that occur in this class of magnetic systems. The fundamental laws of electromagnetism are first presented and then used to introduce the basics of electromagnetic modeling of reluctance actuators. After that, the two main modeling methodologies adopted in the thesis are described. Analytical and numerical solutions are then obtained for the main electromagnetic phenomena that affect the system dynamics. Finally, an energy balance is used to derive an expression for the magnetic force that drives the motion of the actuator.

2.1 Fundamental laws of electromagnetism

Maxwell's equations

The electromagnetic analysis presented in this chapter is based on Maxwell's equations [118–120], whose integral formulation is as follows:

$$\oint_{\partial\Sigma} \mathbf{E} \cdot d\mathbf{l} = -\frac{d}{dt} \iint_{\Sigma} \mathbf{B} \cdot d\mathbf{S} \quad \text{Faraday's law} \quad (2.1)$$

$$\oiint_{\partial\Omega} \mathbf{D} \cdot d\mathbf{S} = \iiint_{\Omega} \rho_f dV \quad \text{Gauss's law} \quad (2.2)$$

$$\oint_{\partial\Sigma} \mathbf{H} \cdot d\mathbf{l} = \iint_{\Sigma} \mathbf{J}_f \cdot d\mathbf{S} + \frac{d}{dt} \iint_{\Sigma} \mathbf{D} \cdot d\mathbf{S} \quad \text{Generalized Ampère's law} \quad (2.3)$$

$$\oiint_{\partial\Omega} \mathbf{B} \cdot d\mathbf{S} = 0 \quad \text{Gauss's law for magnetism} \quad (2.4)$$

In these equations, \mathbf{E} is the electric field, \mathbf{B} is the magnetic flux density, also known as magnetic induction, \mathbf{H} is the magnetic field intensity, also known as magnetic field strength or magnetizing field, \mathbf{D} is the displacement field, \mathbf{J}_f is the free current density,

ρ_f is the free electric charge density, $\partial\Sigma$ is the contour of the arbitrary surface Σ , and $\partial\Omega$ is the boundary surface of the arbitrary volume Ω . The magnetic flux, which is defined as the surface integral of \mathbf{B} ,

$$\phi = \iint \mathbf{B} \cdot d\mathbf{S}, \quad (2.5)$$

is often used to simplify the notation of Faraday's law. The auxiliary fields \mathbf{H} and \mathbf{D} are defined as

$$\mathbf{H} = \frac{\mathbf{B}}{\mu_0} - \mathbf{M}, \quad (2.6)$$

$$\mathbf{D} = \varepsilon_0 \mathbf{E} + \mathbf{P}, \quad (2.7)$$

where μ_0 and ε_0 are respectively the magnetic permeability and electric permittivity of the vacuum, \mathbf{M} is the magnetization field and \mathbf{P} is the polarization field. Except for μ_0 and ε_0 , which are constants, all the previously defined variables may in general depend on position, \mathbf{r} , and time, t . The explicit dependence on these variables is omitted in most parts of the chapter for clarity reasons.

Constitutive relations

In order to solve Maxwell's equations, the relations between the fields \mathbf{E} , \mathbf{D} and \mathbf{P} , as well as between \mathbf{B} , \mathbf{H} and \mathbf{M} , need to be specified. These relations, which depend on the material, are the so-called constitutive relations. For linear isotropic materials, these are given by

$$\mathbf{H} = \frac{\mathbf{B}}{\mu}, \quad (2.8)$$

$$\mathbf{D} = \varepsilon \mathbf{E}, \quad (2.9)$$

where μ and ε are scalar constants that represent, respectively, the magnetic permeability and electric permittivity of the given material. In terms of \mathbf{M} and \mathbf{P} , the constitutive relations are expressed as

$$\mathbf{M} = \chi_m \mathbf{H}, \quad (2.10)$$

$$\mathbf{P} = \varepsilon_0 \chi_e \mathbf{E}, \quad (2.11)$$

where χ_m and χ_e are respectively the magnetic and electric susceptibilities of the material. Considering (2.6)–(2.9), these are related to μ and ε as follows,

$$\frac{\mu}{\mu_0} = (1 + \chi_m) = \mu_r, \quad (2.12)$$

$$\frac{\varepsilon}{\varepsilon_0} = (1 + \chi_e) = \varepsilon_r, \quad (2.13)$$

where μ_r and ε_r are the relative magnetic permeability and relative electric permittivity of the material, respectively. The previous constitutive relations can still be used to describe many nonlinear anisotropic materials, but in that case μ and ε are not scalar constants but tensor functions of \mathbf{B} , \mathbf{E} and possibly their time derivatives and other variables such

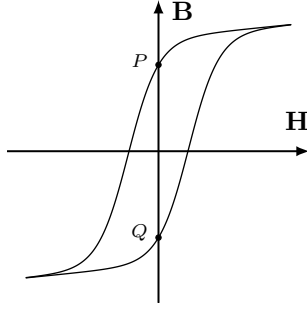


Figure 2.1: Magnetic hysteresis loop. Constitutive relation $\mathbf{H} = \mathbf{B}/\mu$ fails at points P and Q where μ is not defined.

as position, time or temperature. These relations, however, fail in describing hysteretic behaviors, e.g., the \mathbf{B} – \mathbf{H} relation in ferromagnetic materials (see Fig. 2.1).

In addition to these relations, the microscopic form of Ohm’s law,

$$\mathbf{J}_f = \sigma \mathbf{E}, \quad (2.14)$$

where σ is the electrical conductivity of the material, is also necessary to describe how the free current density behaves in terms of the electric field.

Magnetoquasistatic approximation

The magnetoquasistatic model, which is a simplified version of Maxwell’s equations widely adopted in the modeling of electrical machines, is used throughout this thesis. In this approximation, Ampère’s law is used as originally formulated, i.e., without the term including the time derivative of \mathbf{D} ,

$$\oint_{\partial\Sigma} \mathbf{H} \cdot d\mathbf{l} = \iint_{\Sigma} \mathbf{J}_f \cdot d\mathbf{S}. \quad (2.15)$$

The magnetoquasistatic model is generally valid for frequencies below 1 MHz, which is about three orders of magnitude higher than the dynamics of reluctance actuators.

Energy in electromagnetic fields

The work that needs to be done to create a magnetic field in a volume V is given by [121]

$$W_m = \int_V w_m dV, \quad (2.16)$$

where w_m is the magnetic work density—energy per unit volume that has to be spent to change the magnetic field—which in general depends on position, \mathbf{r} , and time, t ,

$$w_m = w_m(\mathbf{r}, t) = \int_0^{\mathbf{B}(\mathbf{r}, t)} \mathbf{H}(\mathbf{r}, t) \cdot \delta\mathbf{B} = \int_{-\infty}^t \mathbf{H}(\mathbf{r}, t) \cdot \frac{\partial\mathbf{B}(\mathbf{r}, t)}{\partial t} dt. \quad (2.17)$$

For magnetically linear materials, i.e., materials that satisfy (2.8) with constant μ , this simplifies into

$$w_m = \frac{1}{2} |\mathbf{H}| |\mathbf{B}| = \frac{1}{2} \mu |\mathbf{H}|^2 = \frac{1}{2} \frac{|\mathbf{B}|^2}{\mu}. \quad (2.18)$$

Note that in this case the work is reversible and all the energy is recoverable. Thus, w_m can be also interpreted as the magnetic energy per unit volume stored in space.

Analogously, the work needed to create an electric field in a volume V is given by

$$W_e = \int_V w_e dV, \quad (2.19)$$

where

$$w_e = w_e(\mathbf{r}, t) = \int_0^{\mathbf{E}(\mathbf{r}, t)} \mathbf{D}(\mathbf{r}) \cdot \delta \mathbf{E} = \int_{-\infty}^t \mathbf{D}(\mathbf{r}, t) \cdot \frac{\partial \mathbf{E}(\mathbf{r}, t)}{\partial t} dt. \quad (2.20)$$

For linear dielectrics, i.e., materials that satisfy (2.9) with constant ε , this simplifies into

$$w_e = \frac{1}{2} |\mathbf{D}| |\mathbf{E}| = \frac{1}{2} \varepsilon |\mathbf{E}|^2 = \frac{1}{2} \frac{|\mathbf{D}|^2}{\varepsilon}. \quad (2.21)$$

Forces in electromagnetic fields

A particle with charge q and velocity \mathbf{v} moving in an electromagnetic field experiences a force, known as Lorentz force [121], given by

$$\mathbf{F} = q \mathbf{E} + q \mathbf{v} \times \mathbf{B}. \quad (2.22)$$

Considering a continuous distribution of charge, the Lorentz force acting on a solid body of volume V is given by the volume integral of the force density \mathbf{f} ,

$$\mathbf{F} = \int_V \mathbf{f} dV, \quad (2.23)$$

where

$$\mathbf{f} = \rho \mathbf{E} + \mathbf{J} \times \mathbf{B}. \quad (2.24)$$

In this equation, ρ is the total charge density, which includes both the free charge density and the bound charge density,

$$\rho = \rho_f - \nabla \cdot \mathbf{P}, \quad (2.25)$$

and \mathbf{J} is the total current density, including the free current density, the magnetization current density and the polarization current density,

$$\mathbf{J} = \mathbf{J}_f + \nabla \times \mathbf{M} + \frac{\partial \mathbf{P}}{\partial t}. \quad (2.26)$$

For more insight into bound charges and currents, see [122].

Using Ampère's law in differential form [123], (2.24) can be rewritten as

$$\mathbf{f} = \rho \mathbf{E} + \frac{1}{\mu_0} (\nabla \times \mathbf{B}) \times \mathbf{B}. \quad (2.27)$$

Then, with some manipulations, it is possible to show [124] that this can be expressed as

$$\mathbf{f} = \nabla \cdot \mathbb{T}_{\text{em}} - \frac{\partial}{\partial t} (\varepsilon_0 \mathbf{E} \times \mathbf{B}), \quad (2.28)$$

where the tensor \mathbb{T}_{em} , known as the Maxwell stress tensor, is given by

$$\mathbb{T}_{\text{em}} = \varepsilon_0 \left(\mathbf{E}\mathbf{E}^\top - \frac{1}{2} |\mathbf{E}| \mathbb{I} \right) + \frac{1}{\mu_0} \left(\mathbf{B}\mathbf{B}^\top - \frac{1}{2} |\mathbf{B}| \mathbb{I} \right). \quad (2.29)$$

In this expression, \mathbb{I} is the identity tensor (identity matrix of size three). For magnetic systems such as reluctance actuators, where generally no net charge is present, the Maxwell stress tensor is usually approximated by only its magnetic term,

$$\mathbb{T}_{\text{em}} = \frac{1}{\mu_0} \left(\mathbf{B}\mathbf{B}^\top - \frac{1}{2} |\mathbf{B}| \mathbb{I} \right). \quad (2.30)$$

Under the magnetoquasistatic approximation, the second term in (2.28) is neglected and, thus, the force density is simplified into

$$\mathbf{f} = \nabla \cdot \mathbb{T}_{\text{em}}. \quad (2.31)$$

As a consequence, the force \mathbf{F} can be reformulated as a surface integral by applying the divergence theorem,

$$\mathbf{F} = \int_V \nabla \cdot \mathbb{T}_{\text{em}} \, dV = \oint_{\partial V} \mathbb{T}_{\text{em}} \cdot d\mathbf{S}, \quad (2.32)$$

where ∂V is the boundary surface of the volume V . That is, the electromagnetic force acting on a body can be computed either by integrating the Lorentz force density over its volume or by integrating the Maxwell stress tensor over its boundary surface.

2.2 Basics of modeling of reluctance actuators

A simplified diagram of a typical linear reluctance actuator is represented in Fig. 2.2. This diagram, which is used to explain the modeling methodology adopted in this thesis, depicts the air gap and part of the core and the coil of the actuator. The length of the air gap is used to define the position of the mover, z , which in this chapter is considered a given input. A coil of N turns, carrying an electric current i , is wrapped around the core and generates a magnetic flux ϕ through its cross section. At the same time, the variation of ϕ induces an equivalent eddy current i_{ec} in the iron. This description is a valid representation for almost any armature arrangement, e.g., plunger-type, E-core or C-core devices, and can also be applied to reluctance actuators with rotary motion simply by using the equivalent angular variables.

The main objective of this chapter is to derive the equations that model the dynamical relation between the previously defined scalar variables. Two are the fundamental equations that describe the electromagnetic behavior of a reluctance actuator. First, the electrical equation of the coil, which is a direct result of Faraday's law,

$$v = Ri + N \frac{d\phi}{dt}, \quad (2.33)$$

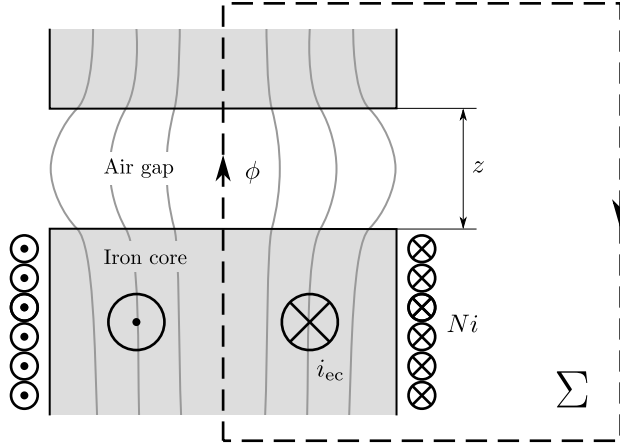


Figure 2.2: Reluctance actuator diagram showing an air gap and part of the iron core. Surface Σ is such that its contour, $\partial\Sigma = \partial\Sigma_{\text{gap}} + \partial\Sigma_{\text{core}}$, matches the main path of the magnetic flux. The arrows indicate the sign convention for ϕ , i and i_{ec} .

where v is the voltage applied across the coil terminals and the only input of the system, R is the internal resistance and the other variables have been previously defined. The flux linkage λ , which is equal to

$$\lambda = N\phi, \quad (2.34)$$

is sometimes used to express (2.33) as $v = Ri + d\lambda/dt$.

The second equation results from the application of Ampère's law [see (2.15)] to the surface Σ defined in Fig. 2.2. According to this diagram, the circulation of the magnetic field intensity can be divided into two terms corresponding to the air gap and the iron core. In addition, the surface integral of the free current density is directly given by the sum of N times the coil current plus the induced eddy current (see the sign convention in the figure). Thus, Ampère's law results in

$$\int_{\partial\Sigma_{\text{gap}}} \mathbf{H} \cdot d\mathbf{l} + \int_{\partial\Sigma_{\text{core}}} \mathbf{H} \cdot d\mathbf{l} = Ni + i_{ec}, \quad (2.35)$$

where $\partial\Sigma_{\text{gap}}$ and $\partial\Sigma_{\text{core}}$ are respectively the air gap and iron core parts of the contour $\partial\Sigma$, and the equivalent eddy current is given by

$$i_{ec} = \iint_{\Sigma_{\text{core}}} \mathbf{J}_f \cdot d\mathbf{S}, \quad (2.36)$$

where Σ_{core} is the part of the surface Σ inside the iron core.

Analytical and numerical approaches can be used to transform the left hand side terms of (2.35), as well as the right hand side term of (2.36), into functions of the scalar variables. In addition, as stated in the previous section, the constitutive relations between \mathbf{B} and \mathbf{H} need also to be provided in order to find a solution. The following sections present the methodologies used in this thesis to obtain the set of differential equations that describe the electromagnetic behavior of reluctance actuators.

2.3 Modeling methodologies

2.3.1 Magnetic equivalent circuits

The magnetic equivalent circuit (MEC) approach is an approximate method for the analysis of magnetic systems [124–127]. It relies on two basic assumptions. First, that the magnetic flux is confined in a region around the so-called *main paths*, which are closed lines only passing through sections of the iron core and the air gaps (see Fig. 2.3). Given that the magnetic permeability of the iron is in general much higher than μ_0 , it is widely accepted that the flux is, with the exception of air gaps, strictly confined within the core section [128]. All these paths, including the volume around them where the flux is nonzero, form the so-called magnetic circuit. On the other hand, it is also assumed that the magnetic fields are uniform in the cross section of the circuit, or at least that they can be approximated by an average value with small error. Under these assumptions, the application of Gauss’s law for magnetism [see (2.4)] to a magnetic system leads to

$$\mathbf{B} = B(l)\hat{\mathbf{l}}, \quad (2.37)$$

$$\mathbf{H} = H(l)\hat{\mathbf{l}}, \quad (2.38)$$

where l is the variable that defines the position along the circuit, $\hat{\mathbf{l}}$ is the unit vector in the direction of l , and B and H are scalar variables that represent the magnitude and sign of, respectively, the magnetic flux density and the magnetic field intensity in the direction given by $\hat{\mathbf{l}}$, i.e., $B = \mathbf{B} \cdot \hat{\mathbf{l}}$ and $H = \mathbf{H} \cdot \hat{\mathbf{l}}$.

As stated, the MEC assumptions lead to a simplified analysis of the magnetic system. In the first place, (2.37) allows for expressing the magnetic flux through any branch of the magnetic circuit as

$$\phi = \iint_{A(l)} \mathbf{B} \cdot d\mathbf{S} = B(l)A(l), \quad (2.39)$$

where l is an arbitrary position along the given branch and $A(l)$ is the cross-sectional area of the circuit at that point. Note that, according to the simplifications adopted and Gauss’s law for magnetism, ϕ must be equal for any position along the branch.

In the second place, (2.38) permits a reformulation of the circulation of the magnetic field intensity in terms of the scalar variable H .

$$\int \mathbf{H} \cdot d\mathbf{l} = \int H dl \quad (2.40)$$

Then, assuming that the materials of the system are characterized by the constitutive relation $H = B/\mu$, the circulation of H along any branch of the circuit can be expressed, using (2.39), as the product of the flux and the reluctance of the given branch,

$$\int H dl = \phi \mathcal{R}, \quad (2.41)$$

where the reluctance \mathcal{R} , which depends on the geometry and the magnetic permeability of the materials of the branch, is given by

$$\mathcal{R} = \int \frac{dl}{\mu A}. \quad (2.42)$$

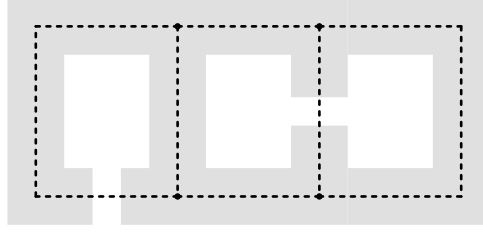


Figure 2.3: Magnetic system. The MEC approach assumes that the magnetic flux is confined within a region around the main paths (dashed lines).

Analytical solutions for the reluctance can only be obtained in cases where the system has a simple geometry. However, it is always possible to partition the magnetic circuit into a number of elements such that each one of them can be approximated by a simple geometric shape with analytical reluctance. Thus, the reluctance of any branch can be obtained as the sum of the reluctances of the elements that belong to that branch,

$$\mathcal{R} = \sum_j \mathcal{R}_j, \quad (2.43)$$

where \mathcal{R}_j is the reluctance of the j th element, e_j , given by

$$\mathcal{R}_j = \int_{e_j} \frac{dl}{\mu A}. \quad (2.44)$$

Consider now a system with a single-branch magnetic circuit, no eddy currents in the core and a coil of N turns and electric current i . In that case, Ampère's law can be rewritten using (2.41) as

$$\phi \mathcal{R} = N i. \quad (2.45)$$

This expression, which is often called Hopkinson's law after John Hopkinson, establishes an equivalence between magnetic and electrical circuits. In this equivalence, the reluctance \mathcal{R} plays the role of the resistance, the magnetic flux ϕ acts as the current and the product $N i$, which is known as magnetomotive force, replaces the voltage. In fact, any multi-branch magnetic circuit can be solved by using Kirchhoff laws, only by substituting the electrical variables in the equations by their respective magnetic counterparts. When Hopkinson's law is combined with (2.33), the electrical equation of a coil transforms into

$$v = R i + N^2 \frac{d}{dt} \left(\frac{i}{\mathcal{R}} \right). \quad (2.46)$$

Furthermore, for a magnetically linear system with no moving parts, i.e., having a constant \mathcal{R} , this leads to

$$v = R i + \frac{N^2}{\mathcal{R}} \frac{di}{dt} = R i + L \frac{di}{dt}, \quad (2.47)$$

which is the well-known differential equation of a coil of constant inductance $L = N^2/\mathcal{R}$.

Despite the advantages of using reluctances, it has been shown in Section 2.1 that the relation $H = B/\mu$ is not able to describe hysteretic effects. Consequently, if magnetic

hysteresis exists in any of the materials of the system and it cannot be assumed negligible, (2.41)–(2.42) must be considered invalid. In that case, the MEC approach can still be used to simplify the circulation of H as

$$\oint_{\partial\Sigma} H \, dl = \int_{\partial\Sigma_\mu} H \, dl + \int_{\partial\Sigma_{\bar{\mu}}} H \, dl = \phi \mathcal{R}_\mu + \int_{\partial\Sigma_{\bar{\mu}}} H \, dl, \quad (2.48)$$

where $\partial\Sigma_\mu$ denotes the part of the circuit that can be characterized using the magnetic permeability, \mathcal{R}_μ is the reluctance of that part and $\partial\Sigma_{\bar{\mu}}$ refers to the rest of $\partial\Sigma$, whose analysis requires a different methodology presented later in this chapter.

The assumptions of the MEC method can also be used to simplify the energy analysis. Considering that a differential volume of the system dV can be expressed as the product of the cross section and a differential length along the circuit, i.e., $dV = A \, dl$, the magnetic work done in any segment of the circuit [see (2.16)–(2.17)] is given by

$$W_m = \int w_m A \, dl, \quad (2.49)$$

where the magnetic work density, which in general depends on the position along the circuit and time, is given by

$$w_m = w_m(l, t) = \int_0^{B(l, t)} H(l, t) \, \delta B = \int_{-\infty}^t H(l, t) \frac{\partial B(l, t)}{\partial t} \, dt. \quad (2.50)$$

The partial derivative of w_m with respect to time can also be obtained from the previous expression as

$$\frac{\partial w_m(l, t)}{\partial t} = H(l, t) \frac{\partial B(l, t)}{\partial t}. \quad (2.51)$$

Furthermore, if the material is magnetically linear [see (2.18)], the expression for the magnetic energy stored in any segment of the circuit is simplified into

$$W_m = \int \left(\frac{1}{2} B H \right) A \, dl = \frac{1}{2} \phi \int H \, dl. \quad (2.52)$$

Then, considering the particular case of (2.45), the magnetic energy of the whole system can be expressed in terms of the flux, the number of turns of the coil and the current,

$$W_m = \frac{1}{2} \phi \oint H \, dl = \frac{1}{2} \phi N i. \quad (2.53)$$

With regard to the application of the MEC methodology to the analysis of reluctance actuators (see Fig. 2.2), it should be highlighted that two different approaches are considered in this thesis. Assuming that the B – H relation in the iron can be described through magnetic permeability, (2.35) is transformed into

$$\phi (\mathcal{R}_{\text{gap}} + \mathcal{R}_{\text{core}}) = N i + i_{ec}, \quad (2.54)$$

where \mathcal{R}_{gap} and $\mathcal{R}_{\text{core}}$ are respectively the reluctances of the air gap and the iron core, given by

$$\mathcal{R}_{\text{gap}} = \int_{\partial\Sigma_{\text{gap}}} \frac{dl}{\mu_0 A}, \quad (2.55)$$

$$\mathcal{R}_{\text{core}} = \int_{\partial\Sigma_{\text{core}}} \frac{dl}{\mu A}. \quad (2.56)$$

On the other hand, if magnetic hysteresis is considered in the model, the application of (2.48) to Ampère’s law leads to

$$\phi \mathcal{R}_{\text{gap}} + \int_{\partial\Sigma_{\text{core}}} H \, dl = N i + i_{\text{ec}}. \quad (2.57)$$

Different expressions for \mathcal{R}_{gap} and $\mathcal{R}_{\text{core}}$, as well as for $\int_{\partial\Sigma_{\text{core}}} H \, dl$ and i_{ec} , are derived and presented in the remaining sections of the chapter.

2.3.2 Finite element method

The magnetic analysis based on the MEC approximation is complemented in this thesis with numerical simulations using the Finite Element Method (FEM). These are used either to numerically solve specific parts of the model or to verify some of the assumptions adopted in the analysis. In particular, two models have been built using the software COMSOL Multiphysics, each corresponding to one of the devices presented in Section 1.4. The geometry of these models, as well as some details of the implemented meshes, are shown in Figs. 2.4 and 2.5. It should be highlighted that the coil of each device is modeled as a single-turn coil of rectangular section with uniform current density and total current $N i$. This simplification is widely used in the simulation of inductors [129], reduces significantly the modeling stage and the simulation time, and is magnetically equivalent to modeling all the turns of the coil. The existing symmetries are also exploited in the models to reduce the computational cost of the simulations.

In general, FEM models cannot be used for real-time estimation or control purposes because the simulation time may vary between a few seconds to several hours depending on the study. Nevertheless, they may provide comprehensive information of the magnetic behavior of reluctance actuators. In this regard, the performed simulations show that the assumptions of the MEC modeling approach are very accurate in the studied devices. This can be seen, e.g., in Figs. 2.6 and 2.7, which show the magnetic flux density in the longitudinal cross sections of the relay and the valve, respectively. As shown, the magnetic flux in both devices is mostly confined in the iron core—with the exception of air gaps—and, as stated by (2.39), the flux density is higher the smaller the cross section of the circuit. Furthermore, the magnetic flux density in any given cross section is also very uniform, which confirms that the average-value approximation of the MEC methodology can be used with small error. This is more clearly seen in Figs. 2.8 and 2.9, which show the flux density in two transverse cross sections of the devices (note that each figure plots two different cross sections of the magnetic circuit of the corresponding device). As can be observed, the flux density has a high uniformity in all the cases.

FEM models can also be used to obtain the reluctance of a magnetic system as an alternative to the analytical method of (2.42)–(2.44). For a single branch magnetic circuit as that of Fig. 2.2, the procedure is as follows: Stationary simulations are firstly performed considering the electric current as the model input, the output results are processed to obtain the magnetic flux in the device, and, finally, the reluctance is obtained from Hopkinson’s law as

$$\mathcal{R} = Ni/\phi. \quad (2.58)$$

Note that Hopkinson’s law can be used in the form of (2.45) because of the stationary condition, which implies that there are no induced currents in the iron. Then, according to

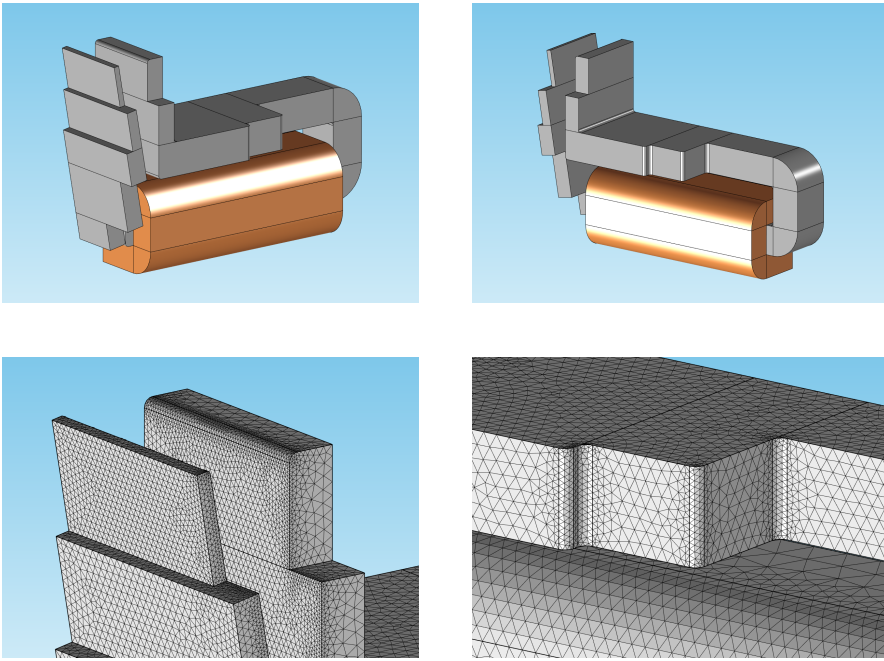


Figure 2.4: Three-dimensional Finite Element model of the studied relay. Geometry (top) and details of the mesh (bottom). The device is symmetric with respect to its longitudinal vertical plane.

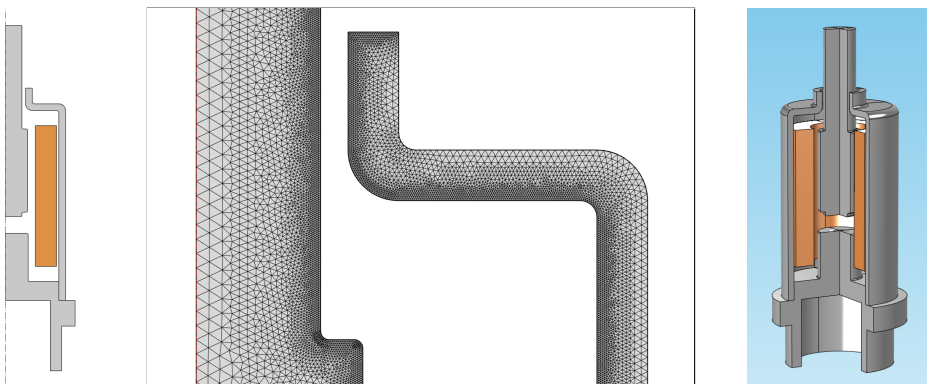


Figure 2.5: Axisymmetric Finite Element model of the studied solenoid valve. Geometry (left), detail of the mesh (center) and revolved shape (right). The device is symmetric with respect to its longitudinal axis.

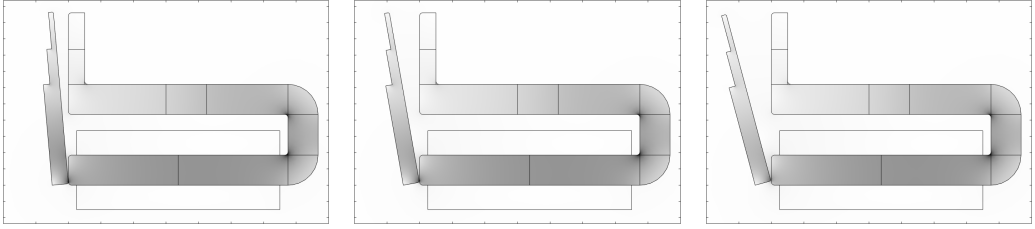


Figure 2.6: Magnetic flux density in the longitudinal cross section of the relay for gap angles of 5, 10 and 15 degrees. Results from stationary FEM simulations (linear iron, $\mu_{r\text{core}} = 100$, $Ni = 150$ A). The color scale goes from white for 0 T to black for 1.25 T.

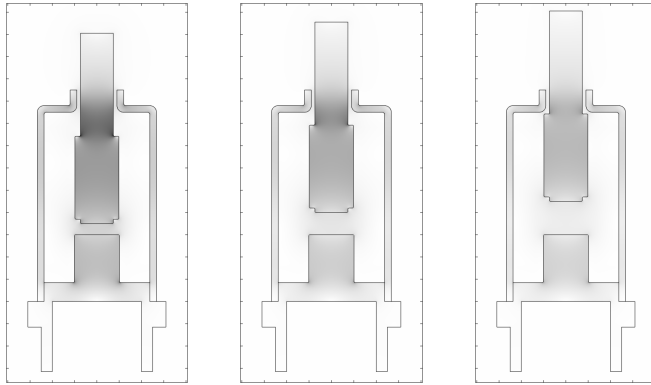


Figure 2.7: Magnetic flux density in the longitudinal cross section of the solenoid valve for gap lengths of 1, 2 and 3 mm. Results from stationary FEM simulations (linear iron, $\mu_{r\text{core}} = 100$, $Ni = 300$ A). The color scale goes from white for 0 T to black for 1.25 T.

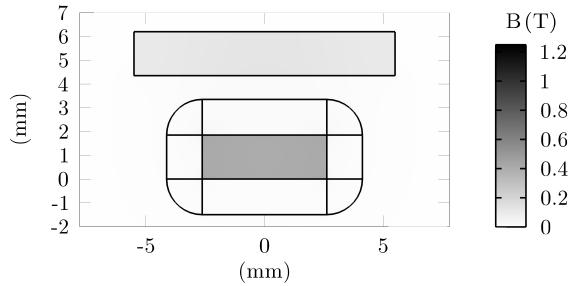


Figure 2.8: Magnetic flux density in a transverse cross section of the relay. Results from stationary FEM simulations (gap angle: 15 degrees, linear iron, $\mu_{r\text{core}} = 100$, $Ni = 150$ A). Lower section average value: 0.410 T. Standard deviation: 4.10 mT (1% of the average value). Upper section average value: 0.115 T. Standard deviation: 7.89 mT (7% of the average value).

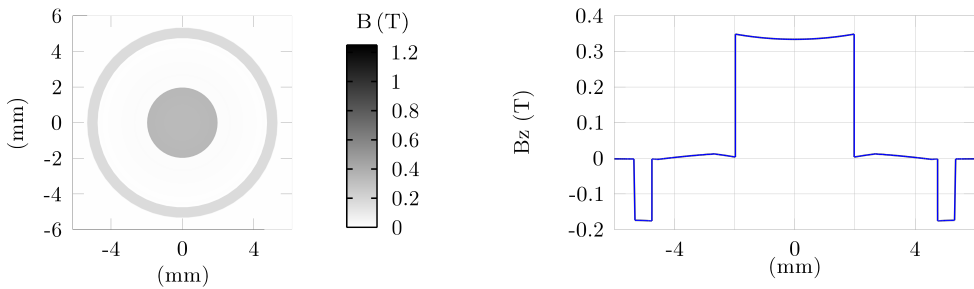


Figure 2.9: Magnetic flux density in the solenoid valve. Transverse cross section (left) and diametrical line (right). Results from stationary FEM simulations (gap length: 3 mm, linear iron, $\mu_{r\text{core}} = 100$, $Ni = 300$ A). Inner section average value: 0.339 T. Standard deviation: 4.40 mT (1.3% of the average value). Outer section average value: 0.174 T. Standard deviation: 0.533 mT (0.3% of the average value).

(2.39), the magnetic flux may be computed in any arbitrary cross section of the circuit. However, since having a perfect description of $A(l)$ is unlikely—it covers not only the core cross section but also the surrounding air where \mathbf{B} is non-zero—the accuracy of the previous expression depends greatly on the selection of $A(l)$. As a result, the applicability of this method is limited in practice. Another expression for the reluctance that prevents from errors when computing ϕ can still be obtained from FEM simulations using the magnetic energy stored in the system. Under the assumption that the core material is magnetically linear, the magnetic energy of the system is given by (2.53). Hence, since W_m can be numerically computed from the FEM results, the flux can be obtained as $\phi = 2W_m/Ni$ and, thus, the reluctance can be calculated as

$$\mathcal{R} = \frac{N^2 i^2}{2W_m}. \quad (2.59)$$

This methodology has been applied to the studied devices using the already presented FEM models. Six different values of the relative magnetic permeability of the core, $\mu_{r\text{core}}$, have been used in the simulations in order to analyze the complete range of usual values for ferromagnetic materials. The highest selected value, which is $\mu_{r\text{core}} = 10^6$, is used as an approximation for infinite magnetic permeability, i.e., the reluctance of the iron core in this case can be considered negligible ($\mathcal{R}_{\text{core}} \approx 0$) and, consequently, \mathcal{R} only consists of the air gap term ($\mathcal{R} \approx \mathcal{R}_{\text{gap}}$). The obtained results are presented in Figs. 2.10 and 2.11, which show both the reluctance and its inverse. This latter variable, which is known as permeance, is equal to the inductance of the device per square turn (L/N^2). For both devices, \mathcal{R} begins with a value that corresponds to zero gap and, accordingly to (2.42), is higher the lower the magnetic permeability of the core. Note that the initial reluctance of the valve for $\mu_{r\text{core}} = 10^6$ is not zero although the core can be assumed perfectly magnetically permeable; this is due to the existence of a secondary annular air gap between the housing and the movable core (see Fig. 2.5). For the rest of positions, given that the air is a low permeable material compared to the core, the reluctance increases with the gap length. However, it is noteworthy that the increase is much higher for the valve than for the relay, which is a result of the particular geometry of each device and the type of motion (linear/angular) of the armature.

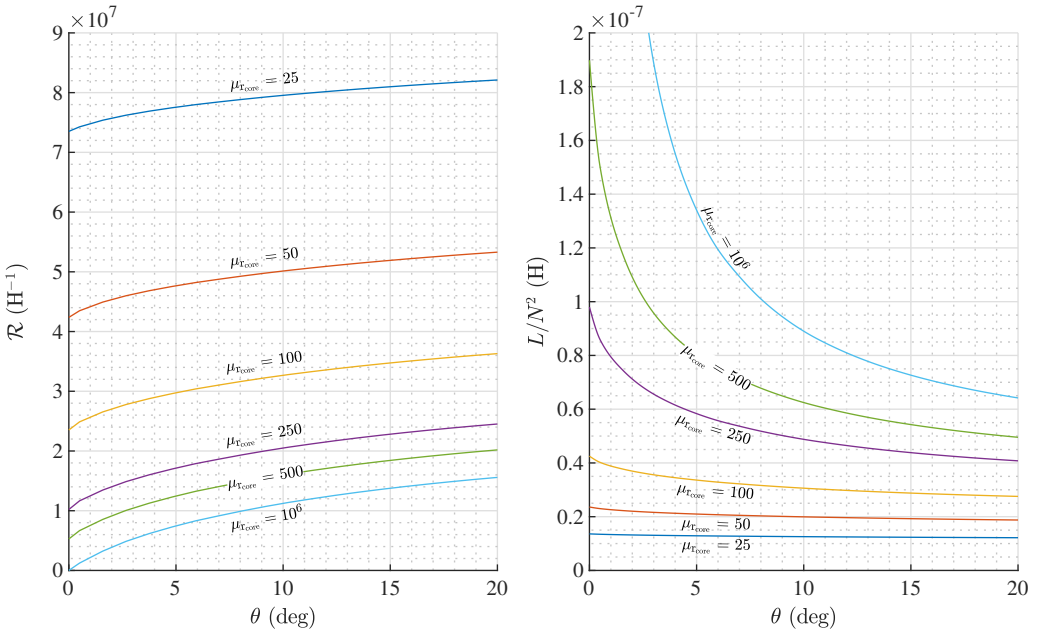


Figure 2.10: Relay reluctance (left) and permeance (right) obtained from FEM simulations as a function of the gap angle, θ , and the core relative permeability, $\mu_{\text{r,core}}$.

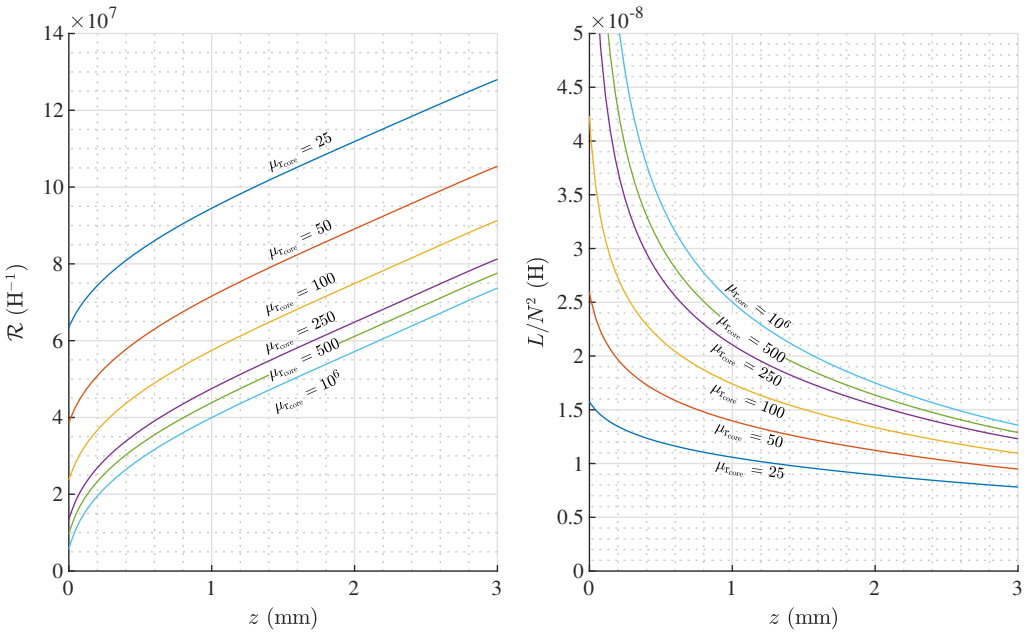


Figure 2.11: Solenoid valve reluctance (left) and permeance (right) obtained from FEM simulations as a function of the gap length, z , and the core relative permeability, $\mu_{\text{r,core}}$.

2.4 Flux fringing

Flux fringing is a phenomenon that occurs in magnetic systems, specifically in the surroundings of air gaps, by which the flux spreads out into the air [130]. As shown in Fig. 2.12, the magnetic flux in the air gap does not flow in straight lines, but in curved trajectories. The reason for this to happen is that the flux, which is mostly confined within the iron core until it reaches the gap, is suddenly transmitted into a very low permeable material without boundaries. Since there is no low-permeability path across the air, the flux lines spread out to fill the space evenly and make full use of the available medium.

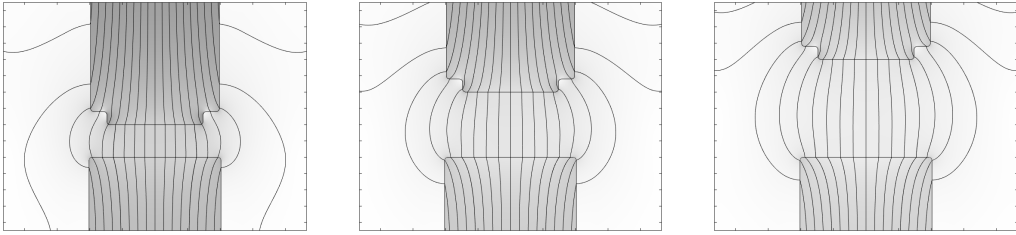


Figure 2.12: Flux fringing in the solenoid valve. Gap lengths of 1, 2 and 3 mm. Results from FEM simulations (linear iron, $\mu_{r\text{core}} = 100$, $Ni = 300$ A). The color scale goes from white for 0 T to black for 1.25 T.

With regard to the dynamical modeling of reluctance actuators, flux fringing causes the effective area of the magnetic circuit to increase in the surroundings of air gaps. As a consequence, an overestimated value of the air gap reluctance is obtained if the gap geometry is assumed to have a constant cross section equal to that of the iron core, i.e., if (2.55) is approximated by

$$\mathcal{R}_{\text{gap}} = \frac{l_{\text{gap}}}{\mu_0 A_{\text{core}}}, \quad (2.60)$$

where

$$l_{\text{gap}} = \int_{\partial\Sigma_{\text{gap}}} dl \quad (2.61)$$

is the length of the air gap and A_{core} is the cross-sectional area of the iron core in the boundaries of the gap. In this connection, the correction factor proposed by McLyman [130] can be used to obtain more accurate values for the reluctance in the case of linear gaps. This factor, which is greater or equal than one, is given by

$$F_{\text{McLyman}}(l_{\text{gap}}) = \begin{cases} 1 & \text{if } l_{\text{gap}} = 0, \\ 1 + \frac{l_{\text{gap}}}{\sqrt{A_{\text{core}}}} \log\left(\frac{2l_w}{l_{\text{gap}}}\right) & \text{if } l_{\text{gap}} > 0, \end{cases} \quad (2.62)$$

where l_w is a dimension related to the winding length and the iron geometry (see the cited reference). The corrected reluctance is then obtained by dividing (2.60) by F_{McLyman} .

The previous correction factor provides reasonable approximations for E-core, C-core or plunger-type reluctance actuators. However, it should be taken into account that it is

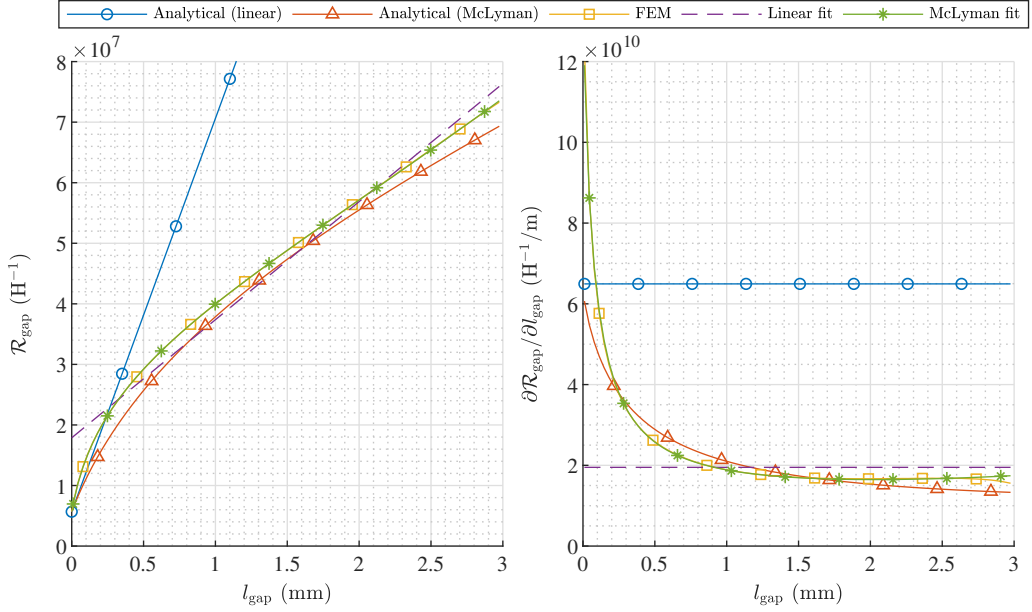


Figure 2.13: Comparison of approaches for modeling the air gap of the studied solenoid valve. Reluctance (left) and partial derivative with respect to the gap length (right).

an empirical expression which may not be accurate enough for more complex geometries. In addition, it cannot be directly applied to rotary motion devices such as the studied relay (see Section 1.4), where neither (2.60) nor (2.62) are clearly defined. For those cases, \mathcal{R}_{gap} can be numerically obtained from FEM models like those presented in the previous section. As explained, the gap reluctance can be computed using a magnetically linear model with an iron permeability much greater than μ_0 . In that case, the reluctance of the iron core can be considered negligible and, consequently, the air gap reluctance is directly provided by (2.59).

As an application example, these three approaches have been used to model the reluctance of the studied solenoid valve. The obtained results, which include also the contribution of the secondary annular gap described in the previous section, are presented in Fig. 2.13. It can be seen that the analytical reluctance with no correction factor is only valid for very small gaps. Indeed, it has very large errors for gap lengths beyond 0.5 mm. On the other hand, the reluctance obtained by applying the correction factor is similar to the FEM reluctance. The root-mean-square deviation (RMSD) between both approaches is $2.8 \cdot 10^6 \text{ H}^{-1}$, which represents about 6.3% of the mean value of the reluctance. In addition, the graph also shows two fittings to the FEM results: one corresponding to a linear reluctance and another one to a corrected reluctance using the McLyman factor. While this latter expression fits almost perfectly, the linear fit achieves a RMSD of $2.4 \cdot 10^6 \text{ H}^{-1}$ (5.9% of the mean value), which is in fact smaller than the RMSD of the theoretical McLyman expression. It is thus concluded that a linear expression fitted by identification methods may also describe accurately the air gap reluctance in some cases.

The second graph of Fig. 2.13 shows the partial derivative of the reluctance with

respect to the gap length. As it will be seen later in the chapter, this variable is one of the factors of the magnetic force in reluctance actuators. The graph shows that, although there are significant differences for small gaps, the FEM model and the McLyman analytical model are qualitatively very similar. In this regard, the existing differences are due to the selected theoretical values of the parameters and, as shown by the McLyman fit, they could be greatly reduced by using identification procedures. On the other hand, the models that assume a reluctance that varies linearly with the gap length—both the theoretical version and the linear fit to the FEM model—are not able to reproduce the qualitative behavior of the other methods, especially for small gaps. As a consequence, these approximations should not be used to compute the force when designing precise dynamical models for reluctance actuators.

In this thesis, both numerical and analytical reluctances of the air gap are used depending on the accuracy and the purpose of the constructed model.

2.5 Magnetic saturation

Magnetic cores are generally made from ferromagnetic materials such as iron, ferrite or magnetic steel, which exhibit a high magnetization when an external magnetic field is applied. This property is advantageous in magnetic systems in order to increase the strength of the magnetic flux and confine it within the core. In this regard, ferromagnetic materials make it possible, e.g., to create coils with inductance values hundreds of times greater than those of air core inductors, or to generate the strong magnetic forces that produce the motion in reluctance actuators.

Magnetization in ferromagnetic materials is produced by the alignment of magnetic moments on an atomic scale [131]. When a moderate magnetic field is applied to a ferromagnetic material, the resulting magnetic alignment is low and the material can be modeled using a constant magnetic permeability. In that case, the reluctance of the core [see (2.56)] has also a constant value given by

$$\mathcal{R}_{\text{core}} = \frac{1}{\mu_{\text{core}}} \int_{\partial\Sigma_{\text{core}}} \frac{dl}{A}, \quad (2.63)$$

where μ_{core} is the permeability of the core material. Nevertheless, if the external magnetic field is strong enough, all the magnetic moments align in the same direction and the magnetization no longer increases. This phenomenon, which is known as magnetic saturation, is usually prevented in the design of inductors by using air gaps that increase the total reluctance. However, it is almost unavoidable in reluctance actuators where air gaps change shape over time and may even disappear at some instants.

In order to incorporate magnetic saturation into a dynamical model, the magnetic core should be divided into several elements with an approximately constant cross-sectional area. This way, $\mathcal{R}_{\text{core}}$ may be calculated as a sum of reluctances,

$$\mathcal{R}_{\text{core}} = \sum_j \frac{l_j}{\mu_{\text{core}}(B_j) A_j}, \quad (2.64)$$

where l_j , A_j and B_j are respectively the length, the cross-sectional area and the (uniform) flux density of the j th element, and μ_{core} is no longer a constant but a function of B . The

core permeability could also be expressed in terms of the magnetic field intensity, but the first option is particularly advantageous in solving the differential equations of the system. Note that, according to (2.39), $B_j = \phi / A_j$, so (2.54) can be directly rewritten as a relation between ϕ , i and i_{ec} .

$$\phi \left(\mathcal{R}_{\text{gap}} + \sum_j \frac{l_j}{\mu_{\text{core}}(\phi/A_j) A_j} \right) = N i + i_{ec} \quad (2.65)$$

Table 2.1 and Fig. 2.14 show different empirical models which may be used to describe magnetic saturation. In particular, the table presents five analytic functions to model the B - H relation and the corresponding expressions for the magnetic permeability in terms of B and H . Graphical representations of these functions are plotted in the figure. The expressions are normalized so that the saturation level and the slope at the origin of all of them are respectively

$$\lim_{H \rightarrow \infty} B = a, \quad \left. \frac{\partial B}{\partial H} \right|_{H=0} = \frac{a}{b}.$$

In this connection, it should be noted that the variable that physically saturates is not B but the magnetization M . However, considering that $B = \mu_0(H + M)$ and that $M \gg H$ in ferromagnetic materials, the increase in B beyond saturation can be assumed negligible. Although this approximation may look trivial, it allows for finding simple explicit functions for both $\mu(H)$ and $\mu(B)$.

The first function in the table, which is known as the Fröhlich-Kennelly model for saturation [132], has been widely used in the dynamical modeling of reluctance actuators [80, 98, 107] due to its simplicity. Note that the absolute value in the denominator provides symmetry around the origin and extends the domain of $B(H)$ and $\mu(H)$ to all real numbers. When using this model, the reluctance (2.64) can be rewritten as

$$\mathcal{R}_{\text{core}} = \sum_j \frac{\mathcal{R}_{0_j}}{1 - |\phi|/\phi_{\text{sat}_j}}, \quad (2.66)$$

where \mathcal{R}_{0_j} and ϕ_{sat_j} are constants that represent, respectively, the reluctance for zero flux and the saturation flux of the j th element, given by

$$\mathcal{R}_{0_j} = \frac{l_j}{\frac{a}{b} A_j}, \quad \phi_{\text{sat}_j} = a A_j.$$

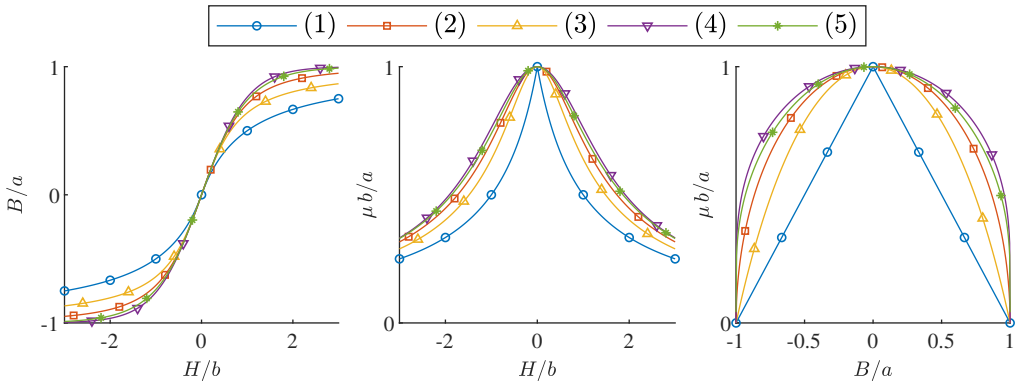
The second saturation model in Table 2.1 provides a different shape while maintaining the good properties of the Fröhlich-Kennelly relation. Furthermore, sigmoid functions such as the arctangent, the hyperbolic tangent or the Gudermannian function (models 3, 4 and 5 in the table, respectively) may also be used to model magnetic saturation when the two previous algebraic functions do not describe accurately the B - H relation. However, note that the permeability functions of these models in the table are not defined for $H = B = 0$. This can be easily solved by redefining μ as a piecewise function,

$$\mu_{\text{sigmoid}} = \begin{cases} a/b, & \text{if } H = B = 0, \\ \mu, & \text{otherwise,} \end{cases} \quad (2.67)$$

where μ_{sigmoid} is the corrected version of the permeability function for these models.

Table 2.1: Candidate functions for modeling magnetic saturation.

	$B-H$	$\mu(H)$	$\mu(B)$
1)	$B = \frac{aH}{b + H }$	$\frac{a}{b + H }$	$\frac{a - B }{b}$
2)	$B = \frac{aH}{\sqrt{b^2 + H^2}}$	$\frac{a}{\sqrt{b^2 + H^2}}$	$\frac{\sqrt{a^2 - B^2}}{b}$
3)	$B = \frac{2a}{\pi} \operatorname{atan}\left(\frac{\pi H}{2b}\right)$	$\frac{2a}{\pi H} \operatorname{atan}\left(\frac{\pi H}{2b}\right)$	$\frac{\pi B}{2b \tan\left(\frac{\pi B}{2a}\right)}$
4)	$B = a \tanh\left(\frac{H}{b}\right)$	$\frac{a}{H} \tanh\left(\frac{H}{b}\right)$	$\frac{B}{b \operatorname{atanh}\left(\frac{B}{a}\right)}$
5)	$B = \frac{4a}{\pi} \operatorname{atan}\left(\tanh\left(\frac{\pi H}{4b}\right)\right)$	$\frac{4a}{\pi H} \operatorname{atan}\left(\tanh\left(\frac{\pi H}{4b}\right)\right)$	$\frac{\pi B}{4b \operatorname{atanh}\left(\tan\left(\frac{\pi B}{4a}\right)\right)}$


 Figure 2.14: Candidate functions for modeling magnetic saturation. $B-H$ relation (left), $\mu(H)$ (center) and $\mu(B)$ (right). The functions are defined in Table 2.1.

2.6 Magnetic hysteresis

Magnetization in ferromagnetic materials is usually associated with magnetic hysteresis [131]. This phenomenon is due to the fact that the alignment of atomic dipoles in ferromagnetic materials, which is the origin of magnetic saturation, is actually an irreversible process that dissipates energy. As a consequence, the \mathbf{B} – \mathbf{H} relation becomes hysteretic, i.e., the flux density at any instant not only depends on the instantaneous excitation, but also on the past history of \mathbf{H} .

Magnetic materials are usually classified as soft or hard depending on the shape of the hysteresis loop (see Fig. 2.15). Soft magnetic materials, which have a narrow hysteresis loop, are commonly used in transformers, motors or electromagnets because of their low energy dissipation. On the other hand, hard magnetic materials have wide hysteresis loops and are used in applications where magnetic remanence—the magnetization that remains when the applied magnetic field is zero—is advantageous, such as magnetic storage devices or permanent magnets.

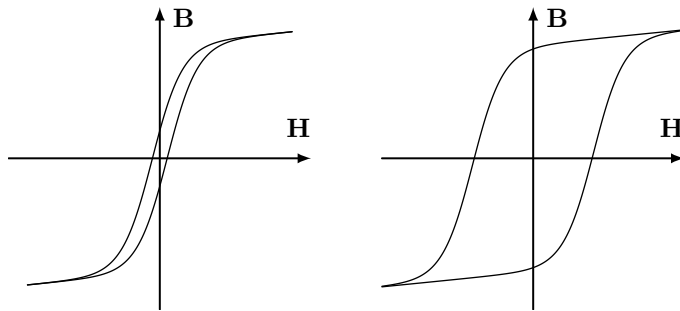


Figure 2.15: Magnetic hysteresis in magnetically soft (left) and hard (right) materials.

Magnetic cores in reluctance actuators are generally made from soft magnetic materials in order to reduce the energy consumption of the device. Hence, assuming that the material has a narrow \mathbf{B} – \mathbf{H} loop, the effects of magnetic hysteresis on the dynamic behavior of the system could be neglected. In those cases, the techniques presented in the previous section to model magnetic saturation are accurate enough to build a dynamical model for the actuator.

Despite the use of soft magnetic materials, it has been shown [23] that magnetic hysteresis still plays a significant role in the dynamics of many reluctance actuators. Hence, if magnetic hysteresis cannot be assumed negligible, the reluctance approach should be completely disregarded for modeling the iron core (see Section 2.3). In this section, a specific formulation of the Preisach model for hysteresis is derived for its use in the dynamical modeling of reluctance actuators. Although many other methodologies may be adopted to model magnetic hysteresis [23], the Preisach model is used in this thesis for being the most common approach in the literature.

Similarly to the analysis of Section 2.5, it is assumed that the core can be divided into several elements of constant cross-sectional area. Under this assumption, the circulation

of the magnetic field intensity in the core can be expressed as

$$\int_{\partial\Sigma_{\text{core}}} H \, dl = \sum_j H_j l_j, \quad (2.68)$$

where l_j and H_j are respectively the length and the (uniform) magnetic field intensity of the j th element. The analysis presented in the following pages provides a relation between B and H that can be used to solve the set of dynamic equations of the actuator.

Classical Preisach Model

The classical Preisach model (CPM) [133, 134] is based on an infinite set of basic hysteresis operators also known as *hysterons* (see Fig. 2.16). Each hysteron is characterized by two threshold values, α and β , which describe the output of the operator in terms of the time-dependent input $u = u(t)$ as

$$\gamma(\alpha, \beta, u, u_{\text{past}}) = \begin{cases} +1, & \text{if } u \geq \alpha, \\ -1, & \text{if } u \leq \beta, \\ \gamma_{\text{past}}, & \text{if } \beta < u < \alpha, \end{cases} \quad (2.69)$$

where u_{past} is the last extremum of u outside the interval (β, α) and γ_{past} is the hysteron output for that value. Considering α and β as coordinates, the infinite hysterons are usually represented as points in the so-called Preisach plane (see Fig. 2.17). Note that, since α is always greater than β , all of the hysterons are in fact located in the $\alpha > \beta$ half-plane.

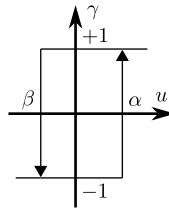


Figure 2.16: Hysteron operator with threshold values α and β .

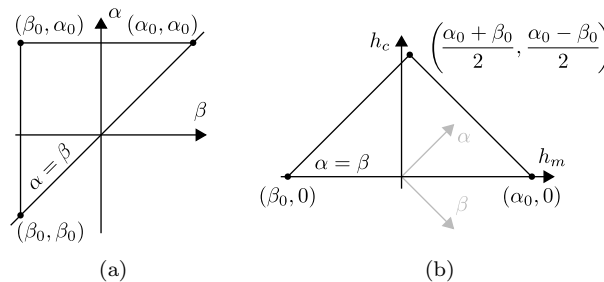


Figure 2.17: Preisach plane in the (a) β - α and (b) h_m - h_c coordinate systems.

The output of the CPM is then given by the sum of the outputs of the infinite number of hysteresis operators,

$$f_{\text{CPM}}(u, \mathcal{U}) = \int_{\alpha > \beta} P(\alpha, \beta) \gamma(\alpha, \beta, u, u_{\text{past}}) \, d\alpha \, d\beta, \quad (2.70)$$

where $\mathcal{U} = \mathcal{U}(t) = \{u(\tau) \mid \tau < t\}$ contains the history of u , from which u_{past} can be obtained for each hysteron, and $P(\alpha, \beta)$ is the Preisach function, which may be interpreted either as a weight function for an infinite set of homogeneously distributed hysterons or as a density function describing a non-homogeneous distribution of hysterons in the Preisach plane. Assuming that the input is bounded between two constants β_0 and α_0 , $\beta_0 \leq u(t) \leq \alpha_0 \, \forall t$, the Preisach function can be considered equal to zero outside the triangle with vertices (β_0, α_0) , (α_0, α_0) , and (β_0, β_0) (see Fig. 2.17a).

In particular, due to the wiping-out property of the CPM [134], the history of any arbitrary input $u(t)$ is fully characterized by a set of previous maxima, $\mathcal{A} = \mathcal{A}(t)$, and a set of previous minima, $\mathcal{B} = \mathcal{B}(t)$, such that

$$\mathcal{A}(t) = \{\alpha_0\} \cup \{u(\tau) \mid \tau < t, u(\tau) \text{ is a maximum,} \\ \max \mathcal{B}(\tau) < u(s) < u(\tau) \, \forall s \in (\tau, t)\}, \quad (2.71)$$

$$\mathcal{B}(t) = \{\beta_0\} \cup \{u(\tau) \mid \tau < t, u(\tau) \text{ is a minimum,} \\ u(\tau) < u(s) < \min \mathcal{A}(\tau) \, \forall s \in (\tau, t)\}. \quad (2.72)$$

That is, a maximum (minimum) of u at time τ is part of \mathcal{A} (\mathcal{B}) at time t if and only if all u after τ and before t has been contained between that maximum (minimum) and the immediately preceding minimum (maximum). If u is initialized from its minimum possible value, i.e., $u(-\infty) = \beta_0$, then $|\mathcal{B}| = |\mathcal{A}|$ for increasing input and $|\mathcal{B}| = |\mathcal{A}| - 1$ for decreasing input, where the operator $|\cdot|$ denotes the cardinality of the set. The notations α_i and β_j refer respectively to the i th largest element of $\mathcal{A} \setminus \{\alpha_0\}$ and the j th smallest element of $\mathcal{B} \setminus \{\beta_0\}$. As shown in Fig. 2.18, the previous sets divide the Preisach plane into two regions, $S^+(u, \mathcal{A}, \mathcal{B})$ and $S^-(u, \mathcal{A}, \mathcal{B})$, in which the output of the hysterons are respectively equal to $+1$ and -1 . Hence, the integral (2.70) can be partitioned into the positive and negative regions.

$$f_{\text{CPM}}(u, \mathcal{A}, \mathcal{B}) = \iint_{S^+} P(\alpha, \beta) \, d\alpha \, d\beta - \iint_{S^-} P(\alpha, \beta) \, d\alpha \, d\beta \quad (2.73)$$

Additionally, defining the integral of the Preisach function over the triangle of vertices (β_j, α_i) , (α_i, α_i) and (β_j, β_j) as

$$T(\alpha_i, \beta_j) = \int_{\beta_j}^{\alpha_i} \int_{\beta}^{\alpha_i} P(\alpha, \beta) \, d\alpha \, d\beta, \quad (2.74)$$

the output of the CPM can be computed by addition and subtraction of triangle integrals. Hence, given $n = |\mathcal{A} \setminus \{\alpha_0\}|$, the output of the model for an increasing input (see Fig. 2.18a) is given by

$$f_{\text{CPM}}^{\nearrow}(u, \mathcal{A}, \mathcal{B}) = -T(\alpha_0, \beta_0) + 2 \sum_{k=1}^n T(\alpha_k, \beta_{k-1}) - 2 \sum_{k=1}^n T(\alpha_k, \beta_k) + 2T(u, \beta_n), \quad (2.75)$$

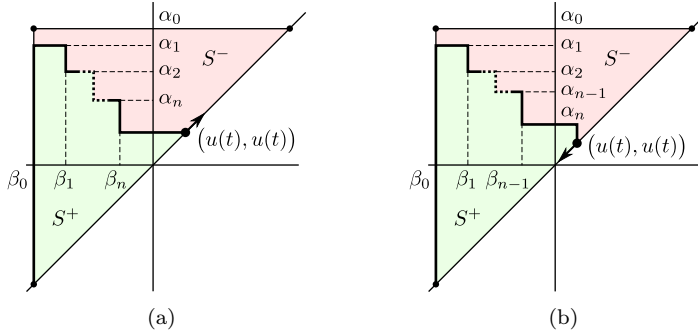


Figure 2.18: Preisach plane division for (a) increasing input and (b) decreasing input. The input is assumed to start at its minimum possible value β_0 .

whereas, for a decreasing input (see Fig. 2.18b), it is equal to

$$f_{\text{CPM}}^{\leftarrow}(u, \mathcal{A}, \mathcal{B}) = -T(\alpha_0, \beta_0) + 2 \sum_{k=1}^n T(\alpha_k, \beta_{k-1}) - 2 \sum_{k=1}^{n-1} T(\alpha_k, \beta_k) - 2T(\alpha_n, u). \quad (2.76)$$

Then, considering that the direction of the input is given by the sign of its time derivative, f_{CPM} can be actually regarded as a piecewise function of \dot{u} ,

$$f_{\text{CPM}}(u, \mathcal{A}, \mathcal{B}) = \begin{cases} f_{\text{CPM}}^{\rightarrow}(u, \mathcal{A}, \mathcal{B}), & \text{if } \dot{u} \geq 0, \\ f_{\text{CPM}}^{\leftarrow}(u, \mathcal{A}, \mathcal{B}), & \text{if } \dot{u} < 0. \end{cases} \quad (2.77)$$

Several functions have been used in the literature as Preisach functions [23]. The most general approach to construct such a function is to assume that P can be expressed as the product of two univariate probability density functions depending on $h_c = (\alpha - \beta)/2$ and $h_m = (\alpha + \beta)/2$ (see Fig. 2.17b), i.e.,

$$P(\alpha, \beta) = f_1(h_c) f_2(h_m) = f_1\left(\frac{\alpha - \beta}{2}\right) f_2\left(\frac{\alpha + \beta}{2}\right). \quad (2.78)$$

In this case, the surface integral (2.74) can be evaluated in the h_m - h_c coordinate system and transformed analytically into a numerically less expensive line integral,

$$T(\alpha_i, \beta_j) = 2 \int_0^{(\alpha_i - \beta_j)/2} f_1(h_c) \left[F_2(h_m) \right]_{\beta_j + h_c}^{\alpha_i - h_c} dh_c, \quad (2.79)$$

where the factor of 2 is the Jacobian of the transformation from β - α to h_m - h_c and $F_2(h_m)$ is the cumulative distribution function corresponding to $f_2(h_m)$.

The Cauchy distribution is known to be the best fit to most of the ferromagnetic materials [135–137]. Its probability density and cumulative distribution functions are

respectively given by

$$f_{\text{Cauchy}}(x | m_x, s_x) = \frac{1}{\pi s_x \left(1 + \left(\frac{x - m_x}{s_x} \right)^2 \right)}, \quad (2.80)$$

$$F_{\text{Cauchy}}(x | m_x, s_x) = \frac{1}{2} + \frac{1}{\pi} \arctan \left(\frac{x - m_x}{s_x} \right), \quad (2.81)$$

where m_x and s_x are the parameters that specify the location and shape of the distribution. In this thesis, both f_1 and f_2 are approximated by means of this distribution.

$$f_1(h_c) = f_{\text{Cauchy}}(h_c | m_{h_c}, s_{h_c}) \quad (2.82)$$

$$f_2(h_m) = f_{\text{Cauchy}}(h_m | m_{h_m}, s_{h_m}) \quad (2.83)$$

Note that, in order to obtain a symmetrical major hysteresis loop about the origin, m_{h_m} must be equal to zero. As a result, the proposed Preisach distribution only depends on three parameters: m_{h_c} , s_{h_c} and s_{h_m} .

Limitations and generalization

When applied to modeling magnetic hysteresis, the CPM has two major drawbacks, namely the zero magnetic permeability at the reversal points and the non-saturating behavior of the magnetization M . These are solved in the so-called generalized Preisach model (GPM) [138] by modeling the magnetic flux density B as the sum of two terms depending on the magnetic field intensity H ,

$$B = f_{\text{GPM}}(H, \mathcal{A}, \mathcal{B}) = B_{\text{Rev}}(H) + B_{\text{Irr}}(H, \mathcal{A}, \mathcal{B}), \quad (2.84)$$

where B_{Rev} is the *reversible* part, which is only dependent on the instantaneous value of H , and B_{Irr} is the *irreversible* part, which depends also on the past maxima, \mathcal{A} , and minima, \mathcal{B} , of H . This latter part is obtained by means of the CPM,

$$B_{\text{Irr}}(H, \mathcal{A}, \mathcal{B}) = \hat{B}_{\text{Irr}} \frac{f_{\text{CPM}}(H, \mathcal{A}, \mathcal{B})}{T(\alpha_0, \beta_0)}, \quad (2.85)$$

where \hat{B}_{Irr} is the saturation level of the irreversible part, $T(\alpha_0, \beta_0)$ acts as normalization factor, and f_{CPM} represents either $f_{\text{CPM}}^{\nearrow}$ or $f_{\text{CPM}}^{\searrow}$ depending on the direction of H . As a consequence, f_{GPM} can be also interpreted as a piecewise function of \dot{H} ,

$$f_{\text{GPM}}(H, \mathcal{A}, \mathcal{B}) = \begin{cases} f_{\text{GPM}}^{\nearrow}(H, \mathcal{A}, \mathcal{B}) = B_{\text{Rev}}(H) + \hat{B}_{\text{Irr}} \frac{f_{\text{CPM}}^{\nearrow}(H, \mathcal{A}, \mathcal{B})}{T(\alpha_0, \beta_0)}, & \text{if } \dot{H} \geq 0, \\ f_{\text{GPM}}^{\searrow}(H, \mathcal{A}, \mathcal{B}) = B_{\text{Rev}}(H) + \hat{B}_{\text{Irr}} \frac{f_{\text{CPM}}^{\searrow}(H, \mathcal{A}, \mathcal{B})}{T(\alpha_0, \beta_0)}, & \text{if } \dot{H} < 0. \end{cases} \quad (2.86)$$

The reversible component, which provides the non-zero permeability at the reversal points, is commonly expressed as the integral with respect to H of an incremental *reversible* permeability,

$$B_{\text{Rev}}(H) = \int_0^H \mu'_{\text{Rev}}(H) dH, \quad (2.87)$$

where $\mu'_{\text{Rev}}(H)$ is usually modeled by an analytical function which is fitted to measurements. Based on the double exponential function used in [23], in this thesis this permeability is modeled by

$$\mu'_{\text{Rev}}(H) = \mu_0 + \mu_1 e^{-|H|/H_1} + \mu_2 e^{-|H|/H_2}, \quad (2.88)$$

where μ_0 is the vacuum permeability and $\mu_1, \mu_2 \in \mathbb{R}$ and $H_1, H_2 \in \mathbb{R}^+$ are parameters to estimate. This expression leads to a reversible flux density equal to

$$B_{\text{Rev}}(H) = \mu_0 H + \text{sgn}(H) \mu_1 H_1 \left(1 - e^{-|H|/H_1}\right) + \text{sgn}(H) \mu_2 H_2 \left(1 - e^{-|H|/H_2}\right). \quad (2.89)$$

Note that, while the use of the absolute value provides symmetry about the origin, the addition of the vacuum permeability in (2.88) guarantees that M saturates. In this regard, considering that the magnetization modeled by the GPM is $M = (f_{\text{GPM}}(H, \mathcal{A}, \mathcal{B})/\mu_0 - H)$ and that $\lim_{H \rightarrow \infty} B_{\text{Irr}} = \hat{B}_{\text{Irr}}$, the saturation level can be obtained as

$$\lim_{H \rightarrow \infty} M = \frac{\mu_1 H_1 + \mu_2 H_2 + \hat{B}_{\text{Irr}}}{\mu_0}. \quad (2.90)$$

This expression can be used, for instance, to set physically meaningful initial values for the parameters to identify.

Time derivative of the GPM

In order to use the GPM in a dynamical model, it is advantageous to obtain the time derivative of B from (2.84) as

$$\dot{B} = \left(\frac{\partial B_{\text{Rev}}}{\partial H} + \frac{\partial B_{\text{Irr}}}{\partial H} \right) \dot{H}. \quad (2.91)$$

According to (2.87), $\partial B_{\text{Rev}}/\partial H = \mu'_{\text{Rev}}(H)$. Thus, an incremental *irreversible* permeability may be analogously defined as

$$\mu'_{\text{Irr}}(H, \mathcal{A}, \mathcal{B}) = \frac{\partial B_{\text{Irr}}(H, \mathcal{A}, \mathcal{B})}{\partial H}, \quad (2.92)$$

so that (2.91) can be expressed as

$$\dot{B} = (\mu'_{\text{Rev}}(H) + \mu'_{\text{Irr}}(H, \mathcal{A}, \mathcal{B})) \dot{H} = \mu'_{\text{GPM}}(H, \mathcal{A}, \mathcal{B}) \dot{H}, \quad (2.93)$$

where $\mu'_{\text{GPM}}(H, \mathcal{A}, \mathcal{B})$ is the incremental permeability of the GPM, given by the sum of the reversible and irreversible permeabilities.

The irreversible incremental permeability can be derived from (2.85) as

$$\mu'_{\text{Irr}}(H, \mathcal{A}, \mathcal{B}) = \frac{\hat{B}_{\text{Irr}}}{T(\alpha_0, \beta_0)} \frac{\partial f_{\text{CPM}}(H, \mathcal{A}, \mathcal{B})}{\partial H}. \quad (2.94)$$

Then, the partial derivative of $f_{\text{CPM}}(H, \mathcal{A}, \mathcal{B})$ with respect to H is obtained from (2.75)–(2.76),

$$\frac{\partial f_{\text{CPM}}(H, \mathcal{A}, \mathcal{B})}{\partial H} = \begin{cases} +2 \frac{\partial T(H, \beta_n)}{\partial H}, & \text{if } \dot{H} \geq 0, \\ -2 \frac{\partial T(\alpha_n, H)}{\partial H}, & \text{if } \dot{H} < 0, \end{cases} \quad (2.95)$$

where the partial derivatives of $T(H, \beta_n)$ and $T(\alpha_n, H)$ with respect to H can be calculated from (2.74) by applying Leibniz's integral rule,

$$\frac{\partial T(H, \beta_n)}{\partial H} = + \int_{\beta_n}^H P(H, \beta) d\beta, \quad (2.96)$$

$$\frac{\partial T(\alpha_n, H)}{\partial H} = - \int_H^{\alpha_n} P(\alpha, H) d\alpha. \quad (2.97)$$

It must be pointed out that, when using the Cauchy-based Preisach distribution proposed in Section 2.6, these integrals can be analytically solved and, consequently, the computation of $\mu'_{\text{GPM}}(H, \mathcal{A}, \mathcal{B})$ is not numerically expensive.

Combining the previous equations, the incremental permeability of the GPM is finally obtained as a function of H , \mathcal{A} , \mathcal{B} and the direction of H ,

$$\mu'_{\text{GPM}}(H, \mathcal{A}, \mathcal{B}) = \begin{cases} \mu'_{\text{GPM}}^{\nearrow}(H, \mathcal{A}, \mathcal{B}) = \mu'_{\text{Rev}}(H) + \frac{2 \hat{B}_{\text{Irr}}}{T(\alpha_0, \beta_0)} \int_{\beta_n}^H P(H, \beta) d\beta, & \text{if } \dot{H} \geq 0, \\ \mu'_{\text{GPM}}^{\searrow}(H, \mathcal{A}, \mathcal{B}) = \mu'_{\text{Rev}}(H) + \frac{2 \hat{B}_{\text{Irr}}}{T(\alpha_0, \beta_0)} \int_H^{\alpha_n} P(\alpha, H) d\alpha, & \text{if } \dot{H} < 0. \end{cases} \quad (2.98)$$

2.7 Eddy currents

Eddy currents, also known as Foucault currents, are loops of induced electric current that appear in conductive materials in the presence of changing magnetic fields [139]. As stated by Faraday's law [see (2.1)], any variation of the magnetic flux across a surface creates an electric field in its contour. Then, according to the microscopic form of Ohm's law [see (2.14)], electric currents will appear if the material is conductive. Note that the minus sign in (2.1) indicates that the direction of the induced current is such that it opposes the variation of the magnetic flux. As a consequence, the presence of eddy currents always slows down the dynamics of a magnetic system. In particular, the effect of eddy currents on reluctance actuators with electrically conductive cores is in general negative. On the one hand, they cause the actuator to be slower than in the case of having a non-conductive core, e.g., a ferrite core. On the other, they increase the energy consumption of the device due to the Joule losses in the iron.

The purpose of this section is to find a differential equation that relates the flux flowing through the core of a magnetic system and the equivalent eddy current induced within it. As an approximation, the theoretical analysis is derived for an infinite cylindrical core made of a magnetically and electrically linear material (see Fig. 2.19). Accordingly to the first assumption of the MEC methodology (see Section 2.3), the flux is assumed to have only longitudinal component (z -coordinate in Fig. 2.19). In addition, the symmetries of the problem make \mathbf{B} only dependent on time, t , and the radial distance, ρ . Since the flux density is a priori unknown, the analysis uses its Taylor series around $\rho = 0$,

$$\mathbf{B}(t, \rho) = B_z(t, \rho) \hat{\mathbf{z}} = \sum_{n=0}^{\infty} (b_n(t) \rho^n) \hat{\mathbf{z}}, \quad (2.99)$$

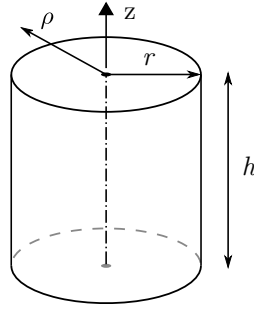


Figure 2.19: Portion of height h of an infinite cylindrical core of radius r . The cylindrical coordinate system (ρ, φ, z) is used in the analysis.

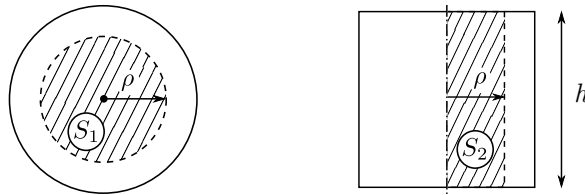


Figure 2.20: Transverse cross section (left) and longitudinal section (right) of the cylindrical core.

where B_z is the z -component of \mathbf{B} and

$$b_n(t) = \frac{1}{n!} \left. \frac{\partial^n B_z}{\partial \rho^n} \right|_{\rho=0}. \quad (2.100)$$

The analysis starts by applying Faraday's law [see (2.1)] to the surface $S_1(\rho)$ (see Fig. 2.20). The circulation of the electric field in the contour $\partial S_1(\rho)$ is firstly obtained as

$$\oint_{\partial S_1(\rho)} \mathbf{E} \cdot d\mathbf{l} = \int_0^{2\pi} E_\varphi \rho d\varphi = E_\varphi 2\pi\rho, \quad (2.101)$$

where E_φ is the φ -component of \mathbf{E} . On the other hand, the magnetic flux across $S_1(\rho)$ is calculated using (2.99) as

$$\begin{aligned} \int_{S_1(\rho)} \mathbf{B} \cdot d\mathbf{S} &= \int_0^\rho B_z 2\pi\rho d\rho = \int_0^\rho \sum_{n=0}^{\infty} (b_n \rho^n) 2\pi\rho d\rho = \\ &= 2\pi \sum_{n=0}^{\infty} \left(b_n \int_0^\rho \rho^{n+1} d\rho \right) = 2\pi \sum_{n=0}^{\infty} \left(b_n \frac{\rho^{n+2}}{n+2} \right). \end{aligned} \quad (2.102)$$

The electric field in the φ -coordinate, which is obtained by substituting the two previous expressions in (2.1), is given by

$$E_\varphi(t, \rho) = - \sum_{n=0}^{\infty} \left(\frac{db_n}{dt} \frac{\rho^{n+1}}{n+2} \right). \quad (2.103)$$

Then, according to Ohm's microscopic law [see (2.14)], the free current density in the φ -coordinate is

$$J_{f\varphi}(t, \rho) = \sigma E_\varphi(t, \rho) = -\sigma \sum_{n=0}^{\infty} \left(\frac{db_n}{dt} \frac{\rho^{n+1}}{n+2} \right). \quad (2.104)$$

The following step of the analysis is to apply Ampère's law [see (2.15)] to the surface $S_2(\rho)$ (see Fig. 2.20). The circulation of the magnetic field $\mathbf{H} = \mathbf{H}(t, \rho)$ in the contour $\partial S_2(\rho)$ is equal to

$$\oint_{\partial S_2(\rho)} \mathbf{H} \cdot d\mathbf{l} = H_z(t, 0) h - H_z(t, \rho) h, \quad (2.105)$$

where H_z is the z-component of \mathbf{H} . On the other hand, the surface integral of the current density on $S_2(\rho)$ is obtained as

$$\begin{aligned} \int_{S_2(\rho)} \mathbf{J}_f \cdot d\mathbf{S} &= h \int_0^\rho J_{f\varphi} d\rho = -h \int_0^\rho \sigma \sum_{n=0}^{\infty} \left(\frac{db_n}{dt} \frac{\rho^{n+1}}{n+2} \right) d\rho = \\ &= -\sigma h \sum_{n=0}^{\infty} \left(\frac{db_n}{dt} \int_0^\rho \frac{\rho^{n+1}}{n+2} d\rho \right) = -\sigma h \sum_{n=0}^{\infty} \left(\frac{db_n}{dt} \frac{\rho^{n+2}}{(n+2)^2} \right). \end{aligned} \quad (2.106)$$

Then, solving Ampère's law for the magnetic field in the z-direction,

$$H_z(t, \rho) = H_z(t, 0) + \sigma \sum_{n=0}^{\infty} \left(\frac{db_n}{dt} \frac{\rho^{n+2}}{(n+2)^2} \right). \quad (2.107)$$

Assuming that the material is magnetically linear, i.e., $\mathbf{B} = \mu \mathbf{H}$ with constant μ , the magnetic flux density in the z-coordinate is obtained from the previous expression as

$$B_z(t, \rho) = \mu H_z(t, \rho) = \mu H_z(t, 0) + \mu \sigma \sum_{n=2}^{\infty} \left(\frac{db_{n-2}}{dt} \frac{\rho^n}{n^2} \right). \quad (2.108)$$

Then, by matching the terms of the same order in (2.99) and (2.108), it is obtained that

$$b_0(t) = B_z(t, 0) = \mu H_z(t, 0), \quad (2.109)$$

$$b_1(t) = 0, \quad (2.110)$$

$$b_n(t) = \frac{\mu \sigma}{n^2} \frac{db_{n-2}}{dt}, \quad \forall n \in \mathbb{N} : n \geq 2. \quad (2.111)$$

Considering (2.110) and (2.111), it is straightforward that all the odd coefficients are equal to zero,

$$b_{2m+1}(t) = 0, \quad \forall m \in \mathbb{N}^0, \quad (2.112)$$

while the even coefficients are given by the sequence

$$b_{2m}(t) = \frac{\mu \sigma}{(2m)^2} \frac{db_{2m-2}}{dt} = \frac{\mu \sigma / 4}{m^2} \frac{db_{2m-2}}{dt}, \quad \forall m \in \mathbb{N}^+. \quad (2.113)$$

Since the initial term of the sequence is b_0 , the general term can be expressed as

$$b_{2m}(t) = \frac{(\mu \sigma / 4)^m}{m!^2} \frac{d^m b_0}{dt^m}, \quad \forall m \in \mathbb{N}^0. \quad (2.114)$$

From (2.112) and (2.114), it is possible to obtain an expression for B_z in terms of b_0 ,

$$\begin{aligned} B_z(t, \rho) &= \sum_{n=0}^{\infty} (b_n(t) \rho^n) = \sum_{m=0}^{\infty} (b_{2m}(t) \rho^{2m}) + \sum_{m=0}^{\infty} (b_{2m+1}(t) \rho^{2m+1}) = \\ &= \sum_{m=0}^{\infty} \left(\frac{(\mu\sigma/4)^m}{m!^2} \frac{d^m b_0}{dt^m} \rho^{2m} \right), \end{aligned} \quad (2.115)$$

and, integrating over the core cross section, also the expression for the magnetic flux,

$$\phi(t) = \int_{S_1(r)} \mathbf{B} \cdot d\mathbf{S} = \int_0^r B_z 2\pi\rho d\rho = \pi r^2 \sum_{m=0}^{\infty} \left(\frac{(\mu\sigma r^2/4)^m}{m!^2 (m+1)} \frac{d^m b_0}{dt^m} \right). \quad (2.116)$$

Similarly, the φ -component of the induced current density is obtained as

$$\begin{aligned} J_{f\varphi}(t, \rho) &= -\sigma \sum_{n=0}^{\infty} \left(\frac{db_n}{dt} \frac{\rho^{n+1}}{n+2} \right) = -\sigma \sum_{m=0}^{\infty} \left(\frac{db_{2m}}{dt} \frac{\rho^{2m+1}}{2m+2} \right) - \sigma \sum_{m=0}^{\infty} \left(\frac{db_{2m+1}}{dt} \frac{\rho^{2m+2}}{2m+3} \right) = \\ &= -\sigma \sum_{m=0}^{\infty} \left(\frac{(\mu\sigma/4)^m}{m!^2} \frac{d^{m+1} b_0}{dt^{m+1}} \frac{\rho^{2m+1}}{2m+2} \right). \end{aligned} \quad (2.117)$$

The equivalent eddy current, i_{ec} , is then given by the integral of $J_{f\varphi}$ over the longitudinal half section.

$$i_{ec}(t) = \int_{S_2(r)} \mathbf{J}_f \cdot d\mathbf{S} = h \int_0^r J_{f\varphi} d\rho = -\frac{hr^2\sigma}{4} \sum_{m=0}^{\infty} \left(\frac{(\mu\sigma r^2/4)^m}{m!^2 (m+1)^2} \frac{d^{m+1} b_0}{dt^{m+1}} \right) \quad (2.118)$$

The dynamic relation between flux ϕ and equivalent eddy current i_{ec} can be derived from (2.116) and (2.118), e.g., by using the Laplace transform. The resulting expression is

$$\sum_{m=0}^{\infty} \left(\frac{(\mu\sigma r^2/4)^m}{m!^2 (m+1)} \frac{d^m i_{ec}}{dt^m} \right) = -\frac{h\sigma}{4\pi} \sum_{m=0}^{\infty} \left(\frac{(\mu\sigma r^2/4)^m}{m!^2 (m+1)^2} \frac{d^{m+1} \phi}{dt^{m+1}} \right). \quad (2.119)$$

Since this equation contains infinite sums of the derivatives of ϕ and i_{ec} , it has no practical applicability. However, different approximations can be obtained by using only a limited number of terms of the summations. In particular, for m up to 0, it is obtained that

$$i_{ec} = -\frac{h\sigma}{4\pi} \frac{d\phi}{dt}, \quad (2.120)$$

which, according to (2.99) and (2.100), corresponds to the case of uniform B_z in the cross section (second assumption of the MEC methodology).

Similar procedures can be followed to obtain solutions for other cross-section geometries. For instance, the first-order approximation for a rectangular cross section [23] is given by

$$i_{ec} = -\frac{wd}{w^2 + d^2} \frac{\sigma h}{12} \frac{d\phi}{dt}, \quad (2.121)$$

where d and w are respectively the depth and width of the rectangle.

In this thesis, it is assumed that the first-order approximation of the ϕ - i_{ec} relation in a given core can always be expressed as

$$i_{ec} = -k_{\text{geom}} \sigma_{\text{core}} l_{\text{core}} \frac{d\phi}{dt}, \quad (2.122)$$

where k_{geom} is a constant that depends on the geometry of the cross section, σ_{core} is the conductivity of the core and

$$l_{\text{core}} = \int_{\partial\Sigma_{\text{core}}} dl \quad (2.123)$$

is the length of the core. In addition, assuming that the core length does not change, this transforms into

$$i_{ec} = -k_{ec} \frac{d\phi}{dt}, \quad (2.124)$$

where $k_{ec} = k_{\text{geom}} \sigma_{\text{core}} l_{\text{core}}$ is constant.

2.8 Magnetic force

The aim of this section is to obtain an explicit expression for the magnetic force that drives the motion in a reluctance actuator. As stated in Section 2.1, this force could be obtained either by integrating the Lorentz force density over the volume of the armature or by integrating the Maxwell stress tensor over its surface. However, the arbitrary shape of the studied actuators makes it very difficult to obtain a general analytical solution through these techniques. Instead, the force expression is derived in this thesis by applying an energy balance to the electromagnetic components of the system. The dot notation for the derivative is used during the analysis on selected variables to simplify the reading.

The electric energy supplied to the coil is the only input of the balance. This energy is transformed into magnetic work—work done to change the magnetic fields—Joule losses and mechanical work. The contribution of electrostatic potential energy to the balance is assumed negligible. The balance is studied in terms of power,

$$\dot{W}_v = \dot{W}_m + \dot{W}_{\text{Joule}} + \dot{W}_{F_m}, \quad (2.125)$$

where \dot{W}_v is the electric power supplied to the coil, \dot{W}_m is the power needed to change the magnetic field, \dot{W}_{Joule} accounts for the power losses due to Joule effect and \dot{W}_{F_m} is the mechanical power done by the magnetic force.

First, the electric power is equal to the product of the voltage across the coil terminals and the current flowing through the wire. Considering (2.33), it can be expressed as

$$\dot{W}_v = v i = \left(R i + N \dot{\phi} \right) i = R i^2 + N \dot{\phi} i. \quad (2.126)$$

Secondly, the expression for the magnetic work is obtained under the usual assumptions of the MEC modeling approach (see Section 2.3). It can be expressed as the sum of two terms,

$$\dot{W}_m = \dot{W}_{\text{mcore}} + \dot{W}_{\text{mgap}}, \quad (2.127)$$

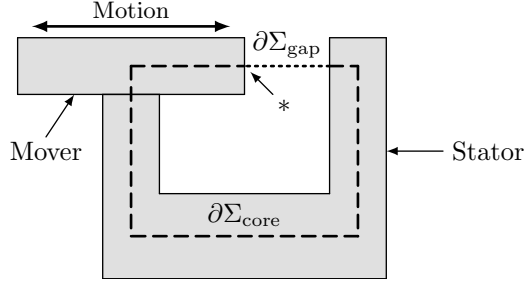


Figure 2.21: Magnetic system. The dashed and dotted lines indicate respectively $\partial\Sigma_{\text{core}}$ and $\partial\Sigma_{\text{gap}}$. The position where $\partial\Sigma_{\text{core}}$ changes its length is marked with an asterisk.

where $\dot{W}_{\text{m}_{\text{core}}}$ and $\dot{W}_{\text{m}_{\text{gap}}}$ are respectively the iron core and the air gap components of \dot{W}_{m} . These can be obtained using (2.49) as

$$\dot{W}_{\text{m}_{\text{core}}} = \frac{d}{dt} \left(\int_{\partial\Sigma_{\text{core}}} w_{\text{m}} A \, dl \right), \quad (2.128)$$

$$\dot{W}_{\text{m}_{\text{gap}}} = \frac{d}{dt} \left(\int_{\partial\Sigma_{\text{gap}}} w_{\text{m}} A \, dl \right). \quad (2.129)$$

Applying Leibniz's integral rule to (2.128), it is expanded as

$$\dot{W}_{\text{m}_{\text{core}}} = w_{\text{m}_{\text{core}}}^* A^* \frac{dl_{\text{core}}}{dt} + \int_{\partial\Sigma_{\text{core}}} \frac{\partial}{\partial t} (w_{\text{m}} A) \, dl. \quad (2.130)$$

The first term of this expression accounts for the power needed to change the magnetic field at those points that move in or out of $\partial\Sigma_{\text{core}}$ (see Fig. 2.21). Thus, $w_{\text{m}_{\text{core}}}^*$ and A^* refer respectively to the magnetic work density and the cross-sectional area of the MEC at the position where $\partial\Sigma_{\text{core}}$ changes its length. Using (2.39) and (2.51), and considering that A inside the core does not depend on time, the previous expression transforms into

$$\dot{W}_{\text{m}_{\text{core}}} = w_{\text{m}_{\text{core}}}^* A^* \frac{dl_{\text{core}}}{dt} + \dot{\phi} \int_{\partial\Sigma_{\text{core}}} H \, dl. \quad (2.131)$$

On the other hand, given that the air is a linear material with $\mu = \mu_0$, (2.129) can be rewritten using (2.18) as

$$\dot{W}_{\text{m}_{\text{gap}}} = \frac{d}{dt} \left(\frac{1}{2} \int_{\partial\Sigma_{\text{gap}}} \frac{B^2}{\mu_0} A \, dl \right), \quad (2.132)$$

and then, using (2.39) and (2.55),

$$\dot{W}_{\text{m}_{\text{gap}}} = \frac{d}{dt} \left(\frac{1}{2} \phi^2 \mathcal{R}_{\text{gap}} \right) = \phi \mathcal{R}_{\text{gap}} \dot{\phi} + \frac{1}{2} \phi^2 \frac{\partial \mathcal{R}_{\text{gap}}}{\partial l_{\text{gap}}} \frac{dl_{\text{gap}}}{dt}. \quad (2.133)$$

Note that, according to the analysis of Section 2.4, the only variable of \mathcal{R}_{gap} which depends on time is l_{gap} . Adding together (2.131) and (2.133) and using (2.57), the expression for

\dot{W}_m is obtained as

$$\dot{W}_m = w_{m_{\text{core}}}^* A^* \frac{dl_{\text{core}}}{dt} + (Ni + i_{\text{ec}}) \dot{\phi} + \frac{1}{2} \phi^2 \frac{\partial \mathcal{R}_{\text{gap}}}{\partial l_{\text{gap}}} \frac{dl_{\text{gap}}}{dt}. \quad (2.134)$$

In addition, considering that l_{gap} is used to define the position of the armature ($l_{\text{gap}} = z$, see Fig. 2.2), \dot{W}_m can be rewritten as

$$\dot{W}_m = \left(w_{m_{\text{core}}}^* A^* \frac{\partial l_{\text{core}}}{\partial z} + \frac{1}{2} \phi^2 \frac{\partial \mathcal{R}_{\text{gap}}}{\partial l_{\text{gap}}} \right) v_z + (Ni + i_{\text{ec}}) \dot{\phi}, \quad (2.135)$$

where it is assumed that the length of the core is a function of the position of the mover, i.e., $l_{\text{core}} = l_{\text{core}}(z)$, and v_z is the velocity of the armature in the direction of increasing z , i.e., $v_z = \dot{z}$.

Thirdly, Joule heating is generated in the coil wire and, due to the presence of Foucault currents, also in the iron core. Hence, \dot{W}_{Joule} can be expressed as the sum of two terms,

$$\dot{W}_{\text{Joule}} = \dot{W}_{\text{Joule}_{\text{coil}}} + \dot{W}_{\text{Joule}_{\text{core}}}. \quad (2.136)$$

The first term, which corresponds to the Joule heating power in the coil, is directly given by the product of its internal resistance and the square of the current.

$$\dot{W}_{\text{Joule}_{\text{coil}}} = R i^2 \quad (2.137)$$

With regard to the second term of (2.136), it must be noted that there is no general analytical solution for the heating power due to eddy currents in a magnetic core [139]. However, an eddy-current resistance, R_{ec} , may be defined such that the eddy-current heating power is analogously given by the product of this resistance and the square of the equivalent eddy current.

$$\dot{W}_{\text{Joule}_{\text{core}}} = R_{\text{ec}} i_{\text{ec}}^2 \quad (2.138)$$

Given that the distribution of eddy currents depends on the geometry of the core and the dynamics of the flux (see Section 2.7), R_{ec} should be generally considered as a function of the length of the core, the instantaneous value of i_{ec} and the time derivatives of both ϕ and i_{ec} .

$$R_{\text{ec}} = R_{\text{ec}} \left(l_{\text{core}}(z), \left\{ \frac{d^n \phi}{dt^n} \mid n \in \mathbb{N}^+ \right\}, \left\{ \frac{d^n i_{\text{ec}}}{dt^n} \mid n \in \mathbb{N}^0 \right\} \right) \quad (2.139)$$

Finally, the mechanical power is given by the product of the magnetic force, F_m , and the velocity of the armature.

$$\dot{W}_{F_m} = F_m v_z \quad (2.140)$$

Then, substituting all the terms in (2.125) and simplifying, it is obtained that

$$0 = \left(w_{m_{\text{core}}}^* A^* \frac{\partial l_{\text{core}}}{\partial z} + \frac{1}{2} \phi^2 \frac{\partial \mathcal{R}_{\text{gap}}}{\partial l_{\text{gap}}} \right) v_z + i_{\text{ec}} \dot{\phi} + R_{\text{ec}} i_{\text{ec}}^2 + F_m v_z. \quad (2.141)$$

The previous expression must be valid for any value of v_z , i_{ec} and $\dot{\phi}$. Hence, since neither $i_{\text{ec}} \dot{\phi}$ nor $R_{\text{ec}} i_{\text{ec}}^2$ depend on the velocity of the armature, these two terms must

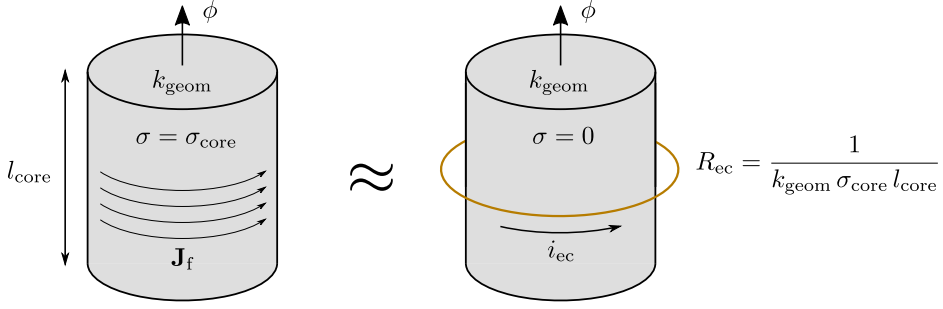


Figure 2.22: Equivalent model for conductive cores.

cancel each other out. This leads to the following expression for the previously defined eddy-current resistance:

$$R_{ec} = -\frac{\dot{\phi}}{i_{ec}}. \quad (2.142)$$

In this connection, note that the approximated model for eddy currents (2.122) leads to an eddy-current resistance equal to

$$R_{ec} = \frac{1}{k_{\text{geom}} \sigma_{\text{core}} l_{\text{core}}}, \quad (2.143)$$

which only depends on the geometry and the conductivity of the core. That is, if the core does not change its length, this approximation is equivalent to having a non-conductive magnetic core with a secondary single-turn coil of constant resistance (see Fig. 2.22).

On the other hand, the rest of the terms of (2.141) provide the following expression for the magnetic force:

$$F_m = -w_{\text{mcore}}^* A^* \frac{\partial l_{\text{core}}}{\partial z} - \frac{1}{2} \phi^2 \frac{\partial \mathcal{R}_{\text{gap}}}{\partial l_{\text{gap}}}. \quad (2.144)$$

Two general cases can be considered with regard to the first term in the expression. If l_{core} is constant during the motion—a reasonable assumption in many geometries, such as E-core or C-core actuators—the first term is equal to zero and the force is given by

$$F_m = -\frac{1}{2} \phi^2 \frac{\partial \mathcal{R}_{\text{gap}}}{\partial l_{\text{gap}}}. \quad (2.145)$$

A different situation occurs in plunger-type actuators such as the studied solenoid valve (see Section 1.4) or the magnetic system of Fig. 2.21. In these cases, the length of the core traversed by magnetic flux is not constant because the armature moves in and out of the circuit. Nevertheless, the length of the main path of the flux, including both the core and the gap, i.e., $l_{\text{gap}} + l_{\text{core}} = z + l_{\text{core}}$, is constant. As a result, $\partial l_{\text{core}} / \partial z = -1$ and, hence, the magnetic force (2.144) simplifies into

$$F_m = w_{\text{mcore}}^* A^* - \frac{1}{2} \phi^2 \frac{\partial \mathcal{R}_{\text{gap}}}{\partial l_{\text{gap}}}. \quad (2.146)$$

In contrast to (2.145), this latter formula accounts for the field changes that the motion produces in both the core and the air gap. However, considering that w_m in the air is in general some orders of magnitude greater than in ferromagnetic materials, it is reasonable to neglect the first term of the expression.

An analogous analysis can be carried out for rotary motion actuators like the studied relay (see Section 1.4). In that case, it can be shown [107] that the motion is driven by a magnetic torque given by

$$\tau_m = -\frac{1}{2} \phi^2 \frac{\partial \mathcal{R}_{\text{gap}}}{\partial \theta_{\text{gap}}}, \quad (2.147)$$

where θ_{gap} is the angle that defines the geometry of the air gap.

Chapter 3

Dynamical Modeling of Reluctance Actuators

After describing the electromagnetic phenomena that occur in reluctance actuators, this chapter focuses on how to build dynamical models that reflect the overall behavior of these systems. For that, the motion dynamics of a one-degree-of-freedom actuator is firstly described and some aspects regarding the modeling of bouncing are also discussed. A two-degree-of-freedom mechanical model is presented as well to show how the methodology can be extended to more complex mechanisms. Then, the electromagnetic and motion equations are combined in the second section, where five different hybrid dynamical models for reluctance actuators are described in order of increasing complexity.

3.1 Mechanics

3.1.1 Mechanical modeling of one-degree-of-freedom actuators

The motion of most reluctance actuators, i.e., C-core, E-core, or plunger-type actuators, has only one degree of freedom. In particular, in single-coil actuators, a magnetic flux is generated through the circuit when the coil is energized, which ultimately creates a magnetic force that pulls the armature towards the yoke. As seen in the previous chapter, this force—or torque—is proportional to the square of the flux, which means that it can act only in one direction. For that reason, a return spring is usually included in these actuators to produce the opposite motion when the coil is de-energized.

The motion of any reluctance actuator can be described by Newton's second law. For a linear motion device, this is expressed as

$$m \ddot{z} = F_m(z, \phi) - k_s(z - z_s) - c \dot{z}, \quad (3.1)$$

where m is the moving mass, F_m is the magnetic force, which is in general a function of the position and the flux (see Section 2.8), k_s is the spring constant, z_s is the mover position

at the spring equilibrium length and c is a damping coefficient. Although gravitational force is sometimes neglected—in many actuators it is much smaller than the elastic force of the spring—it can be incorporated to the model as part of the constant term $k_s z_s$. For rotary motion devices, Newton’s second law leads to a completely analogous expression,

$$I \ddot{\theta} = \tau_m(\theta, \phi) - k_{\theta s} (\theta - \theta_s) - c_\theta \dot{\theta}, \quad (3.2)$$

where I is the moment of inertia of the armature, τ_m is the magnetic torque, and $k_{\theta s}$, θ_s and c_θ are respectively the angular analogues of k_s , z_s and c . Friction in the mechanism is modeled in this thesis by means of a viscous friction term because of its simplicity and identifiability properties [140]. Other more sophisticated methods to model friction can be found in [141].

The position of the mover in reluctance actuators is generally bounded between two limits given by the mechanical design of the device. In particular, there is always a lower bound, z_{\min} , which is the position at which the mover and the stator collide and usually corresponds to the position where the air gap is nonexistent ($z_{\min} = 0$). Besides, it is also common that the position is upper bounded by z_{\max} , which in the great majority of the cases satisfies $z_{\max} < z_s$. In this way, the elastic force of the spring is strictly positive for any possible position of the mover, which ensures that it returns to $z = z_{\max}$ when the coil is not energized.

Assuming that the collisions are purely inelastic, i.e., that all the kinetic energy is dissipated at the impacts, the motion of the actuator can be described by the hybrid automaton of Fig. 3.1. This automaton has three dynamic modes, which correspond to the maximum position (mode $q = 1$), the motion between the limits (mode $q = 2$), and the minimum position (mode $q = 3$). The continuous state, x , is fully characterized by the position, z , and velocity, $v_z = \dot{z}$, of the mover.

$$x = [z \quad v_z]^T \quad (3.3)$$

Nevertheless, the complete state of this model, χ , includes also the dynamic mode, which is denoted by the discrete variable $q \in \{1, 2, 3\}$.

$$\chi = [x^T \quad q]^T \quad (3.4)$$

In the automaton, the function f_2 describes the second-order dynamics of the motion. It is derived from (3.1) as

$$\dot{v}_z = f_2(x, \phi) = \frac{1}{m} \left(F_m(z, \phi) - k_s (z - z_s) - c v_z \right), \quad (3.5)$$

where the flux, ϕ , is considered as the input of the mechanical subsystem. The sets C_1 , C_2 and C_3 , which define the domains of the three dynamic modes, are equal to

$$C_1 = \{z_{\max}\} \times \{0\}, \quad (3.6)$$

$$C_2 = \{x \in \mathbb{R}^2 \mid z_{\min} \leq z \leq z_{\max}\}, \quad (3.7)$$

$$C_3 = \{z_{\min}\} \times \{0\}. \quad (3.8)$$

In all the hybrid automata presented in this chapter, each transition is described by its guard condition—the condition that needs to be satisfied to activate the transition (in

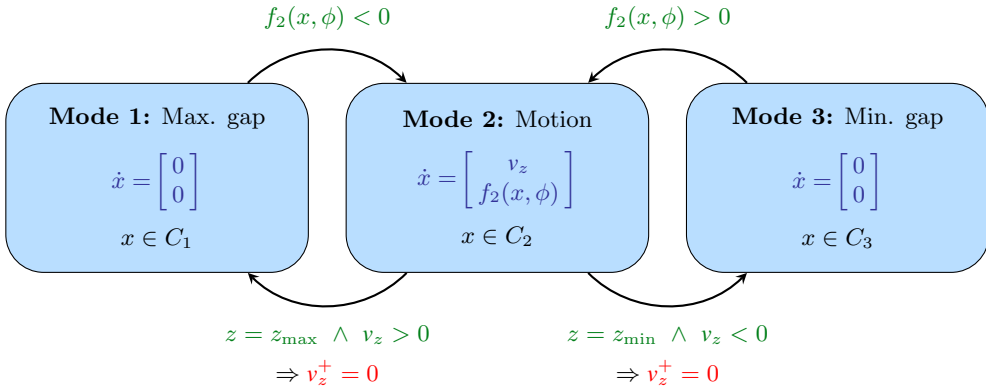


Figure 3.1: Hybrid automaton modeling the motion of the actuator with purely inelastic collisions.

green)—and its reset function—the function that defines how the variables change during the jump (in red)—respectively before and after a right arrow (\Rightarrow). The reset function is explicitly shown only for those variables that change during the jump; if the transition does not imply a jump, only the guard condition is presented. The superscript + is used to specify the values of the variables after the jump.

In particular, the model in Fig. 3.1 operates as follows. If the armature is moving and reaches any of the stroke limits, the automaton jumps to the corresponding static position mode and the velocity is reset to zero. Then, when the net force—magnetic plus elastic—has the correct sign to start the motion, the automaton gets back to the motion mode. It should be noted that, in spite of assuming purely inelastic collisions, bounces may still appear in this model if the velocity and the sum of the magnetic and spring forces at an impact have opposite signs. In that case, the automaton will jump instantaneously to either mode 1 or mode 3 and then back to mode 2.

Elasto-plastic impacts can be incorporated to the model by defining a coefficient of restitution. This coefficient, which was already described by Newton in his *Principia* [142], defines the ratio between the velocities of two objects before and after an impact. Assuming that the stator always remains static, the coefficient of restitution directly provides the ratio between the velocities of the mover before and after the collision. Using the notation already described, this leads to

$$v_z^+ = -\gamma v_z, \quad (3.9)$$

where v_z^+ is the velocity after the impact, γ is the coefficient and the minus sign indicates that the velocity after the collision goes in the opposite direction. Except for some particular cases, the coefficient of restitution ranges from zero for purely inelastic collisions to one for purely elastic impacts. Fig. 3.2 shows the hybrid automaton that models the motion of the actuator including this collision model. Note that in order to avoid Zeno solutions, i.e., solutions with an infinite number of jumps on a finite time interval [143], the automaton only bounces if the absolute value of the velocity at the impact is greater than an arbitrarily small velocity $v_\varepsilon \in \mathbb{R}_{>0}$. Otherwise the collision is assumed inelastic

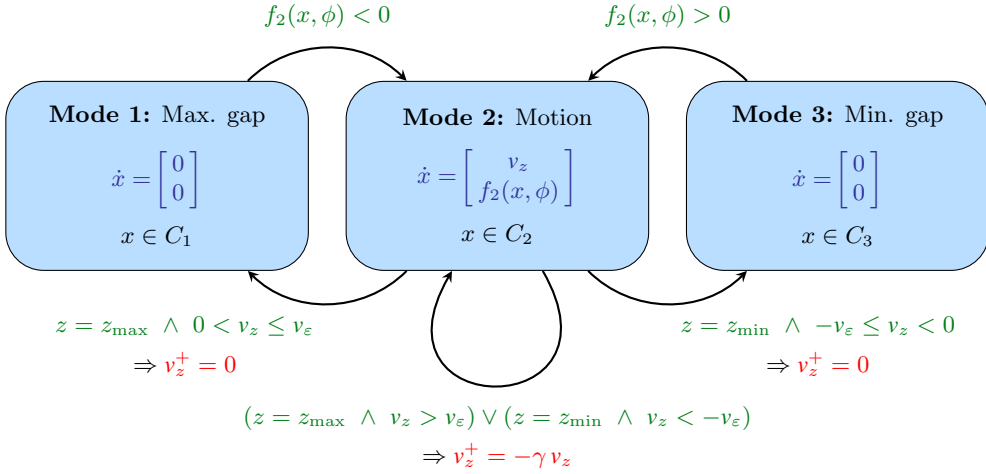


Figure 3.2: Hybrid automaton modeling the motion of the actuator with elasto-plastic collisions.

and the automaton jumps to either mode 1 or mode 3. The state, the function f_2 , and the domains C_1 , C_2 and C_3 of this model are as well given by (3.3)–(3.8).

Although the previous approach achieves great accuracy in modeling elasto-plastic bounces, viscoelastic contact models like the Maxwell–Wiechert model [144] can also be used to characterize the impacts in more detail. The Kelvin–Voigt model [79], which is particularly interesting for its simplicity, approximates the contact force by means of a spring-damping model,

$$F_{KV}(\xi, \dot{\xi}) = \begin{cases} -k_{KV} \xi - c_{KV} \dot{\xi}, & \text{if } \xi \geq 0 \\ 0, & \text{if } \xi < 0 \end{cases} \quad (3.10)$$

where k_{KV} and c_{KV} are respectively the stiffness and damping coefficients of the contact model and ξ is the penetration length. The main advantage of using a contact model is that the motion can be fully described by a single differential equation without need of a hybrid automaton. For instance, for a linear travel actuator, the motion dynamics is completely described by

$$m \ddot{z} = F_m(z, \phi) - k_s (z - z_s) - c \dot{z} - F_{KV, \min}(\xi_{\min}, \dot{\xi}_{\min}) + F_{KV, \max}(\xi_{\max}, \dot{\xi}_{\max}), \quad (3.11)$$

where

$$\xi_{\min} = z_{\min} - z, \quad \xi_{\max} = z - z_{\max}.$$

Despite this clear advantage, choosing proper values for the parameters of a contact model could be a nontrivial task that usually implies manual tuning. In addition, the resulting differential equations are still hybrid and generally stiff, which ultimately leads to higher computational requirements than if a hybrid automaton is implemented. As a result, contact models such as (3.10) are only recommended if there is a strong interest in modeling the bounces accurately or if the complexity of the corresponding automaton clearly justifies the use of this alternative approach.

3.1.2 Mechanical models with multiple degrees of freedom

Although the motion of most reluctance actuators has only one degree of freedom, some particular devices use the armature as the driving element of a kinematic chain composed of several bodies and joints. For instance, the studied relay (see Fig. 3.3) uses the motion of the armature to switch the position of the movable contact between the normally closed contact and the normally open contact. In cases like this, the motion of the device can be analyzed by means of rigid-body models with as many degrees of freedom as required [145]. In order to illustrate the methodology, this section presents a rigid body model to analyze the motion of the studied relay.

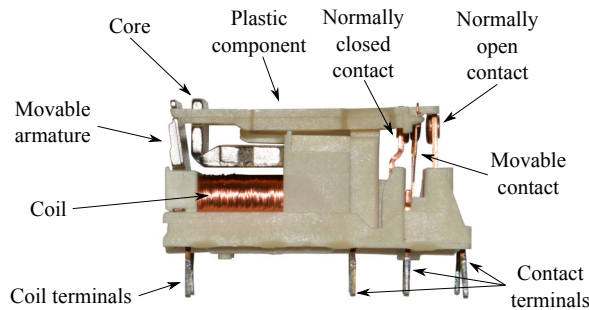


Figure 3.3: Relay.

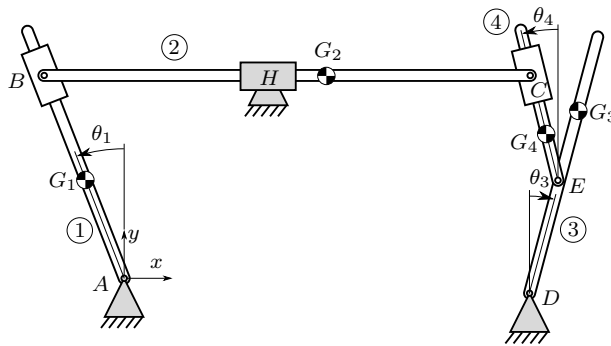


Figure 3.4: Relay mechanical model.

The motion of the relay is modeled by the planar mechanism of Fig. 3.4. This mechanical model is composed of four rigid bodies connected by joints and numbered in circles in the figure. Body 1 models the movable armature and body 2 corresponds to the plastic component. Since the movable contact is made from a flexible copper sheet, it is modeled as the union of two rigid bodies, 3 and 4, which are connected by joint E . Spring torques that model the sheet rigidity are included in joints D and E . The torsion spring that exists at the bottom of the movable armature is also included in the mechanical model in joint A . To model the friction of the whole mechanism, a viscous friction force is included in joint H . The specific notation used in this part of the section is as follows:

x_P, y_P	Coordinates of point P in the x–y coordinate system
$\vec{r}_P = [x_P \ y_P]^T$	Position vector of point P
\vec{PQ}	Vector from point P to point Q
$PQ = \ \vec{PQ}\ $	Euclidean distance between points P and Q
g	Gravity
G_i	Center of mass of rigid body i
m_i	Mass of rigid body i
I_i	Moment of inertia of rigid body i in the x–y plane

Joints A , D and H are fixed and have known positions. If A is selected as the origin of the coordinate system, then

$$\vec{r}_A = [0 \ 0]^T, \quad (3.12)$$

$$\vec{r}_H = [x_H \ y_H]^T, \quad (3.13)$$

$$\vec{r}_D = [x_D \ y_D]^T. \quad (3.14)$$

The position of all the other points of the mechanism depends on angular variables θ_1 , θ_3 and θ_4 . Considering that AG_1 , BC , BG_2 , DE , DG_3 , and EG_4 are known constant lengths of the mechanism, the following vectors of the kinematic chain are calculated:

$$\vec{AG}_1 = [-AG_1 \sin \theta_1 \ AG_1 \cos \theta_1]^T, \quad (3.15)$$

$$\vec{AB} = [-y_H \tan \theta_1 \ y_H]^T, \quad (3.16)$$

$$\vec{BG}_2 = [BG_2 \ 0]^T, \quad (3.17)$$

$$\vec{BC} = [BC \ 0]^T, \quad (3.18)$$

$$\vec{DE} = [DE \sin \theta_3 \ DE \cos \theta_3]^T, \quad (3.19)$$

$$\vec{DG}_3 = [DG_3 \sin \theta_3 \ DG_3 \cos \theta_3]^T, \quad (3.20)$$

$$\vec{EG}_4 = [-EG_4 \sin \theta_4 \ EG_4 \cos \theta_4]^T. \quad (3.21)$$

Then, by adding and subtracting these vectors, the position of centers of mass G_1 , G_2 , G_3 and G_4 and joints B , C and E can be calculated as

$$\vec{r}_{G_1} = \vec{AG}_1, \quad (3.22)$$

$$\vec{r}_{G_2} = \vec{AB} + \vec{BG}_2, \quad (3.23)$$

$$\vec{r}_{G_3} = \vec{r}_D + \vec{DG}_3, \quad (3.24)$$

$$\vec{r}_{G_4} = \vec{r}_D + \vec{DE} + \vec{EG}_4, \quad (3.25)$$

$$\vec{r}_B = \vec{AB}, \quad (3.26)$$

$$\vec{r}_C = \vec{AB} + \vec{BC}, \quad (3.27)$$

$$\vec{r}_E = \vec{r}_D + \vec{DE}, \quad (3.28)$$

Note that, although the previous equations are written in terms of θ_1 , θ_3 and θ_4 , the

proposed mechanism has only two degrees of freedom because these variables are geometrically related by

$$\tan \theta_4 = \frac{x_E(\theta_3) - x_C(\theta_1)}{y_C(\theta_1) - y_E(\theta_3)}. \quad (3.29)$$

Free body diagrams of the four components of the mechanism are presented in Fig. 3.5. All the internal and external forces and torques that act on the bodies are represented in these diagrams by means of arrows, each pointing to the direction which has been defined as positive. Revolute joints A , D and E create internal forces of unknown direction which can be decomposed in the x - and y -coordinates, obtaining F_{Ax} , F_{Ay} , F_{Dx} , F_{Dy} , F_{Ex} and F_{Ey} . Pin-slot joints B and C create forces F_B and F_C , which are respectively perpendicular to the direction of solids 1 and 3, and prismatic joint H creates a force F_H in the y -coordinate and a torque τ_H in the z -coordinate.

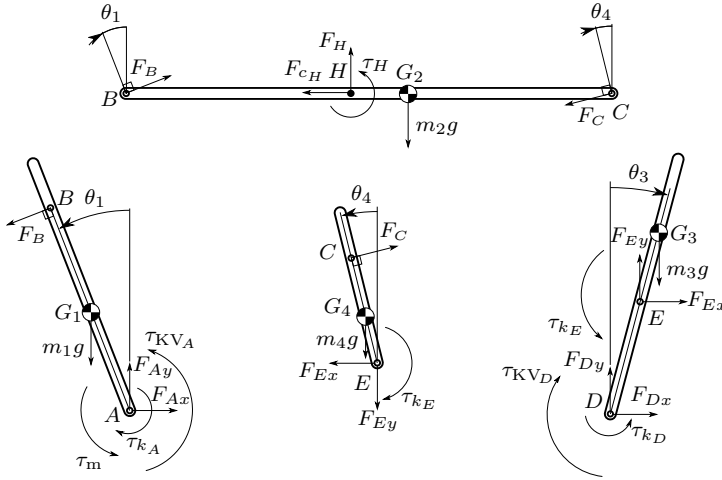


Figure 3.5: Free body diagrams.

Spring torques τ_{k_A} , τ_{k_D} and τ_{k_E} in joints A , D and E are given by Hooke's law,

$$\tau_{k_A} = k_A (\theta_1 - \theta_{1,0}), \quad (3.30)$$

$$\tau_{k_D} = k_D (\theta_3 - \theta_{3,0}), \quad (3.31)$$

$$\tau_{k_E} = k_E (\theta_3 + \theta_4 - \theta_{E,0}), \quad (3.32)$$

where k_A , k_D and k_E are the spring constants and $\theta_{1,0}$, $\theta_{3,0}$ and $\theta_{E,0}$ are the springs natural angles. On the other hand, the viscous friction force F_{c_H} is given by

$$F_{c_H} = c_H \dot{x}_{G_2}, \quad (3.33)$$

where c_H is the damping coefficient.

Similarly to the case of one-degree-of-freedom actuators, the motion of the relay is restricted to specific positions—both in θ_1 and θ_3 —due to the location of the fixed armature and the contacts (see Fig. 3.3). To include these limits in the model, Kelvin-Voigt torques τ_{KV_A} and τ_{KV_D} act in joints A and D when bodies 1 and 3 move beyond

their boundaries. Considering that the motion is restricted to $\theta_1 \in [\theta_{1,\min}, \theta_{1,\max}]$ and $\theta_3 \in [\theta_{3,\min}, \theta_{3,\max}]$, where $\theta_{1,\min}$, $\theta_{1,\max}$, $\theta_{3,\min}$ and $\theta_{3,\max}$ are the position boundaries, these torques are given by

$$\tau_{KV_A} = \begin{cases} -k_{KV_A} (\theta_1 - \theta_{1,\min}) - c_{KV_A} \dot{\theta}_1, & \text{if } \theta_1 < \theta_{1,\min}, \\ -k_{KV_A} (\theta_1 - \theta_{1,\max}) - c_{KV_A} \dot{\theta}_1, & \text{if } \theta_1 > \theta_{1,\max}, \\ 0, & \text{otherwise,} \end{cases} \quad (3.34)$$

$$\tau_{KV_D} = \begin{cases} -k_{KV_D} (\theta_3 - \theta_{3,\min}) - c_{KV_D} \dot{\theta}_3, & \text{if } \theta_3 < \theta_{3,\min}, \\ -k_{KV_D} (\theta_3 - \theta_{3,\max}) - c_{KV_D} \dot{\theta}_3, & \text{if } \theta_3 > \theta_{3,\max}, \\ 0, & \text{otherwise,} \end{cases} \quad (3.35)$$

where k_{KV_A} and k_{KV_D} are the stiffness constants and c_{KV_A} and c_{KV_D} the damping coefficients of the corresponding Kelvin-Voigt contact models.

The weights of the four bodies and magnetic torque τ_m , which acts on body 1 and is given by the electromagnetic model (see Section 2.8), are also included in the mechanism. Equations for linear and angular accelerations are then obtained by applying Newton's second law. Three equations are presented below for each body, which correspond to the net forces in the x- and y-coordinates and the net torque in the z-coordinate. For bodies 1 to 4, torques have been respectively calculated about points A , B , D and E .

Equations for body 1:

$$m_1 \ddot{x}_{G_1} = F_{Ax} - F_B \cos \theta_1, \quad (3.36)$$

$$m_1 \ddot{y}_{G_1} = F_{Ay} - F_B \sin \theta_1 - m_1 g, \quad (3.37)$$

$$I_1 \ddot{\theta}_1 = F_B AB + m_1 g AG_1 \sin \theta_1 + \tau_{KV_A} - \tau_{k_A} + \tau_m. \quad (3.38)$$

Equations for body 2:

$$m_2 \ddot{x}_{G_2} = F_B \cos \theta_1 - F_C \cos \theta_4 - F_{C_H}, \quad (3.39)$$

$$m_2 \ddot{y}_{G_2} = F_B \sin \theta_1 + F_H - m_2 g - F_C \sin \theta_4, \quad (3.40)$$

$$0 = F_H BH - m_2 g BG_2 - F_C BC \sin \theta_4 + \tau_H. \quad (3.41)$$

Equations for body 3:

$$m_3 \ddot{x}_{G_3} = F_{Dx} + F_{Ex}, \quad (3.42)$$

$$m_3 \ddot{y}_{G_3} = F_{Dy} + F_{Ey} - m_3 g, \quad (3.43)$$

$$I_3 \ddot{\theta}_3 = F_{Ey} DE \sin \theta_3 - F_{Ex} DE \cos \theta_3 - m_3 g DG_3 \sin \theta_3 \\ + \tau_{k_D} + \tau_{k_E} - \tau_{KV_D}. \quad (3.44)$$

Equations for body 4:

$$m_4 \ddot{x}_{G_4} = F_C \cos \theta_4 - F_{Ex}, \quad (3.45)$$

$$m_4 \ddot{y}_{G_4} = F_C \sin \theta_4 - F_{Ey} - m_4 g, \quad (3.46)$$

$$I_4 \ddot{\theta}_4 = m_4 g EG_4 \sin \theta_4 - F_C EC - \tau_{k_E}. \quad (3.47)$$

By using (3.12)–(3.35), the previous system of differential equations, which has 12 unknown variables (F_{Ax} , F_{Ay} , F_B , F_H , τ_H , F_C , F_{Dx} , F_{Dy} , F_{Ex} , F_{Ey} , θ_1 and θ_3), permits the resolution of the mechanism.

3.2 Dynamical models for reluctance actuators

The motion of reluctance actuators has been studied in the previous section considering the flux as a known input. In this part of the chapter, the electromagnetic dynamics is incorporated to the dynamical model by using the equations derived in Chapter 2. Five different models are presented in the following pages, ranging from a basic but computationally inexpensive model to a comprehensive and accurate model that includes all the electromagnetic phenomena already studied.

3.2.1 Basic dynamical model

The simplest dynamical model of a reluctance actuator is the one obtained under the assumption that flux fringing, saturation, hysteresis and eddy currents can all be neglected. In that case, the reluctance of the air gap is proportional to the length of the gap [see (2.60)] and the reluctance of the core is constant [see (2.63)]. Thus, the total reluctance of the magnetic circuit can be expressed as

$$\mathcal{R} = \mathcal{R}_{\text{gap}0} + k_{\text{gap}} z + \mathcal{R}_{\text{core}0}, \quad (3.48)$$

where $\mathcal{R}_{\text{gap}0}$ and k_{gap} are respectively the initial value and the slope of the air gap reluctance, and $\mathcal{R}_{\text{core}0}$ is the core reluctance. Note that $\mathcal{R}_{\text{gap}0}$ allows for including secondary gaps in the model like the one that exists in the studied valve, but it is equal to zero in most reluctance actuators. In any case, the two constant terms of the expression can be grouped together, which leads to

$$\mathcal{R} = \mathcal{R}_0 + k_{\text{gap}} z, \quad (3.49)$$

where $\mathcal{R}_0 = \mathcal{R}_{\text{gap}0} + \mathcal{R}_{\text{core}0}$. The electromagnetic dynamics of this system is then fully described by the first-order nonlinear model formed by (2.33), (2.45) and (3.49). From these equations, the time derivative of the magnetic flux can be explicitly expressed as a function of the position of the mover, the flux and the voltage (input of the system).

$$\dot{\phi} = f_3(z, \phi, v) = \frac{v}{N} - \frac{R\phi}{N^2} (\mathcal{R}_0 + k_{\text{gap}} z) \quad (3.50)$$

The complete dynamical model of the actuator, including both the electromagnetic and motion dynamics, is then obtained by joining the above differential equation with the models derived in the previous section. This implies that the continuous state of the system is now not only composed of the position and velocity of the armature, but also of the magnetic flux.

$$x = \begin{bmatrix} z & v_z & \phi \end{bmatrix}^T \quad (3.51)$$

In particular, the dynamics of a linear travel actuator with purely inelastic collisions is described by the hybrid automaton of Fig. 3.6. Similar automata can be obtained for

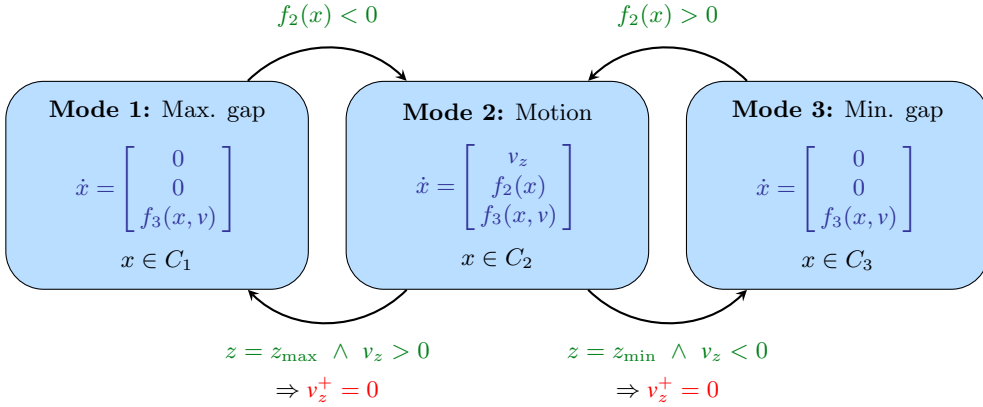


Figure 3.6: Hybrid automaton modeling the dynamics of the actuator.

the case of elasto-plastic collisions by using any of the already presented techniques. As in the previous automata, the state of this model is given by (3.4), i.e., by the union of the continuous state x and the dynamic mode $q \in \{1, 2, 3\}$. The function f_2 is given by (3.5), where the magnetic force is considered an arbitrary function of z and ϕ . In this regard, assuming that F_m is given by (2.145), the reluctance proposed in this basic model leads to a magnetic force which is proportional to the square of the flux and does not depend on the position of the mover.

$$F_m = F_m(\phi) = -\frac{1}{2} k_{\text{gap}} \phi^2 \quad (3.52)$$

The domains C_1 , C_2 and C_3 for this automaton are given by

$$C_1 = \{x \in \mathbb{R}^3 \mid z = z_{\max}, v_z = 0, -\phi_{\text{sat}} \leq \phi \leq \phi_{\text{sat}}\}, \quad (3.53)$$

$$C_2 = \{x \in \mathbb{R}^3 \mid z_{\min} \leq z \leq z_{\max}, -\phi_{\text{sat}} \leq \phi \leq \phi_{\text{sat}}\}, \quad (3.54)$$

$$C_3 = \{x \in \mathbb{R}^3 \mid z = z_{\min}, v_z = 0, -\phi_{\text{sat}} \leq \phi \leq \phi_{\text{sat}}\}, \quad (3.55)$$

where $\phi_{\text{sat}} \in \mathbb{R}_{>0}$ is the saturation level of the flux, which in this basic model is equal to infinity. The same definitions are used in following models with $\phi_{\text{sat}} \neq \infty$.

The presented automaton can be used to predict the dynamic behavior of the three continuous state variables of the system—position, velocity and flux—for any given input profile. Note that, accordingly to (3.51), the functions f_2 and f_3 are represented in the automaton as $f_2(x)$ and $f_3(x, v)$. Additional variables may also be calculated by using the equations of the model. In particular, the electric current through the coil can be obtained from (2.45) and (3.49) as a function of the position of the mover and the magnetic flux.

$$i = \frac{\phi (\mathcal{R}_0 + k_{\text{gap}} z)}{N} \quad (3.56)$$

The basic dynamical model for reluctance actuators is parameterized in terms of ten parameters. Six of them are intrinsic to the motion dynamics (m , k_s , z_s , c , z_{\min} and z_{\max}) and the other four to the electromagnetic part (N , R , \mathcal{R}_0 and k_{gap}).

3.2.2 Dynamical model including saturation

As stated in Section 2.5, magnetic saturation in reluctance actuators is an almost unavoidable phenomenon that changes considerably the dynamics of the system. In order to improve the accuracy of the basic model, the model presented in this subsection incorporates magnetic saturation by using the Fröhlich-Kennelly relation.

Considering that ϕ is uniform along the magnetic circuit and $\phi = B(l)A(l)$, it is clear that the effects of magnetic saturation on segments with different cross sections are different. In order to simplify the analysis, in Section 2.5 it has been proposed that the magnetic core should be divided into several elements with an approximately constant cross-sectional area. In the case that the entire core has an approximately uniform cross-sectional area—a reasonable design criterion that optimizes the use of material—the reluctance of the magnetic circuit can be approximated by

$$\mathcal{R} = \mathcal{R}_{\text{gap}0} + k_{\text{gap}} z + \frac{\mathcal{R}_{\text{core}0}}{1 - |\phi|/\phi_{\text{sat}}}, \quad (3.57)$$

where $\mathcal{R}_{\text{core}0}$ should be interpreted as the reluctance of the core for zero magnetic flux and ϕ_{sat} is the parameter that defines the saturation flux.

The dynamics of the actuator when considering saturation is also described by the hybrid automaton of Fig. 3.6 with domains (3.53)–(3.55). Note however that ϕ_{sat} is no longer equal to infinity but it has a real positive value. The function f_2 does not change with respect to the previous case, but the explicit differential equation for the flux is now given by

$$\dot{\phi} = f_3(x, v) = \frac{v}{N} - \frac{R\phi}{N^2} \left(\mathcal{R}_{\text{gap}0} + k_{\text{gap}} z + \frac{\mathcal{R}_{\text{core}0}}{1 - |\phi|/\phi_{\text{sat}}} \right). \quad (3.58)$$

In addition, the expression for the electric current is also different and is formulated as

$$i = \frac{\phi}{N} \left(\mathcal{R}_{\text{gap}0} + k_{\text{gap}} z + \frac{\mathcal{R}_{\text{core}0}}{1 - |\phi|/\phi_{\text{sat}}} \right). \quad (3.59)$$

As seen, magnetic saturation can be relatively simply incorporated to the dynamical model of the actuator by using the Fröhlich-Kennelly equation. Similar dynamics can also be derived for any of the other saturation models presented in Section 2.5. The resulting structure has twelve parameters, the same six related to the motion than the basic model (m , k_s , z_s , c , z_{min} and z_{max}) and six linked to the electromagnetic dynamics (N , R , $\mathcal{R}_{\text{gap}0}$, k_{gap} , $\mathcal{R}_{\text{core}0}$ and ϕ_{sat}).

3.2.3 Dynamical model including saturation and flux fringing

The effect of flux fringing on the dynamical modeling of reluctance actuators has been studied in Section 2.4. As explained, neglecting this phenomenon leads to an overestimated value of the air gap reluctance and, more importantly, to high errors when estimating the magnetic force, especially for small air gaps. If flux fringing is to be considered in the model, the air gap reluctance can no longer be assumed linear with respect to the length of the gap. In this case, the reluctance of the complete system should be expressed

as

$$\mathcal{R} = \mathcal{R}_{\text{gap}}(z) + \frac{\mathcal{R}_{\text{core0}}}{1 - |\phi|/\phi_{\text{sat}}}, \quad (3.60)$$

where \mathcal{R}_{gap} is a function of z that depends on the geometry of the actuator. Two different approaches have been proposed in the previous chapter to obtain that reluctance: FEM simulations, in which case $\mathcal{R}_{\text{gap}}(z)$ would be stored as a lookup table, or empirical expressions such as the McLyman equation. This latter method, which provides good approximations for E-core, C-core and plunger-type actuators [130], leads to an air gap reluctance equal to

$$\mathcal{R}_{\text{gap}}(z) = \begin{cases} \mathcal{R}_{\text{gap0}}, & \text{if } z = 0, \\ \mathcal{R}_{\text{gap0}} + \frac{\frac{z}{\mu_0 A_{\text{core}}}}{1 + \frac{z}{\sqrt{A_{\text{core}}}} \log\left(\frac{2l_w}{z}\right)}, & \text{if } z > 0. \end{cases} \quad (3.61)$$

The hybrid automaton of Fig. 3.6 is also valid to describe the dynamics of the system when considering saturation and flux fringing. In this case, the differential equation for the magnetic flux is given by

$$\dot{\phi} = f_3(x, v) = \frac{v}{N} - \frac{R\phi}{N^2} \left(\mathcal{R}_{\text{gap}}(z) + \frac{\mathcal{R}_{\text{core0}}}{1 - |\phi|/\phi_{\text{sat}}} \right), \quad (3.62)$$

and the magnetic force, which is one of the terms in f_2 , is now a function that depends not only on the flux, but also on the position of the mover.

$$F_m = F_m(z, \phi) = -\frac{1}{2} \phi^2 \frac{\partial \mathcal{R}_{\text{gap}}(z)}{\partial z} \quad (3.63)$$

It should be noted that, when using the McLyman model, $\partial \mathcal{R}_{\text{gap}}/\partial z$ is not defined for $z = 0$. However, this can be easily solved by using the right-hand limit instead. In that case, the magnetic force is given by

$$F_m(z, \phi) = \begin{cases} -\frac{1}{2} \frac{\phi^2}{\mu_0 A_{\text{core}}}, & \text{if } z = 0, \\ -\frac{1}{2} \frac{\phi^2}{\mu_0 A_{\text{core}}} \frac{1 + \frac{z}{\sqrt{A_{\text{core}}}}}{\left(1 + \frac{z}{\sqrt{A_{\text{core}}}} \log\left(\frac{2l_w}{z}\right)\right)^2}, & \text{if } z > 0. \end{cases} \quad (3.64)$$

Finally, the relation between the electric current and the state variables is

$$i = \frac{\phi}{N} \left(\mathcal{R}_{\text{gap}}(z) + \frac{\mathcal{R}_{\text{core0}}}{1 - |\phi|/\phi_{\text{sat}}} \right). \quad (3.65)$$

In the case of using an FEM-based reluctance, the resulting dynamical model relies on ten parameters (m , k_s , z_s , c , z_{min} , z_{max} , N , R , $\mathcal{R}_{\text{core0}}$ and ϕ_{sat}) and a lookup table to store the values of $\mathcal{R}_{\text{gap}}(z)$. In addition, the partial derivative of the reluctance with respect

to the gap length, $\partial\mathcal{R}_{\text{gap}}/\partial z$, needs to be numerically calculated online or, alternatively, computed offline and stored also in memory. By contrast, no lookup tables are required if an analytical model is used to describe the air gap reluctance. In the particular case that the McLyman expression is used, the dynamical model is fully parametric and depends on thirteen parameters ($m, k_s, z_s, c, z_{\text{min}}, z_{\text{max}}, N, R, \mathcal{R}_{\text{gap0}}, A_{\text{core}}, l_w, \mathcal{R}_{\text{core0}}$ and ϕ_{sat}).

3.2.4 Dynamical model including saturation, flux fringing and eddy currents

Eddy currents have also a substantial impact on the dynamics of magnetic systems with conductive cores. As it can be deduced from (2.119), the overall effect of eddy currents is a reduction of the time derivative of the magnetic flux. In other words, the magnetic flux created by a coil varies more slowly if the core is made of a conductive material. The higher the conductivity of the core, the slower the dynamics of the flux.

The electromagnetic dynamics of a reluctance actuator model including saturation, flux fringing and eddy currents can be derived by using (2.33), (2.54) and (3.60). Besides, as stated in Section 2.7, the MEC assumptions lead to a first-order dynamic relation, given by (2.124), between the flux and the equivalent eddy current i_{ec} . Thus, solving for the derivative of the magnetic flux, it is obtained that

$$\dot{\phi} = f_3(x, v) = \left(\frac{v}{N} - \frac{R\phi}{N^2} \left(\mathcal{R}_{\text{gap}}(z) + \frac{\mathcal{R}_{\text{core0}}}{1 - |\phi|/\phi_{\text{sat}}} \right) \right) \left(1 + \frac{Rk_{\text{ec}}}{N^2} \right)^{-1}. \quad (3.66)$$

Note that the above equation is equal to (3.62) except for the last factor. Hence, considering that

$$\left(1 + \frac{Rk_{\text{ec}}}{N^2} \right)^{-1} < 1, \quad (3.67)$$

it is shown explicitly that $|\dot{\phi}| = |f_3(z, \phi, v)|$ is smaller when eddy currents are considered.

The reluctance of the air gap is the same than in the previous model, so the expression for the magnetic force does not change. Consequently, the motion dynamics remains unaltered. However, the electric current takes a different expression that depends on the eddy-current parameter k_{ec} .

$$i = \frac{\phi}{N} \left(\mathcal{R}_{\text{gap}}(z) + \frac{\mathcal{R}_{\text{core0}}}{1 - |\phi|/\phi_{\text{sat}}} \right) \left(1 + \frac{Rk_{\text{ec}}}{N^2} \right)^{-1} + \frac{v}{R} \left(1 + \frac{N^2}{Rk_{\text{ec}}} \right)^{-1} \quad (3.68)$$

As expected, the current for a non-conductive core ($k_{\text{ec}} = 0$) is equal to (3.65). However, it is noteworthy that the approximation given by (2.124) results in a feedforward term—a term that directly depends on the system input (v)—in the above expression. In this regard, note that in the theoretical case of a superconductive core ($k_{\text{ec}} = \infty$), (3.66) and (3.68) transform respectively into

$$\dot{\phi} = 0, \quad (3.69)$$

$$i = \frac{v}{R}, \quad (3.70)$$

which are the equations that define the behavior of a pure resistor. Two conclusions can be drawn from the above. First, that the model is consistent with the behavior of a hypothetical superconductive core, which would prevent the flux from increasing (Meissner-Ochsenfeld effect, [146]). And secondly, that the model presented in this subsection corresponds to an intermediate situation between a non-conductive and a superconductive core.

The expression for the equivalent eddy current can be derived from the previous equations as a function of the voltage, the position and the flux.

$$i_{ec} = -k_{ec} \left(\frac{v}{N} - \frac{R\phi}{N^2} \left(\mathcal{R}_{\text{gap}}(z) + \frac{\mathcal{R}_{\text{core0}}}{1 - |\phi|/\phi_{\text{sat}}} \right) \right) \left(1 + \frac{Rk_{ec}}{N^2} \right)^{-1} \quad (3.71)$$

When compared to the previous model, the dynamical model including saturation, flux fringing and eddy currents only has the additional parameter k_{ec} . In other words, it either depends on eleven parameters and one or two lookup tables—in the case that the air gap reluctance is computed numerically and stored in memory—or on fourteen parameters—if \mathcal{R}_{gap} is analytically modeled by the McLyman expression.

3.2.5 Dynamical model including saturation, hysteresis, flux fringing and eddy currents

The last dynamical model presented in this chapter incorporates all the electromagnetic phenomena studied in Chapter 2, i.e., saturation, hysteresis, flux fringing and eddy currents. As explained in Section 2.3, the reluctance can no longer be used to model the magnetic core because of the presence of magnetic hysteresis and, consequently, Ampère's law has to be used in the form of (2.57). With regard to the iron term in that expression, it is assumed that the magnetic field intensity in the core can be approximated by an average value H_{core} , so

$$\int_{\partial\Sigma_{\text{core}}} H \, dl = H_{\text{core}} l_{\text{core}}. \quad (3.72)$$

Accordingly, the magnetic flux density in the core is also approximated using an average value B_{core} , which is related to H_{core} by a hysteretic relation. As explained in Section 2.6, this relation is modeled in this thesis by means of the Generalized Preisach Model.

$$B_{\text{core}} = f_{\text{GPM}}(H_{\text{core}}, \mathcal{A}, \mathcal{B}) \quad (3.73)$$

For the sake of clarity, the explicit dependence of f_{GPM} on the extrema sets \mathcal{A} and \mathcal{B} is omitted in some parts of the section. In addition, it is also assumed that the magnetic flux can be expressed as the product of B_{core} and an average cross-sectional area of the core, A_{core} .

$$\phi = B_{\text{core}} A_{\text{core}} \quad (3.74)$$

The explicit differential equation for the magnetic flux can then be obtained using (2.33), (2.57), (2.124) and (3.72)–(3.74),

$$\dot{\phi} = \left(\frac{v}{N} - \frac{R}{N^2} \left(\phi \mathcal{R}_{\text{gap}}(z) + f_{\text{GPM}}^{-1}(\phi/A_{\text{core}}) l_{\text{core}} \right) \right) \left(1 + \frac{Rk_{ec}}{N^2} \right)^{-1}, \quad (3.75)$$

but, as shown, it requires the inversion of the GPM (f_{GPM}^{-1}). This problem has been widely treated in the literature [147–150] and the proposed solutions involve either the use of a modified version of the Preisach model that allows for explicit inversion, or the numerical inversion of the forward model by means of an iterative method. As stated in [149], this latter approach is particularly inefficient in terms of computation.

Nevertheless, considering that the derivatives of B_{core} and H_{core} are linked together by the incremental permeability of the GPM [see (2.93)], i.e.,

$$\dot{B}_{\text{core}} = \mu'_{\text{GPM}}(H_{\text{core}}) \dot{H}_{\text{core}}, \quad (3.76)$$

the previous set of equations can be used to solve explicitly the dynamics of the magnetic field intensity H_{core} instead of that of ϕ .

$$\dot{H}_{\text{core}} = \frac{\frac{v}{N} - \frac{R}{N^2} \left(A_{\text{core}} f_{\text{GPM}}(H_{\text{core}}) \mathcal{R}_{\text{gap}}(z) + H_{\text{core}} l_{\text{core}} \right)}{\left(1 + \frac{R k_{\text{ec}}}{N^2} \right) A_{\text{core}} \mu'_{\text{GPM}}(H_{\text{core}})} \quad (3.77)$$

In contrast to (3.75), the above expression does not require the inversion of the GPM and, consequently, the numerical solution of H_{core} is far more efficient because it requires only one evaluation of f_{GPM} and μ'_{GPM} per integration step. For this reason, the dynamical model presented in this subsection uses the magnetic field intensity in the core as state variable instead of the magnetic flux.

Given that f_{GPM} and μ'_{GPM} depend not only on H_{core} , but also on the sign of its derivative and on the sets \mathcal{A} and \mathcal{B} [see (2.86) and (2.98)], let (3.77) be symbolically expressed as

$$\dot{H}_{\text{core}} = \begin{cases} f_3^{\nearrow}(x, \mathcal{A}, \mathcal{B}, v), & \text{if } \dot{H}_{\text{core}} \geq 0, \\ f_3^{\searrow}(x, \mathcal{A}, \mathcal{B}, v), & \text{if } \dot{H}_{\text{core}} < 0, \end{cases} \quad (3.78)$$

where x is the continuous state for this model, given by

$$x = [z \quad v_z \quad H_{\text{core}}]^{\text{T}}, \quad (3.79)$$

and the functions f_3^{\nearrow} and f_3^{\searrow} use their corresponding versions of f_{GPM} and μ'_{GPM} .

$$f_3^{\nearrow}(x, \mathcal{A}, \mathcal{B}, v) = \frac{\frac{v}{N} - \frac{R}{N^2} \left(A_{\text{core}} f_{\text{GPM}}^{\nearrow}(H_{\text{core}}, \mathcal{A}, \mathcal{B}) \mathcal{R}_{\text{gap}}(z) + H_{\text{core}} l_{\text{core}} \right)}{\left(1 + \frac{R k_{\text{ec}}}{N^2} \right) A_{\text{core}} \mu'_{\text{GPM}}^{\nearrow}(H_{\text{core}}, \mathcal{A}, \mathcal{B})} \quad (3.80)$$

$$f_3^{\searrow}(x, \mathcal{A}, \mathcal{B}, v) = \frac{\frac{v}{N} - \frac{R}{N^2} \left(A_{\text{core}} f_{\text{GPM}}^{\searrow}(H_{\text{core}}, \mathcal{A}, \mathcal{B}) \mathcal{R}_{\text{gap}}(z) + H_{\text{core}} l_{\text{core}} \right)}{\left(1 + \frac{R k_{\text{ec}}}{N^2} \right) A_{\text{core}} \mu'_{\text{GPM}}^{\searrow}(H_{\text{core}}, \mathcal{A}, \mathcal{B})} \quad (3.81)$$

Note that, in order to have an unambiguous definition of the direction of H_{core} , the functions f_3^{\nearrow} and f_3^{\searrow} must have the same sign for any given value of the inputs. Considering (3.77), this is achieved if μ'_{GPM} is strictly positive; a condition which, on the other hand, ensures the physical meaning of the permeability. Since the irreversible term μ'_{irr} is always

greater than or equal to zero (see Section 2.6), a sufficient solution consists in fitting the reversible model (2.88) using the constraint that μ'_{Rev} is strictly positive for any value of H_{core} .

The motion dynamics is driven by the magnetic force (3.63). Using (3.73) and (3.74), this force can be expressed as a function of x , \mathcal{A} and \mathcal{B} .

$$F_m = F_m(x, \mathcal{A}, \mathcal{B}) = -\frac{1}{2} A_{\text{core}}^2 \left(f_{\text{GPM}}(H_{\text{core}}, \mathcal{A}, \mathcal{B}) \right)^2 \frac{\partial \mathcal{R}_{\text{gap}}(z)}{\partial z} \quad (3.82)$$

Then, similarly to the electromagnetic dynamics, the motion dynamics can be symbolically expressed as

$$\ddot{z} = \dot{v}_z = \begin{cases} f_2^{\nearrow}(x, \mathcal{A}, \mathcal{B}), & \text{if } \dot{H}_{\text{core}} \geq 0, \\ f_2^{\searrow}(x, \mathcal{A}, \mathcal{B}), & \text{if } \dot{H}_{\text{core}} < 0, \end{cases} \quad (3.83)$$

where the functions f_2^{\nearrow} and f_2^{\searrow} are derived from (3.5) using (2.86) and (3.82).

$$f_2^{\nearrow}(x, \mathcal{A}, \mathcal{B}) = \frac{1}{m} \left(-\frac{1}{2} A_{\text{core}}^2 \left(f_{\text{GPM}}^{\nearrow}(H_{\text{core}}, \mathcal{A}, \mathcal{B}) \right)^2 \frac{\partial \mathcal{R}_{\text{gap}}(z)}{\partial z} - k_s(z - z_s) - c v_z \right) \quad (3.84)$$

$$f_2^{\searrow}(x, \mathcal{A}, \mathcal{B}) = \frac{1}{m} \left(-\frac{1}{2} A_{\text{core}}^2 \left(f_{\text{GPM}}^{\searrow}(H_{\text{core}}, \mathcal{A}, \mathcal{B}) \right)^2 \frac{\partial \mathcal{R}_{\text{gap}}(z)}{\partial z} - k_s(z - z_s) - c v_z \right) \quad (3.85)$$

As seen in the previous section, the position of the movable armature defines three different dynamic modes: two corresponding to the two position boundaries and another one for the motion between them. In this regard, the hybrid automaton of Fig. 3.6, which considers these three modes, has been used to describe the dynamics of all the previously presented dynamical models. However, when considering magnetic hysteresis, the three modes related to the motion are doubled by the fact that the GPM uses different expressions depending on the direction of its input, which leads to the hybrid functions (3.78) and (3.83). Consequently, the proposed hybrid dynamical model of this subsection (see Fig. 3.7) has six different dynamic modes, which correspond to:

1. Maximum gap and H_{core} increasing.
2. Motion between boundaries and H_{core} increasing.
3. Minimum gap and H_{core} increasing.
4. Maximum gap and H_{core} decreasing.
5. Motion between boundaries and H_{core} decreasing.
6. Minimum gap and H_{core} decreasing.

The complete state of the system, χ , is composed of the dynamic mode, denoted by the discrete variable $q \in \{1, 2, 3, 4, 5, 6\}$, the already defined continuous state x , and, as a particular feature of this hybrid model, also the extrema sets \mathcal{A} and \mathcal{B} . Hence, by a slight misuse of notation,

$$\chi = (x, q, \mathcal{A}, \mathcal{B}). \quad (3.86)$$

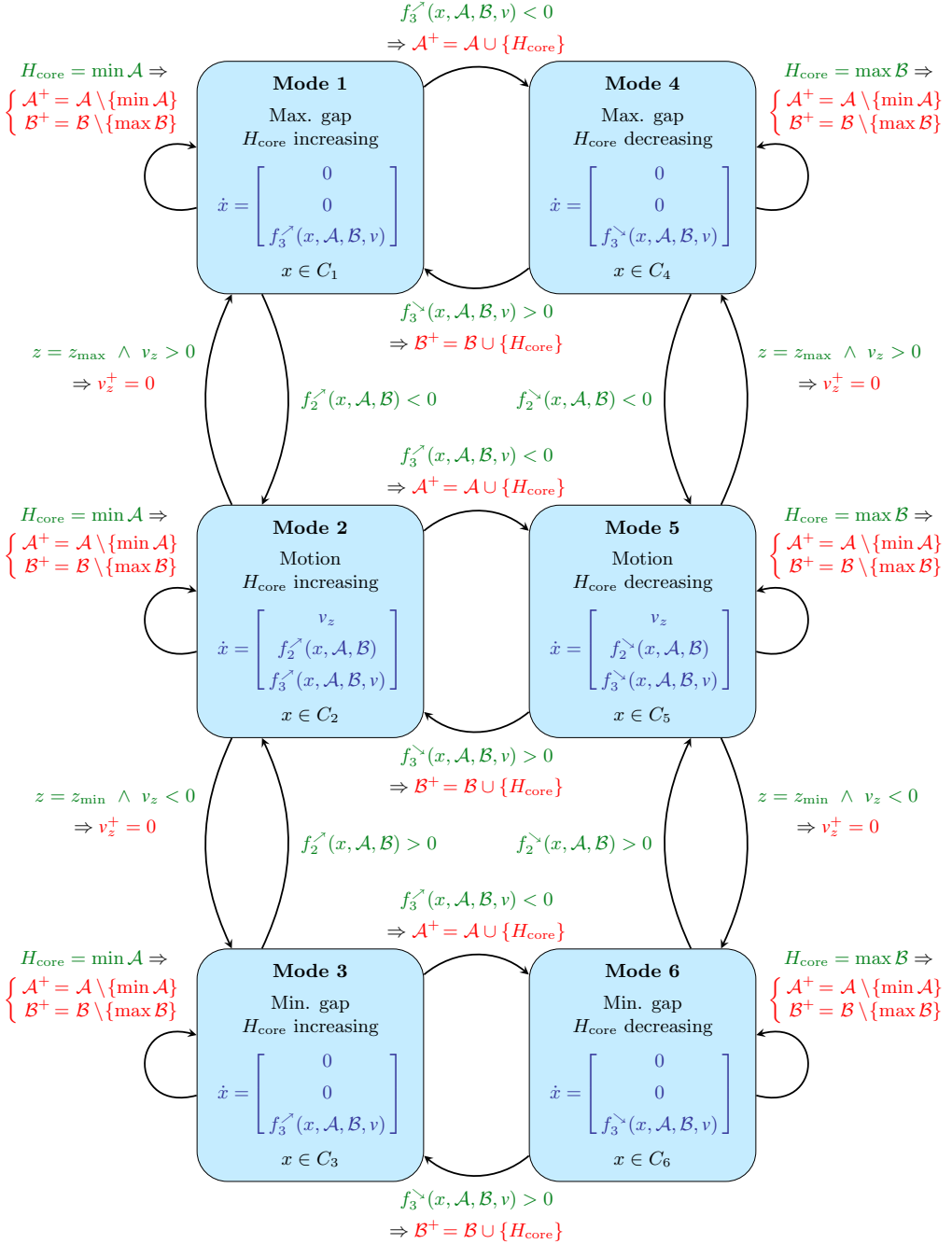


Figure 3.7: Hybrid automaton modeling the dynamics of the actuator in the presence of magnetic hysteresis.

The described dynamic modes are connected in the automaton by the corresponding guard and reset maps. With regard to the motion, the model operates as the previously presented automata. For simplicity, no bouncing phenomenon has been included in the model, but it may be easily incorporated by means of any of the techniques described in Section 3.1. Apart from the jumps related to the motion, two types of jumps may arise in this automaton due to the electromagnetic dynamics. First, those related to the wiping out property of the Preisach model. If the magnetic field varies inside a minor loop, bounded between the maximum value of the minima set, $\max \mathcal{B}$, and the minimum value of the maxima set, $\min \mathcal{A}$, and then it reaches one of the boundaries, the complete loop is wiped out from the history of the model. When this happens, the automaton jumps from its present mode to itself, and during the jump both $\max \mathcal{B}$ and $\min \mathcal{A}$ are removed from the extrema sets. The system also jumps when H_{iron} reaches an extrema. In this regard, if the magnetic field increases and then changes direction, the automaton jumps to the corresponding decreasing mode and the present value of H_{iron} is incorporated to the maxima set. Analogously, if the field first decreases and then increases, the automaton changes mode and the minima set is expanded with the new minimum. It should be noted that, since f_3^{\nearrow} and f_3^{\searrow} always have the same sign, the automaton cannot switch an infinite number of times between the increasing and the decreasing modes in a single time instant. Thus, the Zeno phenomenon [143] is prevented.

Based on the previous description, it is now easy to understand that the domains C_1 , C_2 , C_3 , C_4 , C_5 and C_6 are equal to

$$C_1 = C_4 = \{x \in \mathbb{R}^3 \mid z = z_{\max}, v_z = 0, \max \mathcal{B} \leq H_{\text{core}} \leq \min \mathcal{A}\}, \quad (3.87)$$

$$C_2 = C_5 = \{x \in \mathbb{R}^3 \mid z_{\min} \leq z \leq z_{\max}, \max \mathcal{B} \leq H_{\text{core}} \leq \min \mathcal{A}\}, \quad (3.88)$$

$$C_3 = C_6 = \{x \in \mathbb{R}^3 \mid z = z_{\min}, v_z = 0, \max \mathcal{B} \leq H_{\text{core}} \leq \min \mathcal{A}\}. \quad (3.89)$$

The expressions for the electric current and the equivalent eddy current can also be derived from the equations of the model as

$$i = \frac{1}{N} \left(A_{\text{core}} f_{\text{GPM}}(H_{\text{core}}) \mathcal{R}_{\text{gap}}(z) + H_{\text{core}} l_{\text{core}} \right) \left(1 + \frac{R k_{\text{ec}}}{N^2} \right)^{-1} + \frac{v}{R} \left(1 + \frac{N^2}{R k_{\text{ec}}} \right)^{-1}, \quad (3.90)$$

$$i_{\text{ec}} = -k_{\text{ec}} \left(\frac{v}{N} - \frac{R}{N^2} \left(A_{\text{core}} f_{\text{GPM}}(H_{\text{core}}) \mathcal{R}_{\text{gap}}(z) + H_{\text{core}} l_{\text{core}} \right) \right) \left(1 + \frac{R k_{\text{ec}}}{N^2} \right)^{-1}. \quad (3.91)$$

The Generalized Preisach Model presented in Section 2.6 depends on eight parameters (m_{h_c} , s_{h_c} , s_{h_m} , \hat{B}_{irr} , μ_1 , μ_2 , H_1 and H_2). Besides, A_{core} and l_{core} , which in the previous models are implicitly included in the parameters of the core reluctance, appear now explicitly in the equations. As a consequence, the hybrid dynamical model including saturation, hysteresis, flux fringing and eddy currents presented in this part of the section depends on nineteen parameters (m , k_s , z_s , c , z_{\min} , z_{\max} , N , R , k_{ec} , A_{core} , l_{core} and those of the GPM) and a method to calculate $\mathcal{R}_{\text{gap}}(z)$ and its partial derivative. If the McLyman model is used for that purpose, two additional parameters ($\mathcal{R}_{\text{gap}0}$ and l_w) are incorporated to the model, which results in a total of twenty-one parameters.

3.2.6 Overview of the models

The main results of the section are summarized for comparison in Tables 3.1 to 3.6. These tables show the state (Table 3.1), the parameters (Table 3.2), the electromagnetic dynamics (Table 3.3), the motion dynamics (Table 3.4), and the expressions for the electric current (Table 3.5) and the equivalent eddy current (Table 3.6) for the basic model (B), the model including saturation (S), the model with saturation and flux fringing (S+F), the model with saturation, flux fringing and eddy currents (S+F+EC) and the complete model including saturation, hysteresis, flux fringing and eddy currents (S+H+F+EC).

Table 3.1: State of the dynamical models.

Model	Continuous state	Dynamic mode	Complete state
B	$x = [z \quad v_z \quad \phi]^T$	$q \in \{1, 2, 3\}$	$\chi = [x^T \quad q]^T$
S	$x = [z \quad v_z \quad \phi]^T$	$q \in \{1, 2, 3\}$	$\chi = [x^T \quad q]^T$
S+F	$x = [z \quad v_z \quad \phi]^T$	$q \in \{1, 2, 3\}$	$\chi = [x^T \quad q]^T$
S+F+EC	$x = [z \quad v_z \quad \phi]^T$	$q \in \{1, 2, 3\}$	$\chi = [x^T \quad q]^T$
S+H+F+EC	$x = [z \quad v_z \quad H_{\text{core}}]^T$	$q \in \{1, 2, 3, 4, 5, 6\}$	$\chi = (x, q, \mathcal{A}, \mathcal{B})$

Table 3.2: Parameters of the dynamical models.

Model	Parameters
B	$m, k_s, z_s, c, z_{\min}, z_{\max}, N, R, \mathcal{R}_0, k_{\text{gap}}$
S	$m, k_s, z_s, c, z_{\min}, z_{\max}, N, R, \mathcal{R}_{\text{gap}0}, k_{\text{gap}}, \mathcal{R}_{\text{core}0}, \phi_{\text{sat}}$
S+F	$m, k_s, z_s, c, z_{\min}, z_{\max}, N, R, \mathcal{R}_{\text{gap}}(z)^*, \mathcal{R}_{\text{core}0}, \phi_{\text{sat}}$
S+F+EC	$m, k_s, z_s, c, z_{\min}, z_{\max}, N, R, \mathcal{R}_{\text{gap}}(z)^*, \mathcal{R}_{\text{core}0}, \phi_{\text{sat}}, k_{\text{ec}}$
S+H+F+EC	$m, k_s, z_s, c, z_{\min}, z_{\max}, N, R, \mathcal{R}_{\text{gap}}(z)^*, A_{\text{core}}, l_{\text{core}}, k_{\text{ec}}, m_{h_c}, s_{h_c}, s_{h_m}, \hat{B}_{\text{irr}}, \mu_1, \mu_2, H_1, H_2$

*The air gap reluctance can be stored in memory or modeled by a parametric expression.

Table 3.3: Electromagnetic dynamics.

Model	Explicit differential equation
B	$\dot{\phi} = \frac{v}{N} - \frac{R\phi}{N^2} (\mathcal{R}_0 + k_{\text{gap}} z)$
S	$\dot{\phi} = \frac{v}{N} - \frac{R\phi}{N^2} \left(\mathcal{R}_{\text{gap}0} + k_{\text{gap}} z + \frac{\mathcal{R}_{\text{core}0}}{1 - \phi /\phi_{\text{sat}}} \right)$
S+F	$\dot{\phi} = \frac{v}{N} - \frac{R\phi}{N^2} \left(\mathcal{R}_{\text{gap}}(z) + \frac{\mathcal{R}_{\text{core}0}}{1 - \phi /\phi_{\text{sat}}} \right)$
S+F+EC	$\dot{\phi} = \frac{\frac{v}{N} - \frac{R\phi}{N^2} \left(\mathcal{R}_{\text{gap}}(z) + \frac{\mathcal{R}_{\text{core}0}}{1 - \phi /\phi_{\text{sat}}} \right)}{1 + \frac{Rk_{\text{ec}}}{N^2}}$
S+H+F+EC	$\dot{H}_{\text{core}} = \frac{\frac{v}{N} - \frac{R}{N^2} \left(A_{\text{core}} f_{\text{GPM}}(H_{\text{core}}, \mathcal{A}, \mathcal{B}) \mathcal{R}_{\text{gap}}(z) + H_{\text{core}} l_{\text{core}} \right)}{\left(1 + \frac{Rk_{\text{ec}}}{N^2} \right) A_{\text{core}} \mu'_{\text{GPM}}(H_{\text{core}}, \mathcal{A}, \mathcal{B})}$

Table 3.4: Motion dynamics.

Model	Explicit differential equation
B	$\dot{v}_z = \frac{1}{m} \left(-\frac{1}{2} k_{\text{gap}} \phi^2 - k_s (z - z_s) - c v_z \right)$
S	$\dot{v}_z = \frac{1}{m} \left(-\frac{1}{2} k_{\text{gap}} \phi^2 - k_s (z - z_s) - c v_z \right)$
S+F	$\dot{v}_z = \frac{1}{m} \left(-\frac{1}{2} \phi^2 \frac{\partial \mathcal{R}_{\text{gap}}(z)}{\partial z} - k_s (z - z_s) - c v_z \right)$
S+F+EC	$\dot{v}_z = \frac{1}{m} \left(-\frac{1}{2} \phi^2 \frac{\partial \mathcal{R}_{\text{gap}}(z)}{\partial z} - k_s (z - z_s) - c v_z \right)$
S+H+F+EC	$\dot{v}_z = \frac{1}{m} \left(-\frac{1}{2} A_{\text{core}}^2 (f_{\text{GPM}}(H_{\text{core}}, \mathcal{A}, \mathcal{B}))^2 \frac{\partial \mathcal{R}_{\text{gap}}(z)}{\partial z} - k_s (z - z_s) - c v_z \right)$

Table 3.5: Electric current.

Model	Expression
B	$i = \frac{\phi}{N} (\mathcal{R}_0 + k_{\text{gap}} z)$
S	$i = \frac{\phi}{N} \left(\mathcal{R}_{\text{gap}0} + k_{\text{gap}} z + \frac{\mathcal{R}_{\text{core}0}}{1 - \phi /\phi_{\text{sat}}} \right)$
S+F	$i = \frac{\phi}{N} \left(\mathcal{R}_{\text{gap}}(z) + \frac{\mathcal{R}_{\text{core}0}}{1 - \phi /\phi_{\text{sat}}} \right)$
S+F+EC	$i = \frac{\frac{\phi}{N} \left(\mathcal{R}_{\text{gap}}(z) + \frac{\mathcal{R}_{\text{core}0}}{1 - \phi /\phi_{\text{sat}}} \right)}{1 + \frac{R k_{\text{ec}}}{N^2}} + \frac{v}{R + \frac{N^2}{k_{\text{ec}}}}$
S+H+F+EC	$i = \frac{\frac{1}{N} \left(A_{\text{core}} f_{\text{GPM}}(H_{\text{core}}, \mathcal{A}, \mathcal{B}) \mathcal{R}_{\text{gap}}(z) + H_{\text{core}} l_{\text{core}} \right)}{1 + \frac{R k_{\text{ec}}}{N^2}} + \frac{v}{R + \frac{N^2}{k_{\text{ec}}}}$

Table 3.6: Equivalent eddy current.

Model	Expression
B	$i_{\text{ec}} = 0$
S	$i_{\text{ec}} = 0$
S+F	$i_{\text{ec}} = 0$
S+F+EC	$i_{\text{ec}} = -k_{\text{ec}} \frac{\frac{v}{N} - \frac{R \phi}{N^2} \left(\mathcal{R}_{\text{gap}}(z) + \frac{\mathcal{R}_{\text{core}0}}{1 - \phi /\phi_{\text{sat}}} \right)}{1 + \frac{R k_{\text{ec}}}{N^2}}$
S+H+F+EC	$i_{\text{ec}} = -k_{\text{ec}} \frac{\frac{v}{N} - \frac{R}{N^2} \left(A_{\text{core}} f_{\text{GPM}}(H_{\text{core}}, \mathcal{A}, \mathcal{B}) \mathcal{R}_{\text{gap}}(z) + H_{\text{core}} l_{\text{core}} \right)}{1 + \frac{R k_{\text{ec}}}{N^2}}$

Chapter 4

Measurement and Identification

The previous chapters have addressed the theoretical aspects of the dynamical modeling of reluctance actuators including both the electromagnetism and the motion of the system. This chapter complements what has been previously presented from the experimental point of view. In the first section, several measuring methodologies for reluctance actuators are presented and discussed, and some of the measurements are analyzed and connected to that anticipated by the theory. Then, the second section explains how to use measurements to estimate the values of the unknown parameters of the dynamical models, with special emphasis on the electromagnetic subsystem. The procedure is illustrated by finding the parameters that best fit to one of the devices investigated in this thesis.

4.1 Measurement

4.1.1 Electromagnetic variables

Voltage, current and flux

As stated in previous chapters, the main electromagnetic variables of a single-coil reluctance actuator are the voltage across the coil terminals, the electric current flowing through the wire and the magnetic flux through the magnetic circuit. With regard to the voltage, commercial devices based on reluctance actuators such as power relays and solenoid valves are usually designed for supply voltages between 3 and 48 V. Hence, this variable can be directly measured by means of an oscilloscope. In particular, the Picoscope 4824 oscilloscope (see Fig. 4.1) has been used in many parts of this thesis due to its portability and because it incorporates a built-in signal generator that has been also utilized for some of the experiments. The electric current can be also measured by the scope, either by using a shunt resistor in series with the coil or by means of a current probe (see Fig. 4.2).



Figure 4.1: Picoscope 4824 USB oscilloscope. This scope has been used in most of the experiments because of its portability and its built-in signal generator.



Figure 4.2: Tektronix TCP312A current probe and TCPA300 amplifier. This probe has been utilized in some of the experiments to measure the current through the coil.

Contrary to the voltage and the current of the coil, measuring the magnetic flux through the core of a reluctance actuator is not straightforward. Basically, two different approaches can be found in the literature to measure or estimate the time-dependent value of the flux. On the one hand, secondary coils can be wound around the core to measure the variation of the magnetic flux [23, 151]. Note that, by direct application of Faraday's law (see Chapter 2) the induced voltage in the secondary coil is equal to the derivative of the magnetic flux. Thus, provided that the flux is not constant, an estimation can be obtained by integrating the induced voltage with respect to time. On the other hand, Hall sensors can also be used to measure the flux [20, 21]. Given that these sensors are based on the Hall effect [152], they are able to measure the magnetic flux density even if it is constant in time, which is advantageous in order to detect remanent magnetizations.

Despite the maturity of these methodologies, they still present significant problems. First, the estimation obtained from a secondary coil relies on numerical integration and only contains the ac component of the flux. Secondly, Hall sensors need to be placed in the air gap, which reduces the efficiency and limits the performance of the actuator. And thirdly, they may not even be applicable to some switch-type devices such as the studied solenoid valve, where the core, the gap or the winding are not accessible. For all these reasons, some recent works [24] propose model-based observers to estimate the magnetic flux using only measurements of the voltage and the current through the coil. Apart from solving some of the aforementioned problems, these algorithms have also the advantage that they do not require additional hardware or sensors. In this thesis, the flux is estimated using the algorithm presented in [110]. This estimator, which is one of the contributions of the thesis, is presented later in the document in Chapter 6.

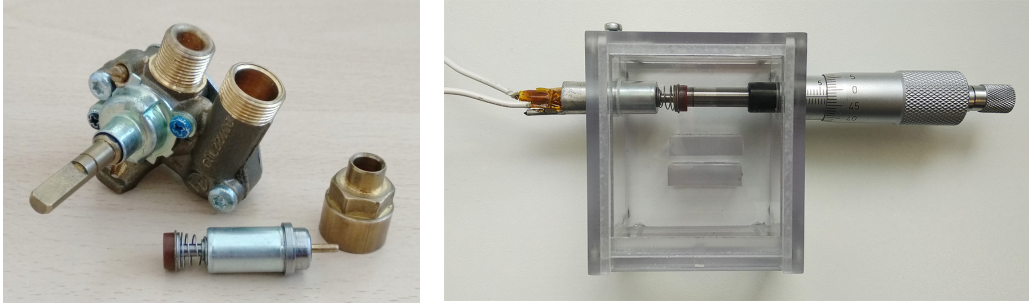


Figure 4.3: Gas faucet (left) and experimental setup (right) used in the tests. The solenoid valve is designed to operate inside the faucet; when inserted, the maximum gap is 0.9 mm. The micrometric screw of the setup permits a precise selection of the plunger travel.

Some measurements of the solenoid valve under normal operating conditions have been recorded to observe the dynamic behavior of the cited variables in a commercial switch-type device. For that, the valve has been inserted in the gas faucet for which it is specifically designed (see Fig. 4.3). When inserted, the plunger travel is limited to 0.9 mm. The response of the valve to four square wave pulses at different supply voltages is shown in Fig. 4.4. It can be seen that the system response changes with the applied voltage, specially during the closing. In this regard, the transient period lasts between 2 and 4 ms in the closing and about 7.5 ms in the opening. The response of the electric current is similar to that of a linear system with the exception of two periods, one during the closing and another one during the opening. As it will be confirmed later in the chapter, these periods are explained by the change of reluctance—and hence, of inductance—of the actuator during the motion of the plunger. The relation between the voltage and current values during the steady-state periods is almost proportional, which corresponds to a constant value of the internal resistance of the coil. On the other hand, the response of the magnetic flux is smoother—there are no sudden changes of direction as it happens with the current—but the relation with respect to the other variables during the steady-state periods is not proportional. Note that, whereas the current increases proportionally with the voltage, the increase of the flux is smaller. As stated in the modeling chapters, this is explained by magnetic saturation in the core.

A second group of experiments has been additionally conducted to observe the dynamical effects of varying the length of the armature travel. For that, an experimental setup with a micrometric screw has been designed and used in the tests (also shown in Fig. 4.3). The response of the system to a square wave pulse for four different values of the plunger travel is presented in Fig. 4.5. As shown, the transient response is greatly affected by the maximum length of the gap, particularly during the closing operation. In this regard, note that the periods when the current deviates from the linear response are longer the bigger the gap length, which agrees with the hypothesis that these periods are due to the motion of the plunger. As a final remark, note that in these experiments the current has been measured using a $5\ \Omega$ shunt resistor. The reason for this is to show that, contrary to the current probe, this measuring methodology reduces the effective voltage applied to the valve.

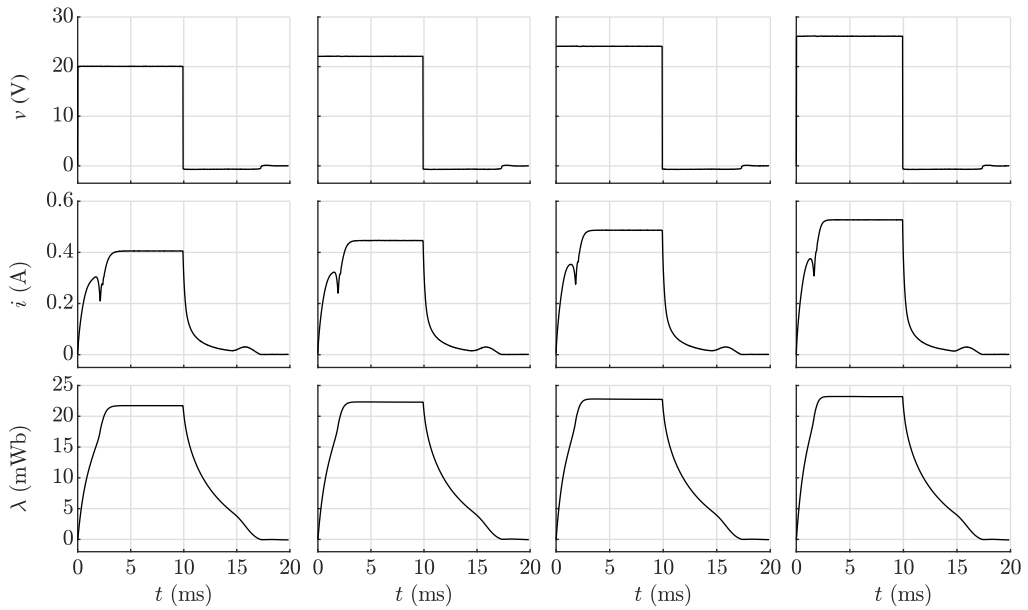


Figure 4.4: Voltage (top), current (middle) and flux linkage (bottom) of the solenoid valve during four square-wave pulses at different supply voltages. $z_{\max} = 0.9$ mm. The current has been measured using a current probe.

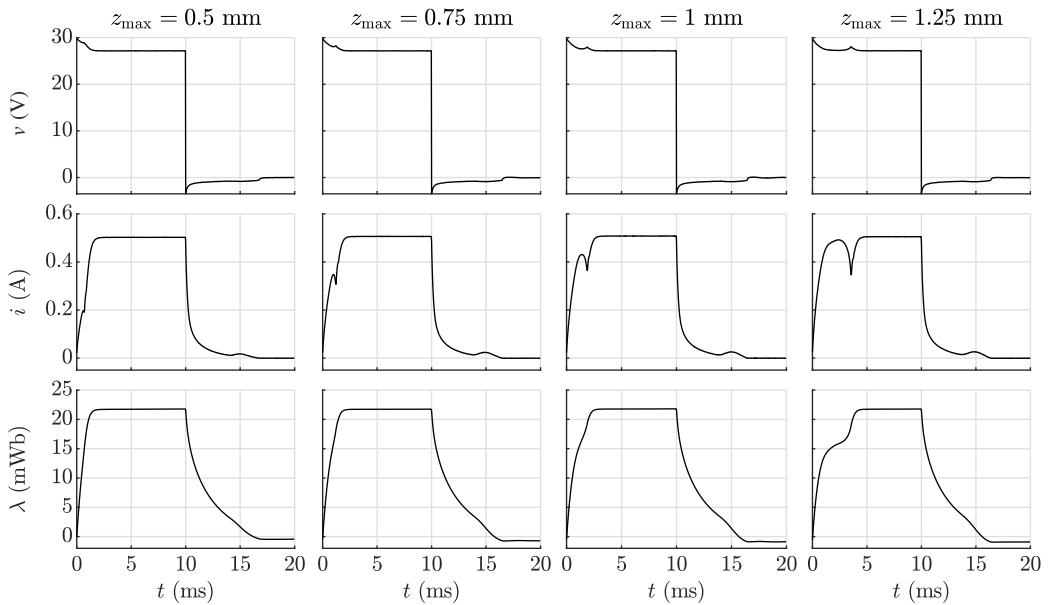


Figure 4.5: Voltage (top), current (middle) and flux linkage (bottom) of the solenoid valve during four square-wave pulses at supply voltage of 30 V. The current has been measured using a 5Ω shunt resistor that reduces the effective voltage applied to the valve.

Electrical contacts

Among all electromechanical devices based on reluctance actuators, power relays and contactors are special in the sense that they connect mechanically two electric circuits: the low-voltage control circuit that feeds the reluctance actuator and the high-voltage power circuit where the electrical load is placed. Consequently, apart from the voltage and the current of the coil, additional electrical measurements can be obtained from the secondary circuit. In particular, it is possible to obtain some information about the motion of the actuator by measuring whether the power terminals are connected or not. In this regard, note that the electrical connections between the moving contact and the fixed contacts depend on the position of the mechanism: The normally closed connection is established when the actuator is at its resting position and the normally open connection corresponds to the zero-gap position of the armature.

Fig. 4.6 represents the response of the single-pole double-throw power relay investigated in this thesis to a 24 V square wave voltage. As shown, the behavior of the current is qualitatively very similar to the results obtained from the solenoid valve. The measurements from the power terminals have been obtained using two voltage dividers; the values 0 and 1 in the figure denote respectively open and closed electrical connections. It can be seen how the connection switches from the normally closed contact to the normally open contact and vice versa, and also that the bounces experienced by the moving contact are reflected in the measurements as short voltage spikes. As it will be shown later in Chapter 7, this information can be used to improve the behavior of the device by means of iterative techniques.

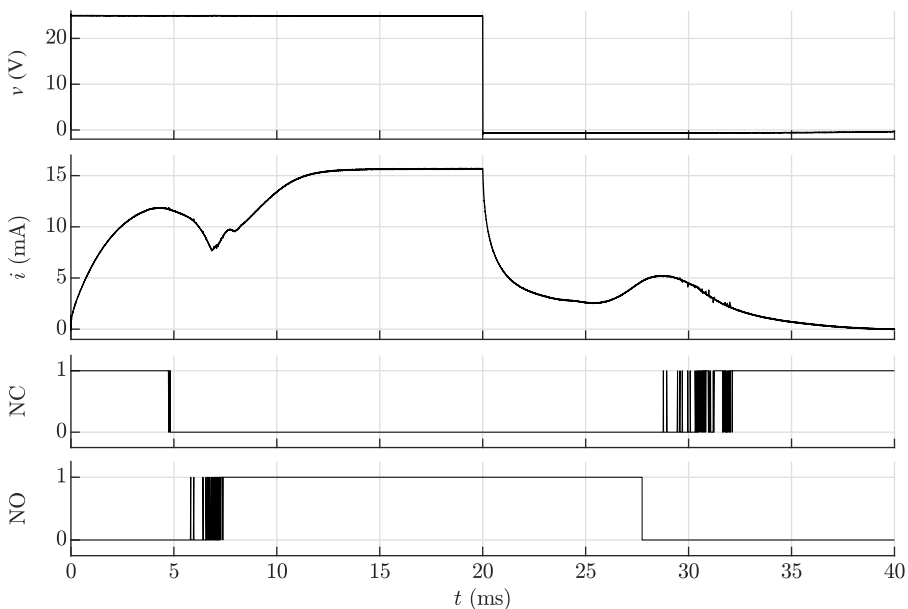


Figure 4.6: Relay response to a 24 V square wave. From top to bottom: voltage, current, normally closed (NC) contact and normally open (NO) contact.

4.1.2 Position

Position measurements in reluctance actuators may provide supplementary information that cannot be extracted from any other variable. If available, this information may be used for several purposes. Firstly, position and velocity records may help to check if some of the assumptions made in the modeling are correct or whether it is necessary to model some particular phenomena. For instance, accurate position measurements will show if the bouncing phenomenon is relevant in the studied actuator or if, on the contrary, it can be neglected. In addition, position measurements may also be employed to estimate the values of some of the parameters of the dynamical models or to evaluate the performance of position estimation algorithms. Furthermore, if real-time measurements were available, they could even be exploited to control the motion of the actuator using a feedback controller.

Measuring the position of a reluctance actuator is, however, not an easy task. The armature travel in short-stroke actuators is usually limited to less than one millimeter and, besides, the motion only lasts a few milliseconds. In order to capture useful information of the movement, the measuring equipment should therefore achieve an accuracy of less than $50\ \mu\text{m}$, which is a tenth of an armature travel of $0.5\ \text{mm}$, and a sampling rate higher than $10\ \text{kHz}$, which results in a minimum of ten samples in a one-millisecond movement. Considering that the measuring process should interfere as little as possible with the normal operation of the device, only optical measurement techniques satisfy the mentioned criteria. In addition to this, it should be noted that measuring the position of the armature of some commercial devices could be very challenging, or even impossible, only for accessibility reasons. For instance, almost all power relays in the market are encapsulated in a protective housing (see Fig. 4.7) which in many cases is part of the mechanism and hence cannot be disassembled. Solenoid valves present similar problems because the plunger is partially or completely concealed inside the housing and, consequently, it is not accessible for measuring.



Figure 4.7: Commercial power relays. The housing provides protection against dirt and humidity, but it blocks the visibility of the moving components.

In the following pages, three different instruments are presented to measure the armature position in short-stroke reluctance actuators: a laser displacement sensor, a line scan camera and a high-speed camera. The three are experimentally analyzed using the power relay investigated in this thesis (see Section 1.4). This relay has been selected for the analysis because, contrarily to other devices such as the solenoid valve, it is concealed in a housing that can be disassembled without affecting the system dynamics. The main results are presented and discussed, and the advantages and disadvantages of each measuring technology are highlighted.

Laser displacement sensor

Laser displacement sensors use laser triangulation to provide fast and accurate measurements of position. They are utilized in several industrial applications including, among others, dimensions measuring, accurate positioning of objects, detection of irregularities or vibration characterization. These instruments reach sampling rates of hundreds of kilohertz and precisions of less than $0.1 \mu\text{m}$, so they amply meet the requirements established. In particular, the analysis presented in this thesis has been performed using an LK-G5000 series laser displacement sensor from the manufacturer Keyence (see Fig. 4.8). This sensor has a sampling rate of up to 392 kHz and a precision of around $1 \mu\text{m}$.



Figure 4.8: Keyence LK-G5000 laser sensor. Sensor head (left) and controller (right).

The motion of the relay has been analyzed in Subsection 3.1.2 using a two-degree-of-freedom rigid body model that includes the motion of the armature and the moving contact. However, considering the geometry of the device, only the position of the armature can be measured using the laser sensor. The location of the measuring point can be seen in Fig. 4.9. Note that the moving contact is not accessible to the laser beam because it is surrounded by the normally closed contact and the normally open contact.

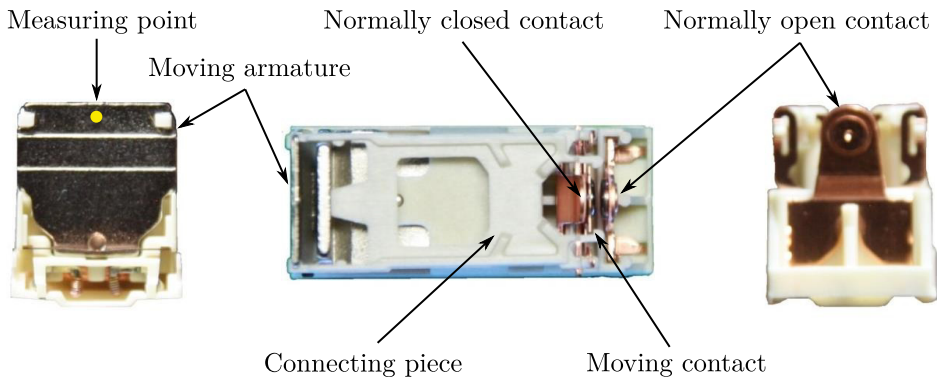


Figure 4.9: Power relay. The measuring point is indicated by a yellow dot. The moving contact is not accessible to the laser beam because it is surrounded by the fixed contacts.

Three different tests have been performed, which correspond to supply voltages of 20, 30 and 40 volt. The results are represented in Figs. 4.10, 4.11 and 4.12. These show how the duration of the two movements—closing and opening—varies with the supply voltage. On the one hand, the closing operation is shorter the higher the voltage. As stated by the theoretical models of Chapters 2 and 3, this is due to the fact that the magnetic flux, and hence the magnetic force, increases more rapidly when the voltage is higher. On the other hand, the duration of the opening operation is almost independent of the supply voltage because it is mainly driven by the spring force. It is noteworthy, however, that the higher the voltage the later the motion begins, which is simply explained by the higher value that the magnetic flux has when the voltage is cut off.

The measurements also show that the sudden change of direction of the current during the closing operation coincides exactly with the moment when the armature reaches its minimum position. Just like the duration of the motion, this phenomenon can also be explained using the models. For instance, if the basic dynamical model is considered, the electric current and the position are related by (3.56). Hence, the time derivative of the current is

$$\frac{di}{dt} = \frac{\mathcal{R}_0 + k_{\text{gap}} z}{N} \frac{d\phi}{dt} + \frac{\phi k_{\text{gap}}}{N} v_z. \quad (4.1)$$

Given that the velocity of the armature, v_z , experiences a jump at the impact, it is straightforward from the previous expression that the current slope will have an abrupt change at that moment. The current slope also experiences a jump during the opening operation when the armature reaches its maximum position, but this change is almost unnoticeable in the measurements because the flux, ϕ , is very low at that moment.

The bouncing phenomenon can also be seen in the measurements. There are noticeable differences between the bounces that exist at the end of each operation: Several bounces have been recorded at the end of the closing operation, but only one bigger bounce appears at the end of the opening. However, considering that the armature and the moving contact are connected by a plastic component, it is not possible to know if these bounces are only due to impacts of the armature or if, on the contrary, they are related to coupled oscillations between the two components.

In conclusion, laser displacement sensors amply meet the precision and frequency specifications required to measure the motion of reluctance actuators. Indeed, the laser sensor used in the tests not only captures accurately the motion of the armature from the maximum to the minimum position and vice versa, but it has enough precision to detect also the bounces that exist at the end of the motion. In addition, the laser controller returns the position measurement in real time as a voltage signal, so it may even be used for control purposes. Nevertheless, the laser beam presents some accessibility problems because it can only measure displacements in the direction of the beam. As a result, the motion of the moving contact of the relay cannot be measured using this technology.

Line scan camera

Line scan cameras are basically high-speed cameras with a single line of pixels. They are usually utilized in industrial applications that require high-speed images of large objects that move only in one direction. By placing the line of pixels perpendicular to the direction of the motion, a two-dimensional image of the object is obtained simply by

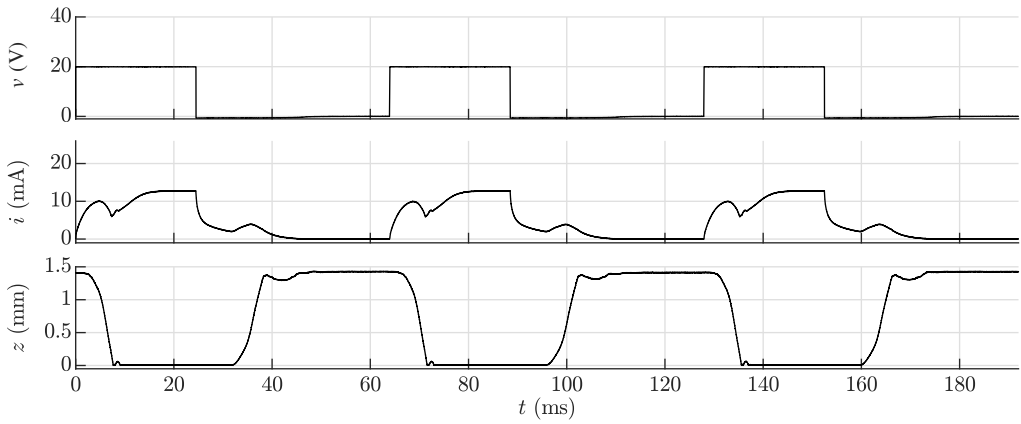


Figure 4.10: Voltage, current and position of the relay during the 20-volt test.

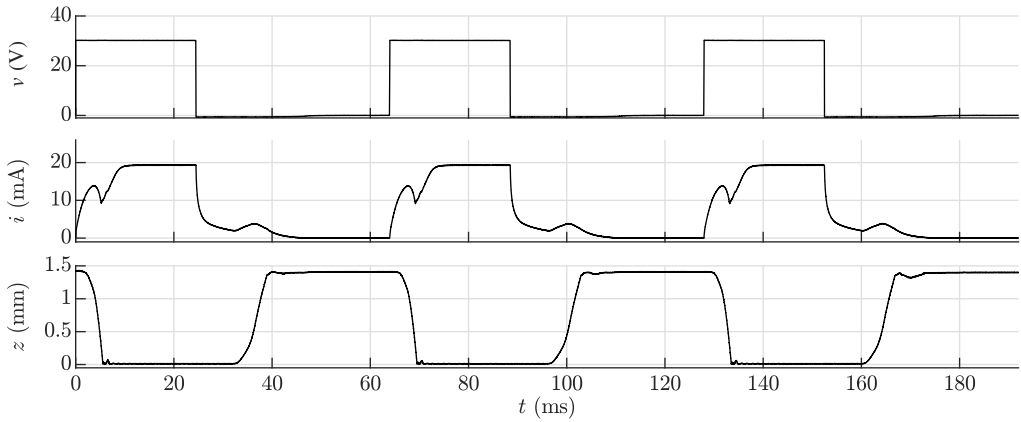


Figure 4.11: Voltage, current and position of the relay during the 30-volt test.

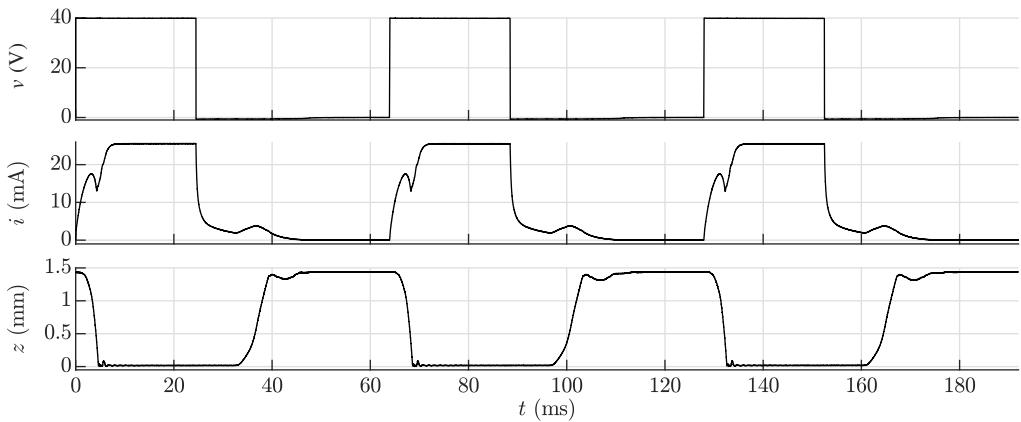


Figure 4.12: Voltage, current and position of the relay during the 40-volt test.

taking successive one-dimensional photos. Line scan cameras are the most cost-effective solution to inspect long rolls of material like paper, plastic or metal, but they could also be used for other purposes.

In this thesis, a Teledyne Dalsa Spyder3 line scan camera (see Fig. 4.13) has been utilized to record the motion of the power relay. This camera has a line of 1024 pixels and features a sampling rate of up to 36 kHz. In order to capture the motion of all the components of the mechanism at the same time, the camera has recorded the line shown in Fig. 4.14. This line contains the armature, the plastic connecting piece and the contacts. The length of the line is about 2 cm, which results in an approximate resolution of $20 \mu\text{m}/\text{pixel}$.



Figure 4.13: Teledyne Dalsa Spyder3 line scan camera with and without lens.

The results corresponding to the recording of a closing operation are also shown in the bottom part of Fig. 4.14. The lighting conditions of the experiment made it impossible to use the maximum sampling rate of the camera, so the image was recorded at 8 kHz. It can be seen that the motion of the armature starts approximately at t_1 and lasts until t_4 . The bouncing phenomenon of this component is not clearly seen in the figure due to the sampling rate of the camera, which is much lower than the laser sensor frequency. The motion of the moving contact is shorter in duration than the motion of the armature: It starts moving approximately at t_2 and hits the fixed contact at t_3 . Note that this is explained by the geometry and disposition of the different components of the device and it justifies the two-degree-of-freedom mechanism proposed for the relay in Subsection 3.1.2. A coupled vibration between the moving contact and the normally open contact can also be seen in the figure after t_3 .

The advantages of line scan cameras with respect to two-dimensional high-speed cameras are that they generally have lower costs and are able to return data in real time. In this regard, it has been shown that this type of camera can be used to record the motion of several components of a power relay at the same time, which is not possible if a single laser displacement sensor is used. On the contrary, the sampling rate and the precision of the investigated camera are not enough to capture the bounces that have been already detected using the laser sensor, which clearly represents a drawback. In addition, understanding and processing a line image is not a straightforward task and, besides, the obtained results rely strongly on the geometry of the device and also on having proper lighting conditions.

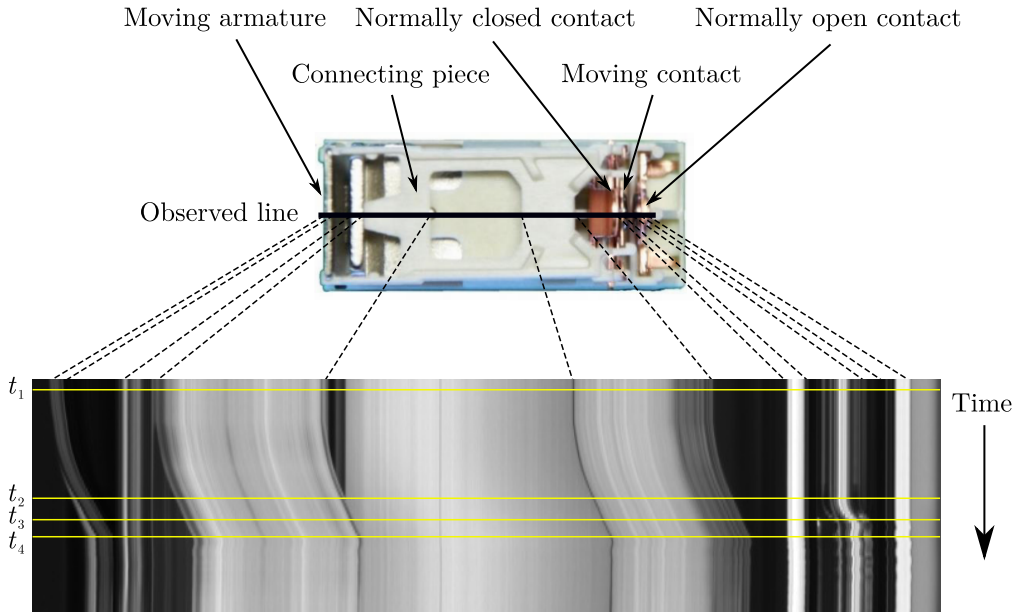


Figure 4.14: Power relay and line observed by the line scan camera (top) and recording of a closing operation (bottom).

High-speed camera

The term high-speed camera is generally used to refer to devices with frame rates higher than a thousand frames per second (fps). These cameras are used to record fast-moving objects whose motion cannot be captured by means of standard cameras. Present-day high-speed cameras are able to film up to a million fps at reduced image resolutions and up to dozens of thousands of fps at resolutions of about one megapixel. In particular, the experiments presented in this section have been conducted using the Fastcam APX-RS high-speed camera from the manufacturer Photron (see Figs. 4.15 and 4.16). This camera achieves a frame rate of 3,000 fps at the maximum resolution of 1024×1024 pixels and higher frame rates of up to a quarter of a million fps at lower resolutions.



Figure 4.15: Photron Fastcam APX-RS high-speed camera.

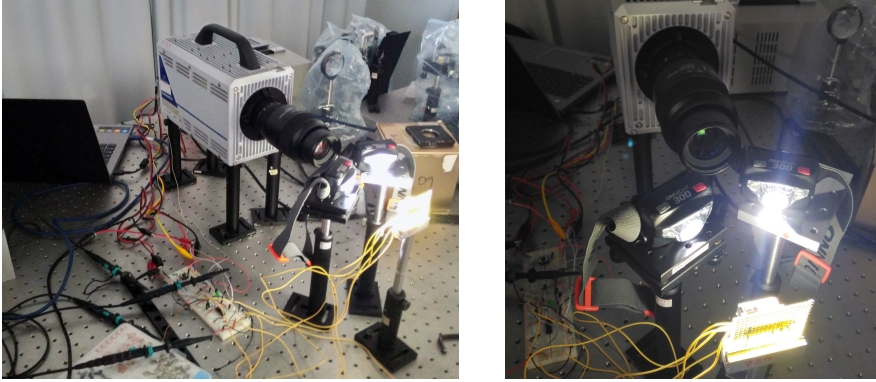


Figure 4.16: Experimental setup designed to record the motion of the power relay.

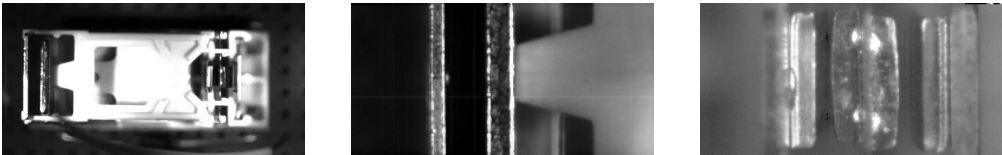


Figure 4.17: Snapshots of the recorded videos. General view (left) zoomed view of the armature (center) and zoomed view of the contacts (right).

Considering the speed and precision requirements presented at the beginning of the section, the camera has been configured to record at 50,000 fps using a resolution of 256×128 pixels. Three different types of videos have been recorded as shown in Fig. 4.17: a general view of the relay that captures the armature and the moving contact at the same time and two zoomed views that permit a more detailed analysis of the motion of each one of these components.

The videos have been processed by means of computer vision techniques [153] to obtain the evolution in time of the positions of the armature and the moving contact. The results obtained from the general view are very similar to those obtained with the line scan camera. Consequently, only the results corresponding to the two zoomed views are presented. The motion of the armature is firstly represented in Fig. 4.18. It can be seen that the results obtained by processing the video are similar to those from the laser sensor. In this connection, note that there are some small bounces at the end of the closing operation and a bigger bounce at the end of the opening. The precision of the measure, however, is worse because of the resolution of the camera. On the other hand, the position measurement obtained for the moving contact during a different operation is shown in Fig. 4.19. This measure is particularly interesting because it cannot be properly obtained by any of the other techniques. It can be seen that the contact moves very fast in both operations. Indeed, it only takes about one millisecond to move from the normally closed contact to the normally open contact and vice versa. In addition, the bounces of the moving contact are also of special interest because they are very different from those of the armature: There is a big bounce at the end of the closing and several smaller bounces at the end of the opening.

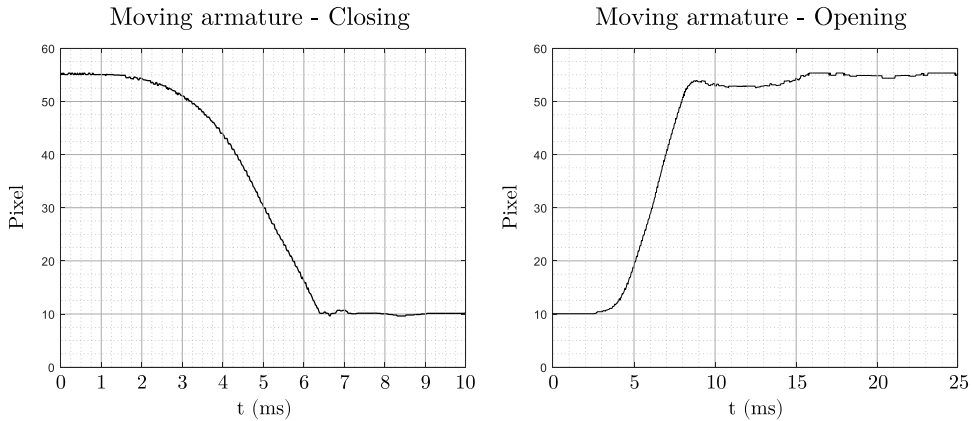


Figure 4.18: Armature position during closing (left) and opening (right) operations. Supply voltage: 25 V. Each pixel corresponds approximately to 31 μm .

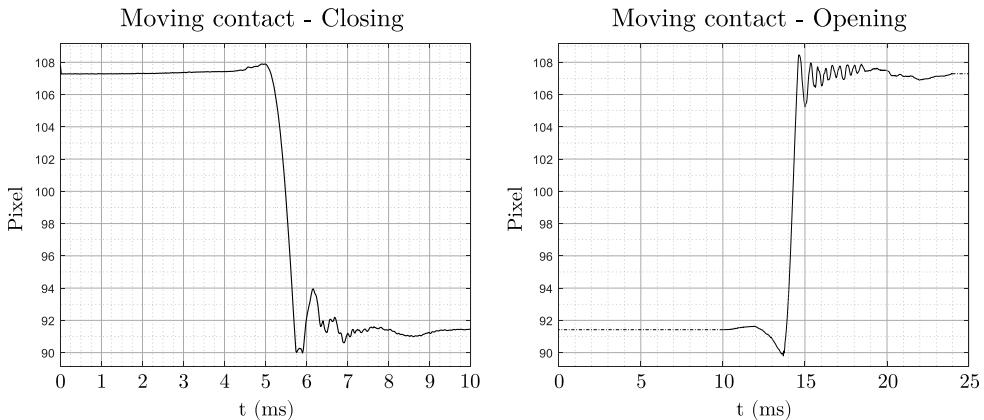


Figure 4.19: Moving contact position during closing (left) and opening (right) operations. Supply voltage: 25 V. Each pixel corresponds approximately to 8.5 μm .

In conclusion, the high-speed camera has some advantages with respect to the other devices that have been used to record the motion of the relay. On the one hand, it can measure the position of the moving contact, which could not be achieved using the laser sensor. On the other, the two-dimensional images obtained from the camera contain much more information than the one-dimensional images of the line scan camera and, in addition, they are more understandable. Despite that, the camera also has some drawbacks. The images are not obtained in real time, which may represent a problem depending on the purpose of the measurements. Besides, processing the videos is time consuming and the quality of the results depends strongly on the lighting conditions. Last but not least, the cost of a high-speed camera with the specifications required for these experiments is around 50,000 euros, whereas both the laser sensor and the line scan camera can be bought for less than 5,000 euros. Note however that this cost is between three and four orders of magnitude higher than the price of a commercial relay or solenoid valve, so the applicability of any of these methods is restricted to laboratory tests.

4.1.3 Acoustic noise

In the previous pages, different methodologies have been presented to measure variables such as the current through the coil or the position of the armature. These variables are closely related to the dynamical models presented in this thesis and, hence, they may be useful to improve the understanding of the electromagnetic dynamics and the motion of reluctance actuators. Another important variable of these devices that is not included in the models is the acoustic noise generated by the actuator during the movement. As stated in the introductory chapter, one of the disadvantages of this class of actuators is that they produce an undesirable audible noise each time they are activated or deactivated. This noise is closely related to the dynamics of the system and is mainly produced by the impacts of the armature with the fixed parts of the actuator. Hence, considering that one of the objectives of the thesis is to design control strategies to achieve soft landing, noise measurements may be used as an indicator of the performance of the controller.

Contrary to the flux or the position, the acoustic noise generated by the actuator can be easily measured using a low-cost microphone. As an illustrative example, Fig. 4.20 shows the noise generated by the power relay in a 20 V square wave activation, together with all the other variables. As shown, there is a clear correspondence between the armature collisions and the noise captured by the microphone. Similarly to the information from the electrical contacts, it will be shown later in Chapter 7 that noise measurements can be used to improve the performance of reluctance actuators by means of iterative control techniques.

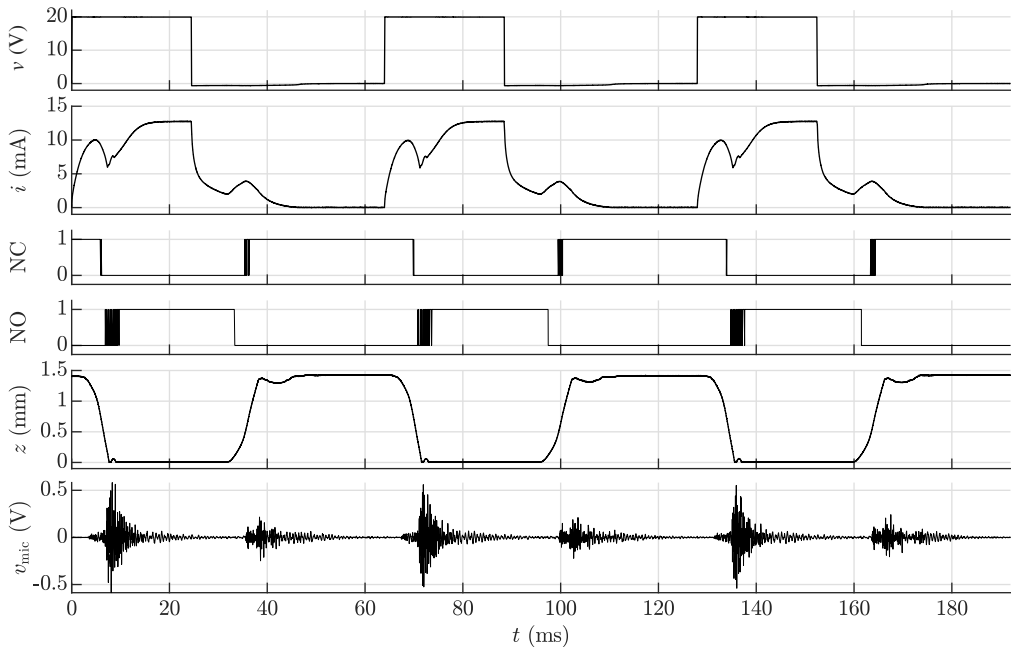


Figure 4.20: Relay response to a 20 V square wave voltage. From top to bottom: voltage, current, normally closed (NC) contact, normally open (NO) contact, armature position and audio signal captured by the microphone (v_{mic}).

4.2 Identification

In the first section of this chapter, several measurements obtained from two commercial devices have been presented and analyzed. In this regard, the dynamic behavior observed in variables such as the current and the position has been explained considering the theoretical aspects presented in the previous chapters. This section shows how to use measurements to identify and validate the dynamical models for reluctance actuators previously described in Chapter 3.

The method presented in the following pages is specifically designed to estimate the parameters of the dynamical model including saturation, hysteresis, flux fringing and eddy currents (S+H+F+EC, see Subsection 3.2.5). This is the most comprehensive model presented in this thesis; the rest of the models could be seen as simplifications of it. The device used to illustrate the methodology is the solenoid valve presented in Section 1.4. This valve is basically a plunger-type reluctance actuator, with the coil wrapped around the plunger and an iron housing that serves both as returning path for the flux and protective cover. The material of the core and the housing is unknown and, hence, the values of the parameters of the reversible part of the generalized Preisach model (GPM)— μ_1 , μ_2 , H_1 and H_2 —and those corresponding to the irreversible part— \hat{B}_{irr} , m_{h_c} , s_{h_c} and s_{h_m} —as well as the eddy current parameter— k_{ec} —need to be estimated by means of experimental tests and identification procedures. The rest of the parameters are known and can be found in Table 4.1. The reluctance of the air gap (see Fig. 4.21) has been obtained from FEM simulations as explained in Chapter 2.

Table 4.1: Known valve parameters. Mechanical damping is assumed negligible.

Parameter	Value	Parameter	Value
R	49 Ω	m	0.85 g
N	1200	k_s	42 N/m
l_{core}	55 mm	z_s	15 mm
A_{core}	12.57 mm ²	c	0 Ns/m

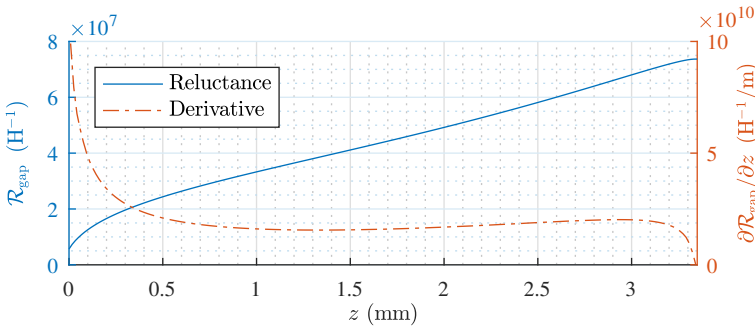


Figure 4.21: Air gap reluctance of the solenoid valve and partial derivative with respect to the gap length. Results from FEM simulations.

4.2.1 Experimental setup

The experimental setup used in the tests is shown in Fig. 4.22 and consists of the following equipment: a Toelner TOE 7621 four-quadrant voltage and current amplifier, a Picoscope 4824 USB oscilloscope that also features an arbitrary waveform generator, a Tektronix TCP312A current probe and its corresponding TCPA300 amplifier, a personal computer with Matlab and the Instrument Control Toolbox and, finally, the valve, which can also be seen in the picture, wrapped in orange electrical tape. The operation of the setup is as follows. First, a current or voltage waveform is designed and programmed in Matlab. When the code is executed, the reference signal is sent to the generator, amplified by the power supply and applied to the valve. At the same time, the oscilloscope measures, registers and sends the values of voltage, v , and current, i , back to the computer. Finally, the data are processed and the magnetic flux, ϕ , is estimated using the SEMERA algorithm [110], which is presented later in Chapter 6.

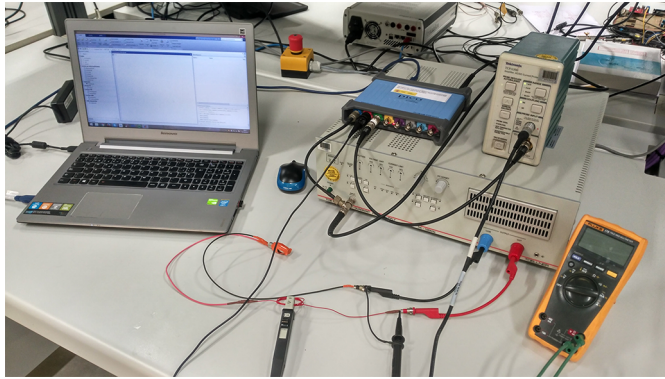


Figure 4.22: Experimental setup used in the tests.

Three different sets of experiments have been performed, each having a specific purpose and based on a particular type of waveform which is repeated at several levels of excitation. The first group of tests is used to determine the values of the parameters of the GPM and have been carried out with the plunger fixed at zero gap ($z = 0$). These use a low-frequency (10 Hz) sinusoidal current input, which minimizes the induced currents and, consequently, improves the identifiability of the hysteresis model. Once the GPM parameters are determined, the second group of experiments is utilized to estimate the value of k_{ec} . In these tests, the position is also externally set at $z = 0$, but, instead of the sinusoidal current, a symmetric square wave voltage is used to induce transient eddy currents in the iron core. Finally, the third set, which is only for validation purposes, consists of a series of normal operating cycles of the valve at different voltages. That is, the plunger is released, the valve is inserted into the gas faucet (see Fig. 4.3), which limits the motion of the plunger from $z_{\min} = 0$ mm up to $z_{\max} = 0.9$ mm, and finally the device is activated using a unipolar square wave voltage. In order to start the tests from a known initial state, a decreasing sine wave current has been applied to the valve before each group of experiments to obtain a demagnetized state in the core (degaussing process). Table 4.2 sums up the described sets of experiments.

Table 4.2: Sets of experiments.

Set	Input wave	Levels	Purpose
1	Current, sinusoidal	8 (25-500 mA)	GPM fitting
2	Voltage, bipolar square	8 (1-18 V)	k_{ec} estimation
3	Voltage, unipolar square	5 (18-26 V)	Validation

4.2.2 Parameter estimation

The identification process of the GPM is similar to that presented in [23] and is carried out using the data from the first set of tests. The measurements of the current, i , and the magnetic flux, ϕ , obtained from the experiments are firstly used to compute the time-dependent values of B_{core} and H_{core} . In this regard, the magnetic flux density is obtained from (3.74) as

$$B_{\text{core}} = \frac{\phi}{A_{\text{core}}}, \quad (4.2)$$

and the magnetic field intensity is calculated from (2.57) and (3.72) assuming that the induced currents are negligible, which leads to

$$H_{\text{core}} = \frac{N i - \phi \mathcal{R}_{\text{gap}}(z=0)}{l_{\text{core}}}. \quad (4.3)$$

The reversible part of the model is identified firstly. For this purpose, measurements of μ'_{Rev} are obtained as the slope $\partial B_{\text{core}}/\partial H_{\text{core}}$ at the reversal points of 64 minor loops at eight different excitation levels. Then, the resulting points are used to fit the model proposed for the reversal permeability, (2.88), by minimizing the root-mean-square error (RMSE). As explained in Subsection 3.2.5, the constraint $\mu'_{\text{Rev}}(H_{\text{core}}) > 0$ for all $H_{\text{core}} \in \mathbb{R}$ is imposed during the fitting to guarantee that the dynamics of H_{core} , given by (3.78), is unambiguously defined. The measured points and the fitted model response are shown in Fig. 4.23.

Once the parameters of the reversible part are determined, the rest of the GPM is identified. In order to match the demagnetized state of the valve, the model also has to be firstly demagnetized, which is simply achieved by setting proper initial values for the extrema sets \mathcal{A} and \mathcal{B} . The selection of the initial number of elements in these sets is a tradeoff between model accuracy and computational time. In this case, the model has been initialized using two symmetric sets composed of a hundred elements in the interval $[-10^4, +10^4]$ A/m, which is the expected range for the magnetic field H_{core} .

$$\mathcal{A}(t=0) = \{ \alpha_k = +10^4 - 100k \text{ A/m} \mid k = 0, 1, \dots, 99 \} \quad (4.4)$$

$$\mathcal{B}(t=0) = \{ \beta_k = -10^4 + 100k \text{ A/m} \mid k = 0, 1, \dots, 99 \} \quad (4.5)$$

As explained in Section 2.6 and given that \mathcal{A} and \mathcal{B} have initially the same number of elements, it is assumed that H_{core} increases at $t = 0$.

The GPM [see (2.84)] is then computed using as input the experimental values of H_{core} obtained from (4.3) and fitted by minimizing the RMSE between the simulated

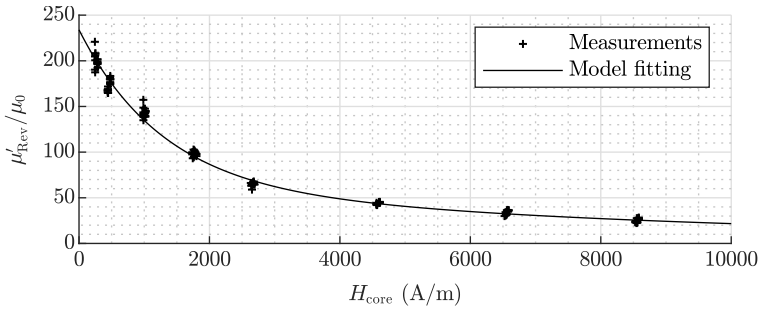


Figure 4.23: Measured values of the reversible part of the incremental permeability and least-squares fit to equation (2.88).

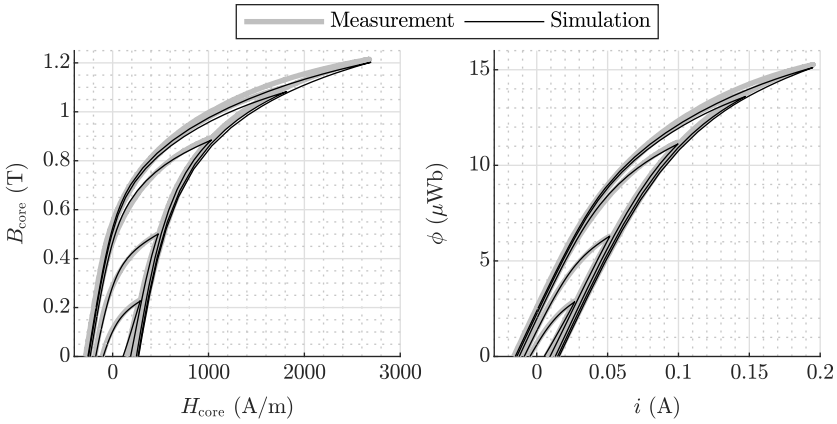


Figure 4.24: Measured hysteresis curves and simulated output of the GPM.

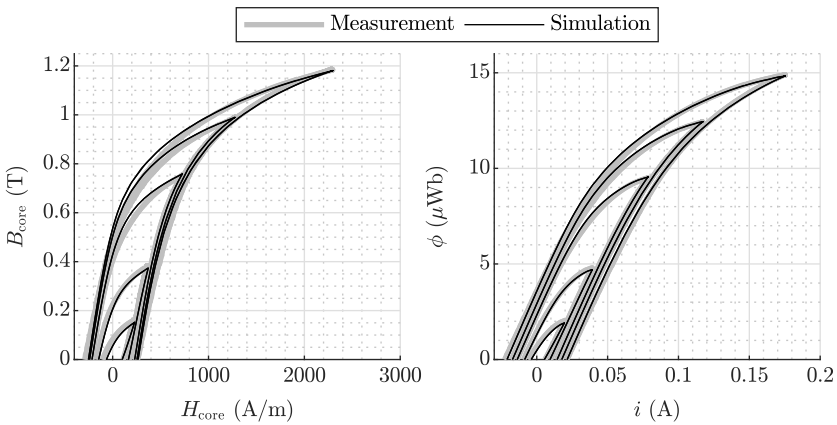


Figure 4.25: Measured response of the system in the presence of hysteresis and eddy currents and simulated output of the hybrid dynamical model.

Table 4.3: Estimated GPM parameters.

Parameter	Value	Parameter	Value
μ_1	168.8 μ_0	\hat{B}_{trr}	0.8103 T
μ_2	64.13 μ_0	m_{h_c}	227.9 A/m
H_1	1262 A/m	s_{h_c}	154.9 A/m
H_2	8821 A/m	s_{h_m}	138.0 A/m

and the measured values of B_{core} . Fig. 4.24 shows the measured hysteresis curves and the simulated response of the GPM after the identification procedure, in both the $B_{\text{core}} - H_{\text{core}}$ and $\phi - i$ planes. Although eight different excitation levels have been used to fit the model, only the smallest five cycles are represented for clarity reasons. The estimated parameters of the GPM are shown in Table 4.3.

The second group of tests is subsequently used to determine the value of the eddy current parameter, k_{ec} , which is assumed constant. During this stage of the identification, the complete dynamical model of the actuator is utilized instead of only the GPM. However, since the position of the plunger is externally set to $z = z_{\text{min}} = 0$ mm, only the dynamic modes 3 and 6 are active (see Fig. 3.7). The aim of the identification is to minimize the following weighted RMSE,

$$J = J(k_{\text{ec}}) = \sqrt{\frac{\int (i_{\text{exp}}(t) - i_{\text{sim}}(t))^2 dt}{\int (i_{\text{exp}}(t))^2 dt} + \frac{\int (\phi_{\text{exp}}(t) - \phi_{\text{sim}}(t))^2 dt}{\int (\phi_{\text{exp}}(t))^2 dt}}, \quad (4.6)$$

where “exp” and “sim” refer respectively to the values measured in the experiments and those obtained by simulation. The result of the optimization leads to a value of k_{ec} equal to 1637 A/V. The responses of both the system and the model in the presence of hysteresis and eddy currents are shown in Fig. 4.25. Note that, while the $B_{\text{core}} - H_{\text{core}}$ relation remains unchanged because it is only affected by hysteresis and saturation, the $\phi - i$ cycle becomes wider due to the effect of eddy currents.

The previous identification procedure has been specifically designed to estimate the values of the parameters of the dynamical model including saturation, hysteresis, flux fringing and eddy currents. However, the parameters of the other models presented in Chapter 3 can also be estimated using the same experimental measurements. As stated at the beginning of the section, these models could be seen merely as simplifications of the former. They differ basically in three aspects: the magnetic model used for the core, the inclusion or not of eddy currents and the reluctance of the air gap. With regard to the core, note that any of the magnetic relations presented in Sections 2.5 and 2.6 can be fitted to the measurements of the first set of experiments as done with the GPM (see Fig. 4.24). On the other hand, the air gap reluctance obtained from FEM simulations (see Fig. 2.13) can be also used to obtain the simplified models of Section 2.4.

4.2.3 Validation and analysis

Once the parameters have been estimated, the performance of the S+H+F+EC model is evaluated using the data of the third set of experiments. It should be recalled that, unlike in the other two sets of tests, in this case the plunger is allowed to move freely between $z_{\min}=0$ mm and $z_{\max}=0.9$ mm. Thus, all the dynamic modes of the hybrid automaton (see Fig. 3.7) may be reached.

The results of the validation process are shown in Fig. 4.26. The first plot in the figure shows the voltage signal that has been used as input of both the real actuator and the dynamical model. The measured and simulated values of the electric current and the magnetic flux are respectively presented in the second and third plots. It can be seen that the agreement between the measurements and the simulation is very good. The mean absolute error (MAE) of the current is 2.665 mA, which represents about 1.23 % of the mean value of i , and the MAE of the flux is 0.1450 μWb , which is about 1.33 % of the mean value of ϕ .

Additionally, the figure also presents the simulated values of the magnetic field intensity in the core, the position of the plunger and the dynamic mode of the automaton. As shown, the behavior of the system during the five operations is qualitatively similar. The plunger is initially at rest at $z=z_{\max}$ (dynamic mode 1) and, once the voltage pulse is applied, both the current and the flux begin to increase rapidly. After some time, the magnetic flux reaches a value such that the magnetic force given by (3.63) exceeds the spring force and, consequently, the plunger starts moving ($q=2$). Although depending on the applied voltage, the motion is always very fast and the minimum gap position is reached within the next 2 ms. Since mechanical bouncing has not been modeled, the position remains static ($q=3$) while the electromagnetic variables evolve towards a stationary state. Then, when the voltage is cut off, H_{core} starts to decrease and the automaton jumps to dynamic mode 4. The system remains at $z=z_{\min}$ until the magnetic force is not large enough to maintain the position. At that moment, the model jumps to $q=5$ and the plunger starts the backward motion, which lasts about 2.6 ms for all the excitation levels. Finally, the position reaches $z=z_{\min}$, the automaton jumps to $q=6$, and the flux and the current return again to a stationary state.

A more detailed analysis of the results is obtained by comparing the S+H+F+EC model with the other dynamical models of Chapter 3: the basic model, the model including saturation, the S+F model and the S+F+EC model. For that purpose, the parameters of these simplified models have been firstly estimated as previously explained. Then, four different simulations—one with each model—have been conducted using as input the voltage signal already presented. The simulation results are presented in Figs. 4.27 to 4.30 and summarized in Table 4.4. It is shown that the accuracy of the simulations increases with the complexity of the model and, hence, the S+H+F+EC model is the most accurate model. In this connection, note that the greatest improvements in accuracy are achieved with the inclusion of magnetic saturation and magnetic hysteresis. The basic dynamical model has the lowest accuracy—note the effects of neglecting saturation—but, by contrast, it requires the least computational effort. On average, the dynamical model including saturation, the S+F model and the S+F+EC model require, respectively, about 12 %, 24 % and 37 % more computing time per integration step than the basic model. On the other hand, the S+H+F+EC is around 19 times more expensive to evaluate, which is

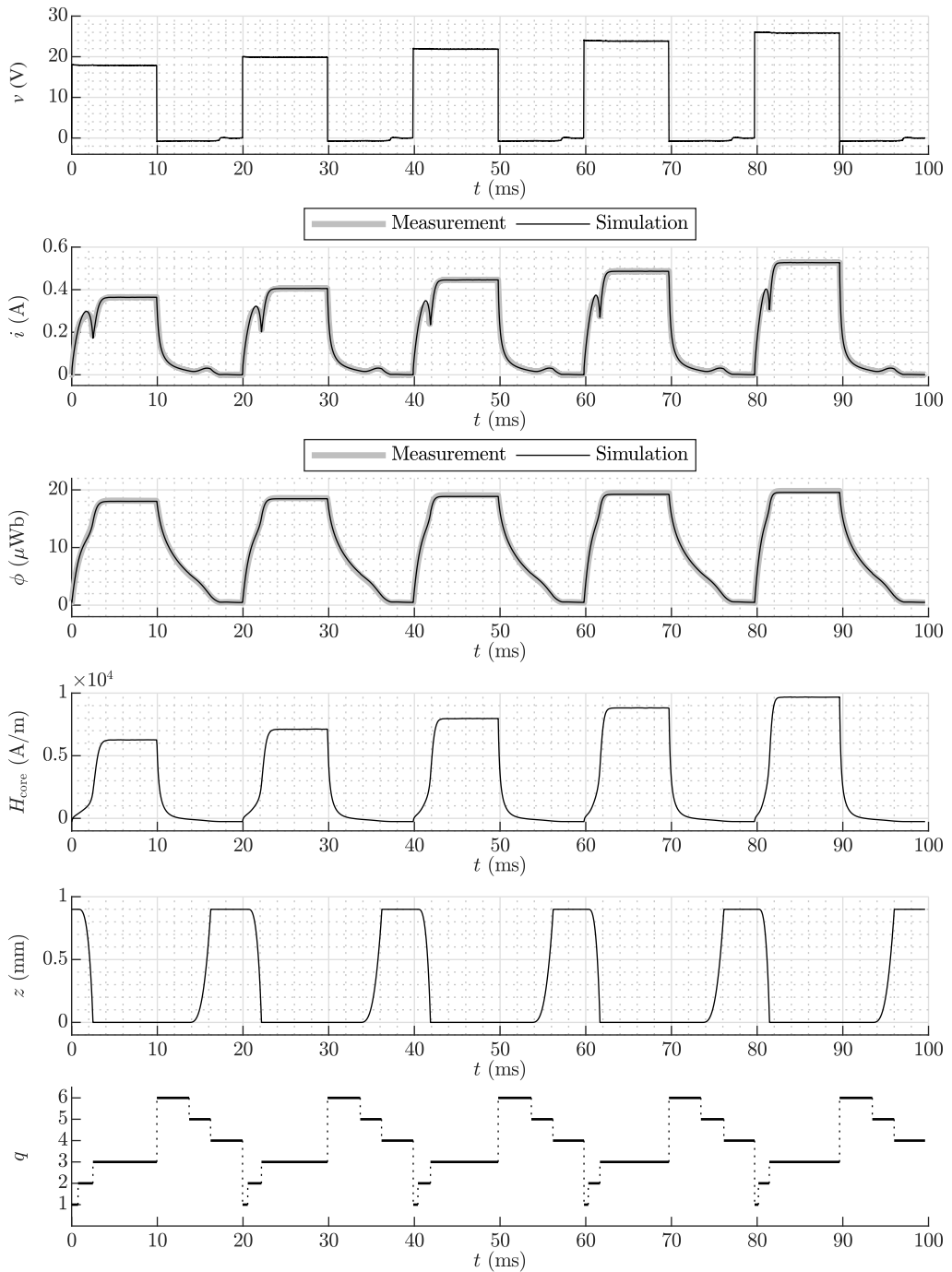


Figure 4.26: Validation of the S+H+F+EC dynamical model. From top to bottom, voltage (input), measured and simulated current, measured and simulated flux, simulated magnetic field intensity, simulated position, and simulated dynamic mode.

caused by the numerical integrals performed by the hysteresis model at each integration step (see Section 2.6). Selecting a model for a given application is consequently a tradeoff between model accuracy and computing effort. Overall, the S+H+F+EC model is better suited for accurate offline simulations and the rest of the models are more appropriate for online estimation and control.

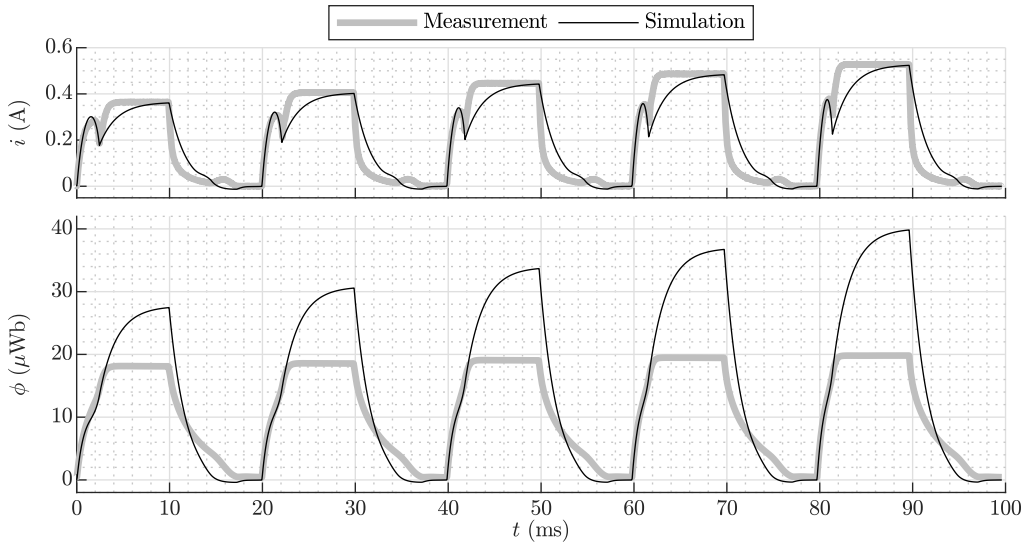


Figure 4.27: Validation of the basic dynamical model. Electric current (top) and magnetic flux (bottom).

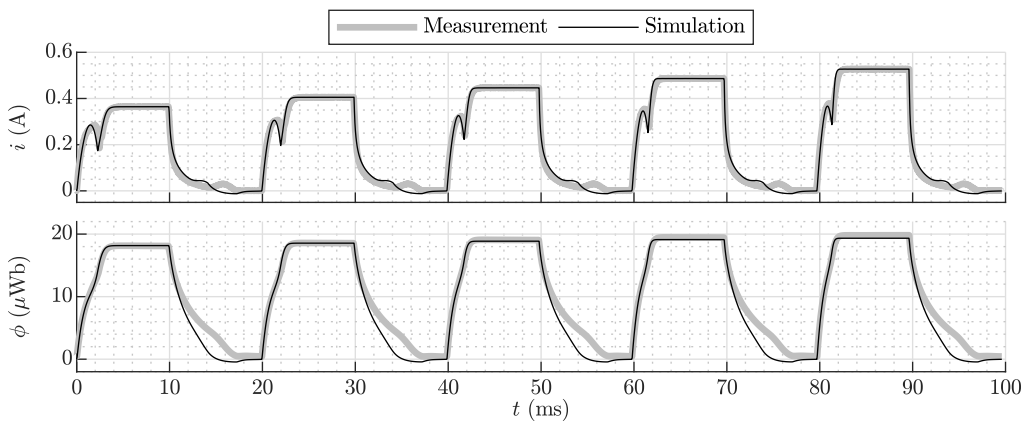


Figure 4.28: Validation of the dynamical model including saturation. Electric current (top) and magnetic flux (bottom).

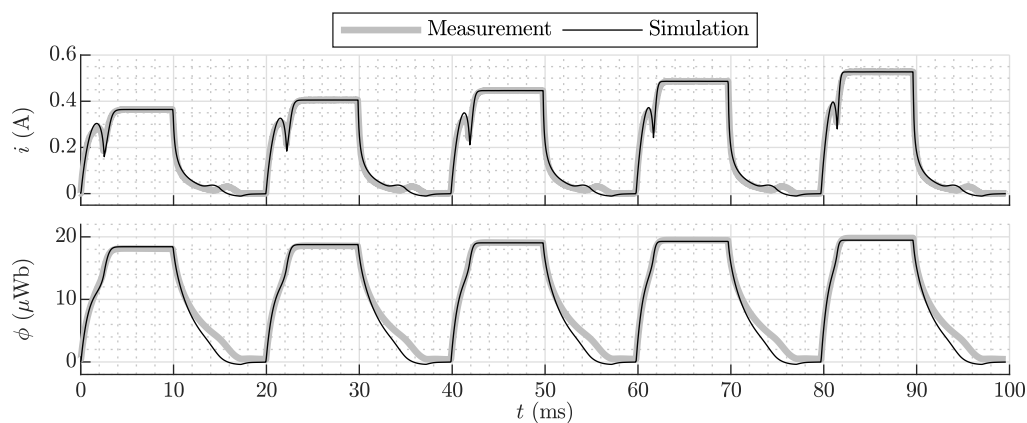


Figure 4.29: Validation of the S+F dynamical model. Electric current (top) and magnetic flux (bottom).

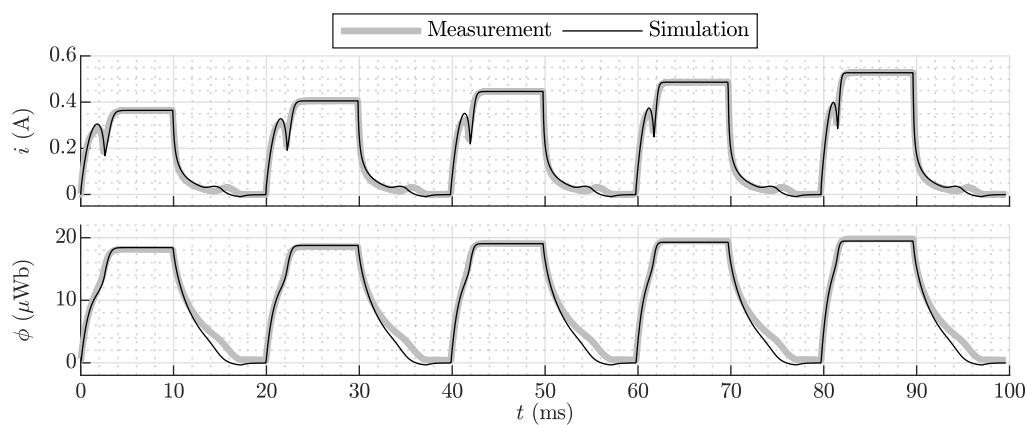


Figure 4.30: Validation of the S+F+EC dynamical model. Electric current (top) and magnetic flux (bottom).

Table 4.4: Root-mean-square errors (RMSE) and mean absolute errors (MAE) obtained with the five dynamical models presented in the chapter.

Model	RMSE(i) (mA)	MAE(i) (mA)	RMSE(ϕ) (μWb)	MAE(ϕ) (μWb)
B	68.83	45.34	8.298	5.794
S	17.82	11.91	1.504	1.011
S+F	14.30	9.655	1.097	0.7577
S+F+EC	14.26	9.167	0.9491	0.6771
S+H+F+EC	5.752	2.665	0.1700	0.1450

Chapter 5

Control

Once the modeling part has been presented, the second part of this thesis focuses on aspects related to control and estimation in reluctance actuators. In particular, the main goal is to investigate different approaches to achieve soft landing, i.e., trajectories that minimize impacts at the end of the motion. In this chapter, the basic properties of control theory are first analyzed using the differential equations derived in the first part of the thesis. Then, feedback linearization is proposed as a method to design trajectory tracking controllers for reluctance actuators. Finally, open-loop optimal control is proposed as an alternative to achieve soft landing when position measurements or estimations are not available.

5.1 Control systems properties

In this section, the basic properties of control systems theory—stability, controllability and observability—are investigated to determine whether or not it is possible to control the motion of reluctance actuators.

5.1.1 Stability

The existence, location and stability of equilibrium points in reluctance actuators are studied by applying the definitions and theorems of the books by Khalil [93] and Slotine and Li [154], as well as the article on hybrid dynamical systems by Goebel, Sanfelice and Teel [143].

Stability of continuous systems

Given the continuous nonlinear autonomous system

$$\dot{x} = f(x), \tag{5.1}$$

where x is the state, x_{eq} is said to be an equilibrium point of the system if

$$f(x_{\text{eq}}) = 0. \tag{5.2}$$

An equilibrium point x_{eq} of (5.1) is said to be:

- Stable if, for each $\varepsilon > 0$, there exists $\delta = \delta(\varepsilon) > 0$ such that

$$\|x(t=0) - x_{\text{eq}}\| < \delta \implies \|x(t) - x_{\text{eq}}\| < \varepsilon, \quad \forall t \geq 0$$

- Asymptotically stable if it is stable and δ can be chosen such that

$$\|x(t=0) - x_{\text{eq}}\| < \delta \implies \lim_{t \rightarrow \infty} x(t) = x_{\text{eq}}$$

- Unstable if it is not stable.

In other words, an equilibrium point is stable if all solutions of the system starting in a neighborhood of the equilibrium point stay close to that point. Furthermore, an equilibrium point is asymptotically stable if all solutions tend to that point as time goes to infinity.

The stability of the nonlinear system (5.1) can be analyzed via linearization. Given the Jacobian matrix of f , evaluated at the equilibrium point x_{eq} ,

$$J_f(x_{\text{eq}}) = \left. \frac{\partial f}{\partial x} \right|_{x=x_{\text{eq}}}$$

it can be stated that x_{eq} is:

- Asymptotically stable if the real part of all the eigenvalues of $J_f(x_{\text{eq}})$ is negative.
- Unstable if the real part of at least one of the eigenvalues of $J_f(x_{\text{eq}})$ is positive.

This theorem, which is known as Lyapunov's indirect method, is the simplest approach to analyze the stability of a given equilibrium point for a nonlinear system. However, no conclusions can be drawn from the method when the real part of all the eigenvalues of $J_f(x_{\text{eq}})$ is less than or equal to zero. In that case, stability must be analyzed by means of other methods [93, 154].

For systems that depend on an external input u ,

$$\dot{x} = f(x, u), \tag{5.3}$$

the instantaneous value of u determines the existence and location of equilibrium points. Given a constant value of the input, the system (5.3) can be cast in the form of (5.1) and, hence, the equilibrium points may be obtained and evaluated as previously explained. In that case, $x_{\text{eq}} = x_{\text{eq}}(u)$ is said to be an equilibrium point of (5.3) if

$$f(x_{\text{eq}}, u) = 0. \tag{5.4}$$

In order to analyze the existence and location of equilibrium points in reluctance actuators, the basic dynamical model is considered (see Subsection 3.2.1). The differential

equations of this third-order system are

$$\dot{z} = f_1(x) = v_z, \quad (5.5)$$

$$\dot{v}_z = f_2(x) = \frac{1}{m} \left(-\frac{1}{2} k_{\text{gap}} \phi^2 - k_s (z - z_s) - c v_z \right), \quad (5.6)$$

$$\dot{\phi} = f_3(x, u) = \frac{u}{N} - \frac{R}{N^2} \phi (\mathcal{R}_0 + k_{\text{gap}} z), \quad (5.7)$$

where $z \in [z_{\min}, z_{\max}]$ and $v_z \in \mathbb{R}$ are respectively the position and velocity of the armature, $\phi \in \mathbb{R}$ is the flux through the core, $x = [z \ v_z \ \phi]^\top$ is the state vector, the input $u \in \mathbb{R}$ is the voltage across the coil terminals, and $m, k_{\text{gap}}, k_s, z_s, c, N, R$ and \mathcal{R}_0 are positive parameters. Note that any equilibrium point of the system must satisfy $v_z = 0$, i.e., the armature velocity must be zero. Hence, in the following analysis only the z - and ϕ -coordinates of the equilibrium points are analyzed and discussed.

The equilibrium points of the system in the z - ϕ plane correspond to the points of intersection of the curves $f_2(x) = 0$ and $f_3(x, u) = 0$. Fig. 5.1 shows these curves for three different values of constant u ($u = 0, u = u_1 > 0$ and $u = u_2 > u_1$). It can be seen that, depending on the value of the input, one, two or three different equilibrium points may exist. In particular, there are three equilibrium points for $u = 0$ (squares in the figure), which correspond to the points of intersection of the parabola given by $f_2(x) = 0$ and the two straight lines, $\phi = 0$ and $z = -\mathcal{R}_0/k_{\text{gap}}$, that result from $f_3(x, 0) = 0$. As the absolute value of u increases, the hyperbola given by $f_3(x, u) = 0$ and the parabola still intersect at three points (circles in the figure). However, there are two values of the input, $u = u_a$ and $u = u_b$, for which the parabola and the hyperbola become tangent and, hence, two of the three points are coincident. These inputs and the corresponding points of tangency are given by

$$u_a = \frac{2R \sqrt{6k_s(\mathcal{R}_0 + k_{\text{gap}}z_s)^3}}{9Nk_{\text{gap}}} \quad u_b = -u_a, \quad (5.8)$$

$$z_a = \frac{2}{3}z_s - \frac{\mathcal{R}_0}{3k_{\text{gap}}} \quad z_b = z_a, \quad (5.9)$$

$$\phi_a = \frac{\sqrt{6k_s(\mathcal{R}_0 + k_{\text{gap}}z_s)}}{3k_{\text{gap}}} \quad \phi_b = -\phi_a. \quad (5.10)$$

For $|u| > u_a$ both curves intersect only at one point (triangle in the figure), so only one equilibrium point exists in the model.

The z - and ϕ -coordinates of the equilibrium points are represented in Fig. 5.2 as functions of the input. In this figure, stability is indicated by means of different types of line: Stable points are represented with a solid line, while unstable points are represented using dash-dot lines. It is shown that, among the three different equilibrium points that may exist in the system, two of them (blue and red lines) are unstable and symmetric to each other with respect to $(\phi, u) = (0, 0)$. While one of them (blue line) exists only for $u > u_b, z < z_b$ and $\phi < \phi_b$, the other (red line) exists only for $u < u_a, z < z_a$ and $\phi > \phi_a$. The third point (yellow line) is stable, but it only exists for a narrow range of positions ($z_a \leq z \leq z_s$). Note that, for zero input, this point corresponds exactly to the position at which the spring has its natural length ($z = z_s$).

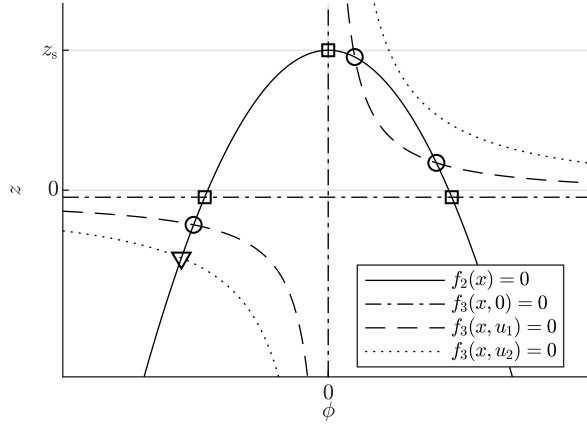


Figure 5.1: Existence and location of equilibrium points in the z - ϕ plane. The points of intersection of the curves $f_2(x) = 0$ and $f_3(x, u) = 0$ vary with u ($0 < u_1 < u_2$). The equilibrium points when $u = 0$, $u = u_1$ and $u = u_2$ are respectively marked with squares (three points), circles (three points) and a triangle (one point).

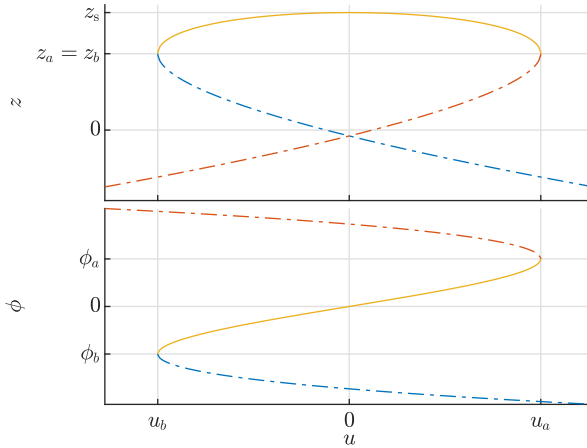


Figure 5.2: Existence, location and stability of equilibrium points as a function of the input. Position (top) and magnetic flux (bottom). Stable/unstable points are represented with solid/dash-dot lines.

The previous results show that open-loop stabilization in reluctance actuators is only possible for positions at which the spring is close to its equilibrium length. Hence, the utility of the stable equilibrium point found in the analysis is very limited in practice, at least in switch-type devices like relays and valves. In addition, considering that this thesis focuses on actuators whose position is bounded between $z_{\min} = 0$ and $z_{\max} < z_s$ (see Section 3.1), it is evident that some of the positions that result from solving $f(x, u) = 0$ may not even exist in reality. The hybrid dynamics of the system—described by the hybrid automata of Section 3.2—is considered hereafter in the analysis in order to determine the effects of these position boundaries.

Stability of hybrid systems

Hybrid dynamical systems are systems that exhibit both continuous and discrete dynamics. In particular, hybrid automata are a class of hybrid systems whose dynamics can be described, using a finite set $Q \subset \mathbb{N}$ of dynamic modes, by

$$\dot{x} = f_{\text{Mode } q}(x), \quad q \in Q, \quad x \in C_q, \quad (5.11)$$

$$(x^+, q^+) = g_{\text{Mode } q}(x), \quad q \in Q, \quad x \in D_q, \quad (5.12)$$

where x is the continuous state, q denotes the dynamic mode, and $f_{\text{Mode } q}$, $g_{\text{Mode } q}$, C_q and D_q are respectively the flow map, the reset map, the domain and the guard set of mode q . Hybrid automata operate as follows. When x belongs to the domain C_q , it evolves continuously as described by $f_{\text{Mode } q}$. Then, if it reaches the guard set D_q , both x and the dynamic mode q jump instantaneously according to $g_{\text{Mode } q}$. For more insight into hybrid automata and hybrid systems, including the existence and uniqueness of solutions, the reader is referred to [143].

Equilibrium points in hybrid systems are those locations at which the state does not flow nor jump. Hence, a point $(x_{\text{eq}}, q_{\text{eq}})$ is said to be an equilibrium point of the hybrid automaton (5.11)–(5.12) if

$$f_{\text{Mode } q_{\text{eq}}}(x_{\text{eq}}) = 0, \quad q_{\text{eq}} \in Q, \quad x_{\text{eq}} \in C_{q_{\text{eq}}} \cap \overline{D_{q_{\text{eq}}}}. \quad (5.13)$$

Like continuous systems, hybrid systems may also depend on an external input u . These systems can be generally described by

$$\dot{x} = f_{\text{Mode } q}(x, u), \quad q \in Q, \quad x \in C_q(u), \quad (5.14)$$

$$(x^+, q^+) = g_{\text{Mode } q}(x, u), \quad q \in Q, \quad x \in D_q(u), \quad (5.15)$$

where the flow map, the reset map, the domain and the guard set of all the dynamic modes might be functions of u . In this case, the existence and location of equilibrium points depends on the instantaneous value of u . A point $(x_{\text{eq}}, q_{\text{eq}}) = (x_{\text{eq}}(u), q_{\text{eq}}(u))$ is said to be an equilibrium point of the hybrid automaton (5.14)–(5.15) if

$$f_{\text{Mode } q_{\text{eq}}}(x_{\text{eq}}, u) = 0, \quad q_{\text{eq}} \in Q, \quad x_{\text{eq}} \in C_{q_{\text{eq}}}(u) \cap \overline{D_{q_{\text{eq}}}(u)}. \quad (5.16)$$

Stability in hybrid systems can be also evaluated by means of Lyapunov's indirect method, simply by considering that the Jacobian matrix is in this case dependent on both x_{eq} and q_{eq} .

$$J_f(x_{\text{eq}}, q_{\text{eq}}) = \left. \frac{\partial f_{\text{Mode } q_{\text{eq}}}}{\partial x} \right|_{x=x_{\text{eq}}} \quad (5.17)$$

In this part of the section, the hybrid automaton of Fig. 3.6 is used to analyze the existence and location of equilibrium points in reluctance actuators with a limited range of motion. All the maps and sets required to describe the hybrid behavior of the basic dynamical model can be found in Subsection 3.2.1. Since this automaton has three dynamic modes, the equilibrium points are the solutions of (5.16) for $q \in \{1, 2, 3\}$. Then, considering that z_{min} is equal to zero, three different cases arise depending on the value of z_{max} . The results are presented in Fig. 5.3 and discussed in the following paragraphs.

Although not very common in practice, the first case (Fig. 5.3a) corresponds to a maximum position greater than the equilibrium position of the spring, i.e., $z_{\max} > z_s$. In this case, it can be seen that there is only one equilibrium point for $u = 0$, which corresponds to the spring equilibrium position. As u increases, this stable point approaches $(z, \phi) = (z_a, \phi_a)$ and, for $u > u_a$, it vanishes. Equivalent results exist for $u < 0$ using u_b , z_b and ϕ_b . More interesting is the behavior of the other two points. It is shown that there exists a stable point at the minimum position ($z = z_{\min}$) for voltages $u \in (-\infty, u_d] \cup [u_c, +\infty)$, where u_c and u_d are obtained from the points of intersection of $f_2(x) = 0$ and $f_3(x, u) = 0$ when $z = z_{\min} = 0$.

$$u_c = \frac{R \mathcal{R}_0}{N} \sqrt{\frac{2 k_s z_s}{k_{\text{gap}}}} \quad u_d = -u_c \quad (5.18)$$

This stable point explains why the mover and the stator of a reluctance actuator stay together at $z = z_{\min}$ when the input is high enough (in absolute value). In this connection, (5.18) determines the voltages at which the mover takes off from the minimum position and, consequently, this expression may be of great use in the design of new actuators. The magnetic fluxes corresponding to these two points, ϕ_c and ϕ_d , are given by

$$\phi_c = \sqrt{\frac{2 k_s z_s}{k_{\text{gap}}}} \quad \phi_d = -\phi_c. \quad (5.19)$$

The third point, which is unstable, varies its position between $z = z_{\min}$ and $z = z_a = z_b$.

The second case (Fig. 5.3b) arises when the maximum position of the mover is less than the spring equilibrium position and, at the same time, greater than z_a , i.e., $z_a < z_{\max} < z_s$. As shown in the figure, this case is completely equivalent to the first one except for the first equilibrium point, which stays at $z = z_{\max}$ for voltages $u_f < u < u_e$, where u_f and u_e are obtained from the intersections of $f_2(x) = 0$ and $f_3(x, u) = 0$ when $z = z_{\max}$.

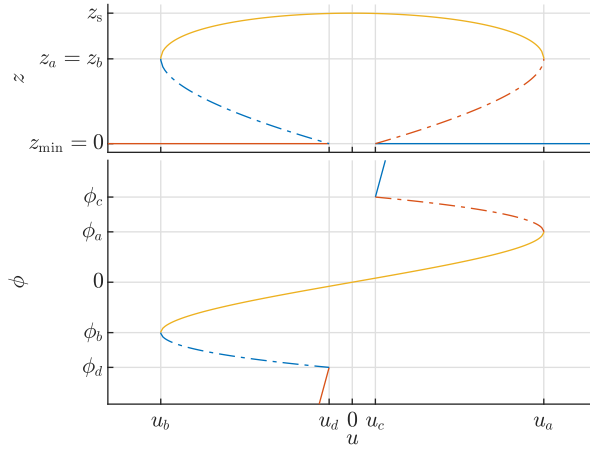
$$u_e = \frac{R(\mathcal{R}_0 + k_{\text{gap}} z_{\max})}{N} \sqrt{\frac{2 k_s (z_s - z_{\max})}{k_{\text{gap}}}} \quad u_f = -u_e \quad (5.20)$$

The magnetic fluxes at these two points, ϕ_e and ϕ_f , are equal to

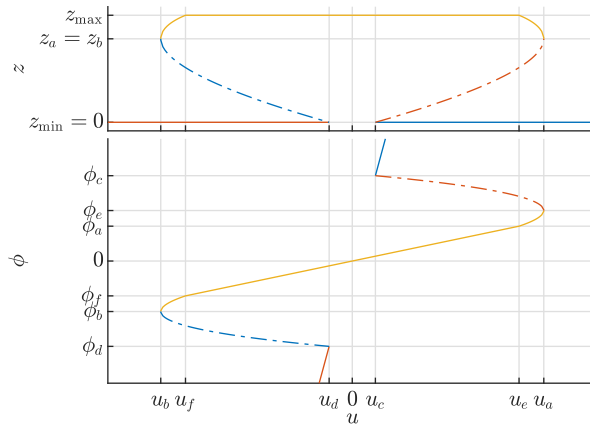
$$\phi_e = \sqrt{\frac{2 k_s (z_s - z_{\max})}{k_{\text{gap}}}} \quad \phi_f = -\phi_e. \quad (5.21)$$

Similarly to u_c and u_d , these voltages determine the conditions at which the actuator takes off from its maximum position, so (5.20) could also be useful for design purposes.

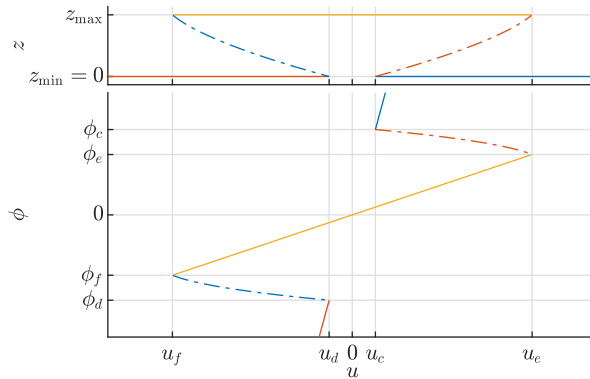
The third and last case (Fig. 5.3c), which is the most common in switch-type devices, corresponds to a maximum position $z_{\max} < z_a$. Although similar to the previous cases, the key aspect of this situation is that stable equilibrium points only exist at $z = z_{\min}$ and $z = z_{\max}$. Hence, if the input is steadily increased, the armature will move from z_{\max} to z_{\min} when the voltage reaches $u = u_e$. Then, when the voltage is reduced down to u_c , the mover will take off from z_{\min} and move back to z_{\max} . This hysteretic behavior, which is probably the most distinctive feature of switch-type devices, is related to most of the problems that are intrinsic to this class of electromechanical systems (see Section 1.1). The third equilibrium point, which is unstable but varies between $z = z_{\min}$ and $z = z_{\max}$, can be exploited for control purposes as it will be shown in the next section.



(a) Case 1: $z_{\min} = 0$ and $z_{\max} > z_s$.



(b) Case 2: $z_{\min} = 0$ and $z_a < z_{\max} < z_s$.



(c) Case 3: $z_{\min} = 0$ and $z_{\max} < z_a$.

Figure 5.3: Existence, location and stability of equilibrium points when the motion is restricted. Stable/unstable points are represented with solid/dash-dot lines.

5.1.2 Controllability

Controllability is a fundamental property of control systems. A system $\dot{x} = f(x, u)$ is said to be controllable at $x(t_0) = x_0$ if, for any final state x_f , it is possible to find an external input $u = u(t)$, $t \geq t_0$ that moves the state from x_0 to x_f in finite time. A system is said to be completely controllable, or simply controllable, if it is controllable for any initial state.

Controllability of linear time-invariant (LTI) systems was investigated by Kalman in the early 1960s [155]. Given the LTI system

$$\dot{x} = Ax + Bu, \quad (5.22)$$

where $x \in \mathbb{R}^n$ is the state, $u \in \mathbb{R}^m$ is the external input, $A \in \mathbb{R}^{n \times n}$ is the (constant) state transition matrix and $B \in \mathbb{R}^{n \times m}$ is the (constant) input matrix, Kalman showed that the system is controllable if and only if the controllability matrix, given by

$$C = [B \quad AB \quad A^2B \quad \dots \quad A^{n-1}B], \quad (5.23)$$

is full rank, i.e., $\text{rank}(C) = n$. The rank condition provides a simple method to evaluate the controllability of LTI systems, but it cannot be directly applied to nonlinear systems.

The generalization of linear controllability to nonlinear systems was developed using Lie theory [156] by Haynes and Hermes [157], Lobry [158], Sussman and Jurdjevic [159] and Hermann and Krener [160], among others, during the 1970s. Based on these works, Hunt [161] derived sufficient controllability conditions for the affine nonlinear system

$$\dot{x} = f(x) + \sum_{i=1}^m g_i(x) u_i, \quad (5.24)$$

where $x \in M \subset \mathbb{R}^n$, $f : M \rightarrow \mathbb{R}^n$, $u_i \in \mathbb{R} \forall i$ and $g_i : M \rightarrow \mathbb{R}^n \forall i$. In particular, if g_1, \dots, g_m are linearly independent and involutive on M , the system is controllable at x if there exists an integer k such that the controllability matrix

$$C_k(x) = \left[g_1(x), \dots, g_m(x), \text{ad}_f g_1(x), \dots, \text{ad}_f g_m(x), \dots, \text{ad}_f^{k-1} g_1(x), \dots, \text{ad}_f^{k-1} g_m(x) \right] \quad (5.25)$$

has full rank, i.e., $\text{rank}(C_k(x)) = n$. In this matrix, $\text{ad}_f g_i$ is the Lie bracket of f and g_i , given by

$$\text{ad}_f g_i(x) = [f(x), g_i(x)] = J_{g_i} f(x) - J_f g_i(x) = \frac{\partial g_i}{\partial x} f(x) - \frac{\partial f}{\partial x} g_i(x),$$

and recursive Lie brackets are formed as

$$\text{ad}_f^i g_i(x) = \left[f(x), \text{ad}_f^{i-1} g_i(x) \right].$$

For single input systems, (5.24) transforms into

$$\dot{x} = f(x) + g(x)u, \quad (5.26)$$

where $u \in \mathbb{R}$ and $g : M \rightarrow \mathbb{R}^n$. Thus, controllability reduces to the full rank condition of the matrix

$$\mathcal{C}_k(x) = \left[g(x), \text{ad}_f g(x), \dots, \text{ad}_f^{k-1} g(x) \right]. \quad (5.27)$$

The dynamical system (5.5)–(5.7) is in the form of (5.26), with f and g given by

$$f(x) = \begin{bmatrix} v_z \\ \frac{1}{m} \left(-\frac{1}{2} k_{\text{gap}} \phi^2 - k_s (z - z_s) - c v_z \right) \\ -\frac{R}{N^2} \phi (\mathcal{R}_0 + k_{\text{gap}} z) \end{bmatrix}, \quad g(x) = \begin{bmatrix} 0 \\ 0 \\ \frac{1}{N} \end{bmatrix}. \quad (5.28)$$

The controllability matrix for this model structure and $k = 3$ is

$$\mathcal{C}_3(x) = \begin{bmatrix} 0 & 0 & -\frac{k_{\text{gap}} \phi}{Nm} \\ 0 & \frac{k_{\text{gap}} \phi}{Nm} & \frac{c k_{\text{gap}} \phi}{Nm^2} \\ \frac{1}{N} & \frac{R(\mathcal{R}_0 + k_{\text{gap}} z)}{N^3} & \frac{R^2(\mathcal{R}_0 + k_{\text{gap}} z)^2}{N^5} + \frac{R k_{\text{gap}} v_z}{N^3} \end{bmatrix}, \quad (5.29)$$

and it has full rank provided that ϕ is different from zero. Thus, Hunt's sufficient condition guarantees that the system is controllable except for the undefined case $\phi = 0$. Nevertheless, it is straightforward from (5.7) that any input $u \neq 0$ will move ϕ away from zero, so it can be concluded that the system is completely controllable.

5.1.3 Observability

Observability is another central property of control systems. A dynamical system of the form $\dot{x} = f(x, u)$ with output $y = h(x)$ is said to be observable at $x(t_0) = x_0$ if, for any possible sequence of states $x(t)$ and inputs $u(t)$, the state x_0 can be determined from measurements of the output signal $y(t)$, $t > t_0$ in finite time. A system is said to be completely observable, or simply observable, if it is observable for any given state.

Like controllability, observability of LTI systems was formulated and investigated by Kalman in the 1960s [155]. For the LTI system (5.22), with output $y \in \mathbb{R}^p$ given by

$$y = Cx, \quad (5.30)$$

where $C \in \mathbb{R}^{p \times n}$ is the (constant) output matrix, Kalman stated that a necessary and sufficient condition for the system to be observable is that the observability matrix

$$\mathcal{O} = \begin{bmatrix} C \\ CA \\ CA^2 \\ \vdots \\ CA^{n-1} \end{bmatrix} \quad (5.31)$$

has full rank, i.e., $\text{rank}(\mathcal{O}) = n$.

Observability of nonlinear systems was investigated in the late 1960s and early 1970s by Kostyukovskii [162], Kou, Elliott and Tarn [163] and Hermann and Krener [160], among others. These latter authors showed that, for the nonlinear system

$$\begin{cases} \dot{x} = f(x, u) \\ y = h(x) \end{cases} \quad (5.32)$$

where $x \in M \subset \mathbb{R}^n$, $u \in \mathbb{R}^m$, $f : M \times \mathbb{R}^m \rightarrow \mathbb{R}^n$, $y \in \mathbb{R}^p$ and $h : M \rightarrow \mathbb{R}^p$, a sufficient condition for the system to be observable at x is that there exists an integer k such that the observability matrix

$$\mathcal{O}_k(x) = \begin{bmatrix} \frac{\partial h}{\partial x} \\ \frac{\partial (\mathcal{L}_f h)}{\partial x} \\ \vdots \\ \frac{\partial (\mathcal{L}_f^{k-1} h)}{\partial x} \end{bmatrix} \quad (5.33)$$

has full rank, i.e., $\text{rank}(\mathcal{O}_k(x)) = n$. In this matrix, $\mathcal{L}_f h$ is the Lie derivative of the function h with respect to the vector field f , given by

$$\mathcal{L}_f h(x) = J_h f(x) = \frac{\partial h}{\partial x} f(x),$$

and higher order Lie derivatives are calculated as

$$\mathcal{L}_f^i h(x) = \mathcal{L}_f \mathcal{L}_f^{i-1} h(x) = \frac{\partial (\mathcal{L}_f^{i-1} h)}{\partial x} f(x).$$

Observability of reluctance actuators is critical in order to design feedback controllers of the position. As stated in Subsection 4.1.2, real-time measurements of the position are generally not available in practical situations. Hence, the position and velocity of the mover need to be estimated if a feedback controller is to be implemented. In order to analyze the observability of the system, it is assumed that only the current through the coil is measured. In this regard, note that the basic dynamical model is in the form of (5.32), with f given by (5.5)–(5.7) and output (see Subsection 3.2.1) equal to

$$y = i = h(x) = \frac{\phi(\mathcal{R}_0 + k_{\text{gap}} z)}{N}. \quad (5.34)$$

The observability matrix for this model structure and $k = 3$ is

$$\mathcal{O}_3(x) = \begin{bmatrix} \frac{k_{\text{gap}} \phi}{N} & 0 & \frac{\mathcal{R}_0 + k_{\text{gap}} z}{N} \\ \frac{2 R k_{\text{gap}} \phi (\mathcal{R}_0 + k_{\text{gap}} z)}{N^3} & \frac{k_{\text{gap}} \phi}{N} & \frac{R (\mathcal{R}_0 + k_{\text{gap}} z)^2}{N^3} + \frac{k_{\text{gap}} v_z}{N} \\ o_{3,1}(x) & o_{3,2}(x) & o_{3,3}(x) \end{bmatrix}, \quad (5.35)$$

where

$$\begin{aligned} o_{3,1}(x) &= -\frac{k_{\text{gap}} k_s \phi}{Nm} + \frac{3 R k_{\text{gap}}^2 v_z \phi}{N^3} - \frac{3 R^2 k_{\text{gap}} \phi (\mathcal{R}_0 + k_{\text{gap}} z)^2}{N^5}, \\ o_{3,2}(x) &= -\frac{c k_{\text{gap}} \phi}{Nm} - \frac{3 R k_{\text{gap}} \phi (\mathcal{R}_0 + k_{\text{gap}} z)}{N^3}, \\ o_{3,3}(x) &= -\frac{k_{\text{gap}} (3 k_{\text{gap}} \phi^2 + 2 c v_z + 2 k_s (z - z_s))}{2 Nm} - \frac{3 R k_{\text{gap}} v_z (\mathcal{R}_0 + k_{\text{gap}} z)}{N^3} \\ &\quad + \frac{R^2 (\mathcal{R}_0 + k_{\text{gap}} z)^3}{N^5}. \end{aligned}$$

Since the reluctance of the magnetic circuit is strictly positive, i.e., $(\mathcal{R}_0 + k_{\text{gap}} z) > 0$ for all $z \in [z_{\min}, z_{\max}]$, it can be seen that $\mathcal{O}_3(x)$ has full rank provided that ϕ is different from zero¹. Hence, the sufficient condition of Hermann and Krener guarantees that the system is observable except for the undefined case $\phi = 0$. However, it is straightforward from (5.34) that, given that the reluctance is always positive, the current i is equal to zero if and only if $\phi = 0$ independently of the values of z and v_z . Thus, these two latter variables cannot be observed from i when there is no flux. Since mass-spring-damper systems are intrinsically stable, the conclusion is that the system is observable when $\phi \neq 0$ and detectable—all unobservable modes are stable [164]—when $\phi = 0$.

5.2 Feedback control

The analysis presented in the previous section has shown that reluctance actuators are controllable systems and, in addition, that they have an equilibrium point that could be used for control purposes. In this section, feedback linearization is proposed as a method to design trajectory tracking controllers for the position assuming that the state of the system is accessible either by measurements or by estimation techniques. The theoretical fundamentals of feedback linearization are presented and then applied to the design of a nonlinear position controller for reluctance actuators. The controller is evaluated by simulation using a soft-landing trajectory that prevents from impacts at the end of the motion. For more insight into the theoretical aspects of feedback linearization, the reader is referred to the book by Khalil [93].

5.2.1 Feedback linearization

Given the single-input single-output affine dynamical system

$$\begin{cases} \dot{x} = f(x) + g(x) u \\ y = h(x) \end{cases} \quad (5.36)$$

where $x \in M \subset \mathbb{R}^n$, $f : M \rightarrow \mathbb{R}^n$, $g : M \rightarrow \mathbb{R}^n$, $u \in \mathbb{R}$, $y \in \mathbb{R}$ and $h : M \rightarrow \mathbb{R}$, feedback linearization deals with the question of whether it is possible to find a control law

$$u = \alpha(x) + \beta(x) v, \quad (5.37)$$

¹In order for \mathcal{O}_3 to be full rank, the state variables must satisfy some additional conditions apart from $\phi \neq 0$. However, higher order observability matrices ($\mathcal{O}_k(x)$, $k > 3$) show that the rank condition only fails for $\phi = 0$.

where $\alpha : M \rightarrow \mathbb{R}$, $\beta : M \rightarrow \mathbb{R}$ and $v \in \mathbb{R}$, and a change of variables

$$\xi = T(x), \quad (5.38)$$

where $\xi \in \mathbb{R}^n$ and $T : M \rightarrow \mathbb{R}^n$, that transform the nonlinear system into an equivalent LTI system on ξ ,

$$\dot{\xi} = A\xi + Bv, \quad (5.39)$$

where $A \in \mathbb{R}^{n \times n}$ and $B \in \mathbb{R}^n$ are constant.

The nonlinear system (5.36) is said to have relative degree ρ , $1 \leq \rho \leq n$, in a region $M_0 \subset M$ if the ρ -th time derivative of the output,

$$\frac{d^\rho y}{dt^\rho} = \frac{d^\rho(h(x))}{dt^\rho} \quad (5.40)$$

is the first time derivative that depends on u for all $x \in M_0$. As shown in [93], the system has relative degree ρ in M_0 if it satisfies

$$\mathcal{L}_g \mathcal{L}_f^i h(x) = 0, \quad i = 0, 1, \dots, \rho - 2 \quad \mathcal{L}_g \mathcal{L}_f^{\rho-1} h(x) \neq 0, \quad (5.41)$$

for all $x \in M_0$, where \mathcal{L} denotes the Lie derivative as defined in the previous section.

A single-input affine dynamical system

$$\dot{x} = f(x) + g(x)u, \quad (5.42)$$

where $x \in M \subset \mathbb{R}^n$, $f : M \rightarrow \mathbb{R}^n$, $g : M \rightarrow \mathbb{R}^n$ and $u \in \mathbb{R}$, is feedback linearizable in a region $M_0 \subset M$ if there exists a function $h : M \rightarrow \mathbb{R}$ such that the system

$$\begin{cases} \dot{x} = f(x) + g(x)u \\ y = h(x) \end{cases} \quad (5.43)$$

has relative degree n for all $x \in M_0$. In that case, the n -th derivative of y is given by

$$\frac{d^n y}{dt^n} = \mathcal{L}_f^n h(x) + \mathcal{L}_g \mathcal{L}_f^{n-1} h(x) u. \quad (5.44)$$

Hence, by using the state feedback law (5.37), with α and β equal to

$$\alpha(x) = -\frac{\mathcal{L}_f^n h(x)}{\mathcal{L}_g \mathcal{L}_f^{n-1} h(x)}, \quad \beta(x) = \frac{1}{\mathcal{L}_g \mathcal{L}_f^{n-1} h(x)}, \quad (5.45)$$

the previous differential equation simplifies into

$$\frac{d^n y}{dt^n} = v. \quad (5.46)$$

Then, using the change of variables

$$T(x) = \begin{bmatrix} h(x) \\ \mathcal{L}_f h(x) \\ \vdots \\ \mathcal{L}_f^{n-1} h(x) \end{bmatrix}, \quad (5.47)$$

the state vector ξ is formed by y and its first $n - 1$ time derivatives,

$$\xi = \begin{bmatrix} y \\ \frac{dy}{dt} \\ \vdots \\ \frac{d^{n-1}y}{dt^{n-1}} \end{bmatrix}, \quad (5.48)$$

so the equivalent system (5.39) becomes a chain of n integrators, i.e., A and B are

$$A = \begin{bmatrix} 0_{(n-1) \times 1} & I_{n-1} \\ 0 & 0_{1 \times (n-1)} \end{bmatrix}, \quad B = \begin{bmatrix} 0_{(n-1) \times 1} \\ 1 \end{bmatrix}, \quad (5.49)$$

where I_{n-1} is the identity matrix of size $n - 1$ and $0_{p \times q}$ denotes a null matrix of p rows and q columns.

With regard to reluctance actuators, feedback linearization is investigated for a third-order dynamical system of the form

$$\dot{z} = v_z, \quad (5.50)$$

$$\dot{v}_z = \frac{1}{m} \left(-\frac{1}{2} \phi^2 \frac{\partial \mathcal{R}_{\text{gap}}(z)}{\partial z} - k_s (z - z_s) - c v_z \right), \quad (5.51)$$

$$\dot{\phi} = \left(\frac{u}{N} - \frac{R \phi \mathcal{R}(z, \phi)}{N^2} \right) \left(1 + \frac{R k_{\text{ec}}}{N^2} \right)^{-1}, \quad (5.52)$$

where the state variables $z \in [z_{\min}, z_{\max}]$ and $v_z \in \mathbb{R}$ are respectively the position and velocity of the armature, $\phi \in (-\phi_{\text{sat}}, +\phi_{\text{sat}})$ is the flux through the core, and the input $u \in \mathbb{R}$ is the voltage across the coil terminals. In these equations, m , k_s , z_s , c , N , R , k_{ec} and ϕ_{sat} are positive model parameters and the reluctance \mathcal{R} is considered as a function of the position and the magnetic flux, $\mathcal{R} = \mathcal{R}(z, \phi) = \mathcal{R}_{\text{gap}}(z) + \mathcal{R}_{\text{core}}(\phi)$. Note that this description is valid for all the dynamical models of Chapter 3, with the only exception of the model that includes magnetic hysteresis.

The system (5.50)–(5.52) is in the form of (5.42), with $x = [z \ v_z \ \phi]^T$, domain

$$M = \{ [z \ v_z \ \phi]^T \mid z \in [z_{\min}, z_{\max}], \ v_z \in \mathbb{R}, \ \phi \in (-\phi_{\text{sat}}, +\phi_{\text{sat}}) \}, \quad (5.53)$$

and f and g equal to

$$f(x) = \begin{bmatrix} v_z \\ \frac{1}{m} \left(-\frac{1}{2} \phi^2 \frac{\partial \mathcal{R}_{\text{gap}}(z)}{\partial z} - k_s (z - z_s) - c v_z \right) \\ -\frac{R \phi \mathcal{R}(z, \phi)}{N^2} \left(1 + \frac{R k_{\text{ec}}}{N^2} \right)^{-1} \end{bmatrix}, \quad (5.54)$$

$$g(x) = \begin{bmatrix} 0 \\ 0 \\ \frac{1}{N} \left(1 + \frac{R k_{\text{ec}}}{N^2} \right)^{-1} \end{bmatrix}. \quad (5.55)$$

Since the variable to be controlled is the position of the mover, z , let the function h be selected as

$$y = h(x) = z. \quad (5.56)$$

In this case, it is obtained that

$$\mathcal{L}_g h(x) = 0, \quad (5.57)$$

$$\mathcal{L}_g \mathcal{L}_f h(x) = 0, \quad (5.58)$$

$$\mathcal{L}_g \mathcal{L}_f^2 h(x) = -\frac{N\phi}{m(N^2 + Rk_{ec})} \frac{\partial \mathcal{R}_{\text{gap}}(z)}{\partial z}. \quad (5.59)$$

Thus, considering that $\partial \mathcal{R}_{\text{gap}}/\partial z > 0$ for all $z \in [z_{\min}, z_{\max}]$ (see Section 2.4), the system satisfies the conditions in (5.41) with $\rho = n = 3$ in the convex regions

$$M_0^- = \{x = [z \ v_z \ \phi]^\top \mid z \in [z_{\min}, z_{\max}], \ v_z \in \mathbb{R}, \ \phi \in (-\phi_{\text{sat}}, 0)\}, \quad (5.60)$$

$$M_0^+ = \{x = [z \ v_z \ \phi]^\top \mid z \in [z_{\min}, z_{\max}], \ v_z \in \mathbb{R}, \ \phi \in (0, +\phi_{\text{sat}})\}, \quad (5.61)$$

i.e., for all $x \in M$ such that $\phi \neq 0$. Thus, it is feedback linearizable in either M_0^+ or M_0^- . In this thesis we arbitrarily choose to work in the domain M_0^+ .

With h as defined in (5.56), the functions α and β of the control law (5.37) are

$$\begin{aligned} \alpha(x) = -\frac{\mathcal{L}_f^3 h(x)}{\mathcal{L}_g \mathcal{L}_f^2 h(x)} &= \frac{k_{\text{aux}} c \phi}{2m} + \frac{R\phi \mathcal{R}(z, \phi)}{N} + \frac{k_{\text{aux}} c (k_s (z - z_s) + c v_z)}{m\phi \mathcal{R}'_{\text{gap}}(z)} \\ &\quad - \frac{k_{\text{aux}} k_s v_z}{\phi \mathcal{R}'_{\text{gap}}(z)} - \frac{k_{\text{aux}} v_z \phi \mathcal{R}''_{\text{gap}}(z)}{2 \mathcal{R}'_{\text{gap}}(z)}, \end{aligned} \quad (5.62)$$

$$\beta(x) = \frac{1}{\mathcal{L}_g \mathcal{L}_f^2 h(x)} = -\frac{m k_{\text{aux}}}{\phi \mathcal{R}'_{\text{gap}}(z)}, \quad (5.63)$$

where

$$\mathcal{R}'_{\text{gap}}(z) = \frac{\partial \mathcal{R}_{\text{gap}}(z)}{\partial z}, \quad \mathcal{R}''_{\text{gap}}(z) = \frac{\partial^2 \mathcal{R}_{\text{gap}}(z)}{\partial z^2}, \quad k_{\text{aux}} = N + \frac{Rk_{ec}}{N}.$$

The change of variables (5.47) results in the linearizing state

$$\xi = \begin{bmatrix} \xi_1 \\ \xi_2 \\ \xi_3 \end{bmatrix} = T(x) = \begin{bmatrix} z \\ v_z \\ \frac{1}{m} \left(-\frac{1}{2} \phi^2 \mathcal{R}'_{\text{gap}}(z) - k_s (z - z_s) - c v_z \right) \end{bmatrix}, \quad (5.64)$$

and the equivalent LTI system obtained as a result of feedback linearization is a chain of three integrators,

$$\begin{bmatrix} \dot{\xi}_1 \\ \dot{\xi}_2 \\ \dot{\xi}_3 \end{bmatrix} = \begin{bmatrix} 0 & 1 & 0 \\ 0 & 0 & 1 \\ 0 & 0 & 0 \end{bmatrix} \begin{bmatrix} \xi_1 \\ \xi_2 \\ \xi_3 \end{bmatrix} + \begin{bmatrix} 0 \\ 0 \\ 1 \end{bmatrix} v, \quad (5.65)$$

where ξ_1 , ξ_2 and ξ_3 are respectively the position, velocity and acceleration of the armature.

5.2.2 Trajectory tracking controller design

Once the system (5.50)–(5.52) has been linearized and transformed into the equivalent LTI system (5.65), position controllers can be designed using classical linear techniques. In particular, the main goal in switching reluctance actuators is to design a controller such that the position follows a predefined soft-landing trajectory $r = r(t)$. Since the linearizing state ξ is composed of the position, the velocity and the acceleration of the armature, the position reference can actually be used to define a reference trajectory for the entire state vector. This reference signal, $\xi_r = \xi_r(t)$, is formed by $r(t)$ and its first two time derivatives.

$$\xi_r(t) = \begin{bmatrix} r(t) \\ \dot{r}(t) \\ \ddot{r}(t) \end{bmatrix} \quad (5.66)$$

Let the trajectory error be defined as $\tilde{\xi} = \xi_r - \xi$. Considering (5.39), the dynamics of $\tilde{\xi}$ is given by

$$\dot{\tilde{\xi}} = \dot{\xi}_r - \dot{\xi} = \dot{\xi}_r + A\tilde{\xi} - A\xi_r - Bv. \quad (5.67)$$

Since the equivalent LTI system is a chain of integrators, with A and B in the form of (5.49), it can be shown that

$$\dot{\xi}_r - A\xi_r = B \frac{d^3 r}{dt^3} = B \ddot{r}. \quad (5.68)$$

Consequently, the error dynamics can be reformulated as

$$\dot{\tilde{\xi}} = A\tilde{\xi} - B(v - \ddot{r}). \quad (5.69)$$

Then, selecting v as

$$v = w + \ddot{r}, \quad (5.70)$$

it is finally obtained that

$$\dot{\tilde{\xi}} = A\tilde{\xi} - Bw, \quad (5.71)$$

which is an LTI system on $\tilde{\xi}$ and, hence, can be controlled using any of the well known linear techniques [165]. In particular, using the proportional control law

$$w = K\tilde{\xi}, \quad (5.72)$$

the system transforms into

$$\dot{\tilde{\xi}} = (A - BK)\tilde{\xi}. \quad (5.73)$$

Then, if K is designed such that the matrix $A - BK$ is Hurwitz, the previous system is asymptotically stable at the origin and, consequently, the actuator will track the predefined trajectory.

This final step completes the design of the nonlinear controller for the actuator via feedback linearization. The complete control law to track the reference $r(t)$ can be obtained by combining all the previous expressions as

$$u = u(x, t) = \alpha(x) + \beta(x) \left(K \left(\xi_r(t) - T(x) \right) + \ddot{r}(t) \right). \quad (5.74)$$

5.2.3 Simulation results

In this part of the section, the nonlinear controller designed in previous pages is validated by simulation. The dynamics of the model during the movement stage is described by (5.50)–(5.52), and the reluctance has the form

$$\mathcal{R}(z, \phi) = k_{\text{gap}} z + \frac{\mathcal{R}_{\text{core0}}}{1 - |\phi|/\phi_{\text{sat}}}, \quad (5.75)$$

where k_{gap} , $\mathcal{R}_{\text{core0}}$ and ϕ_{sat} are positive parameters. This reluctance results from the sum of an air component that is proportional to the gap length and an iron component that includes magnetic saturation by means of the Fröhlich-Kennelly model. In order to analyze the effects of the position boundaries, the controller is evaluated using the hybrid automaton presented in Fig. 3.6. The nominal values of the parameters are presented in Table 5.1. The voltage is bounded between -50 V and $+50$ V.

The soft-landing trajectory designed for the actuator is

$$r(t) = \begin{cases} z_0 & \text{if } 0 \leq t < t_0, \\ s(t) & \text{if } t_0 \leq t \leq t_f, \\ z_f & \text{if } t > t_f, \end{cases} \quad (5.76)$$

where z_0 is the initial position, z_f is the final position and $s(t)$ is a fifth degree polynomial that satisfies

$$s(t_0) = z_0, \quad s(t_f) = z_f, \quad \dot{s}(t_0) = \dot{s}(t_f) = \ddot{s}(t_0) = \ddot{s}(t_f) = 0. \quad (5.77)$$

The reference trajectory starts from z_0 at $t = t_0$ with zero velocity and zero acceleration, and it reaches z_f at $t = t_f$ also with null velocity and acceleration. Two different cases are considered: the closing operation, where $z_0 = z_{\text{max}}$ and $z_f = z_{\text{min}}$, and the opening, where $z_0 = z_{\text{min}}$ and $z_f = z_{\text{max}}$. Considering that the system is open-loop stable at both $z = z_{\text{min}}$ and $z = z_{\text{max}}$ (see Section 5.1), it is assumed that $z(0) = \xi_1(0) = z_0$ and $v_z(0) = \xi_2(0) = 0$. That is, the initial position and velocity tracking errors are equal to zero. The purpose of the interval $0 \leq t < t_0$ is that, regardless of the initial magnetic flux, the system reaches a stationary state at some $t < t_0$ such that the magnetic force and the spring force at the initial position are in balance. Note that, since $v_z(t) = 0$, $\forall t < t_0$, ξ_3 in this interval is equal to the sum of those two forces [see (5.64)]. Thus, since ξ_3 will converge towards the reference $\ddot{r} = 0$, the system will be pushed towards force equilibrium. By a proper selection of t_0 , this interval prepares the actuator for the take-off and allows the motion to start immediately at $t = t_0$. Besides, considering that $\xi(t_0) = \tilde{\xi}(t_0) = [0 \ 0 \ 0]^T$, and that $(A - BK)$ is Hurwitz, the tracking error will be equal to zero during the entire trajectory, i.e., the controller will achieve perfect tracking.

Two different cases have been simulated, which correspond to the two possible operations of the actuator. In both cases, the proportional gain K of the controller has been designed to achieve a response time of 0.25 ms, and the parameters of the reference trajectory have been set by simulation to $t_0 = 0.5$ ms and $t_f = 4$ ms. The results, which are presented in Fig. 5.4, are in accordance with the theoretical analysis. As shown, the controller achieves perfect tracking of the proposed trajectory and, thus, soft-landing is accomplished. In this regard, note that the position and velocity errors are identically

zero during the entire simulation. An initial error has been considered in ξ_3 to analyze the performance of the controller in the interval $[0, t_0)$. As expected, although the position error is zero for all $t < t_0$, the controller still forces the flux to reach a value for which the forces are in equilibrium ($\xi_3 = 0$). Since t_0 is large enough, the tracking error at $t = t_0$ is zero and thus the motion starts immediately. As a final remark, note that the state stays inside the linearizable region M_0^+ [see (5.60)] during the entire trajectory.

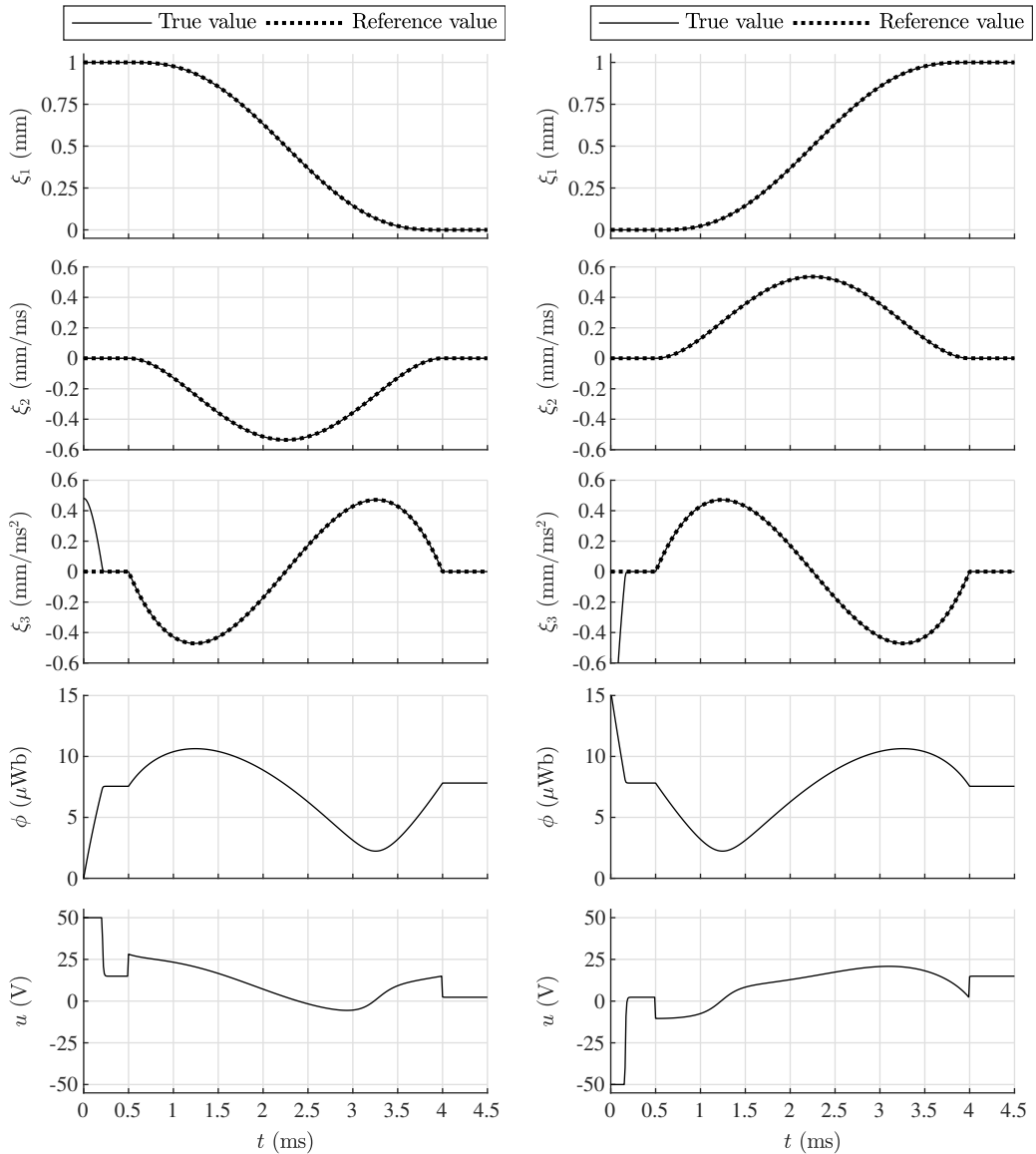


Figure 5.4: Soft-landing feedback control for the closing (left) and opening (right) operations. From top to bottom: position ($\xi_1 = z$), velocity ($\xi_2 = v_z$), linearizing state 3 (ξ_3) magnetic flux (ϕ) and voltage (u).

Table 5.1: Model parameters.

Parameter	Value	Parameter	Value	Parameter	Value
R	75 Ω	ϕ_{sat}	25 μWb	z_{s}	15 mm
N	1200	k_{ec}	0 A/V	c	0 Ns/m
k_{gap}	$2.7 \cdot 10^{10}$ H^{-1}/m	m	1.6 g	z_{min}	0 mm
$\mathcal{R}_{\text{core0}}$	$3.25 \cdot 10^6$ H^{-1}	k_{s}	55 N/m	z_{max}	1 mm

5.3 Open-loop control

In the previous section, it has been shown that feedback control could achieve great performance in controlling the trajectory of reluctance actuators. Nevertheless, the proposed strategies require the use of additional sensors (see Subsection 4.1.2) or the design of estimation algorithms in order to close the control loop when applied to a real actuator. In addition, several technical and cost-related challenges may raise in real-time implementations, particularly with respect to the presence of measurement noise or the computational requirements of the algorithms.

As an alternative, this section focuses on the design and analysis of open-loop soft-landing control policies for this class of actuators. Despite the lack of robustness of open-loop control, it has the great advantage that it can be easily implemented in practice without need of additional sensors or estimation algorithms. Besides, since open-loop policies can be stored in memory, the computational requirements of this approach are also very low. In the following pages, different time-optimal and energy-optimal trajectories are designed for a nominal actuator by means of the Pontryagin principle [166, 167]. Then, the robustness of the obtained policies on perturbed systems is evaluated via Monte Carlo simulations.

5.3.1 Optimal trajectory design

Model dynamics

As in the previous section, the problem is theoretically formulated for a third-order dynamical system of the form

$$\dot{z} = f_1(x) = v_z, \quad (5.78)$$

$$\dot{v}_z = f_2(x) = \frac{1}{m} \left(-\frac{1}{2} \phi^2 \frac{\partial \mathcal{R}(z, \phi)}{\partial z} - k_{\text{s}}(z - z_{\text{s}}) - c v_z \right), \quad (5.79)$$

$$\dot{\phi} = f_3(x, u) = \left(\frac{u}{N} - \frac{R \phi \mathcal{R}(z, \phi)}{N^2} \right) \left(1 + \frac{R k_{\text{ec}}}{N^2} \right)^{-1}, \quad (5.80)$$

where $z \in [z_{\text{min}}, z_{\text{max}}]$ and $v_z \in \mathbb{R}$ are respectively the position and velocity of the mover, $\phi \in [-\phi_{\text{sat}}, \phi_{\text{sat}}]$ is the magnetic flux, $x = [z \ v_z \ \phi]^T$ is the state vector and the input $u \in \mathbb{R}$ is the voltage across the coil terminals. Recall that m , k_{s} , z_{s} , c , N , R and k_{ec} are positive model parameters. The reluctance \mathcal{R} is considered as a function of the position and the

magnetic flux, i.e., $\mathcal{R} = \mathcal{R}(z, \phi)$. Besides, according to the equations of Section 2.5,

$$\mathcal{R}(z, \phi) = \mathcal{R}(z, -\phi) > 0, \quad (5.81)$$

i.e., the reluctance is positive and symmetric about zero flux. This implies that the magnetic force, which is given by

$$F_m = -\frac{1}{2} \phi^2 \frac{\partial \mathcal{R}(z, \phi)}{\partial z}, \quad (5.82)$$

does not depend on the sign of the flux. Since this force is the input of the mechanical subsystem (see Section 3.1), this feature clearly limits the control possibilities for the actuator.

Furthermore, let $x^a = [z^a \ v_z^a \ \phi^a]^\top$ be the solution to (5.78)–(5.80) obtained for input $u(t) = f_u(t)$ and initial state $x(t_0) = [z_0 \ v_{z0} \ \phi_0]^\top$, and let $x^b = [z^b \ v_z^b \ \phi^b]^\top$ be the solution for input $u(t) = -f_u(t)$ and $x(t_0) = [z_0 \ v_{z0} \ -\phi_0]^\top$. Then, (5.81) implies also that

$$z^a(t) = z^b(t), \quad (5.83)$$

$$v_z^a(t) = v_z^b(t), \quad (5.84)$$

$$\phi^a(t) = -\phi^b(t), \quad (5.85)$$

for all $t \geq t_0$. In other words, identical position and velocity trajectories are obtained if both the flux and the voltage invert their signs. Thus, in order to discard redundant solutions with regard to the motion, only the trajectories with $\phi(t) \geq 0$ are considered valid in this section.

Problem formulation and solution method

The problem of finding a bounded time-dependent input $u = u(t)$ which achieves a soft-landing trajectory for the actuator is formulated as follows:

$$\underset{u(t)}{\text{minimize}} \quad J = \int_{t_0}^{t_f} V(x, u) dt, \quad (5.86)$$

$$\text{subject to} \quad \dot{x} = f(x, u), \quad (5.87)$$

$$v \leq u \leq \omega, \quad (5.88)$$

$$\phi \geq 0 \quad (5.89)$$

$$x(t_0) = [z_0 \ 0 \ \phi_0]^\top, \quad (5.90)$$

$$x(t_f) = [z_f \ 0 \ \phi_f]^\top, \quad (5.91)$$

where J is the performance index, t_0 and t_f are the initial and final times, V is a scalar function, v and ω are constant values that define the lower and upper bounds of u , z_0 and z_f are the initial and final positions, and ϕ_0 and ϕ_f are the initial and final values of the magnetic flux. It is assumed that $v < 0 < \omega$.

The trajectory must start at the initial position, $z(t_0) = z_0$, at rest, $v_z(t_0) = 0$. Considering the system under study, z_0 corresponds to either z_{\min} (opening operation) or z_{\max} (closing operation). The takeoff occurs when the net force is equal to zero,

$$f_2 \left(\begin{bmatrix} z_0 & 0 & \phi_0 \end{bmatrix}^\top \right) = 0, \quad (5.92)$$

which results in a condition for the initial flux ϕ_0 . At the end of the motion, the actuator must reach the final position, $z(t_f) = z_f$, which is either z_{\max} (opening operation) or z_{\min} (closing operation), with zero velocity, $v_z(t_f) = 0$. Additionally, in order to maintain that position, the final acceleration must also be set equal to zero,

$$f_2 \left(\begin{bmatrix} z_f & 0 & \phi_f \end{bmatrix}^\top \right) = 0, \quad (5.93)$$

which provides the condition for the final flux ϕ_f .

A solution of the problem (5.86)–(5.91) can be found by following the Pontryagin method. In this regard, it should be noted that (5.89) is not explicitly handled in the procedure; it is simply used to rule out redundant solutions with identical mechanical trajectories. The optimal input is obtained by building the Hamiltonian

$$\mathcal{H}(x, p, u) = V(x, u) + p^\top f(x, u), \quad (5.94)$$

where $p = [p_1 \ p_2 \ p_3]^\top$ is the costate, and then applying the Pontryagin principle,

$$\mathcal{H}(x^*, p^*, u^*) \leq \mathcal{H}(x^*, p^*, u) \quad \forall u \in [v, \omega], \quad (5.95)$$

where $x^* = [z^* \ v_z^* \ \phi^*]^\top$, $p^* = [p_1^* \ p_2^* \ p_3^*]^\top$ and u^* are the optimal state, costate and input, respectively. This step results in the input expressed as a function of the state and the costate.

$$u^* = u^*(x^*, p^*) \quad (5.96)$$

The dynamics of the Hamiltonian system are subsequently obtained as

$$\dot{x}^*(t) = + \frac{\partial \mathcal{H}^*}{\partial p^*}, \quad \dot{p}^*(t) = - \frac{\partial \mathcal{H}^*}{\partial x^*}, \quad (5.97)$$

where $\mathcal{H}^* = \mathcal{H}(x^*, p^*, u^*(x^*, p^*))$, and the trajectory is numerically computed using (5.90) and (5.91) as boundary conditions. Finally, the optimal open-loop policy is obtained by replacing x^* and p^* in (5.96) by their numerical values.

Time-optimal policy

The time-optimal control policy is the one that minimizes the time taken by the actuator to go from z_0 to z_f . In order to find such solution, the function V is selected as

$$V(x, u) = 1, \quad (5.98)$$

which results in $J = t_f - t_0$ and in the Hamiltonian

$$\mathcal{H}(x, p, u) = 1 + p_1 f_1(x) + p_2 f_2(x) + p_3 f_3(x, u). \quad (5.99)$$

Using (5.78)–(5.80) to apply the Pontryagin principle leads to

$$p_3^* u^* \leq p_3^* u \quad \forall u \in [v, \omega], \quad (5.100)$$

which allows for obtaining u^* as a piecewise function of p_3^* .

$$u^*(x^*, p^*) = \arg \min_{u \in [v, \omega]} (p_3^* u) = \begin{cases} \omega & \text{if } p_3^* < 0 \\ v & \text{if } p_3^* > 0 \end{cases} \quad (5.101)$$

Note however that u^* is not defined for $p_3^* = 0$, which suggests that the time-optimal control problem is singular. This can be easily avoided by redefining V as

$$V(x, u) = 1 + \epsilon u^2, \quad (5.102)$$

where $\epsilon > 0$ is an infinitely small number. Then, applying the Pontryagin principle with the regularized version of V leads to

$$u^*(x^*, p^*) = \lim_{\epsilon \rightarrow 0} \left(\arg \min_{u \in [v, \omega]} \left(\epsilon u^2 + \frac{p_3^* u}{N + \frac{R k_{ec}}{N}} \right) \right) = \begin{cases} \omega & \text{if } p_3^* < 0, \\ 0 & \text{if } p_3^* = 0, \\ v & \text{if } p_3^* > 0, \end{cases} \quad (5.103)$$

which is defined for all values of p_3^* and, consequently, will not lead to singularity intervals.

Since t_f is free—it is the variable to minimize—an additional boundary condition is needed to solve the problem. The necessary conditions for optimality obtained from the classical theory of the calculus of variations [166, p. 65] [167, p. 188] provide such extra condition as

$$\mathcal{H}(x^*(t_f), p^*(t_f), u^*(x^*(t_f), p^*(t_f))) = 0. \quad (5.104)$$

Energy-optimal policy

The time-optimal solution determines the minimum amount of time required by the system to follow a soft-landing trajectory. Trajectories lasting longer than that limit can be obtained, e.g., by solving an energy-optimal problem. For that, the function V is selected as

$$V(x, u) = u^2, \quad (5.105)$$

which results in the Hamiltonian

$$\mathcal{H}(x, p, u) = u^2 + p_1 f_1(x) + p_2 f_2(x) + p_3 f_3(x, u). \quad (5.106)$$

In this case, the Pontryagin principle states that

$$u^{*2} + \frac{p_3^* u^*}{k_{\text{aux}}} \leq u^2 + \frac{p_3^* u}{k_{\text{aux}}} \quad \forall u \in [v, \omega] \quad (5.107)$$

where

$$k_{\text{aux}} = N + \frac{R k_{ec}}{N}. \quad (5.108)$$

Consequently, the energy-optimal policy is given by

$$u^*(x^*, p^*) = \arg \min_{u \in [v, \omega]} \left(u^2 + \frac{p_3^* u}{k_{\text{aux}}} \right) = \begin{cases} \omega & \text{if } p_3^* < -2 k_{\text{aux}} \omega, \\ -\frac{p_3^*}{2 k_{\text{aux}}} & \text{if } -2 k_{\text{aux}} \omega \leq p_3^* \leq -2 k_{\text{aux}} v, \\ v & \text{if } p_3^* > -2 k_{\text{aux}} v, \end{cases} \quad (5.109)$$

which is defined for all values of p_3^* .

5.3.2 Simulation results

In this part of the section, different soft-landing optimal solutions for the closing and opening operations of a particular reluctance actuator model are presented and compared. The dynamical model used in the simulations is the same than in Subsection 5.2.3. In this regard, recall that the collisions modeled by the hybrid automaton of Fig. 3.6 are perfectly inelastic, i.e., all the kinetic energy is dissipated at impacts. However, bounces will still exist when the velocity and the sum of the magnetic and spring forces at an impact have opposite signs. The voltage is bounded between $v = -50$ V and $\omega = 50$ V.

Nominal system

For each of the two operations, five different soft-landing policies have been obtained using the nominal model. These correspond to the time-optimal (TO) solution and four energy-optimal (EO) strategies. The TO policy has been firstly computed to determine the minimum time required by the system to achieve a soft-landing motion. Then, EO solutions have been found for final times equal to 102% (EO₁), 105% (EO₂), 110% (EO₃) and 120% (EO₄) of the TO final time. The results of the simulations are presented in Fig. 5.5. For the sake of clarity, the figure only includes the TO, EO₂ and EO₄ solutions; the other two are intermediate trajectories. The contact instant using each policy is marked with a dot. The electric current, which is given by

$$i = \frac{\phi \mathcal{R}(z, \phi)}{N} \left(1 + \frac{R k_{\text{ec}}}{N^2} \right)^{-1} + \frac{u}{R} \left(1 + \frac{N^2}{R k_{\text{ec}}} \right)^{-1}, \quad (5.110)$$

is also represented in the figure.

As shown in the graphs, the TO policy is of Bang-off-Bang type, i.e., the input switches between v , 0 and ω . During the closing operation, this strategy increases rapidly the flux to generate a strong force towards zero gap. Then, the magnetic force is decreased to zero until nearly the end of the motion, when it is again increased so that the mover arrives with zero acceleration. On the other hand, the motion during the opening operation is primarily governed by the elastic force. The initial flux is rapidly decreased to zero so that no magnetic force opposes the motion. Then, at the end of the trajectory, the flux is increased to generate a force that slows down the plunger and makes it reach the final position with zero velocity. The trajectory of the electric current is qualitatively similar to the trajectory of the flux and consists in a succession of periods of maximum increase, maximum decrease and zero current. As expected, the EO policies are smoother and

cause the input to vary continuously on the interval $[v, \omega]$, but this is evidently achieved at the expense of having larger final times. Although there is not a great difference, the asymmetry in the forces causes the two operations to have different optimal-time durations (2.511 ms for closing and 2.401 ms for opening).

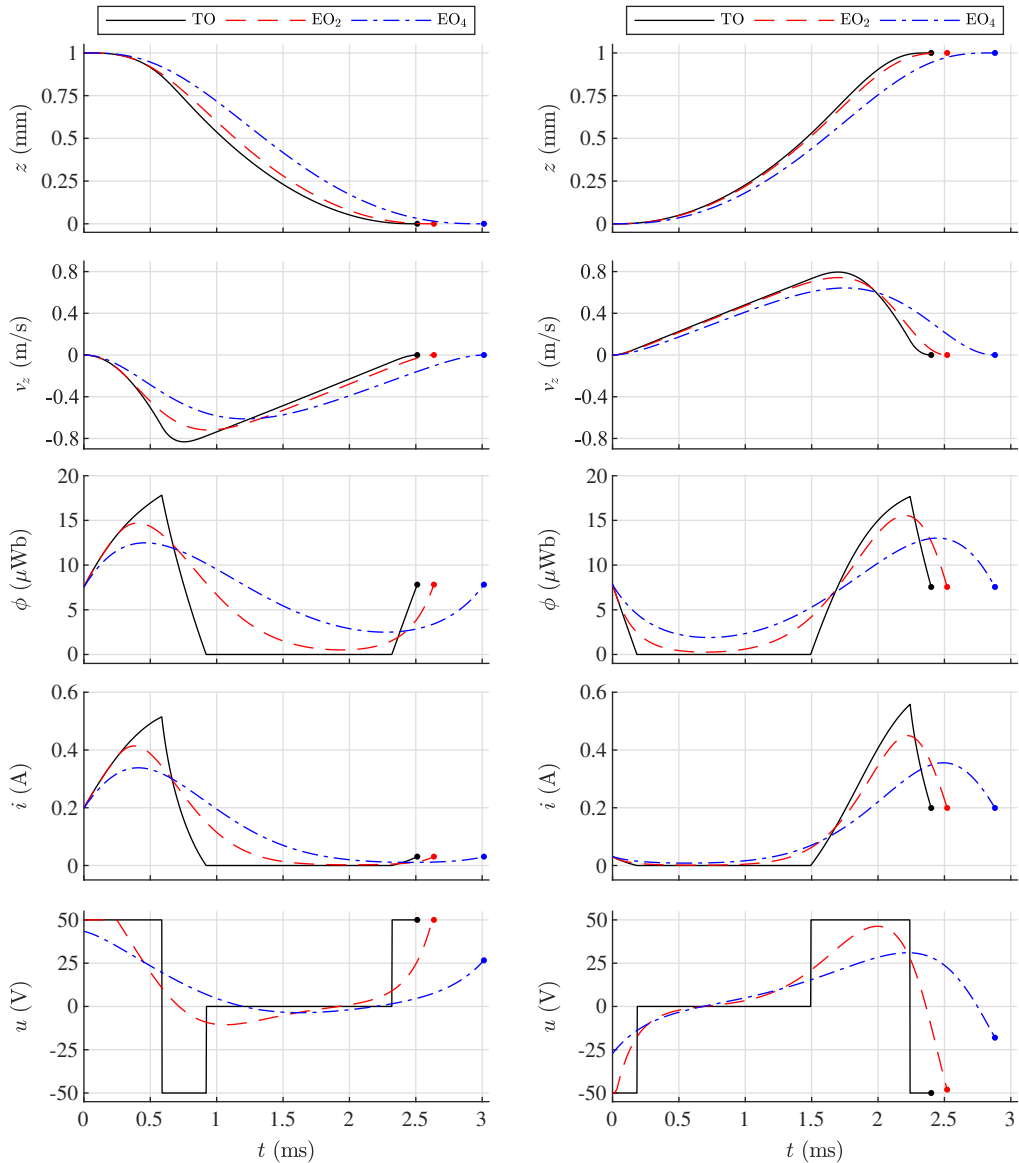


Figure 5.5: Optimal soft-landing trajectories for the closing (left) and opening (right) operations. From top to bottom: position, velocity, magnetic flux, electric current and voltage (input).

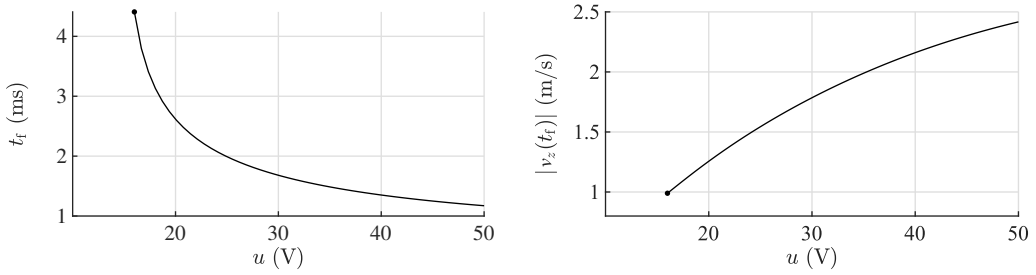


Figure 5.6: Final time (left) and absolute value of the impact velocity (right) in non-controlled constant-voltage closing operations. The case of minimum impact velocity is marked with a dot. Lower voltages do not produce motion.

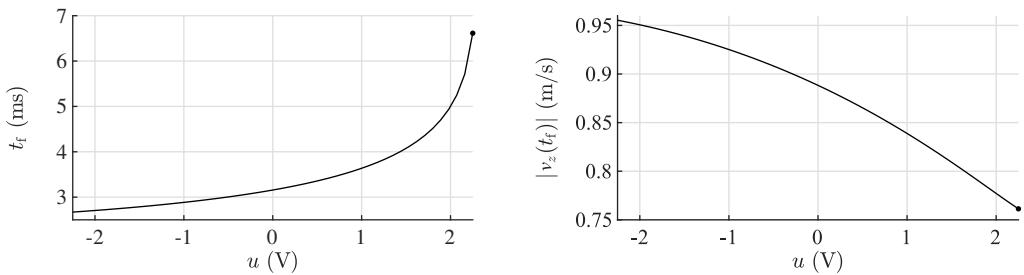


Figure 5.7: Final time (left) and absolute value of the impact velocity (right) in non-controlled constant-voltage opening operations. The case of minimum impact velocity is marked with a dot. Higher voltages do not produce motion.

The nominal model has been also used for an additional analysis. In this regard, note that the usual non-controlled activation policy for switch-type devices consists in applying a constant positive voltage in the closing operation and another voltage—zero or very close to zero—in the opening. Hence, the effect of these voltages on the final time and the impact velocity has been analyzed. The results are presented in Figs. 5.6 and 5.7. As shown, the minimum achievable impact velocity at the end of the closing operation is about 0.99 m/s, which corresponds to a voltage of about 16 V and a final time of 4.5 ms. On the other hand, the impact velocity on the opening operation could be reduced down to 0.76 m/s when using a 2.25 V dc voltage. Lower voltages for the closing or higher for the opening do not produce motion. These values are used as a benchmark to analyze the performance of the designed optimal control policies on perturbed systems.

Perturbed system

As stated, the difficulty in measuring or estimating variables and the very high speed of switch-type reluctance actuators motivate the search of open-loop soft-landing control policies that can be easily implemented and applied in practice. Considering that the main problem of open-loop control is the lack of robustness against disturbances, the result of applying the already presented input profiles on perturbed systems is analyzed

in this part of the section.

For that, 25,000 Monte Carlo simulations have been performed for each operation and control policy using the hybrid model in Fig. 3.6. The nominal parameter vector

$$\theta = [R \quad N \quad k_{\text{gap}} \quad \mathcal{R}_{\text{core0}} \quad \phi_{\text{sat}} \quad m \quad k_s \quad z_s]^T \quad (5.111)$$

is replaced in the simulations by θ_{pert} , which is randomly generated from a normal distribution, $\theta_{\text{pert}} \sim N(\theta, \Sigma^2)$, where $\Sigma = \text{diag}(0.01 \theta)$. The value of Σ has been set accordingly to the usual variability of the parameters in commercial actuators. The rest of the parameters remain unchanged. Considering that the mover may bounce at the end of the motion, two different variables are extracted from each simulation. First, the final time, t_{end} , which is not the time of the first impact but the time at which the motion ends, i.e., the impact time of the last bounce. Secondly, an equivalent impact velocity, v_{eq} , calculated as

$$v_{\text{eq}} = + \sqrt{\frac{m_{\text{pert}}}{m} \sum_i (v_z(t_i))^2}, \quad (5.112)$$

where m_{pert} is the perturbed mass and $\{t_i\}$ is the set of time instants at which an impact occurs. This variable represents the velocity that the nominal system should have in order to dissipate on one impact the same amount of kinetic energy than the perturbed system on all the bounces. Since the simulations can take longer than t_f , where t_f is the nominal final time, the input is extended in time using a constant voltage (50 V for closing and 0 V for opening).

The results for the closing and opening operations are respectively presented in Figs. 5.8 and 5.9. In both figures, it can be seen that the best values obtained in the simulations are close to those of the nominal case. However, almost all the simulations take longer times and have nonzero values of v_{eq} , which means that soft landing is not perfectly achieved. In any case, it must be noted that the equivalent impact velocities in the great majority of the simulations are smaller than the impact velocities of the non-controlled case (indicated by dash-dot lines in the graphs). In this regard, the mean values are between 45% and 70% smaller than if no control is applied. Therefore, it can be concluded that all the proposed policies are advantageous in the search of soft landing with respect to the standard activation.

Focusing on the closing operation (see Fig. 5.8), it can be seen that the best results are undoubtedly those corresponding to the TO policy. The median and mean values, as well as the interquartile range, are better in both the impact velocity and the final time. There is a worsening trend with t_f and, consequently, the worst results are those given by the EO₄ policy. Additionally, the histograms show that the simulations in which there are bounces are slightly worse in both variables, and the effect is similar for the five proposed policies. The bouncing phenomenon is however much more pronounced in the opening operation (see Fig. 5.9), which leads to very different results depending on whether there are bounces or not. In this regard, note that there is no best policy for this operation with respect to the impact velocity (see, e.g., that the TO policy has the best median value, but it has the worst third quartile). In any case, the minimum mean impact velocity corresponds to the EO₃ policy, whereas the minimum mean final time is obtained with the TO strategy.

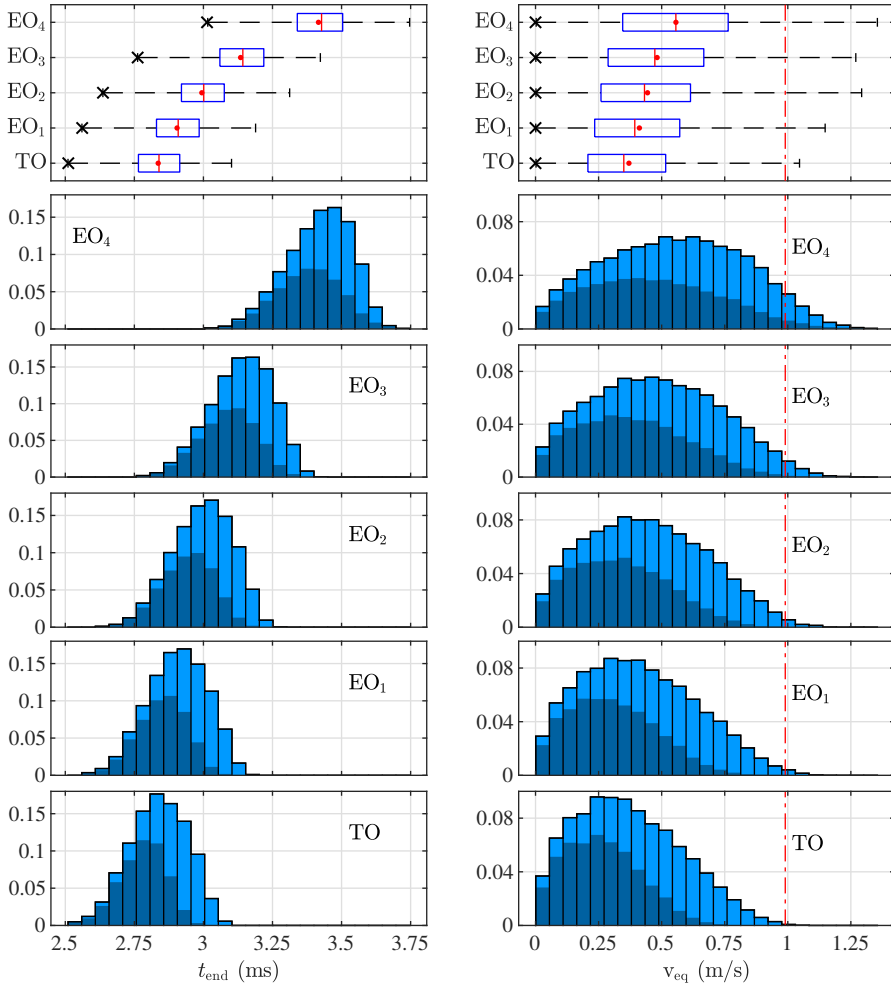


Figure 5.8: Box plot and relative frequency histograms of t_{end} (left) and v_{eq} (right) using the open-loop control policies proposed for the closing operation. In the box plot, the crosses indicate the values obtained in the nominal case and the dots are the mean values of the distributions. The whiskers extend to the most extreme data points. The dark fraction of the histogram represents the simulations with no bounces. The dash-dot line indicates the lowest possible impact velocity of the nominal non-controlled case.

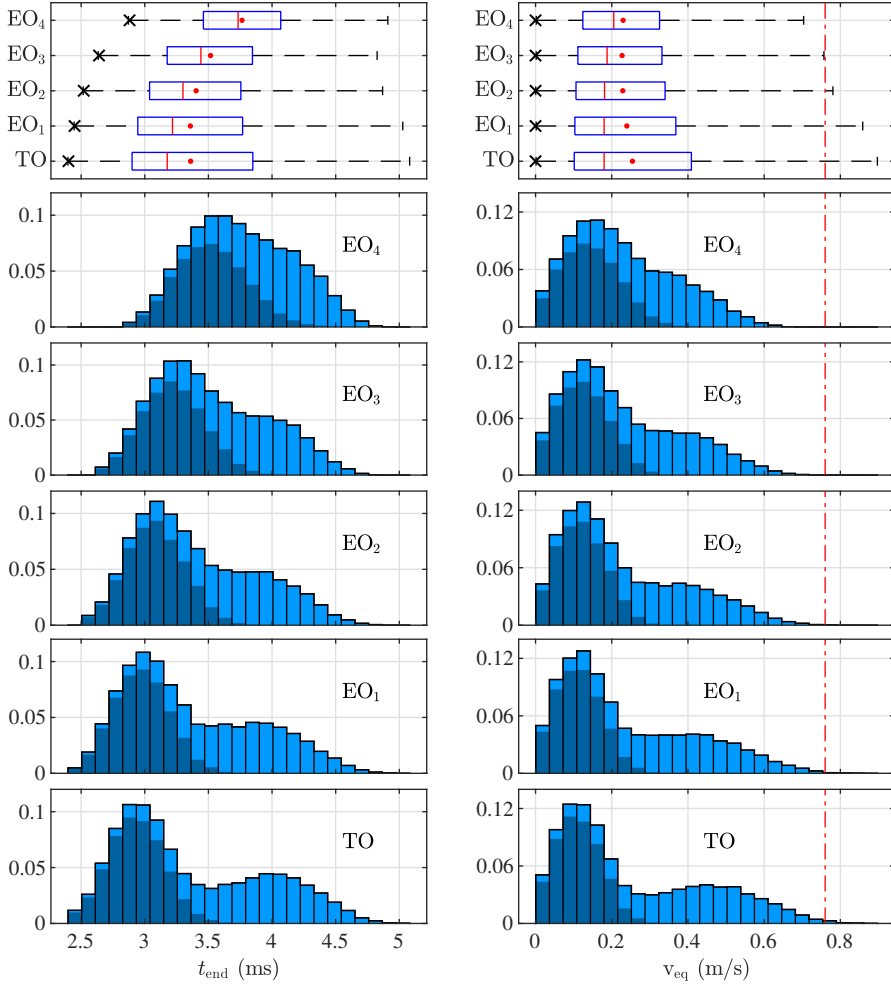


Figure 5.9: Box plot and relative frequency histograms of t_{end} (left) and v_{eq} (right) using the open-loop control policies proposed for the opening operation. In the box plot, the crosses indicate the values obtained in the nominal case and the dots are the mean values of the distributions. The whiskers extend to the most extreme data points. The dark fraction of the histogram represents the simulations with no bounces. The dash-dot line indicates the lowest possible impact velocity of the nominal non-controlled case.

Chapter 6

Estimation

This chapter deals with online state and parameter estimation in reluctance actuators. Similarly to the modeling chapters, the estimation problem is addressed in two parts that correspond to the electromagnetic and motion dynamics. In the first section, two different algorithms are presented to estimate online the resistance, the inductance and the flux of an actuator, only by using measurements of the coil voltage and current. Then, the second and final section addresses the problem of position estimation. Three different approaches are presented and then compared in terms of accuracy and robustness.

6.1 Resistance, inductance and flux estimation

The identification method presented in Chapter 4 to characterize the model dynamics assumes that flux measurements are available and that the true value of resistance is known. In this regard, flux estimates may be obtained, e.g., by integrating the induced voltage in secondary coils [23, 151] or by using a Hall sensor [20, 21]. Nevertheless, those methods require additional hardware, have significant drawbacks [24] and may not even be applicable to some actuators such as the studied solenoid valve where the core, the gap or the winding are not accessible. On the other hand, the coil resistance may be directly measured by means of several instruments, but resistance measuring techniques usually require the system to be in steady state and it is known in the literature [168] that this variable may change during the actuator operation due to temperature fluctuations.

This section presents the Stochastic ElectroMagnetic Estimation for Reluctance Actuators (SEMERA) algorithm, which is able to estimate online the resistance, the inductance and the flux linkage, as well as additional variables, only by using discrete-time measurements of the coil voltage and current. In addition to providing a solution for the aforementioned problems, the resistance estimation can be exploited, e.g., as a temperature sensor of the device, and the flux linkage may be used to estimate the magnetic force that drives the motion [107] or to detect magnetic hysteresis and saturation [59]. The observer is based on the celebrated Kalman filter theory [169] and, in contrast to some other approaches [24], relies only on a simple model of a variable inductor that is

not dependent on the position of the armature. Besides, it includes a confidence interval (CI) evaluation method that detects the instants of low signal-to-noise ratio (SNR) and an expert rule that assigns values to the estimated variables during these periods.

Additionally, an efficient integral estimator, whose reset condition is based on the cyclic operation of switches and valves, has been also developed primarily for comparative purposes. The algorithms have been validated by simulation and then applied to the two devices studied in this thesis by means of a microcontroller-based prototype. Both simulation and experimental results are presented and analyzed.

6.1.1 SEMERA algorithm

As already stated, the SEMERA algorithm is based on the Kalman filter theory. This part of the section presents the model used by the estimator and an analysis of the resulting equations in terms of observability. The notations $\hat{x}_{k/k-1}$ and $\hat{x}_{k/k}$ are used to denote, respectively, the *a priori* and *a posteriori* estimates of the state x at step k .

Observation model and process model

The observation model of the filter is based on the differential equation of an inductor with internal resistance,

$$v(t) = R(t) i(t) + \frac{d\lambda(t)}{dt}, \quad (6.1)$$

where $v(t)$ is the voltage across its terminals, $R(t)$ is the internal electrical resistance, $i(t)$ is the electric current and $\lambda(t)$ is the flux linkage. Note that the resistance is assumed time-dependent in order to account for temperature changes during the operation [168]. The continuous-time equation is discretized by backward differentiation,

$$v_k = R_k i_k + \frac{\lambda_k - \lambda_{k-1}}{\Delta}, \quad (6.2)$$

where Δ is the sampling period and the subscripts are used to indicate the time step. First-order forward and central difference formulas may be used as alternatives to discretize (6.1), but they result in a one-step delay in the estimation of R . On the other hand, higher order backward-differentiation expressions could also be utilized, but at the expense of increasing the order of the filter and the complexity of the model.

The flux linkage λ is usually expressed as the product of the apparent inductance L and the electric current, $\lambda = L i$. Hence, the previous equation can be transformed into

$$v_k = R_k i_k + \frac{L_k i_k - L_{k-1} i_{k-1}}{\Delta}, \quad (6.3)$$

where the inductance L is considered a time-dependent variable because, as seen in previous chapters, it changes with the position of the actuator. A different discrete version of (6.1) may be obtained if the derivative of λ is first expanded,

$$v(t) = R(t) i(t) + \frac{dL(t)}{dt} i(t) + L(t) \frac{di(t)}{dt}, \quad (6.4)$$

and then the derivatives of L and i are replaced by their backward discrete approximations. Although the equations of the filter are derived using (6.1), it can be shown that both approximations have discretization errors $\mathcal{O}(\Delta)$ and provide similar results.

Experimental measurements of voltage and current are required by the filter at each time step. Since measurement processes always add noise to the actual variables, let the voltage observation, \bar{v} , and the current observation, \bar{i} , be defined as

$$\bar{v}_k = v_k + \tilde{v}_k, \quad (6.5)$$

$$\bar{i}_k = i_k + \tilde{i}_k, \quad (6.6)$$

where \tilde{v} and \tilde{i} are additive noises that affect, respectively, the voltage measurement and the current measurement. Combining (6.3)–(6.6) and reorganizing terms,

$$\bar{v}_k = \bar{i}_k R_k + \frac{\bar{i}_k L_k - \bar{i}_{k-1} L_{k-1}}{\Delta} + \tilde{v}_k - \tilde{i}_k \left(R_k + \frac{L_k}{\Delta} \right) + \tilde{i}_{k-1} \frac{L_{k-1}}{\Delta}. \quad (6.7)$$

It is easy to see now that (6.7) can be used as the observation equation of a filter,

$$\bar{y}_k = H_k x_k + v_k, \quad (6.8)$$

where \bar{y}_k is the observed output, H_k is the observation matrix, x_k is the filter state vector, and v_k is the observation noise at time step k , simply by selecting these variables as

$$\bar{y}_k = \bar{v}_k, \quad (6.9)$$

$$H_k = \begin{bmatrix} \bar{i}_k & \bar{i}_k/\Delta & -\bar{i}_{k-1}/\Delta \end{bmatrix}, \quad (6.10)$$

$$x_k = \begin{bmatrix} R_k & L_k & L_{k-1} \end{bmatrix}^\top, \quad (6.11)$$

$$v_k = \tilde{v}_k - \tilde{i}_k (R_k + L_k/\Delta) + \tilde{i}_{k-1} L_{k-1}/\Delta. \quad (6.12)$$

This structure may resemble the equations used for real-time identification of autoregressive models [170], but note that the elements of x_k are not independent parameters because L_k and L_{k-1} are time-connected. Note also that the observation noise v_k depends on the state and may be rewritten as

$$v_k = \tilde{v}_k - \tilde{C}_k x_k, \quad (6.13)$$

where

$$\tilde{C}_k = \begin{bmatrix} \tilde{i}_k & \tilde{i}_k/\Delta & -\tilde{i}_{k-1}/\Delta \end{bmatrix}. \quad (6.14)$$

Then, assuming that $\{\tilde{v}_k\}$ and $\{\tilde{i}_k\}$ are independent random processes with zero mean and known variances, $\text{var}(\tilde{v}_k) = \sigma_v^2$ and $\text{var}(\tilde{i}_k) = \sigma_i^2$, it can be shown that v_k is a zero-mean random variable with variance given by

$$\Omega_k = \text{var}(v_k) = \sigma_v^2 + x_k^\top \begin{bmatrix} \sigma_i^2 & \frac{\sigma_i^2}{\Delta} & 0 \\ \frac{\sigma_i^2}{\Delta} & \frac{\sigma_i^2}{\Delta^2} & 0 \\ 0 & 0 & \frac{\sigma_i^2}{\Delta^2} \end{bmatrix} x_k. \quad (6.15)$$

On the other hand, the process model used by the filter is

$$x_{k+1} = F x_k + G w_k, \quad (6.16)$$

where F and G are the discrete-time state and input matrices with proper dimensions and w_k is the input—or process—noise. This structure leads to the prediction model

$$\hat{x}_{k+1/k} = F \hat{x}_{k/k}. \quad (6.17)$$

Given the dynamic behavior of the system, the proposed process model approximates R as a constant parameter and L as a variable that changes linearly in time. This leads to the predictions

$$\hat{x}_{k+1/k}^{(1)} = \hat{R}_{k+1/k} = \hat{R}_{k/k} = \hat{x}_{k/k}^{(1)}, \quad (6.18)$$

$$\hat{x}_{k+1/k}^{(2)} = \hat{L}_{k+1/k} = \hat{L}_{k/k} + (\hat{L}_{k/k} - \hat{L}_{k-1/k}) = 2\hat{x}_{k/k}^{(2)} - \hat{x}_{k/k}^{(3)}, \quad (6.19)$$

$$\hat{x}_{k+1/k}^{(3)} = \hat{L}_{k/k} = \hat{x}_{k/k}^{(2)}, \quad (6.20)$$

where the superscript (p) refers to the p th element of the vector. Consequently, the state transition matrix proposed is

$$F = \begin{bmatrix} 1 & 0 & 0 \\ 0 & 2 & -1 \\ 0 & 1 & 0 \end{bmatrix}. \quad (6.21)$$

It must be noted that this model differs from those usually used in adaptive Kalman filtering [171]. Apart from not assuming a constant inductance, the main difference is that this process model does not include the dynamics of the actual system; the only equation linking the filter to the actuator is the observation equation. In this way, the algorithm can be applied to any variable reluctance device independently of its particular design.

Substituting (6.21) in (6.16), solving for Gw_k and then approximating according to the Taylor series, the expression for the input term of the process model is obtained as

$$Gw_k = \begin{bmatrix} R_{k+1} - R_k \\ L_{k+1} - 2L_k + L_{k-1} \\ 0 \end{bmatrix} \approx \begin{bmatrix} \dot{R}_k \Delta \\ \ddot{L}_k \Delta^2 \\ 0 \end{bmatrix}, \quad (6.22)$$

where \dot{R} and \ddot{L} are, respectively, the first derivative of R and the second derivative of L with respect to time. In order to distinguish between constants and variables, w_k and G are selected as

$$w_k = \begin{bmatrix} \dot{R}_k \\ \ddot{L}_k \end{bmatrix}, \quad G = \begin{bmatrix} \Delta & 0 \\ 0 & \Delta^2 \\ 0 & 0 \end{bmatrix}. \quad (6.23)$$

Then, assuming that $\{\dot{R}_k\}$ and $\{\ddot{L}_k\}$ are independent, zero-mean random processes with known variances, $\text{var}(\dot{R}_k) = \sigma_R^2$ and $\text{var}(\ddot{L}_k) = \sigma_L^2$, the covariance matrix of the process noise is given by

$$Q = \text{var}(w_k) = \begin{bmatrix} \sigma_R^2 & 0 \\ 0 & \sigma_L^2 \end{bmatrix}. \quad (6.24)$$

The initial values of resistance and inductance, R_0 and L_0 , are assumed to be random independent variables with known expected values, $E(R_0) = \mu_{R_0}$ and $E(L_0) = \mu_{L_0}$, and known variances, $\text{var}(R_0) = \sigma_{R_0}^2$ and $\text{var}(L_0) = \sigma_{L_0}^2$. Hence, considering that $L_{-1} = L_0$, the expected value of the initial state and the initial covariance matrix are given by

$$\mu_{x_0} = E(x_0) = [\mu_{R_0} \quad \mu_{L_0} \quad \mu_{L_0}]^T, \quad (6.25)$$

$$P_0 = \text{var}(x_0) = \begin{bmatrix} \sigma_{R_0}^2 & 0 & 0 \\ 0 & \sigma_{L_0}^2 & \sigma_{L_0}^2 \\ 0 & \sigma_{L_0}^2 & \sigma_{L_0}^2 \end{bmatrix}. \quad (6.26)$$

Observability and convergence

The observability of the proposed model is now analyzed to ensure the feasibility of the estimator. In this regard it should be noted that, since observability is a structural property, in this case it cannot be analyzed through the observation equation of the filter, (6.8), because H_k depends on the measurement noise. Instead, the structural output equation,

$$y_k = C_k x_k, \quad (6.27)$$

where y_k is the true output—not to be confused with the observation \bar{y}_k —and C_k is the output matrix at step k , has to be considered. Given that the model output is the voltage through the coil, $y_k = v_k$, and that the state vector has been already selected in (6.11), the output matrix is obtained from (6.3) as

$$C_k = [i_k \quad i_k/\Delta \quad -i_{k-1}/\Delta]. \quad (6.28)$$

Note that, according to (6.6) and (6.10),

$$H_k = C_k + \tilde{C}_k. \quad (6.29)$$

Now, since the model (6.16), (6.27) is linear, observability can be analyzed by means of the observability matrix. Strictly speaking, the presented time-variant model is observable in the interval $t \in [k\Delta, (k+n)\Delta]$ if and only if the matrix

$$O_{[k, k+n]} = \begin{bmatrix} C_k \\ C_{k+1}F \\ \dots \\ C_{k+n}F^n \end{bmatrix} \quad (6.30)$$

is full rank. Given the arbitrary size of the previous matrix, the observability is analyzed in the interval $t \in [k\Delta, (k+2)\Delta]$, which, given the size of the state vector, is the shortest possible interval of observability. In this case, the observability matrix is given by

$$O_{[k, k+2]} = \begin{bmatrix} i_k & \frac{i_k}{\Delta} & -\frac{i_{k-1}}{\Delta} \\ i_{k+1} & \frac{2i_{k+1} - i_k}{\Delta} & -\frac{i_{k+1}}{\Delta} \\ i_{k+2} & \frac{3i_{k+2} - 2i_{k+1}}{\Delta} & \frac{i_{k+1} - 2i_{k+2}}{\Delta} \end{bmatrix}, \quad (6.31)$$

and the model is observable provided that the determinant,

$$\det(O_{[k, k+2]}) = (2i_{k-1}i_{k+1}^2 + 2i_k^2i_{k+2} - i_k^2i_{k+1} - i_ki_{k+1}^2 - i_{k-1}i_ki_{k+2} - i_{k-1}i_{k+1}i_{k+2})/\Delta^2, \quad (6.32)$$

is different from zero. Thus, the previous polynomial provides a method to analyze the time-dependent observability of the proposed model and shows that, with a proper excitation, it is possible to find an interval where the state is observable.

Regarding the possible types of excitation, it is noteworthy the case of linear evolution of the electric current, i.e., $i_{k+j} = i_k + jd$ with $j \in \mathbb{N}$ and constant $d \in \mathbb{R}$. In this case, observability can be analyzed considering that the output matrix can be expressed, for any time step, in terms of i_k ,

$$C_{k+j} = \begin{bmatrix} i_k + jd & \frac{i_k + jd}{\Delta} & -\frac{i_k + (j-1)d}{\Delta} \end{bmatrix}, \quad (6.33)$$

and that the j th power of F is given by

$$F^j = \begin{bmatrix} 1 & 0 & 0 \\ 0 & j+1 & -j \\ 0 & j & 1-j \end{bmatrix}. \quad (6.34)$$

Then, it can be shown that, starting from the third, the j th row of the observability matrix is a linear combination of the two previous ones.

$$C_{k+j-1}F^{j-1} = 2C_{k+j-2}F^{j-2} - C_{k+j-3}F^{j-3} \quad (6.35)$$

Thus, the rank of $O_{[k, k+n]}$ is equal or less than two independently of the value of n . This leads to the conclusion that no information can be extracted from intervals where i has a linear evolution over time. In this regard, note that steady state periods also meet this property with $d = 0$.

The selection of the inductance as state variable is now discussed. Since one of the aims of the algorithm is to estimate the flux linkage, it might seem that (6.2) is a better choice than (6.3) to be used as output equation of the model. In fact, if the state vector is selected as

$$x_k^* = [R_k \quad \lambda_k \quad \lambda_{k-1}]^\top, \quad (6.36)$$

an alternative output equation can be obtained from (6.2),

$$y_k = C_k^* x_k^*, \quad (6.37)$$

where

$$C_k^* = [i_k \quad 1/\Delta \quad -1/\Delta]. \quad (6.38)$$

Then, assuming a prediction model of constant R and constant variation of λ , i.e., a model whose state matrix is also given by (6.21), it can be shown that the j th row of the observability matrix of the alternative filter is equal to

$$C_{k+j-1}^* F^{j-1} = [i_{k+j-1} \quad 1/\Delta \quad -1/\Delta]. \quad (6.39)$$

Since the second and third columns of this observability matrix are proportional, the alternative model is not observable independently of the system excitation and the length of the observation interval. Consequently, this version of the filter is not feasible and, therefore, the selection of the inductance as state variable instead of the flux linkage is clearly justified.

The convergence of the filter is now studied. Considering that (6.16), (6.27) is a time-varying discrete-time linear model, a sufficient condition for exponential stability of the filter is that the pairs (F, G) and (F, C_k) are, respectively, uniformly controllable and uniformly observable [172]. Since (F, G) is time-invariant, controllability and uniform controllability are equivalent and guaranteed by the full rank of the controllability matrix $[G \ FG \ F^2G]$. On the other hand, the pair (F, C_k) is uniformly observable in the interval $t \in [k\Delta, (k+n)\Delta]$ if the observability Gramian

$$W_{O[k, k+n]} = \sum_{j=k}^{k+n} (C_i F^{j-k})^\top C_i F^{j-k} \quad (6.40)$$

satisfies, for some constants β_1 and β_2 ,

$$0 < \beta_1 I \leq W_{O[k, k+n]} \leq \beta_2 I, \quad (6.41)$$

where I is the identity matrix with proper dimensions. Given (6.21), (6.28), and (6.40), it is easy to see that β_2 exists whenever the current i is bounded—a condition which is always met in practice. Then, in order to ensure the uniform observability of the model and, hence, the exponential stability of the filter, it is only necessary to check that the current excitation is such that it guarantees the existence of β_1 .

As a final remark, remember that, since $W_{O[k, k+n]} = (O_{[k, k+n]})^\top O_{[k, k+n]}$, then

$$\text{rank}(O_{[k, k+n]}) = 3 \Leftrightarrow W_{O[k, k+n]} > 0, \quad (6.42)$$

which, together with (6.41), shows that observability is a necessary condition for uniform observability.

Algorithm equations

The operations performed by the SEMERA estimator are summarized in Algorithm 6.1, where $\Sigma_{k/k-1}$ and $\Sigma_{k/k}$ are, respectively, the covariance matrices of the *a priori* and *a posteriori* state estimates. For more insight into the equations of lines 8–12, see the original paper by Kalman [169] or the book by Anderson and Moore [170]. It must be noted that, when considering the probability of x_k conditioned to \bar{y}_k , the Kalman gain is obtained as

$$K_k = \text{cov}(x_k, \bar{y}_k) (\text{var}(\bar{y}_k))^{-1}. \quad (6.43)$$

Thus, for the usual case of deterministic H_k , it is equal to

$$K_k = \Sigma_{k/k-1} H_k^\top (H_k \Sigma_{k/k-1} H_k^\top + \Omega_k)^{-1}. \quad (6.44)$$

However, in this particular case H_k is not deterministic but stochastic, so K_k takes a different value. Given (6.8), (6.13) and (6.29), \bar{y}_k may be expressed as $\bar{y}_k = C_k x_k + \tilde{v}_k$,

which leads to

$$K_k = \Sigma_{k/k-1} C_k^\top (C_k \Sigma_{k/k-1} C_k^\top + \sigma_v^2)^{-1}. \quad (6.45)$$

Since C_k is not available in practice, the SEMERA algorithm computes an estimate of the Kalman gain, \hat{K}_k , by using H_k instead of C_k .

$$\hat{K}_k = \Sigma_{k/k-1} H_k^\top (H_k \Sigma_{k/k-1} H_k^\top + \sigma_v^2)^{-1} \quad (6.46)$$

The estimates of the coil resistance and inductance, \hat{R} and \hat{L} , are extracted from the first and second elements of the *a posteriori* state estimate of the filter, provided that the SNRs of \bar{i}_k and \bar{i}_{k-1} , which are used to calculate H_k , are sufficiently large. This condition is checked by a detector based on a CI that discards, with a certain probability, that the current measurements are noise-only. Hence, the *a posteriori* estimates at step k are considered valid only if the values of \bar{i}_k and \bar{i}_{k-1} are outside the interval $[-n_\sigma \sigma_i, n_\sigma \sigma_i]$, where n_σ is set according to the selected confidence. Otherwise, the measurements are regarded as mostly noise and the estimates are calculated as $\hat{R}_k = \hat{R}_{k-1}$ and $\hat{L}_k = \mu_{L_0}$, i.e., the resistance estimation is kept constant and the inductance is estimated to be equal to the expected initial value. This latter estimation, which may be regarded as an expert rule, is justified by the fact that non-latching switch-type devices always return to the initial position when the excitation is cut off. Consequently, the filter initial state must correspond to the resting position of the device. On the other hand, the estimate of the flux linkage is calculated as $\hat{\lambda} = \hat{L} \bar{i}$.

Additional estimates can be obtained if the number of turns of the coil, N , is known. Given that the flux linkage is equal to the product of the magnetic flux through the core, ϕ , and the number of turns of the coil, N , the flux can be estimated as $\hat{\phi} = \hat{\lambda}/N = \hat{L} \bar{i}/N$. The reluctance of the device may also be estimated as $\hat{\mathcal{R}} = N^2/\hat{L}$.

Algorithm 6.1 SEMERA algorithm

Require: $\mu_{x_0}, P_0, F, G, Q, \sigma_v^2, \sigma_i^2, \Delta, n_\sigma$

- 1: $\hat{x}_{1/0} := \mu_{x_0};$ ▷ Initialize *a priori* state estimate
 - 2: $\Sigma_{1/0} := P_0;$ ▷ Initialize *a priori* state covariance
 - 3: Register \bar{i}_0 and start time counter.
 - 4: **for** $k := 1$ **to** ∞ **do**
 - 5: Wait until $t = k\Delta$; Register \bar{v}_k and \bar{i}_k ;
 - 6: $\bar{y}_k := \bar{v}_k$;
 - 7: $H_k := [\bar{i}_k \quad \bar{i}_k/\Delta \quad -\bar{i}_{k-1}/\Delta]$;
 - 8: $\hat{K}_k := \Sigma_{k/k-1} H_k^\top (H_k \Sigma_{k/k-1} H_k^\top + \sigma_v^2)^{-1}$;
 - 9: $\hat{x}_{k/k} := \hat{x}_{k/k-1} + \hat{K}_k (\bar{y}_k - H_k \hat{x}_{k/k-1})$;
 - 10: $\Sigma_{k/k} := (I - \hat{K}_k H_k) \Sigma_{k/k-1}$;
 - 11: $\hat{x}_{k+1/k} := F \hat{x}_{k/k}$;
 - 12: $\Sigma_{k+1/k} := F \Sigma_{k/k} F^\top + G Q G^\top$;
 - 13: **if** $|\bar{i}_k| > n_\sigma \sigma_i \wedge |\bar{i}_{k-1}| > n_\sigma \sigma_i$
 - 14: **then** $\hat{R}_k := \hat{x}_{k/k}^{(1)}$; $\hat{L}_k := \hat{x}_{k/k}^{(2)}$;
 - 15: **else** $\hat{R}_k := \hat{R}_{k-1}$; $\hat{L}_k := \mu_{L_0}$;
 - 16: $\hat{\lambda}_k := \hat{L}_k \bar{i}_k$;
 - 17: **end for**
-

6.1.2 Integral estimator

In addition to the SEMERA algorithm, an integral estimator has been also designed. The basic idea of this algorithm consists in transforming (6.1) into integral form, so that the flux linkage can be expressed as

$$\lambda(t) = \lambda(t_0) + \int_{t_0}^t (v(\tau) - R(\tau) i(\tau)) d\tau, \quad (6.47)$$

where t_0 is an arbitrary reference of known flux. Expressed in discrete time, it becomes

$$\lambda_k = \lambda_0 + \Delta \sum_{j=1}^k (v_j - R_j i_j), \quad (6.48)$$

where $\lambda_0 = \lambda(t_0)$. Based on this equation, the calculation of λ would be immediate if perfect measurements of v , R and i were available. However, given that only measurements of voltage and current can be obtained, a constant average value of resistance, \hat{R} , is used during the calculations instead of the time-dependent variable. Thus, replacing v and i by their respective experimental measurements, \bar{v} and \bar{i} , the flux linkage is estimated as

$$\hat{\lambda}_k = \lambda_0 + \Delta \left(\sum_{j=1}^k \bar{v}_j - \hat{R} \sum_{j=1}^k \bar{i}_j \right). \quad (6.49)$$

Since this estimate relies on an open-loop integration, even the slightest error in \hat{R} may lead to significant cumulative errors in $\hat{\lambda}$. Thus, it becomes necessary to establish a condition in which the two integrals of the estimator are set to zero. Switch-type electromechanical devices like relays and valves operate periodically and always return to the same state at the end of the activation-deactivation cycle. Hence, the reset event can be established, e.g., at the beginning of each energizing operation, this being understood as each time the device is supplied with voltage to start the motion. Note that at that initial point there is no magnetic field generated by the coil, so the flux has a known constant value λ_0 . Besides, for devices without permanent magnetization, $\lambda_0 = 0$.

Additionally, for a given operation that begins at step n and lasts m sampling periods, the estimator should achieve $\hat{\lambda}_n = \hat{\lambda}_{n+m}$. Together with (6.49), this condition provides the following adaptive rule for recalculating the resistance at the reset events:

$$\hat{R} = \sum_{j=n+1}^{n+m} \bar{v}_j \left(\sum_{j=n+1}^{n+m} \bar{i}_j \right)^{-1}. \quad (6.50)$$

Since only one resistance value is obtained for each operation, the integral estimator cannot account for rapid variations of R . However, this should not represent a significant problem because changes in resistance are mainly due to temperature variations with slow dynamics [168].

Once the estimate of the flux linkage is obtained, an estimate of the inductance is also calculated as

$$\hat{L}_k = \frac{\hat{\lambda}_k}{\bar{i}_k}. \quad (6.51)$$

In order to avoid divisions by zero and prevent from high estimation errors when the current SNR is low, the algorithm makes use of the same CI-detector than the SEMERA algorithm. Hence, the previous expression is used at step k only when the absolute values of \bar{i}_k and \bar{i}_{k-1} are higher than n_σ times the standard deviation of the current measurement noise. Otherwise, the inductance is considered equal to μ_{L_0} . The operations performed by the integral estimator are summarized in Algorithm 6.2.

Algorithm 6.2 Integral estimator

Require: $\mu_{R_0}, \mu_{L_0}, \lambda_0, \sigma_i^2, \Delta, n_\sigma$

```

1:  $\hat{R} := \mu_{R_0};$  ▷ Initialize  $\hat{R}$ 
2:  $S_v := 0; S_i := 0;$  ▷ Initialize integrals
3: for  $k := 1$  to  $\infty$  do
4:   Wait until  $t = k\Delta$ ; Register  $\bar{v}_k$  and  $\bar{i}_k$ ;
5:    $S_v := S_v + \bar{v}_k; S_i := S_i + \bar{i}_k$ ;
6:    $\hat{\lambda}_k := \lambda_0 + \Delta (S_v - \hat{R} S_i)$ ;
7:   if  $|\bar{i}_k| > n_\sigma \sigma_i \wedge |\bar{i}_{k-1}| > n_\sigma \sigma_i$ 
8:     then  $\hat{L}_k := \hat{\lambda}_k / \bar{i}_k$ ;
9:     else  $\hat{L}_k := \mu_{L_0}$ ;
10:  if start of energizing operation
11:    then  $\hat{R} := S_v / S_i; S_v := 0; S_i := 0$ ;
12:  end for

```

6.1.3 Simulation results

In order to analyze the performance of the proposed estimators, the dynamical model including magnetic saturation (see Subsection 3.2.2) has been used to carry out some simulations. The values of the model parameters, which correspond approximately with those of the studied solenoid valve, are presented in Table 6.1. On the other hand, the parameters used by the estimator are shown in Table 6.2. The variances and expected values of R_0 and L_0 have been set according to real measurements of several solenoid valves in their resting positions ($z = z_{\max}$) using an impedance analyzer. In addition, a proper value for $\sigma_{\hat{L}}$ has been obtained by simulating the actuator dynamics under a square wave input. Since R is not expected to have great variations in reality, $\sigma_{\hat{R}}$ has been set to an arbitrary small value. Besides, actual measurements from voltage and current sensors have been analyzed to assign realistic values to σ_v and σ_i in the simulations. The probability of the CI has been set to a conservative value of 99.9% because it is considered that, even if the SNR of the current is high enough, it is always preferable to use the expert rule with small values of \bar{i}_k . The sampling period, which is $\Delta = 50 \mu\text{s}$, has been optimized by simulation in order to minimize the estimation error. In this regard, the Nyquist-Shannon sampling theorem may help in setting both upper and lower bounds for Δ according to the dynamics of the system and the desired filtering performance.

The simulation results are presented in Fig. 6.1 and correspond to a series of activations and deactivations of the actuator at supply voltage of 30 V. In total, four cycles of 20 ms are represented in the figures. The first two plots show respectively the simulated

Table 6.1: Model parameters.

Parameter	Value	Parameter	Value
m	1.6 g	N	1200
k_s	55 N/m	R	76 Ω
z_s	15 mm	$\mathcal{R}_{\text{gap}0}$	10^7 H^{-1}
c	0.4 Ns/m	k_{gap}	$2.7 \cdot 10^{10} \text{ H}^{-1}/\text{m}$
z_{min}	0 mm	$\mathcal{R}_{\text{core}0}$	$3.25 \cdot 10^6 \text{ H}^{-1}$
z_{max}	0.9 mm	ϕ_{sat}	20 μWb

Table 6.2: Filter parameters (Valve case).

Parameter	Value	Parameter	Value
μ_{R_0}	77.5 Ω	$\sigma_{\hat{R}}$	1 Ω/s
σ_{R_0}	1 Ω	$\sigma_{\hat{L}}$	10^8 H/s^2
μ_{L_0}	50 mH	σ_v	15 mV
σ_{L_0}	5 mH	σ_i	1 mA
-	-	n_σ	3.29 (99.9% CI)

measurements of voltage and current, i.e., the variables used by the estimators. The result of the CI-based noise detector, which classifies the current measurements as high-quality (HQ) or low-quality (LQ), is also represented in the second plot. Then, the three following graphs show the estimations of resistance, inductance and flux linkage together with their respective true values. Note that the simulated value of resistance has been deliberately set to a value other than the initial value of the filters, μ_{R_0} , so that the transient response could be analyzed. The sixth and seventh graphs show, respectively, the SNRs of the voltage measurement and the current measurement, which are calculated as $\text{SNR}_v = 20 \log_{10}(\bar{v}/\tilde{v})$ and $\text{SNR}_i = 20 \log_{10}(\bar{i}/\tilde{i})$. Finally, the last plot represents, for each time instant, the number of time steps since the last observable state. Note that, according to the size of the state vector, the minimum number of time steps required for a state to be observable is two.

It can be seen that the performances of the two estimators during the first activation-deactivation cycle are considerably different. Since the integral estimator does not modify the resistance value until the first reset event, the small error in \hat{R} (less than 2%) leads to much higher errors (greater than 100%) when estimating both the inductance and the flux linkage. Indeed, the inductance estimate of the integral estimator goes far beyond the limits of the graph and it has not been completely represented for clarity reasons. On the other hand, the SEMERA algorithm has a similar behavior at the beginning, but it is able to correct the estimates during the operation and achieves much lower estimation errors, near to zero, before the end of the first cycle. This is partially due to the fact that the flux linkage is estimated through the inductance, which forces $\hat{\lambda}$ to decrease rapidly when the current measurement approaches zero.

Then, after the first cycle, the estimations present a different behavior. As can be seen, the resistance and flux linkage estimations given by both estimators are almost equal to the true values, so it can be concluded that the two filters achieve a very good performance

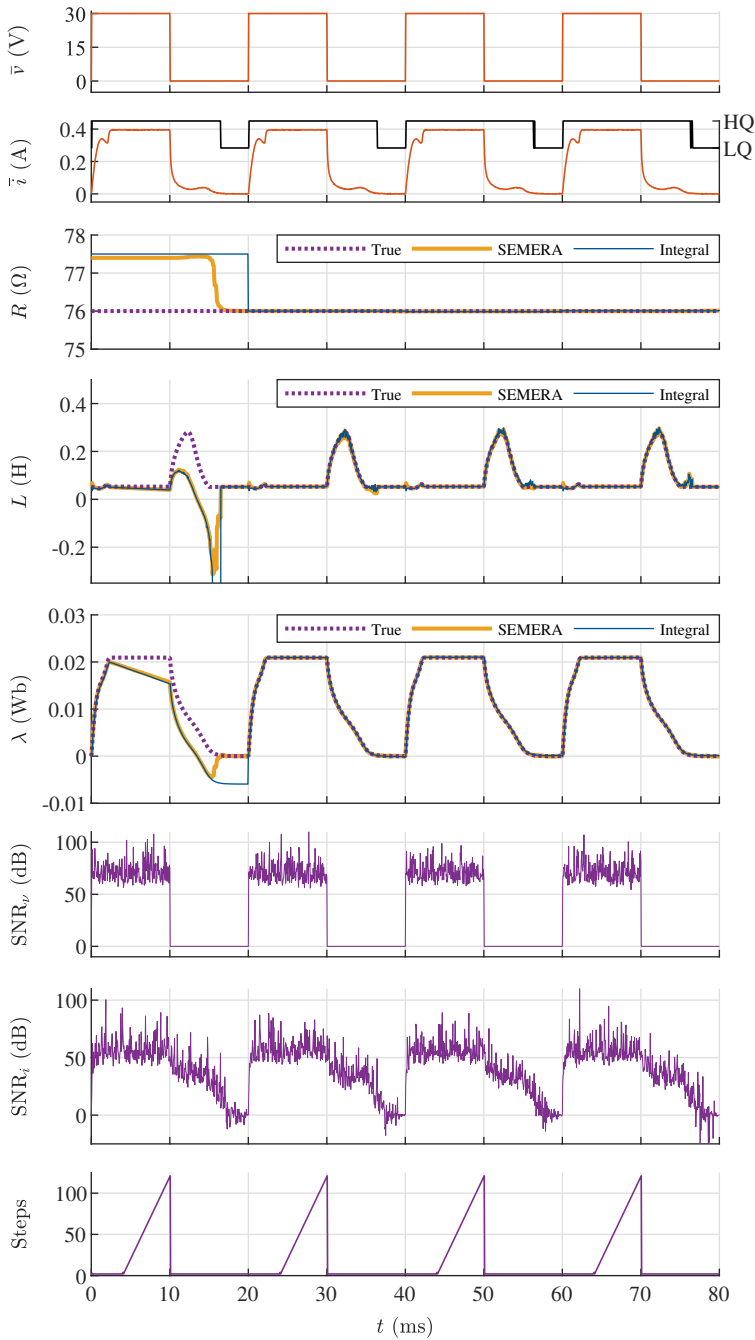


Figure 6.1: Simulation results. Four activation-deactivation cycles. From top to bottom: voltage measurement, current measurement (with CI-based classification), resistance estimation, inductance estimation, flux linkage estimation, voltage SNR, current SNR and time steps since the last observable state.

with respect to these variables. On the other hand, the inductance estimations are also very close to the true values except during two periods for each operation: a short transient after the voltage positive step ($t = 20, 40$ and 60 ms) and a period after the current drops close to zero ($t = 35, 55$ and 75 ms). Whereas the first periods are intrinsic to the dynamics of the estimators, the second ones are related to a low SNR of the current measurement. In this connection, it can be seen that the noisy behavior starts when SNR_i falls approximately below 30 dB, and the problem is later detected and overcome by means of the CI-based detector, which acts approximately for $\text{SNR}_i < 20$ dB.

It is also noteworthy that there is no need to design a specific activation signal to provide observability; the standard square-wave voltage usually applied to activate these devices provides minimum-time observability except during the steady-state periods. In this regard, note that constant current is simply a particular case of linear evolution in time, $i_{k+j} = i_k + jd$, with $d = 0$. Hence, the results are in accordance with the observability analysis previously presented.

The root-mean-square errors (RMSE) of the estimates during the simulation have been calculated and are presented in Tables 6.3 and 6.4. With regard to the errors during the first operation (see Table 6.3), it is shown that the SEMERA estimator performs better, particularly for the inductance estimation. After the first cycle, once the estimators have converged, the errors (see Table 6.4) are one or two orders of magnitude smaller, but the SEMERA performance is still better for the three variables.

Table 6.3: Estimation errors during the first operation ($t < 20$ ms).

Algorithm	RMSE (\hat{R})	RMSE (\hat{L})	RMSE ($\hat{\lambda}$)
SEMERA	1.244 Ω	0.1022 H	3.602 mWb
Integral	1.500 Ω	0.2512 H	4.645 mWb
<i>Ratio (S/I)</i>	<i>0.8296</i>	<i>0.4069</i>	<i>0.7756</i>

Table 6.4: Estimation errors after the first operation ($t > 20$ ms).

Algorithm	RMSE (\hat{R})	RMSE (\hat{L})	RMSE ($\hat{\lambda}$)
SEMERA	4.199 m Ω	5.022 mH	0.1136 mWb
Integral	10.30 m Ω	5.158 mH	0.1445 mWb
<i>Ratio (S/I)</i>	<i>0.4077</i>	<i>0.9735</i>	<i>0.7866</i>

6.1.4 Experimental results

Considering the promising results obtained by simulation, the performance of both estimators under real conditions has been also investigated. For this purpose, both filters have been implemented on a low-cost ARM-Cortex M3 microcontroller and tested using the solenoid valve and the power relay investigated in this thesis. Both devices have been activated and deactivated periodically at supply voltage of 30 V as in the simulations. When applied to the valve, the filter parameters are those already presented in Table 6.2.

Table 6.5: Filter parameters (Relay case).

Parameter	Value	Parameter	Value
μ_{R_0}	1560 Ω	$\sigma_{\dot{r}}$	20 Ω/s
σ_{R_0}	100 Ω	$\sigma_{\dot{l}}$	$5 \cdot 10^9$ H/s ²
μ_{L_0}	1 H	σ_v	15 mV
σ_{L_0}	250 mH	σ_i	0.05 mA
-	-	n_σ	3.29 (99.9% CI)

On the other hand, Table 6.5 shows the parameters for the case of the power relay, which has very different values of inductance and resistance. The value of σ_i is also different because a different current sensing method has been used on this latter device. The sampling period, which is $\Delta = 50 \mu\text{s}$ as in the simulations, is enough to run both algorithms in 32 bit floating point. In this regard, the computing time per iteration is approximately 38 μs for the SEMERA algorithm and 2 μs for the integral estimator.

Since the true values of resistance, inductance and flux linkage are not accessible in reality, an offline non-causal version of the integral estimator has been also implemented to provide a deeper analysis. Unlike the online version, which uses data of each operation to recalculate the resistance and estimate the variables of the following one, this estimator firstly computes the resistance of each and every operation and then estimates the rest of the variables. Hence, although it also assumes a constant value between reset events, the most accurate value possible of \hat{R} is utilized.

The results corresponding to the valve and the relay are respectively presented in Figs. 6.2 and 6.3. Considering the offline estimates as the most accurate, it can be seen that the dynamics of the online estimations are very close to the simulation results already presented. It is shown that the highest errors occur during the first activation-deactivation cycle, when the small resistance estimation error leads to high errors in \hat{L} , although the SEMERA estimations converge faster to the true values. The two estimators behave similarly once the first cycle has finished: They provide very good estimations of R , L and λ . The noisy behavior of \hat{L} during the periods of low SNR_i , which has been already observed in the simulations, can also be noticed here in the relay test (around $t = 85, 135$ and 185 ms), although it is almost unnoticeable in the valve experiment. Nevertheless, the CI-based classifier is able to detect the problem and the expert rule corrects the estimation when SNR_i is very low.

Regarding the evolution of the variables, it can be firstly seen that the resistances of both devices keep an almost constant value during the experiments, which is the expected behavior. The same applies to the flux linkage, which oscillates between zero and a maximum steady value. Finally, the inductance plot shows that, as already discussed in previous chapters, this variable depends not only on the position of the mechanism but also on the magnetic flux. Note that, if the inductance were a bijective function of the position, it would oscillate strictly between two values corresponding to the bounds of the motion, which is clearly not the case.

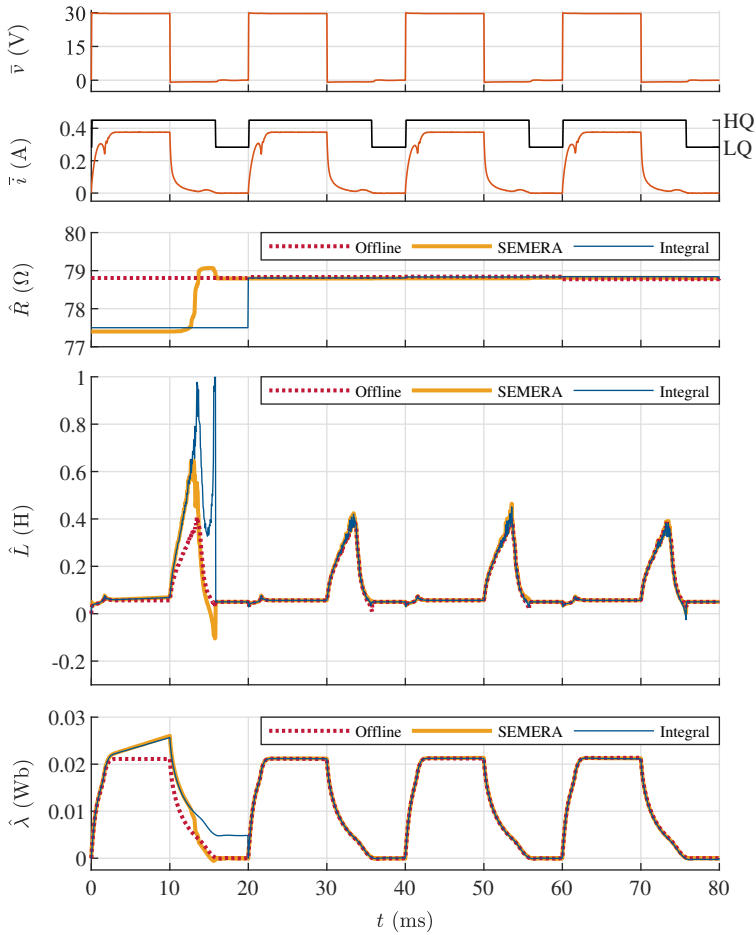


Figure 6.2: Valve experiments results. From top to bottom: voltage measurement, current measurement (with CI-based classification), resistance estimation, inductance estimation and flux linkage estimation.

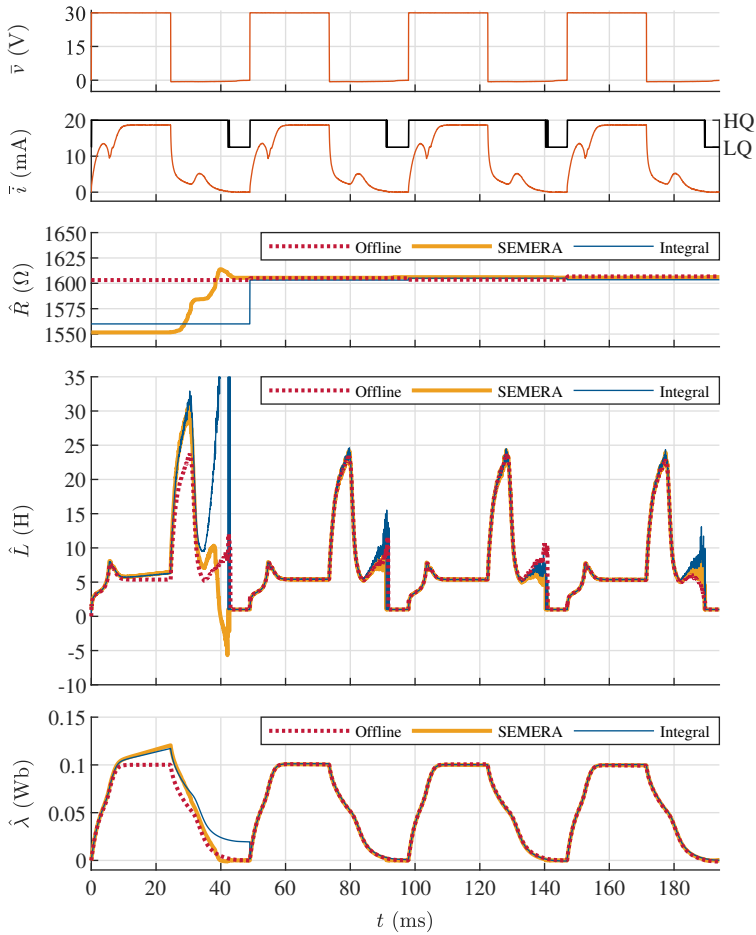


Figure 6.3: Relay experiments results. From top to bottom: voltage measurement, current measurement (with CI-based classification), resistance estimation, inductance estimation and flux linkage estimation.

6.1.5 Discussion

Two different algorithms have been presented to estimate the flux linkage and the time-variant electrical parameters of reluctance actuators, i.e., the resistance and the inductance, even under temperature variations and measurement noise. Since they only use voltage and current measurements, both algorithms provide an efficient method to obtain flux and resistance estimations without need of additional equipment. For this same reason, they can be applied without limitations to encapsulated devices such as the studied solenoid valve where no instrument can be used to measure the flux. Clearly, this represents an advantage with respect to other flux-measurement techniques.

The SEMERA algorithm has proved to be highly accurate and able to handle long unobservable periods and poor SNRs. Besides, it is fully applicable to any reluctance actuator independently of the shape, the materials or the mechanical design, because it only relies on the electrical equation of a variable inductor. Consequently, it is much more versatile than model-based estimators [24]. On the other hand, the reset estimator also achieves good precision while requiring simpler calculations. However, an application problem may be encountered with this latter approach: If the time between operations is long enough that the temperature changes considerably, the corresponding change in the electrical resistance may lead to high transient errors that will not be reduced until the end of a complete operation.

Apart from the aforementioned variables, additional estimates may also be derived. For instance, the resistance may be used to estimate the temperature of the device or to detect faults, and the flux linkage estimation allows for characterizing the relation between flux and electric current. Furthermore, it is known in the literature that the inductance is related to the position of the device and, consequently, that it may be used to estimate this latter variable. A further discussion on this possibility is presented below.

Position estimation via inductance estimates

Many previous works [58, 97, 173–175] have proposed position tracking controllers that rely on non-dynamical models of the inductance as a function of the position and possibly the electric current, i.e., models of the form

$$L = L(z, i). \quad (6.52)$$

The general idea is to estimate the inductance using past and present measurements of voltage and current,

$$\hat{L}(t) = \hat{L}(\{ \bar{i}(\tau) \mid \tau \leq t \}, \{ \bar{v}(\tau) \mid \tau \leq t \}), \quad (6.53)$$

and then estimate the position by minimizing the error between the estimation and the inductance given by the model.

$$\hat{z}(t) = \arg \min_{z \in [z_{\min}, z_{\max}]} \left| L(z, \bar{i}(t)) - \hat{L}(t) \right| \quad (6.54)$$

Although this estimation method has some obvious drawbacks—it may be greatly affected by measurement noise and both modeling and estimation errors—it has been

evaluated using the simulations of Subsection 6.1.3. Considering that the reluctance of the dynamical model including saturation is given by (3.57), and that inductance and reluctance are related by $L = N^2/\mathcal{R}$, the position estimation obtained by this method is

$$\hat{z}(t) = \begin{cases} z_{\min}, & \text{if } z^*(t) < z_{\min}, \\ z^*(t), & \text{if } z_{\min} \leq z^*(t) \leq z_{\max}, \\ z_{\max}, & \text{if } z^*(t) > z_{\max}, \end{cases} \quad (6.55)$$

where

$$z^*(t) = \frac{1}{k_{\text{gap}}} \left(\frac{N^2}{\hat{L}(t)} - \mathcal{R}_{\text{gap}0} - \frac{\mathcal{R}_{\text{core}0}}{1 - \frac{|\hat{L}(t)\bar{i}(t)|}{N\phi_{\text{sat}}}} \right). \quad (6.56)$$

The results, which have been computed using the data from the simulation of Fig. 6.1, are plotted in Fig. 6.4. Due to its better performance, only the estimation from the SEMERA algorithm is represented in the figure. As shown, the position estimation during the first operation is very inaccurate, which is mainly due to the estimation errors in \hat{L} . Indeed, the RMSE of the estimation during the first 20 milliseconds is 0.557 mm, which is around 62% of the plunger stroke—more than if the position is assumed to be static at $(z_{\min} + z_{\max})/2$. Nevertheless, after the first cycle, when the estimation error in \hat{L} is very close to zero, the estimation RMSE is reduced to 0.046 mm, which is about 5% of the plunger travel. Although no errors have been considered in the estimation model, these results suggest that the position of a reluctance actuator might be estimated using only measurements of the electrical signals, i.e., voltage and current. In the next section, this method and other estimation approaches are analyzed in a more realistic scenario and compared in terms of accuracy and robustness.

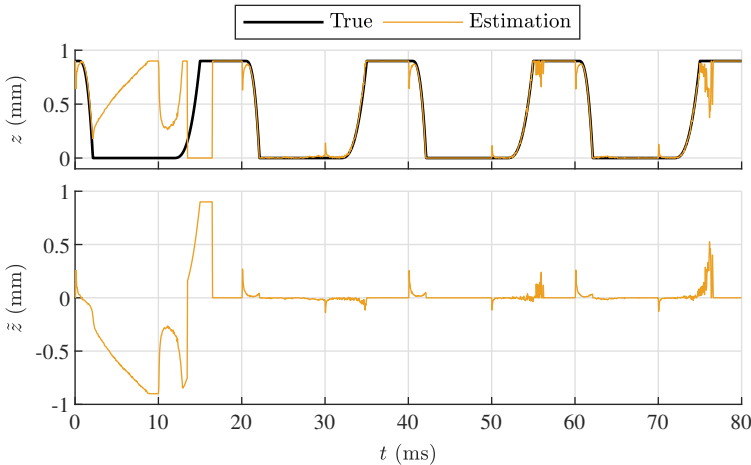


Figure 6.4: Position estimation via inductance estimation. True value and estimate (top) and estimation error (bottom). The inductance estimate is obtained using the SEMERA algorithm. Model and estimator use the same reluctance model and parameters values.

6.2 Position estimation

As stated in previous chapters, the major problem when controlling the motion of a reluctance actuator is that the position of the mover with respect to the stator cannot be measured—at least not with affordable sensors—and therefore feedback control can only be applied via estimation techniques. In this connection, it has been shown at the end of the preceding section that inductance estimations may be used to estimate the armature position in this class of actuators. As proposed by some works in the literature, this could be achieved using a model that predicts the relation between these two variables. If this relation is perfectly modeled, i.e., if there are no modeling errors, the inductance technique has proven to be a reasonably good method to estimate the position. In that case, the estimation performance is only limited by the dynamics of the inductance estimator and by measurement noise, so it may even be improved by additional filtering.

These results suggest that feedback position control in reluctance actuators may be indeed achieved using estimation methods. However, since having a perfect model of the actuator is a rare situation in practice, a more realistic scenario needs to be considered in the analysis. Given that accurate position measurements are difficult to obtain (see Subsection 4.1.2), the dynamical model including saturation, hysteresis, flux fringing and eddy currents (S+H+F+EC, see Subsection 3.2.5) is used in this section in place of a real actuator. In particular, the implemented model considers an air gap reluctance given by the McLyman expression. The model parameters are shown in Table 6.6. This model has been used to carry out a reference simulation (see Fig. 6.5) that is used throughout the section to evaluate and compare three different position estimation methods. As shown, the simulation consists of three activation-deactivation cycles, each using a different voltage signal which leads to different dynamic responses of the magnetic flux, the armature position and the current through the coil. Apart from the voltage, which is the input of the model, the electric current is the only variable of the actuator that is considered measurable. In this regard, it is assumed that the current measurement is corrupted by a zero-mean Gaussian noise with a standard deviation of 1 mA.

It should be noted that this dynamical model depends on two sets, \mathcal{A} and \mathcal{B} , which cannot be determined in a real actuator unless it is first demagnetized. For this reason, this model is not used as part of the estimator, but only as a substitute of a real actuator whose armature position is to be estimated. Instead, the estimators designed in this section are based on two of the dynamical models presented in Chapter 3: the basic dynamical model and the model including saturation, flux fringing and eddy currents (S+F+EC). Although these models do not consider magnetic hysteresis and, hence, are less accurate than the complete model, they are better suited for state estimation due to their structure and low computational requirements. The nominal parameters of these models are shown in Tables 6.7 and 6.8. As can be seen, the mechanical parameters— m , k_s , z_s , c , z_{\min} and z_{\max} —and those related with the coil— N and R —are exactly the same than those of the complete model. On the other hand, the parameters that model the magnetic behavior of the actuator have been obtained by fitting the magnetic relations for the core and the air gap used in these models to the relations used by the S+H+F+EC model, i.e., the Preisach model of hysteresis and the McLyman reluctance. The least-squares fits of these magnetic models are represented in Figs. 6.6 and 6.7. The robustness of the estimators against parameter uncertainty is also discussed at the end of the section.

Table 6.6: Parameters of the S+H+F+EC dynamical model used in place of the actuator.

Parameter	Value	Parameter	Value	Parameter	Value
m	1.6 g	R	75 Ω	s_{h_c}	150 A/m
k_s	55 N/m	$\mathcal{R}_{\text{gap}0}$	$6 \cdot 10^6 \text{ H}^{-1}$	s_{h_m}	150 A/m
z_s	15 mm	l_w	15 mm	\hat{B}_{irr}	0.8 T
c	0.5 Ns/m	A_{core}	12.57 mm ²	μ_1	170 μ_0
z_{min}	0 mm	l_{core}	55 mm	μ_2	65 μ_0
z_{max}	1 mm	k_{ec}	1500 A/V	H_1	1250 A/m
N	1200	m_{h_c}	200 A/m	H_2	9000 A/m

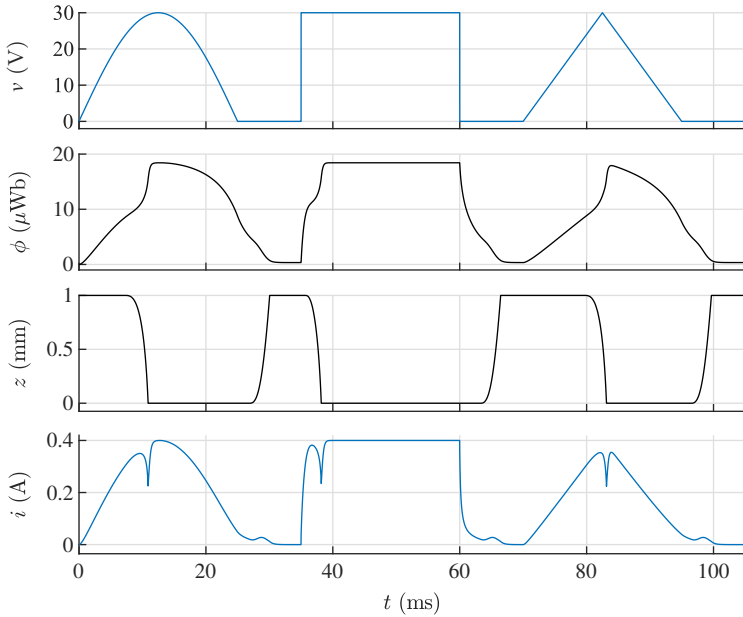


Figure 6.5: Reference simulation used throughout the section to evaluate the position estimation methods. From top to bottom: voltage (input of the system), magnetic flux, position and electric current. Only the voltage and the current are used by the estimators.

Table 6.7: Nominal parameters of the basic dynamical model used for estimation.

Parameter	Value	Parameter	Value
m	1.6 g	z_{max}	1 mm
k_s	55 N/m	N	1200
z_s	15 mm	R	75 Ω
c	0.5 Ns/m	\mathcal{R}_0	$1.84 \cdot 10^7 \text{ H}^{-1}$
z_{min}	0 mm	k_{gap}	$3.09 \cdot 10^{10} \text{ H}^{-1}/\text{m}$

Table 6.8: Nominal parameters of the S+F+EC dynamical model used for estimation.

Parameter	Value	Parameter	Value
m	1.6 g	R	75Ω
k_s	55 N/m	$\mathcal{R}_{\text{gap}0}$	$6 \cdot 10^6 \text{ H}^{-1}$
z_s	15 mm	l_w	15 mm
c	0.5 Ns/m	A_{core}	12.57 mm^2
z_{min}	0 mm	$\mathcal{R}_{\text{core}0}$	$2.76 \cdot 10^6 \text{ H}^{-1}$
z_{max}	1 mm	ϕ_{sat}	$21.2 \mu\text{Wb}$
N	1200	k_{ec}	1500 A/V

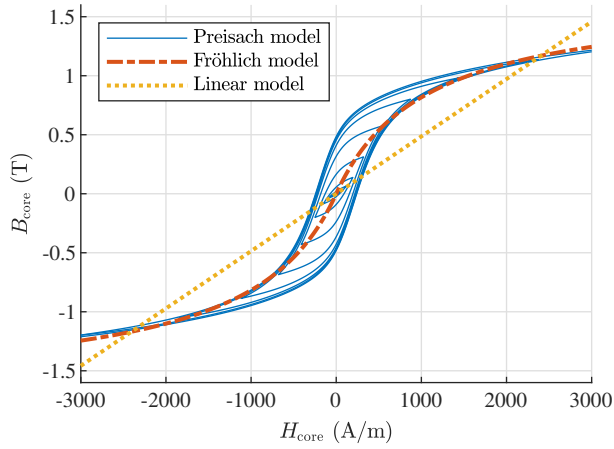


Figure 6.6: Magnetic relation given by the Preisach model and least-squares fits of the Fröhlich and linear models. The Preisach model is used by the S+H+F+EC dynamical model acting in place of a real actuator. The Fröhlich and linear relations are respectively used by the S+F+EC model and the basic model, both used for estimation.

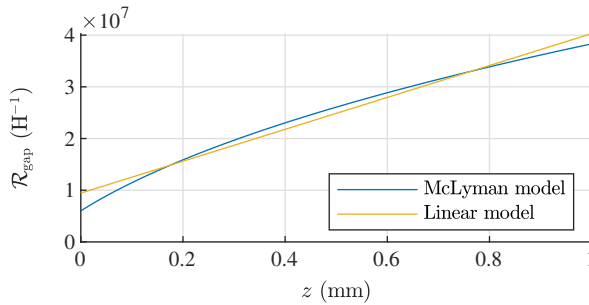


Figure 6.7: Air gap reluctance given by the McLyman model and least-squares fit of a linear reluctance model. The McLyman model is used by both the S+H+F+EC model acting in place of the actuator and the S+F+EC model used for estimation. The linear reluctance model is used by the basic dynamical model, which is also used for estimation.

6.2.1 Position estimation via inductance estimation

The first approach studied in this section is the one already introduced, i.e., estimating the armature position using inductance estimates and a model that relates these two variables. With regard to the inductance estimation, the SEMERA algorithm presented in the previous section has been used to obtain a time-dependent estimate of the apparent inductance of the actuator during the reference simulation. The result of this estimation procedure, which only uses voltage and current measurements, is shown in Fig. 6.8.

At this point it should be recalled that, for a system without magnetic hysteresis, the points of the B - H curve are confined to the first and third quadrants and the inductance is a strictly positive variable that can be expressed in terms of the reluctance as

$$L = \frac{N^2}{\mathcal{R}}, \quad (6.57)$$

where \mathcal{R} depends on the geometry of the actuator—defined in part by the position of the armature—and the magnetic properties of the materials. However, as stated in Section 2.3, the reluctance is not a valid description for a system with magnetic hysteresis because the points of the B - H relation may lie in any of the four quadrants (see Fig. 6.6). In that case, the apparent inductance can still be computed as the quotient between the flux linkage and the electric current,

$$L = \frac{N\phi}{i}, \quad (6.58)$$

but, as shown in Fig. 6.8, it is not defined for $i = 0$. As a result, the inductance estimation and the true value diverge when the current is zero or very close to zero.

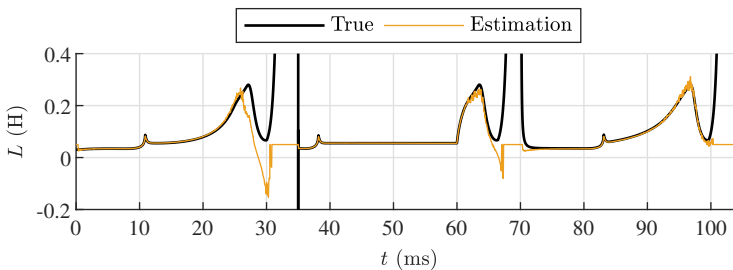


Figure 6.8: Apparent inductance of the actuator and estimation obtained from the SEMERA algorithm. The estimation error is unbounded because, due to magnetic hysteresis, the true apparent inductance goes to infinity as the current approaches zero.

Magnetic hysteresis is therefore a problematic issue when estimating the position of a reluctance actuator by means of inductance estimates. Since there is no hysteresis model that provides a relation between inductance and position for any given value of the current, there is no other alternative than using approximate models. In particular, the inductance of the basic dynamical model is given by

$$L = \frac{N^2}{\mathcal{R}} = \frac{N^2}{\mathcal{R}_0 + k_{\text{gap}} z}. \quad (6.59)$$

Hence, following the procedure presented at the end of the previous section, the position could be estimated as

$$\hat{z}(t) = \begin{cases} z_{\min}, & \text{if } z^*(t) < z_{\min}, \\ z^*(t), & \text{if } z_{\min} \leq z^*(t) \leq z_{\max}, \\ z_{\max}, & \text{if } z^*(t) > z_{\max}, \end{cases} \quad (6.60)$$

where

$$z^*(t) = \frac{1}{k_{\text{gap}}} \left(\frac{N^2}{\hat{L}(t)} - \mathcal{R}_0 \right). \quad (6.61)$$

On the other hand, the inductance of the S+F+EC model is

$$L = \frac{N^2}{\mathcal{R}} = \frac{N^2}{\mathcal{R}_{\text{gap}}(z) + \frac{\mathcal{R}_{\text{core0}}}{1 - |\phi|/\phi_{\text{sat}}}}, \quad (6.62)$$

where $\mathcal{R}_{\text{gap}}(z)$ is a bijective function. Considering that the flux can be estimated from the inductance estimate and the current measurement as $\hat{\phi} = \hat{L}\bar{i}/N$, the position estimation corresponding to this model is given by (6.60), with z^* equal to

$$z^*(t) = \mathcal{R}_{\text{gap}}^{-1} \left(\frac{N^2}{\hat{L}(t)} - \frac{\mathcal{R}_{\text{core0}}}{1 - \frac{|\hat{L}(t)\bar{i}(t)|}{N\phi_{\text{sat}}}} \right), \quad (6.63)$$

where $\mathcal{R}_{\text{gap}}^{-1}$ is the inverse function of \mathcal{R}_{gap} .

6.2.2 Position estimation via flux linkage estimation

The motion of reluctance actuators (see Section 3.1) can be generally described by

$$\dot{z} = v_z, \quad (6.64)$$

$$\dot{v}_z = \frac{1}{m} (F_m(z, \phi) - k_s(z - z_s) - c v_z), \quad (6.65)$$

where $z \in [z_{\min}, z_{\max}]$ is the position, $v_z \in \mathbb{R}$ is the velocity, $\phi \in [-\phi_{\text{sat}}, \phi_{\text{sat}}]$ is the magnetic flux and F_m is the magnetic force, which depends on the position and the flux. In this connection, it should be noted that two different algorithms have been presented in the previous section to estimate the magnetic linkage, which is the product of the magnetic flux and the number of turns of the coil, $\lambda = N\phi$. Hence, it seems reasonable to use that information to estimate the magnetic force and, by using a mechanical model of the actuator, also the position and velocity of the armature. In fact, the flux linkage estimation obtained for the reference simulation (see Fig. 6.9) is much more accurate than the inductance estimation, so it is expected that the estimation error using this approach is better than using the inductance. Note that these estimation results are mainly due to the fact that, contrary to the inductance, the flux is a physical variable that is always defined for any value of the current. Hence, provided that the flux estimator is stable, the

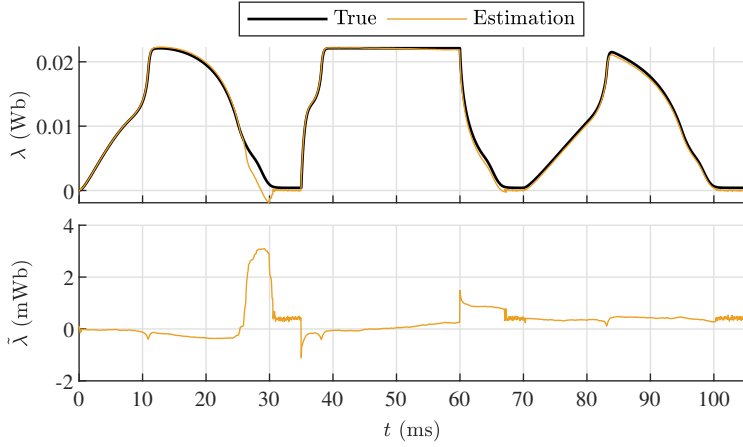


Figure 6.9: Flux linkage of the actuator and estimation obtained from the SEMERA algorithm (top) and estimation error (bottom, note the different scale). The estimation error is bounded because the estimator is stable and the true value of the flux linkage is bounded.

estimation error of the flux will be bounded even in the presence of magnetic hysteresis, a condition which cannot be met by the inductance estimation error.

Thus, given an estimate $\hat{\lambda}$ of the magnetic linkage of a reluctance actuator, the position and velocity of the armature can be estimated by the dynamic observer

$$\dot{\hat{z}} = \hat{v}_z, \quad (6.66)$$

$$\dot{\hat{v}}_z = \frac{1}{m} \left(\hat{F}_m(\hat{z}, \hat{\lambda}/N) - k_s(\hat{z} - z_s) - c\hat{v}_z \right), \quad (6.67)$$

where $\hat{z} \in [z_{\min}, z_{\max}]$ and $\hat{v}_z \in \mathbb{R}$ are respectively the position and velocity estimates and \hat{F}_m is an approximate function for the magnetic force. By defining the position and velocity estimation errors as $\tilde{z} = z - \hat{z}$ and $\tilde{v}_z = v_z - \hat{v}_z$, it can be shown that

$$\begin{bmatrix} \dot{\tilde{z}} \\ \dot{\tilde{v}}_z \end{bmatrix} = \begin{bmatrix} 0 & 1 \\ -k_s/m & -c/m \end{bmatrix} \begin{bmatrix} \tilde{z} \\ \tilde{v}_z \end{bmatrix} + \begin{bmatrix} 0 \\ \tilde{F}_m/m \end{bmatrix}, \quad (6.68)$$

where $\tilde{F}_m = F_m(z, \phi) - \hat{F}_m(\hat{z}, \hat{\lambda}/N)$ is the force estimation error. Considering that k_s , c and m are positive parameters, the eigenvalues of the state transition matrix of (6.68) lie in the negative half-plane. Consequently, the estimation errors will be bounded if the force estimation error \tilde{F}_m is also bounded. That is, the observer will be stable if there exists $\beta > 0$ such that

$$\left| \tilde{F}_m \right| = \left| F_m(z, \phi) - \hat{F}_m(\hat{z}, \hat{\lambda}/N) \right| < \beta \quad (6.69)$$

for all possible values of z , \hat{z} , ϕ and $\hat{\lambda}$.

As shown in Section 2.8, the magnetic force in a reluctance actuator is given by

$$F_m(z, \phi) = -\frac{1}{2} \phi^2 \frac{\partial \mathcal{R}_{\text{gap}}(z)}{\partial z}, \quad (6.70)$$

where $\partial\mathcal{R}_{\text{gap}}/\partial z$ is a continuous function of $z \in [z_{\min}, z_{\max}]$. Thus, given that both z and ϕ are bounded, the magnetic force is also bounded. In particular, since the air gap reluctance of the S+H+F+EC model used in this section is modeled by the McLyman expression, the magnetic force is given by (3.64).

The basic dynamical model assumes that the magnetic force is given by (3.52). Hence, if this model is used to estimate the magnetic force, it is obtained that

$$\hat{F}_{\text{m}} = -\frac{1}{2} \frac{k_{\text{gap}}}{N^2} \hat{\lambda}^2. \quad (6.71)$$

Considering that the flux linkage estimation is bounded, the previous expression shows that the force estimation given by the basic model is also bounded. As a consequence, the condition in (6.69) is satisfied and the corresponding position estimator is stable. On the other hand, the S+F+EC model uses also the McLyman expression, so the force estimate associated with this model is simply given by

$$\hat{F}_{\text{m}}(\hat{z}, \hat{\lambda}/N) = F_{\text{m}}(\hat{z}, \hat{\lambda}/N). \quad (6.72)$$

Since both \hat{z} and $\hat{\lambda}$ are bounded, the force estimate is also bounded and, hence, the position estimator based on the S+F+EC model is stable as well.

6.2.3 Position estimation via current measurements

Two different approaches to estimate the position of reluctance actuators have been already presented in this section. As stated, both alternatives rely on estimates of other variables—inductance and flux linkage—that can be obtained using any of the dynamic observers presented in the first part of this chapter. Considering that the convergence of these observers depends on the system excitation (see the convergence analysis in Section 6.1.1), there is no guarantee that the inductance and flux estimates are fast enough to provide satisfactory results with regard to position estimation. For this reason, a different approach is presented in this subsection.

This position estimation method is also based on a mechanical model of the system which, as stated, is driven by a magnetic force created in the air gap. Hence, the estimator has also the form of (6.66)–(6.67). The difference is, however, that the magnetic flux used to estimate F_{m} is not obtained using the aforementioned observers, but by a non-dynamical approach that relies directly on measurements of the electric current. In this connection, it has been shown in Chapter 3 that the electric current can be expressed in general as a function of the magnetic flux, the armature position and the voltage across the coil terminals.

$$i = h(\phi, z, v) \quad (6.73)$$

Assume now that, for any given $z \in [z_{\min}, z_{\max}]$ and $v \in \mathbb{R}$, the function h is a bijection with respect to ϕ in the domain $[-\phi_{\text{sat}}, \phi_{\text{sat}}]$. In that case, it is possible to express the magnetic flux as a function of the current, the position and the voltage,

$$\phi = \eta(i, z, v), \quad (6.74)$$

where η is such that $i = h(\eta(i, z, v), z, v)$ for all $i \in \mathbb{R}$, $z \in [z_{\min}, z_{\max}]$ and $v \in \mathbb{R}$. Hence, the magnetic flux may be estimated by

$$\hat{\phi} = \eta(\bar{i}, \hat{z}, v), \quad (6.75)$$

where \bar{i} is the current measurement and \hat{z} is the position estimate.

This method has the advantage that the observer does not rely on estimations whose convergence rate may depend on the system excitation. By contrast, it relies on the possibility of finding the function η or, alternatively, an approximate version of it. In this regard, it should be noted that the function h of the S+H+F+EC model not only depends on ϕ , z and v , but also on H_{core} and the extrema sets \mathcal{A} and \mathcal{B} [see (3.90)]. Thus, it can be concluded that, for a reluctance actuator with magnetic hysteresis, it is not possible to find a function η in the form of (6.74). As a result, approximate models need to be used.

When using the basic dynamical model, the relation between the current and the flux is given by (3.56). Hence, the flux may be estimated as

$$\hat{\phi} = \frac{N\bar{i}}{\mathcal{R}_0 + k_{\text{gap}}\hat{z}}. \quad (6.76)$$

On the other hand, the electric current of the S+F+EC model is given by (3.71), which leads to the estimation

$$\hat{\phi} = \begin{cases} \text{sgn}(\bar{i} - \varphi(v)) \left(\frac{\phi_{\text{sat}}(\mathcal{R}_{\text{core0}} + \mathcal{R}_{\text{gap}}(\hat{z}))}{2\mathcal{R}_{\text{gap}}(\hat{z})} + \frac{|\bar{i} - \varphi(v)| - \gamma(\hat{z}, \bar{i}, v)}{2a\mathcal{R}_{\text{gap}}(\hat{z})} \right), & \text{if } \mathcal{R}_{\text{gap}}(\hat{z}) \neq 0 \\ \frac{(\bar{i} - \varphi(v))\phi_{\text{sat}}}{|\bar{i} - \varphi(v)| + a\phi_{\text{sat}}\mathcal{R}_{\text{core0}}}, & \text{if } \mathcal{R}_{\text{gap}}(\hat{z}) = 0, \end{cases} \quad (6.77)$$

where

$$a = \left(N + \frac{Rk_{\text{ec}}}{N} \right)^{-1}, \quad \varphi(v) = v \left(R + \frac{N^2}{k_{\text{ec}}} \right)^{-1},$$

$$\gamma(\hat{z}, \bar{i}, v) = \sqrt{\left(a\phi_{\text{sat}}(\mathcal{R}_{\text{core0}} + \mathcal{R}_{\text{gap}}(\hat{z})) + |\bar{i} - \varphi(v)| \right)^2 - 4a\phi_{\text{sat}}\mathcal{R}_{\text{gap}}(\hat{z})|\bar{i} - \varphi(v)|},$$

and the sign function is defined as

$$\text{sgn}(x) = \begin{cases} -1, & \text{if } x < 0, \\ 0, & \text{if } x = 0, \\ +1, & \text{if } x > 0. \end{cases} \quad (6.78)$$

As seen for the previous estimation method, the stability of these observers is guaranteed if $\hat{\phi}$ is bounded. In view of (6.76) and (6.77), this condition is satisfied if both \bar{i} and v are bounded, a condition which is always met in practice.

6.2.4 Simulation results and discussion

The performance of the three previous estimation approaches is now analyzed and compared by simulation. For that purpose, the position of the actuator during the reference experiment (see Fig. 6.5) has been estimated using all the possible combinations between the three methods and the two models proposed for estimation.

The results obtained when using the nominal sets of parameters are shown in Figs. 6.10, 6.11 and 6.12. The first of these figures shows the results corresponding to the method based on inductance estimations. It can be seen that, in contrast to the preliminary results obtained at the end of the previous section, the estimations obtained in this case are not very accurate. The RMSE when using the basic model and the S+F+EC model are, respectively, 0.322 mm and 0.234 mm, and the maximum absolute errors reach in both cases 1 mm, which is the complete armature travel. Besides, the general behavior of the estimates is not consistent with the dynamics of the actuator. Note, e.g., that the estimation given by the basic model remains at an intermediate position for t between 40 and 60 ms, which is not possible considering that the voltage during this period is constant (see the stability analysis of Subsection 5.1.1). These results are explained by the fact that magnetic hysteresis is considered in the dynamical model used in place of the actuator. As previously stated in the section, magnetic hysteresis is problematic when using the inductance estimation method, mainly because this variable is not defined when the current is equal to zero. Thus, the conclusion is that this approach should not be considered for reluctance actuators where the effects of magnetic hysteresis are not negligible.

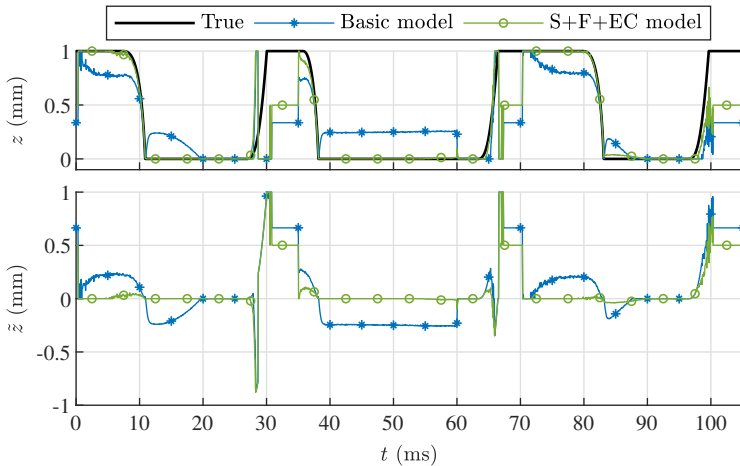


Figure 6.10: Position estimation via inductance estimation. True value and estimates (top) and estimation errors (bottom).

Secondly, Fig. 6.11 shows the results that correspond to the method based on flux linkage estimations. In this case, it can be seen that the qualitative behavior of the position estimate is in accordance with the dynamics of the actuator, which results from the use of a mechanical model in the observer. As a consequence, the RMSEs of the estimations are lower than in the case of using the inductance method: 0.190 mm for

the basic model (-41%) and 0.078 mm for the S+F+EC model (-67%). The maximum absolute errors are also smaller: 0.811 mm for the basic model and 0.662 mm for the S+F+EC model. It should be recalled that, in this case, the only difference between both models is the expression used to estimate the magnetic force. Since the S+F+EC model uses the same expression than the complete model, its corresponding position estimate is better than that of the basic model, which is affected by modeling errors. In any case, note that both observers are affected by flux linkage estimation errors, particularly for times between 25 and 30 ms, and also between 60 and 65 ms (see $\hat{\lambda}$ in Fig. 6.9).

Finally, the results from the method based on electric current measurements are presented in Fig. 6.12. Similarly to the case of the flux approach, the behavior of the position estimates in this case is also consistent with the motion dynamics. The estimation RMSEs are 0.297 mm for the basic model and 0.177 mm for the S+F+EC model, and the maximum absolute errors are respectively 1 mm and 0.872 mm. Thus, the estimation performance of this method is in all the cases between the two other approaches. Since the only difference with respect to the flux approach is the origin of the flux estimate, it can be concluded that it is better to estimate the flux by means of the SEMERA algorithm rather than using the method of Subsection 6.2.3. The results of the S+F+EC observer are better than those of the basic observer for the reasons already discussed in the previous paragraph.

The main estimation results obtained for the three approaches and the two models when using the nominal parameters are shown for comparison in Table 6.9. These results show that, assuming that the observer model uses the parameters that best fit to the actuator, the best approach to estimate the armature position is to combine the flux linkage estimation from the SEMERA algorithm and a mechanical model of the system. Besides, it is also shown that the estimations are better the more precise is the model used by the estimator. In this regard, the estimates obtained using the S+F+EC model are between 25% and 60% better than those of the basic model. Nevertheless, the maximum absolute errors achieved by the estimators—greater than half the armature travel—show that these techniques are still far from being used for control purposes, at least in reluctance actuators where magnetic hysteresis is not negligible.

Finally, the robustness of the three approaches and the two models against parameter uncertainty has been also analyzed. For that purpose, two different Monte Carlo analyses have been performed varying the values of the parameters used in the estimation. With the exception of z_{\min} and z_{\max} , all the parameters of Tables 6.7 and 6.8 have been perturbed according to normal distributions centered at the nominal values. The two analyses correspond to standard deviations of 1% and 5%. The results are respectively presented in Tables 6.10 and 6.11. It can be seen that, despite the relatively low accuracy of the estimators, they are in general robust. For both analyses, the mean RMSE of ten thousand perturbed simulations is only slightly greater than the RMSE of the nominal case. There are, however, certain combinations of parameters that result in much bigger errors. This is indicated in the tables by the maximum RMSE, which represents the worst-case situations found in the analyses for each approach and estimation model. As a final remark, note that the best position estimation method for the two analyses is still the same than that for the nominal situation: estimate the flux using the SEMERA algorithm and then estimate the position using a mechanical model.

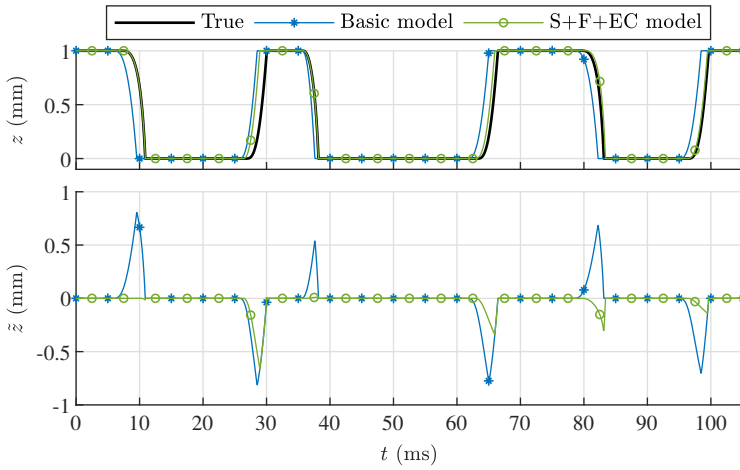


Figure 6.11: Position estimation via flux linkage estimation. True value and estimates (top) and estimation errors (bottom).

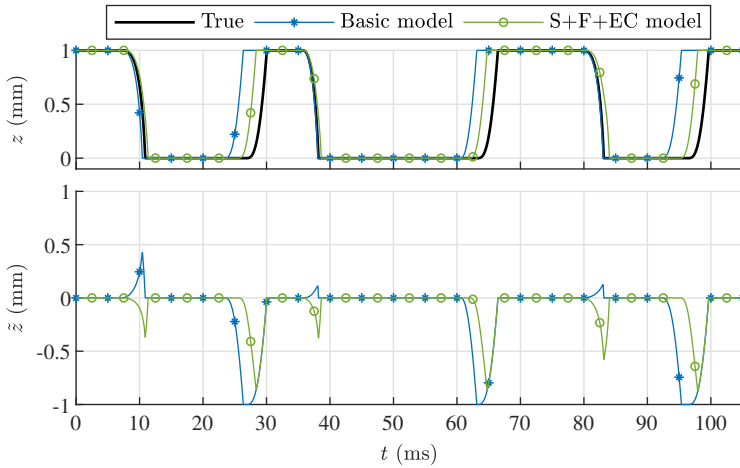


Figure 6.12: Position estimation via current measurements. True value and estimates (top) and estimation errors (bottom).

Table 6.9: Position estimation errors obtained for the three estimation approaches and the two dynamical models when using the nominal sets of parameters. Root-mean-square errors (RMSE) and maximum absolute errors (MaxAE). Units in millimeters.

Nominal parameters		Estimation method		
		Inductance	Flux	Current
Basic model	RMSE	0.322	0.190	0.297
	MaxAE	1	0.811	1
S+F+EC model	RMSE	0.234	0.078	0.177
	MaxAE	1	0.662	0.872

Table 6.10: Position estimation errors obtained for the three estimation approaches and the two dynamical models when considering a 1% standard deviation in the parameters. Results from 10,000 Monte Carlo simulations. Mean root-mean-square errors (MRMSE) and maximum root-mean-square errors (MaxRMSE). Units in millimeters.

1% Perturbed parameters		Estimation method		
		Inductance	Flux	Current
Basic model	MRMSE	0.322	0.190	0.297
	MaxRMSE	0.329	0.194	0.299
S+F+EC model	MRMSE	0.234	0.078	0.178
	MaxRMSE	0.242	0.088	0.195

Table 6.11: Position estimation errors obtained for the three estimation approaches and the two dynamical models when considering a 5% standard deviation in the parameters. Results from 10,000 Monte Carlo simulations. Mean root-mean-square errors (MRMSE) and maximum root-mean-square errors (MaxRMSE). Units in millimeters.

5% Perturbed parameters		Estimation method		
		Inductance	Flux	Current
Basic model	MRMSE	0.325	0.191	0.299
	MaxRMSE	0.373	0.212	0.342
S+F+EC model	MRMSE	0.239	0.083	0.187
	MaxRMSE	0.287	0.140	0.454

Chapter 7

Run-to-Run Control

In a previous chapter it has been shown that feedback control may be an effective method to achieve soft landing in reluctance actuators provided that real-time measurements or estimates of the position are available. Nevertheless, the cost of the instruments required to measure the position and the accuracy of the estimators presented in this thesis motivate the search for alternative solutions. This chapter explores the applicability of Run-to-Run control methods to switch-type reluctance actuators. This class of techniques, which is specifically designed for systems that operate in a repetitive manner, use measurements obtained in previous repetitions to gradually improve the performance of the system. In the chapter, the theoretical fundamentals of Run-to-Run control are first introduced. Then, the particularities of the algorithms designed for reluctance actuators are presented and discussed. Experimental results are included to show the applicability of the proposal and some convergence-related issues are also discussed.

7.1 Problem formulation and solution method

Dynamic optimization of reluctance actuators

The control problem is addressed in this chapter as a dynamic optimization problem. In this regard, note that reluctance actuators are dynamical systems driven by a voltage input. Different voltage waveforms lead to different operations with different results. The ultimate objective of the problem presented in this thesis is to find the voltage waveform that minimizes a function of the final state and/or the path followed by the system during its operation, e.g., the impact velocity, the bounce duration, the acoustic energy or the switching time. For that purpose, two different approaches have been already presented in Chapter 5, one based on the design of a soft-landing trajectory that is tracked by the actuator using a feedback controller (see Section 5.2) and another one based on the solution of the dynamic optimization problem for a nominal system (see Section 5.3).

A distinctive feature of the solution presented in this chapter is that it benefits from the fact that switch-type reluctance actuators work in a repetitive manner, i.e., they always

perform the same operations with the same objectives: closing and opening the air gap. Hence, the control problem must be solved for each and every repetition of the process. In addition, it has been shown in Chapter 4 that some variables can be measured during the operation, so the problem falls into the field of measurement-based optimization. Thus, assuming that measurements from previous operations can be stored and used to take decisions in the current one, the control problem may be generally formulated as

$$\underset{t_{f_i}, u_i([t, t_{f_i}])}{\text{minimize}} \quad J_i = G(x_i(t_{f_i})), \quad (7.1)$$

$$\text{subject to} \quad \dot{x}_i = f(x_i, u_i) + d_i, \quad (7.2)$$

$$x_i(t_{0_i}) = x_0, \quad (7.3)$$

$$y_i = h(x_i) + v_i, \quad (7.4)$$

$$S(u_i, x_i) \leq 0, \quad (7.5)$$

$$T(x_i(t_{f_i})) \leq 0, \quad (7.6)$$

$$\text{given} \quad \mathcal{Y}_i(t) = \{y_i(\tau) \mid t_{0_i} \leq \tau \leq t\}, \quad (7.7)$$

$$\{\mathcal{Y}_j(t_{f_j}) \mid j < i\}, \quad (7.8)$$

where the subscript i refers to the i th repetition of the process, J is the scalar variable to minimize, G is the cost function, t_0 and t_f are respectively the initial and final times, u is the input, x is the state, f is a (not necessarily continuous) map, d is an additive disturbance, x_0 is the initial state, y is the measured output, $\mathcal{Y}(t)$ is the set of measurements up to time t , h is the output function, v is the measurement additive noise and S and T are functions that define, respectively, path and final state constraints. Note that (7.1) defines a cost that only depends on the final state. Nevertheless, if the scalar variable to minimize depends also on the path followed, this formulation can still be used by applying a simple transformation [176].

Looking for a solution: the Run-to-Run approach

As seen in the previous chapters, several strategies can be considered to solve the problem. However, the repetitive operating nature of switch-type reluctance actuators encourages the search for a different approach. This particular feature enables the operation of these devices to be analyzed as a batch process [177] and, together with the possibility of measuring some variables of the system, permits the use of certain learning-type control techniques [178].

In particular, this thesis explores the so-called Run-to-Run (R2R) algorithms [179], a class of techniques that have been mostly used in the semiconductor industry to control the silicon wafer manufacturing process [180]. In addition, they have been also utilized in the chemical industry [181] and, more recently, with medical purposes [182], obtaining satisfactory results in both fields. R2R techniques are especially indicated for systems that perform a process in a repetitive mode and only permit off-line measurements. As Srinivasan et al. explain in [177], off-line measurements include not only measurements taken at the end of the process but also variables obtained by post-processing experimental data recorded during the operation. This latter is the case of switch-type reluctance

devices, because some of their interest variables, e.g., the bounce duration or the total acoustic energy, cannot be known until the operation has completely finished.

In the literature, R2R strategies are classified as explicit or implicit depending on whether they use or not a dynamical model of the system [177]. In this regard, selecting either an explicit or an implicit method depends greatly on the possibility of finding an accurate parametric model for the maps f and h . When this is possible, explicit methods use measurements to adjust the parameters of the model at the end of each operation. Then, the optimal input profile is computed as explained in Section 5.3 and implemented in open-loop. On the other hand, implicit R2R algorithms combine measurements and optimization methods—generally direct search methods [183]—to guide the system behavior towards an optimum without need of a dynamical model. This second option is explored in this part of the thesis for its flexibility to be applied to different actuators and also for its ability to deal with some measurements, e.g., the noise generated by the actuator or the electrical contacts (see Section 4.1), which cannot be directly handled by explicit methods.

Although switch-type actuators always perform the same operations, their dynamic response may differ between repetitions due to the use of different input waveforms or because of external disturbances. When using a R2R direct method, all the controllable elements for each repetition of the process must be completely defined by a finite set of decision variables. Thus, a finite-dimensional decision vector for the i th operation, ν_i , can be built. This vector can be modified between operations but it is kept constant during each one. However, even though all the decision variables are determined prior to the next operation, this does not strictly require that the input be fully determined because closed-loop controllers may still exist to improve reference tracking and prevent from disturbances. Note that such implementation may benefit from the R2R algorithm by including the controller parameters in the decision vector. That way, both the reference profile and the control strategy can be optimized at once.

Additionally, the system performance is evaluated at the end of the process by means of a finite set of evaluation variables. Like the decision variables, the evaluation variables of the i th repetition are also grouped in a finite-dimensional evaluation vector ψ_i . When using an implicit R2R strategy, the cost to minimize needs to be directly calculated from the measurements and, generally, it is expressed as a function Γ of the evaluation vector. Assuming that ψ_i is assessed from the set of measurements \mathcal{Y}_i at the final time of the i th operation, t_{f_i} , the problem formulation including the implicit R2R strategy becomes

$$\underset{\nu_i}{\text{minimize}} \quad J_i = \Gamma(\psi_i), \quad (7.9)$$

$$\text{subject to} \quad (7.2)\text{--}(7.6),$$

$$r_i = V(t, \nu_i), \quad (7.10)$$

$$u_i = K(r_i, y_i, \nu_i), \quad (7.11)$$

$$t_{f_i} = L(\nu_i), \quad (7.12)$$

$$\psi_i = W(\mathcal{Y}_i(t_{f_i})), \quad (7.13)$$

$$\text{given} \quad (7.8),$$

where r is the reference signal, defined by the function V , K is the feedback law, L is

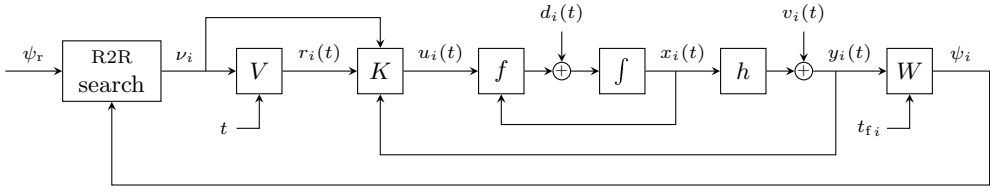


Figure 7.1: Implicit R2R control loop. The input of the plant for the i th operation, $u_i(t)$, is calculated by the closed-loop control law, K , while the reference, $r_i(t)$, and the controller parameters are set by the R2R algorithm.

the function that defines the final time and W is the evaluation function. As a complete overview, Fig. 7.1 depicts the block diagram of a dynamical system controlled by an implicit R2R method.

Despite the temporal dynamics of the system, the distinctive feature of implicit R2R methods is that they analyze the process as a non-dynamical black-box system whose input and output are, respectively, the decision and evaluation vectors. Thus, from the point of view of the R2R algorithm, the problem is directly faced as

$$\underset{\nu_i}{\text{minimize}} \quad J_i = \Gamma(\psi_i), \quad (7.14)$$

$$\text{subject to} \quad \psi_i = \mathcal{F}(\nu_i) + \mu_i, \quad (7.15)$$

$$\text{given} \quad \{\nu_j \mid j < i\}, \quad (7.16)$$

$$\{\psi_j \mid j < i\}, \quad (7.17)$$

where \mathcal{F} is an unknown function that relates the decision and evaluation vectors and μ_i is a variable that includes the effects of disturbances and measurement noise during the i th operation. Note that the structure of \mathcal{F} is not given to the R2R algorithm, but it can be experimentally evaluated because it is actually defined by (7.2)–(7.4) and (7.10)–(7.13).

Although the problem (7.14)–(7.17) is posed from the perspective of optimization theory, the R2R approach is also suitable for control purposes only by selecting a proper cost function. Hence, if the goal is for the evaluation vector to reach a reference value ψ_r , costs of the type $J_i = \|\psi_i - \psi_r\|_p$, where $\|\cdot\|_p$ means p -norm, may then be defined.

Particularities of Run-to-Run methods on switch-type reluctance actuators

The particular features of reluctance actuators have to be taken into account when applying a R2R method. The main difference with respect to other processes where R2R control has been applied is that these devices do not perform a single repetitive process but two: the *making* or *closing* process and the *breaking* or *opening* process. Excluding special devices, every switch-type reluctance device performs these two tasks: making when the coil is energized and breaking when it is de-energized. The operation may then be controlled by a single R2R algorithm or, more interestingly, by two separated but coordinated algorithms that optimize the two processes independently.

Note however that making and breaking follow one another and are not completely independent because the initial conditions of the one match exactly the final state of the

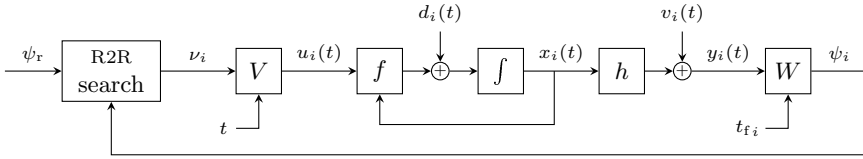


Figure 7.2: Implicit R2R control loop without a continuous closed-loop controller. The input of the plant for the i th operation, $u_i(t)$, is completely defined by the R2R algorithm.

other. Given that the initial state is assumed to be constant [see (7.3)], in this particular case it should be also guaranteed that the final state of the two processes be constant or at least nearly constant. In this way, both operations are made independent and the performance of the algorithm is likely to improve. For clarity purposes, the subscripts “m” and “b” are used in this and the following sections to refer to the variables and functions specific to the making and breaking parts of the method. The variables with no “m” or “b” are used equally by the two parts.

Additionally, although closed-loop controllers may be included in the R2R loop (see K in Fig. 7.1) and their parameters added to the decision vector, in this thesis only the case where no such type of controller exists is analyzed, i.e.,

$$K(r_i, y_i, \nu_i) = r_i \iff u_i(t) = V(t, \nu_i). \quad (7.18)$$

This configuration (see Fig. 7.2) implies that the input of the i th operation, $u_i(t)$, is fully defined by the decision vector ν_i . The actuator has consequently no feedback during each operation but only between them, hence not being able to reject random disturbances. However, since the usual disturbances of this class of actuators, i.e., changes in ambient temperature or mechanical wear [168], have very low dynamics compared to the one of the device, the algorithm will deal with them by modifying the input profile between repetitions. One of the advantages of this implementation is that few real-time calculations are needed, thus permitting the use of low-cost microcontrollers.

All the R2R methods designed for reluctance actuators require the following functions:

- V_m and V_b , which define the input vectors of the i th making and the i th breaking operations, $u_{m_i}(t)$ and $u_{b_i}(t)$, as functions of the corresponding decision vectors, $\nu_{m_i} \in \mathbb{R}^{n_m}$ and $\nu_{b_i} \in \mathbb{R}^{n_b}$.

$$u_{m_i}(t) = V_m(t, \nu_{m_i}) \quad u_{b_i}(t) = V_b(t, \nu_{b_i}) \quad (7.19)$$

As explained before, the algorithm needs the initial and final states of both making and breaking to be as constant as possible. For this reason, it is recommended that each input vector be composed of two temporal stages. First, a transient stage which depends on the decision vector and changes between operations, thus permitting the system to follow different paths and resulting in different evaluation vectors. And secondly, a constant stage not depending on the decision vector, always of the same value and being long enough so that the system can reach a steady state.

- W_m and W_b , which define the evaluation vectors of the i th making and the i th breaking processes, ψ_{m_i} and ψ_{b_i} , as functions of the measurements recorded during

the corresponding operations, $\mathcal{Y}_{m_i}(t_{fm_i})$ and $\mathcal{Y}_{b_i}(t_{fb_i})$.

$$\psi_{m_i} = W_m(\mathcal{Y}_{m_i}(t_{fm_i})) \quad \psi_{b_i} = W_b(\mathcal{Y}_{b_i}(t_{fb_i})) \quad (7.20)$$

- Γ_m and Γ_b , which define, respectively, the costs J_{m_i} and J_{b_i} of the i th making and the i th breaking of the system.

$$J_{m_i} = \Gamma_m(\psi_{m_i}) \quad J_{b_i} = \Gamma_b(\psi_{b_i}) \quad (7.21)$$

Algorithm

The sequence of operations described in Algorithm 7.1 is the basis of all the R2R methods presented in the chapter. In this algorithm, \mathcal{V}_{m_i} and \mathcal{V}_{b_i} are sets that contain all the decision vectors evaluated up to the i th repetition of the process,

$$\mathcal{V}_{m_i} = \{\nu_{m_j} \mid j \leq i\}, \quad \mathcal{V}_{b_i} = \{\nu_{b_j} \mid j \leq i\}, \quad (7.22)$$

and \mathcal{J}_{m_i} and \mathcal{J}_{b_i} contain the costs obtained as a result of the application of these decision vectors,

$$\mathcal{J}_{m_i} = \{J_{m_j} \mid j \leq i\}, \quad \mathcal{J}_{b_i} = \{J_{b_j} \mid j \leq i\}. \quad (7.23)$$

In addition, Θ_m and Θ_b are the sets of parameters used respectively by the making and breaking SEARCH algorithms. Together with the previously described functions, the selection of the search algorithm is one of the aspects that most influence the performance of the R2R method, particularly with regard to the rate of convergence. Further aspects of the search algorithm are discussed later in the chapter.

As shown, the R2R algorithm contains an infinite loop that is repeated every time the actuator is activated and deactivated during its normal operation. The sequence of operations is as follows. The decision vector for the next making process is prepared and added to the history of the search. When a making command is received from an upper level controller, the MAKE function is invoked. This function (see Algorithm 7.2) supplies the actuator with the input profile defined by the decision vector and, at the same time, records the available measurements. Then, the performance of the making operation is evaluated by computing the evaluation vector and the cost J_m . Back to the main thread, the making cost is stored in memory. Then, the algorithm jumps to the operations that correspond to the breaking process, which follow a completely equivalent sequence. The decision vector for the breaking is firstly obtained from the search algorithm and stored in memory, the BREAK function is invoked (see Algorithm 7.3) and, finally, the cost of the breaking operation, J_b , is incorporated to the history of the search.

It must be emphasized that the R2R loop does not stop when a predefined condition is satisfied—as optimization methods do—but it is designed to be endlessly executed during the normal operation of the device. Given that the search for a better performance does not finish at some certain point, the proposed strategy is able to adapt the activation signal when the system dynamics changes due to wear, deformations or temperature changes, among others. In essence, this is the feature that provides the robustness of implicit R2R methods with respect to nominal solutions.

Algorithm 7.1 Reluctance actuator R2R loop

Require: $\mathcal{V}_{m0}, \mathcal{V}_{b0}, \mathcal{J}_{m0}, \mathcal{J}_{b0}, \Theta_m, \Theta_b$

```

1:  $i := 0$ ;
2: loop
3:    $\nu_{mi+1} := \text{SEARCH}(i, \mathcal{V}_{mi}, \mathcal{J}_{mi}, \Theta_m)$ ;           ▷ Find the next making point
4:    $\mathcal{V}_{mi+1} := \mathcal{V}_{mi} \cup \{\nu_{mi+1}\}$ ;                       ▷ Add point to history
5:   Wait for making order;
6:    $J_{mi+1} := \text{MAKE}(\nu_{mi+1})$ ;                               ▷ Make
7:    $\mathcal{J}_{mi+1} := \mathcal{J}_{mi} \cup \{J_{mi+1}\}$ ;                     ▷ Add cost to history
8:    $\nu_{bi+1} := \text{SEARCH}(i, \mathcal{V}_{bi}, \mathcal{J}_{bi}, \Theta_b)$ ;       ▷ Find the next breaking point
9:    $\mathcal{V}_{bi+1} := \mathcal{V}_{bi} \cup \{\nu_{bi+1}\}$ ;                   ▷ Add point to history
10:  Wait for breaking order;
11:   $J_{bi+1} := \text{BREAK}(\nu_{bi+1})$ ;                               ▷ Break
12:   $\mathcal{J}_{bi+1} := \mathcal{J}_{bi} \cup \{J_{bi+1}\}$ ;                     ▷ Add cost to history
13:   $i := i + 1$ ;
14: end loop

```

Algorithm 7.2 Making Function

```

1: function MAKE( $\nu_m$ )
2:    $u_m(t) := V_m(t, \nu_m)$ ;                                   ▷ Prepare input
3:   Apply  $u_m(t)$  and register  $y_m(t)$ ;
4:    $\psi_m := W_m(\mathcal{Y}_m(t_{fm}))$ ;                               ▷ Evaluate output
5:    $J_m := \Gamma_m(\psi_m)$ ;                                   ▷ Compute cost
6:   return  $J_m$ 
7: end function

```

Algorithm 7.3 Breaking Function

```

1: function BREAK( $\nu_b$ )
2:    $u_b(t) := V_b(t, \nu_b)$ ;                                   ▷ Prepare input
3:   Apply  $u_b(t)$  and register  $y_b(t)$ ;
4:    $\psi_b := W_b(\mathcal{Y}_b(t_{fb}))$ ;                               ▷ Evaluate output
5:    $J_b := \Gamma_b(\psi_b)$ ;                                   ▷ Compute cost
6:   return  $J_b$ 
7: end function

```

7.2 Design of the Run-to-Run controller

As stated in the previous section, implicit R2R methods can be divided into three different parts: the definition and parameterization of the input profile, the evaluation of the output measurements and the search algorithm. Considering the large number of options that exist for each of these elements, the possibilities to design a R2R algorithm are almost endless. In this section, some particular choices—two input profiles, two evaluation variables and a search algorithm—are proposed with the aim of building a R2R controller for reluctance actuators.

7.2.1 Input definition and output evaluation

When using an implicit R2R method, the performance of the system during a specific operation is evaluated by a cost function that depends on the evaluation variables. Consequently, the definition of these variables and the cost function itself determine the desired dynamic behavior at which the R2R algorithm should aim. In this regard, the best possible performance of a given dynamical system is always limited by the input constraints. In an implicit R2R method, this translates into the definition of the nominal input profile and the parameterization used to modify that profile. In this part of the section, two evaluation variables and two different input profiles are presented to control the dynamic behavior of reluctance actuators.

With the purpose of obtaining an implementation as simple as possible, the digital electronic circuit of Fig. 7.3 is proposed to activate the actuator. Two transistors and a resistor network permit the system to be controlled by a digital activation signal, $a(t)$. A coil suppression circuit is included in the network to prevent from voltage spikes when the voltage is cut off. This part of the circuit can be configured as a single free-wheeling diode (Configuration 1) or as a diode in series with a Zener diode (Configuration 2). Although simple, this activation circuit is able to generate voltage and current profiles with the same features than the time-optimal soft-landing strategies obtained in Section 5.3 (see Fig. 7.4). When it is activated, the supply voltage V_{dc} is directly applied to the actuator and both the magnetic flux and the current increase until a steady state is reached. Then, if the transistor is cut off, the suppression circuit forces the current to decrease according to the characteristic curves of the diodes. Finally, if the current drops down to zero, the diodes stop conducting and the current remains at zero until the circuit is again activated.

Besides the voltage across the coil, $v(t)$, which can be directly measured, a shunt resistor R_s permits the measuring of the coil current $i(t)$. In addition, a low-cost microphone is also included in the setup to measure the noise generated by the actuator during the switching operations (see Subsection 4.1.3). In the case that the device to be controlled is a relay, the measurements of the electrical contacts (see Subsection 4.1.1) are also recorded. According to the system described, the input and output vectors to be used by the R2R algorithm can thus be defined as

$$u(t) = a(t), \quad y(t) = [v(t) \quad i(t) \quad v_{mic}(t) \quad NC(t) \quad NO(t)]^T, \quad (7.24)$$

where v_{mic} is the voltage signal from the microphone and $NC(t)$ and $NO(t)$ are, respectively, the signals obtained from the normally closed and the normally open contacts.

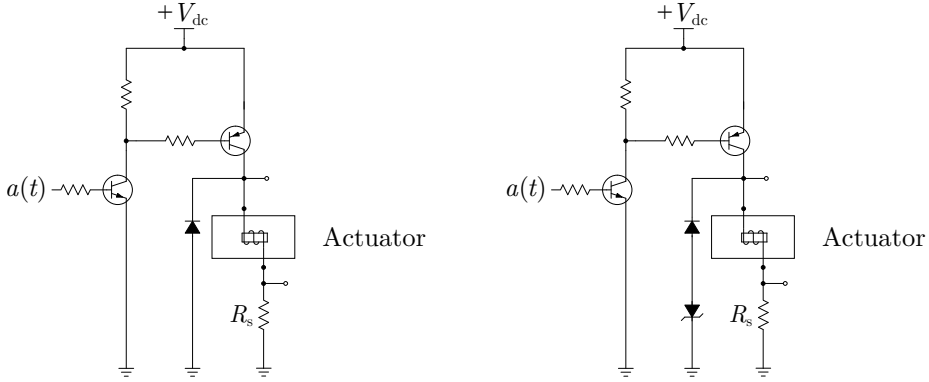


Figure 7.3: Activation circuit diagram. Configuration 1 (left) and Configuration 2 (right). The circuit is controlled by the digital signal $a(t)$.

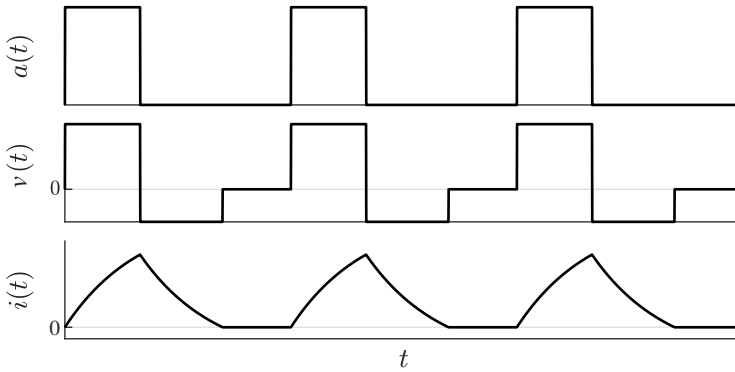
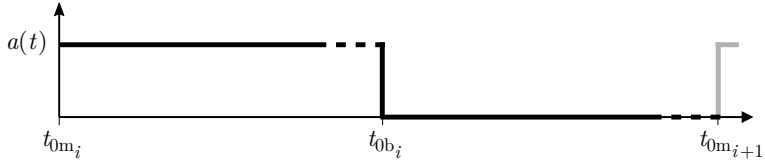


Figure 7.4: Typical voltage and current profiles generated by the activation circuit.

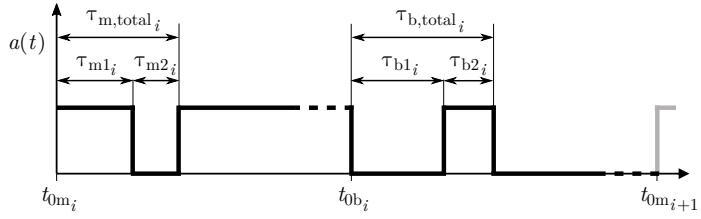
As explained in the previous section, the algorithms presented in this chapter do not include a classical closed-loop controller, i.e., the inputs of the system for the i th making and the subsequent breaking, $u_{mi}(t)$ and $u_{bi}(t)$, need to be completely described by the functions V_m and V_b according to the decision vectors ν_{mi} and ν_{bi} . Considering the system under study, this means that it is necessary to define the time-dependent making and breaking profiles for signal $a(t)$, which is the only input, as well as the parameterization of these profiles according to two sets of decision variables.

Since the performance of the whole control strategy depends greatly on the selection of these profiles, two different alternatives are proposed to provide a more comprehensive analysis. Both are based on the square wave signal standardly used to activate commercial switch-type devices (see Fig. 7.5a). The signal profile of type A (see Fig. 7.5b), which is the simplest variant of the standard signal, depends on two decision variables for the making and another two for the breaking. Hence, the decision vectors when using this type of signal are defined as

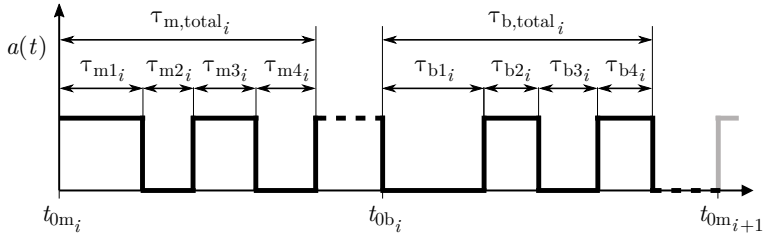
$$\nu_m = [\tau_{m1} \quad \tau_{m2}]^T, \quad \nu_b = [\tau_{b1} \quad \tau_{b2}]^T. \quad (7.25)$$



(a) Standard square-wave signal used to activate switch-type devices. The i th making and breaking processes begin, respectively, at times t_{0m_i} and t_{0b_i} .



(b) Type A signal profile. The i th making signal begins at time t_{0m_i} and is parameterized by τ_{m1_i} and τ_{m2_i} . The i th breaking begins at time t_{0b_i} and is defined by τ_{b1_i} and τ_{b2_i} .



(c) Type B signal profile. The i th making signal begins at time t_{0m_i} and is parameterized by τ_{m1_i} , τ_{m2_i} , τ_{m3_i} and τ_{m4_i} . The i th breaking begins at time t_{0b_i} and is defined by τ_{b1_i} , τ_{b2_i} , τ_{b3_i} and τ_{b4_i} .

Figure 7.5: Activation signals.

On the other hand, the type B signal profile (see Fig. 7.5c), which is more flexible, is described by four decision variables for the making and another four for the breaking. In this case, the four-dimensional decision vectors are defined as

$$\nu_m = [\tau_{m1} \quad \tau_{m2} \quad \tau_{m3} \quad \tau_{m4}]^T, \quad \nu_b = [\tau_{b1} \quad \tau_{b2} \quad \tau_{b3} \quad \tau_{b4}]^T. \quad (7.26)$$

Note that both types of signals, either for making or for breaking, are characterized by two temporal stages which correspond to those described in the previous section. Firstly, an adjustable and transient stage which lasts $\tau_{m,total_i}$ for the i th making and $\tau_{b,total_i}$ for the complementary breaking. And secondly, a constant stage which lasts indefinitely until the subsequent process is started. Recall that these constant stages ensure that the final state of each making or breaking and, consequently, the initial state of the following process, has always a similar value. Furthermore, considering the system dynamics (see Subsection 5.1.1), they are also necessary to guarantee that the actuator reaches and maintains the desired final position.

With regard to the outputs, two different evaluation variables are proposed in this

thesis: one linked to the noise measurements and another one obtained, if applicable, from the measurements of the electrical contacts. The noise generated by the actuator during a making or breaking operation, which can always be measured, is respectively rated by the variables ρ_m or ρ_b . These are defined as the integrals of the squared value of the microphone signal during the corresponding operations, i.e.,

$$\rho_m = \int_{t_{0m}}^{t_{m,\text{total}}+\Delta} v_{\text{mic}}^2 dt, \quad \rho_b = \int_{t_{0b}}^{t_{b,\text{total}}+\Delta} v_{\text{mic}}^2 dt, \quad (7.27)$$

where Δ is a small amount of time used to account for noise propagation delays. On the other hand, assuming that the device to be controlled is a relay, the measurements of the electrical contacts can also be used by the R2R algorithm. In particular, the bounce duration at the end of the making movement, β_m , and its equivalent for the breaking operation, β_b , are proposed as complementary evaluation variables. Whereas the bounces at the end of the making process can be assessed from the signal of the normally open contact, the bounce duration during the breaking operation can be calculated from the normally closed connection (see Fig. 7.6). The evaluation vectors proposed for the two processes are therefore

$$\psi_m = [\rho_m \quad \beta_m]^T, \quad \psi_b = [\rho_b \quad \beta_b]^T. \quad (7.28)$$

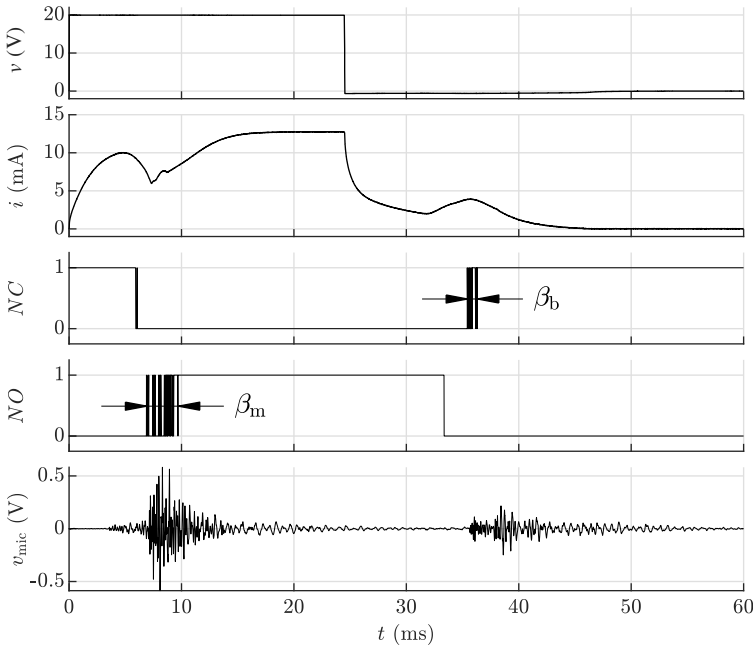


Figure 7.6: Measurements obtained from a power relay in a standard activation-deactivation cycle. The bounce duration can be assessed from the electrical contacts.

7.2.2 Search algorithm

Whereas the selection of the evaluation variables and the definition of the input profiles determine the best possible performance that the system can achieve in a single operation, the search algorithm is the element that guides the R2R search towards the optimum. Although similar, the difference between R2R search algorithms and optimization algorithms is that the former do not have any stopping criterion because they are designed to run endlessly. As already stated, this is the feature that allows R2R methods to adapt to changes in the system due, e.g., to wear or temperature variations, rather than always using a nominal solution.

In essence, any optimization algorithm can be modified to work as a search algorithm. However, gradient based optimization methods are generally not very well suited to R2R control for two different reasons. Firstly, there is no guarantee that the cost function is convex, which will probably cause the algorithm to get stuck in a local minimum. An secondly, the dynamic response of the system for a given decision vector may differ between repetitions due to external disturbances, which results in a non-deterministic behavior of the cost function and, probably, in errors when computing the gradient. For these reasons, derivative-free optimization algorithms are generally better choices to be used in the R2R field.

In this thesis, a direct search algorithm [183, 184] is proposed to guide the search of the R2R controller. The term “direct search” was coined by Hooke and Jeeves in the introduction to his 1961 paper: ‘We use the phrase “direct search” to describe sequential examination of trial solutions involving comparison of each trial solution with the “best” obtained up to that time together with a strategy for determining (as a function of earlier results) what the next trial solution will be.’ Presently, the term direct search is generally used to refer to any derivative-free optimization algorithm and, specifically, to those that do not base the selection of the next candidate solution on a response model that has been built using previous evaluations of the cost function.

In particular, the proposal presented in this chapter can be classified as a pattern search R2R algorithm [185]. It is influenced by the *Evolutionary Operation* described by Box in the 1950s [186], which consisted in introducing little deviations in the operation of a repetitive process to get more information of the system and, if possible, to improve its performance. The presented algorithm combines this concept with other features from present pattern search methods [187, 188] in order to achieve a better convergence. In addition, some features have been specifically designed and incorporated to the algorithm so that it is able to operate in a R2R context.

Considering the two operations performed by switch-type reluctance actuators, the parameters that control the behavior of this R2R search algorithm are the following:

- $M_m \in \mathbb{R}^{n_m \times p_m}$ and $M_b \in \mathbb{R}^{n_b \times p_b}$, meshes for the making and breaking algorithms. Their columns define the search directions around the current centroids, c_m and c_b . The candidate points for the next iteration of the algorithm are the columns of the matrices P_m and P_b , given by

$$P_m = 1_{p_m} \otimes c_m + \alpha_m M_m, \quad P_b = 1_{p_b} \otimes c_b + \alpha_b M_b, \quad (7.29)$$

where $1_{p_m} \in \mathbb{R}^{1 \times p_m}$ and $1_{p_b} \in \mathbb{R}^{1 \times p_b}$ are row vectors with all components equal to 1,

\otimes denotes the Kronecker product and $\alpha_m \in \mathbb{R}$ and $\alpha_b \in \mathbb{R}$ are the mesh size factors.

Given that the decision variables may have different dimensions and magnitudes, it is highly recommended to use scaled meshes. Given $\delta_m \in \mathbb{R}^{n_m}$ and $\delta_b \in \mathbb{R}^{n_b}$, vectors whose elements define characteristic ranges of the decision variables, several types of scaled meshes may be used, e.g., scaled- $2n$ -meshes,

$$M_m = [\text{diag}(\delta_m), -\text{diag}(\delta_m)], \quad M_b = [\text{diag}(\delta_b), -\text{diag}(\delta_b)], \quad (7.30)$$

or scaled- $n+1$ -meshes,

$$M_m = [\text{diag}(\delta_m), -\delta_m], \quad M_b = [\text{diag}(\delta_b), -\delta_b], \quad (7.31)$$

where $\text{diag}(\delta)$ is the square diagonal matrix with the elements of δ on the main diagonal.

- α_{m0} and α_{b0} , initial values of the mesh size factors.
- $\alpha_{m\min}$, $\alpha_{b\min}$, $\alpha_{m\max}$ and $\alpha_{b\max}$, minimum and maximum values of the mesh size factors.
- ϵ_m and ϵ_b , mesh expansion factors, which multiply the mesh size factors when a new point is found. In the case that no better solution is found in the iteration, the meshes are contracted by multiplying by $1/\epsilon_m$ or $1/\epsilon_b$.
- ν_{m0} and ν_{b0} , initial decision vectors.
- $\nu_{m\min}$, $\nu_{b\min}$, $\nu_{m\max}$ and $\nu_{b\max}$, lower and upper bounds for the decision vectors.

Algorithm 7.4 shows the set of instructions of the proposed R2R direct search function, which has been specifically designed to be used as the SEARCH function of the main R2R loop (see Algorithm 7.1). In this pseudocode, the operator $\text{ncols}(M)$ refers to the number of columns of the matrix M , $\text{col}(k, P)$ refers to the k th column of P and the saturation function, sat , is defined as

$$\text{sat}(x, a, b) = \begin{cases} a & \text{if } x < a, \\ x & \text{if } a \leq x \leq b, \\ b & \text{if } x > b. \end{cases} \quad (7.32)$$

In the first call to the function, all the variables used by the algorithm are initialized. A new set of candidate solutions—a poll, in the pattern search terminology—is created based on the initial centroid, the initial mesh size factor and the mesh. Then, one of the candidate points is returned each time the function is invoked. At the end of the poll, instead of moving directly to the best point found, the present centroid is re-evaluated in order to detect possible changes in the system. This is one of the features that has been incorporated to the algorithm to account for non-deterministic behaviors of the cost function. When a complete poll has been evaluated, a new one is created. If any of the points evaluated in the preceding poll is better than the centroid, the center of the new poll is updated and the mesh is expanded. On the other hand, if there is no improvement, the centroid is kept at the same position and the mesh is contracted.

Note that, contrary to pattern search optimization methods, which stop when the mesh size is smaller than a predefined value, this R2R search algorithm does not stop when $\alpha \leq \alpha_{\min}$. Instead, it saturates the size of the mesh to the minimum value and continues the search. The selection of α_{\min} is therefore a tradeoff between exploration and exploitation. Small values may lead to better solutions as the search moves forward, but the algorithm could get stuck if the exploration region becomes very small. On the contrary, big values of α_{\min} will cause the algorithm to avoid local minima and to detect changes in the system more easily, but the coarser discretization of the search space will probably lead to worse final solutions.

Algorithm 7.4 R2R direct search function

```

1: function SEARCH( $i, \mathcal{V}_i, \mathcal{J}_i, \{M, \alpha_0, \alpha_{\min}, \alpha_{\max}, \epsilon, \nu_0, \nu_{\min}, \nu_{\max}\}$ )
2: Internal:  $k, c, \alpha, p, P, new\_poll$  ▷ Internal variables
3:   if  $i = 0$  then ▷ Initialization (first operation)
4:      $c := \nu_0$ ; ▷ Poll centroid
5:      $\alpha := \alpha_0$ ; ▷ Mesh size factor
6:      $p := \text{ncols}(M)$ ; ▷ Poll size
7:      $P := 1_p \otimes c + \alpha M$ ; ▷ Poll candidates
8:      $k := 1$ ; ▷ Index of the next candidate
9:      $new\_poll := \text{false}$ ; ▷ New poll flag
10:  end if
11:  if  $new\_poll$  then ▷ If a new poll needs to be generated
12:    if  $\exists q \in [i - p, i - 1] : J_q < J_i$  then ▷ If there is an improvement
13:       $c := \nu_q$ ; ▷ Update centroid
14:       $\alpha := \text{sat}(\alpha \epsilon, \alpha_{\min}, \alpha_{\max})$ ; ▷ Expand mesh
15:    else ▷ If there is no improvement
16:       $\alpha := \text{sat}(\alpha / \epsilon, \alpha_{\min}, \alpha_{\max})$ ; ▷ Contract mesh
17:    end if
18:     $P := 1_p \otimes c + \alpha M$ ; ▷ New poll candidates
19:     $k := 1$ ; ▷ Index of the next candidate
20:     $new\_poll := \text{false}$ ;
21:  end if
22:  if  $k = p + 1$  then ▷ End of poll
23:     $\nu_{i+1} := c$ ; ▷ Re-evaluate centroid
24:     $new\_poll := \text{true}$ ; ▷ Activate new poll flag
25:  else ▷ Poll continues
26:     $\nu_{i+1} := \text{sat}(\text{col}(k, P), \nu_{\min}, \nu_{\max})$ ; ▷ Return candidate
27:     $k := k + 1$ ; ▷ Index of the next candidate
28:  end if
29:  return  $\nu_{i+1}$ ;
30: end function

```

7.3 Experimental results

Several experiments have been conducted to evaluate the performance of the R2R controller designed in the preceding section. The results presented in the following pages correspond to the application of the R2R algorithm to the power relay investigated in this thesis (see Section 1.4). For simplicity of the analysis, the costs of the making and breaking operations have been respectively defined as $J_m = \beta_m$ and $J_b = \beta_b$, i.e., the purpose of the algorithm in all the experiments is to reduce the bounce duration. The use of other cost functions is discussed in the following section.

Considering the two possible configurations of the activation circuit (see Fig. 7.3) and the two activation signals proposed (see Fig. 7.5), a total of four evaluations of the algorithm have been performed. In all of them, the supply voltage V_{dc} has been set to the nominal value of the relay, which is 24 V, and a 47 V Zener diode has been used in the tests when the circuit is in Configuration 2.


Some of the algorithm parameters used in the experiments—those related to the meshes—are independent of the activation signal used and equal for the making and breaking sub-algorithms. The meshes are initialized at the maximum size, i.e., $\alpha_{m0} = \alpha_{b0} = \alpha_{mmax} = \alpha_{bmax} = 1$, and may be reduced to minimum mesh size factors of $\alpha_{mmin} = \alpha_{bmin} = 2^{-10}$, approximately a thousandth of the original size. The mesh expansion factors are $\epsilon_m = \epsilon_b = 2$, which is a standard value in pattern search methods. On the other hand, the values of the parameters of the algorithm that are related to the decision vectors are different depending on which signal is used. These are presented in Table 7.1. The upper and lower bounds have been selected considering the characteristic times of a standard switching process (see Fig. 7.7) and providing sufficiently wide margins. The initial decision vectors have been defined as the midpoints between these bounds, and the characteristic range vectors have been selected as the distance between those points and each of the limits. Scaled- $2n$ -meshes have been used in this evaluation and, consequently, the making and breaking meshes when using the Type A and the Type B signals have, respectively $p_m = p_b = 4$ and $p_m = p_b = 8$ columns.

Table 7.1: Algorithm parameters used in the evaluation.

Parameter	Value (Signal A)	Value (Signal B)
ν_{mmin}	$[1 \ 0]^T$ ms	$[1 \ 0 \ 0 \ 0]^T$ ms
ν_{mmax}	$[7.5 \ 2.5]^T$ ms	$[7.5 \ 2.5 \ 2.5 \ 2.5]^T$ ms
ν_{m0}	$[4.25 \ 1.25]^T$ ms	$[4.25 \ 1.25 \ 1.25 \ 1.25]^T$ ms
δ_m	$[3.25 \ 1.25]^T$ ms	$[3.25 \ 1.25 \ 1.25 \ 1.25]^T$ ms
ν_{bmin}	$[2 \ 0]^T$ ms	$[2 \ 0 \ 0 \ 0]^T$ ms
ν_{bmax}	$[15 \ 5]^T$ ms	$[15 \ 5 \ 5 \ 5]^T$ ms
ν_{b0}	$[8.5 \ 2.5]^T$ ms	$[8.5 \ 2.5 \ 2.5 \ 2.5]^T$ ms
δ_b	$[6.5 \ 2.5]^T$ ms	$[6.5 \ 2.5 \ 2.5 \ 2.5]^T$ ms

Table 7.2 presents, for the two circuit configurations, the average contact bounce duration when applying the standard square wave signal and the best Type A and Type B signals found after 25 iterations of the search algorithm. Although the results may be improved if further iterations are performed, they show that the presented strategy is highly effective. The contact bounce reduction with respect to the standard activation, for both the making and breaking operations, is in all the cases above 70%. In some of them, it even reaches 90%, which is far superior to the results obtained by the state-of-the-art strategies [82].

Table 7.2: Contact bounce duration. Average results of 50 operations.

	Configuration 1		Configuration 2	
	Making	Breaking	Making	Breaking
	β_m (ms)	β_b (ms)	β_m (ms)	β_b (ms)
Square signal	1.791	3.228	1.792	4.576
Type A signal*	0.144	0.324	0.293	0.909
<i>Reduction</i>	<i>91.96%</i>	<i>89.97%</i>	<i>83.64%</i>	<i>80.13%</i>
Type B signal*	0.281	0.291	0.516	0.452
<i>Reduction</i>	<i>84.32%</i>	<i>90.97%</i>	<i>71.19%</i>	<i>90.12%</i>

*Best signal found, for each circuit configuration, in the first 25 iterations.

Figs. 7.8 and 7.9 show, for the circuit Configuration 1, a making and a breaking operation when applying, respectively, the best Type A and Type B signals. In these figures, the contact bounce reduction with respect to the standard activation (see Fig. 7.7) can be clearly seen. Additionally, the change in the values of the parameters can also be noticed. For instance, focusing on signal A, the initial parameters $\tau_{m1} = 4.25$ ms, $\tau_{m2} = 1.25$ ms, $\tau_{b1} = 8.5$ ms and $\tau_{b2} = 2.5$ ms, have at the end of the 25th iteration the values $\tau_{m1} = 3.69$ ms, $\tau_{m2} = 0.48$ ms, $\tau_{b1} = 7.85$ ms and $\tau_{b2} = 0.44$ ms. It must be noted, however, that contact bounce might be reduced at the expense of a longer switching time, as it happens with the Type B making signal (see Fig. 7.9).

The performance of the algorithm along the iterations has also been analyzed. Figs. 7.10 and 7.11 show the contact bounce duration of all the making and breaking operations carried out by the algorithm when using, respectively, the Type A and the Type B signals. Note that, as can be seen in Algorithm 7.4, the search method performs a total of $p + 1$ evaluations per iteration, i.e., 5 when using the Type A signal and 9 when using the Type B signal. As expected, the contact bounce duration for the best points (green lines) has a decreasing trend along the iterations, i.e., the algorithm works properly from the optimization perspective. More interesting is the fact that the average and the worst points (yellow and red lines, respectively) have also an improving trend. This means that the algorithm not only is able to find better points from one iteration to another, but also to move the complete set of points to better regions which, in addition, are increasingly closer to the optimum. In this respect, note that although some of the first operations have a long contact bounce duration, there exists an iteration from which all the making and breaking operations are better than the standard square wave activation (black horizontal

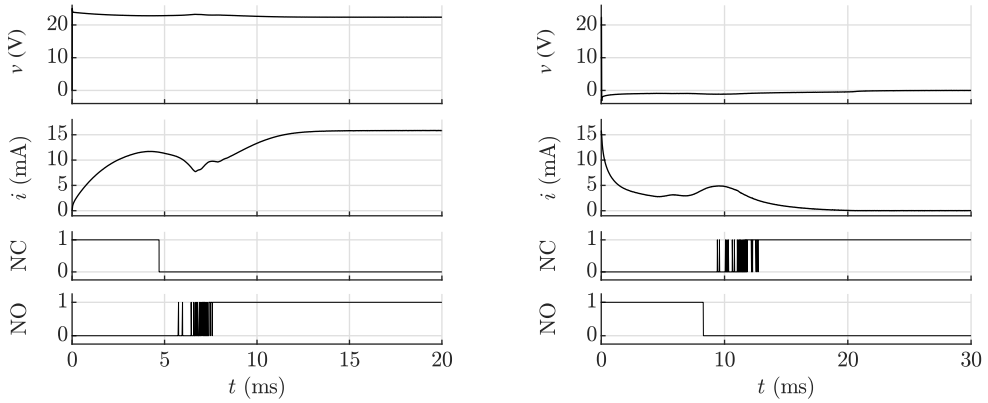


Figure 7.7: Standard square wave voltage making (left) and breaking (right) operations. Circuit Configuration 1.

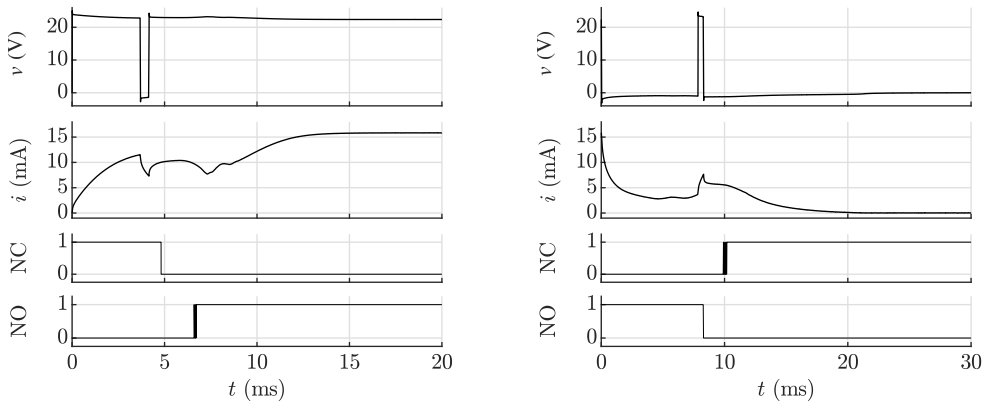


Figure 7.8: Type A activation signal. Best making (left) and breaking (right) operations found in 25 iterations of the algorithm. Circuit Configuration 1.

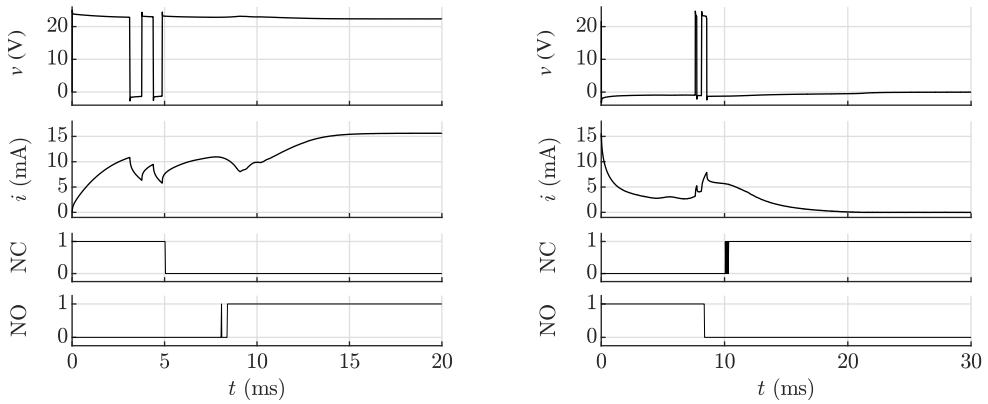


Figure 7.9: Type B activation signal. Best making (left) and breaking (right) operations found in 25 iterations of the algorithm. Circuit Configuration 1.

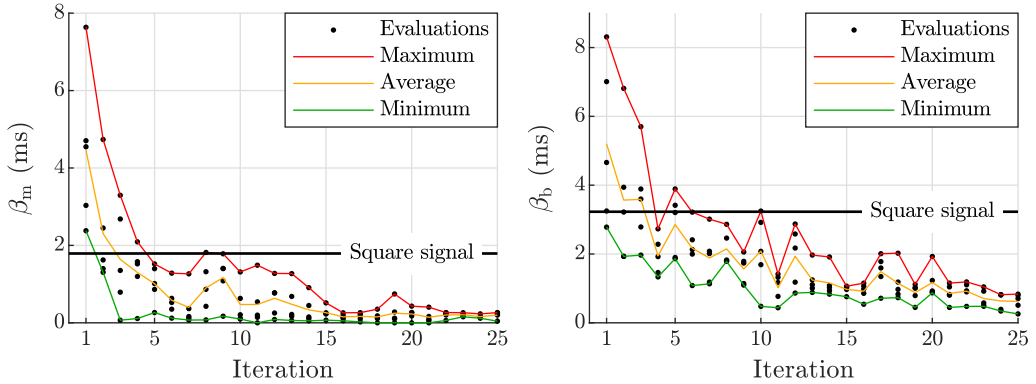


Figure 7.10: Type A activation signal. Contact bounce duration in all the evaluations performed by the algorithm during the first 25 iterations. Making (left) and breaking (right) operations. Circuit Configuration 1.

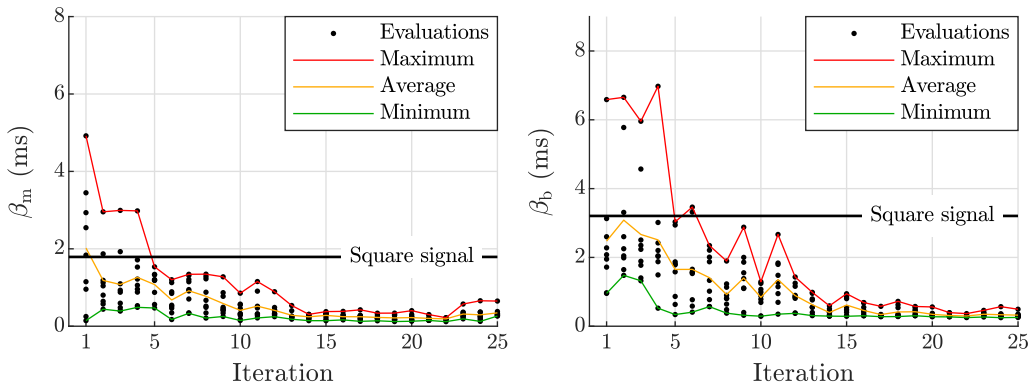


Figure 7.11: Type B activation signal. Contact bounce duration in all the evaluations performed by the algorithm during the first 25 iterations. Making (left) and breaking (right) operations. Circuit Configuration 1.

line). Besides, this initial stage may be reduced, or even eliminated, if the decision vectors are properly initialized, e.g., by using a nominal solution (see Section 5.3) or results from a previous laboratory execution of the algorithm.

A final issue is the choice of the best type of signal to reduce contact bounce. Although no one can be considered completely superior, each performs better in a particular aspect. On the one hand, the Type A signal, which is simpler and depends on less parameters, moves under the level of the square signal in less experimental evaluations. On the other hand, the Type B signal, which is more flexible but depends on more parameters, needs more evaluations but may potentially reach higher bounce reductions. Hence, there is a tradeoff between potential bounce reduction and speed of convergence and, thus, the selection of a particular signal will depend on the final application.

7.4 Discussion

The results presented in the previous section confirm that R2R control may be an effective strategy to improve the performance of switch-type reluctance actuators. In this connection, it has been shown that offline measurements from previous repetitions can be used, in a computationally inexpensive way, to guide the dynamic behavior of a given device towards a desired objective. In this section, some additional issues about the versatility and the convergence of implicit R2R controllers are further discussed.

7.4.1 Versatility

One of the main advantages of implicit R2R methods is their versatility. Since these algorithms do not use any dynamical model of the system, they can be easily adapted to work under different operating conditions. In fact, the proposed algorithm has proved to be able to reduce the bouncing duration in a power relay using two different activation signals and two different configurations of the activation circuit. Considering that the search algorithm does not stop when a good solution is found, but instead it always re-evaluates the current point and looks for better ones, it is expected that the R2R algorithm will also be able to adapt the activation signal when the system dynamics changes due, e.g., to wear, plastic deformations or temperature variations.

It is also true, however, that the experiments of the preceding section make use of the measurements of the electrical contacts, which are generally available in relays and contactors but not in other devices based on reluctance actuators such as solenoid valves. For that reason, additional experiments have been performed assuming that these measurements are not available. Given that in this case β_m and β_b cannot be used, the costs related to the breaking and making operations of the device have been redefined as $J_m = \rho_m$ and $J_b = \rho_b$. Recall that ρ_m and ρ_b are the variables that evaluate the acoustic noise generated by the actuator which, as shown in Subsection 4.1.3, is directly connected to the impacts of the moving components.

The results obtained in one of these experimental evaluations are shown in Figs. 7.12 and 7.13. In order to further highlight the versatility of the proposal, the presented results correspond to a different type of relay (note the differences in the voltage-current relation). Whereas the first of the figures shows the measurements from a standard square wave voltage activation, the second graph shows the results of the best making and breaking operations found in 25 iterations of the algorithm. Similarly to the results of the previous section, it can be seen that the algorithm is also effective in reducing the acoustic noise, especially in the breaking operation where the noise has almost vanished. The interesting point, however, is that the bounces have been also highly reduced, and this has been achieved using only the microphone measurements. Two main conclusions can be drawn from these results. First, that the presented R2R algorithm is highly versatile because it is able to operate under several different conditions, which includes different cost functions and even different devices. And secondly, that the audio signal from a low-cost microphone can be used to reduce the bouncing phenomenon in a switch-type device when other types of measurements are not available.

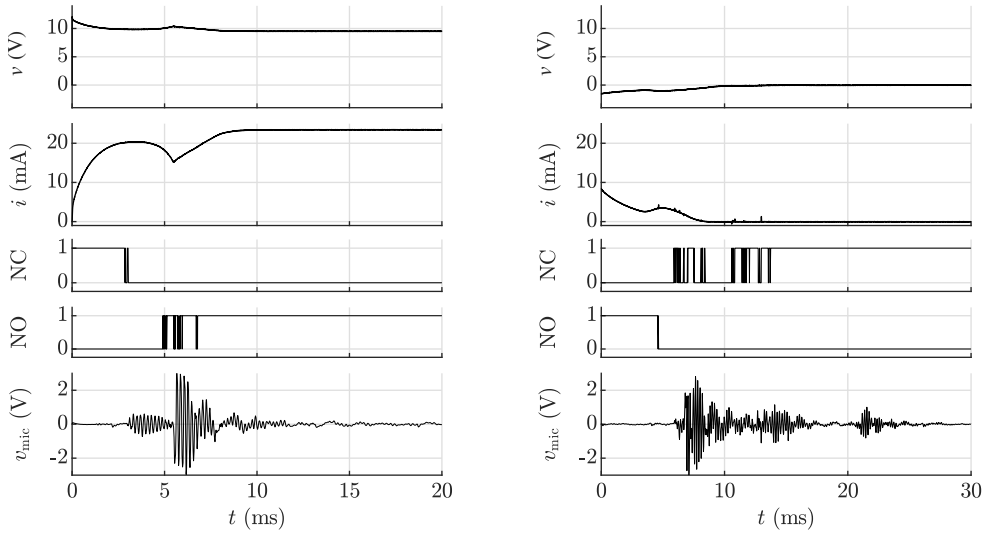


Figure 7.12: Standard square-wave making (left) and breaking (right) operations. Circuit Configuration 1.

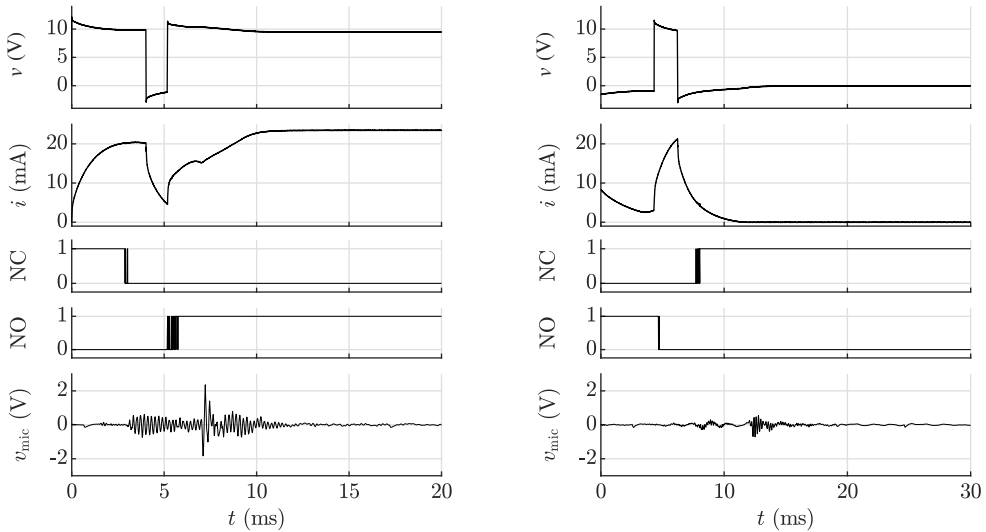


Figure 7.13: Type A activation signal. Best making (left) and breaking (right) operations found in 25 iterations of the algorithm. Circuit Configuration 1.

7.4.2 Convergence

Although implicit R2R methods are highly versatile because they do not use any model of the dynamical system, this feature may also represent a problem in terms of convergence. These methods rely on a search algorithm that has little prior information about the system and, thus, the only option to advance in the search is to perform experimental evaluations of each candidate solution. Considering that the cost function is generally not convex and, besides, that it may even have a non-deterministic behavior, the algorithm may take too many iterations to reach a solution near to the optimal one. In fact, it is very difficult to prove that the algorithm will converge to a minimum of the cost function, and even more to ensure that the solution found is the global optimum.

Given that each evaluation of the cost function represents an actual operation of the system, the most meaningful variable to compare different search algorithms is the average cost obtained up to certain repetition. In this respect, note that in a R2R application not only it is important to find a single good solution, but also the path of solutions found during the process. Considering a R2R controller for reluctance actuators, there are actually two different average costs, given by

$$\bar{J}_{mi} = \frac{1}{i} \sum_{j=1}^i J_{mj}, \quad \bar{J}_{bi} = \frac{1}{i} \sum_{j=1}^i J_{bj}, \quad (7.33)$$

where \bar{J}_{mi} and \bar{J}_{bi} are, respectively, the average costs of the making and breaking operations up to the i th repetition.

In order to illustrate how to analyze different search algorithms in terms of convergence, the direct search algorithm proposed in this thesis is compared with a surrogate-based search algorithm. Surrogate-based optimization [189, 190] refers to a class of algorithms specifically designed to optimize functions using as few evaluations as possible. This class of techniques has been generally used to optimize expensive objective functions, i.e., functions that take a long time to evaluate. However, considering that they are able to find near-to-optimal solutions in just a few iterations, these algorithms may be a good choice to improve the convergence of implicit R2R methods.

The main difference between direct search algorithms and surrogate-based methods is that the latter use the evaluations of the objective function to build an approximate model of that function. Thus, the main advantage of these algorithms is that they can use the constructed model to select the best candidate solution according to some predefined criteria, e.g., improving the accuracy of the model or looking for the optimal solution of the function. Despite that, it is also true that they have much higher computational requirements than direct search algorithms because the surrogate model needs to be updated after each function evaluation and, besides, an offline optimization process has to be performed in order to find the next candidate solution.

Among all surrogate-based algorithms, Bayesian optimization methods [191–193] are particularly interesting in the R2R field because they are able to deal with stochastic behaviors of the objective function. The distinctive feature of these algorithms is that they build a surrogate model based on Gaussian assumptions (see Fig. 7.14) and, hence, they are able to account for uncertainty. Since the stopping criterion of most of these methods is just the number of iterations, they can be directly used for R2R control simply

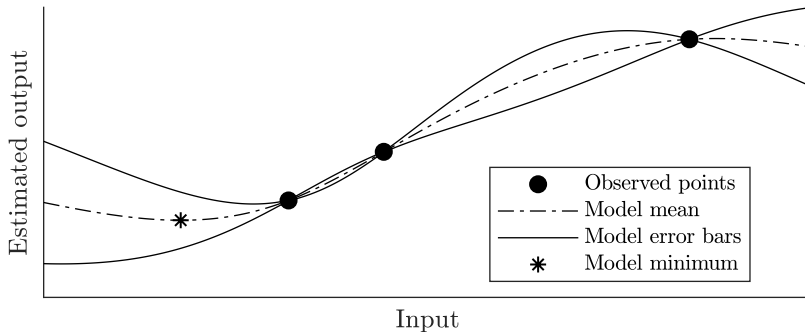


Figure 7.14: Example of surrogate model used in Bayesian optimization.

by removing that condition. Apart from that, the only modification required to operate in a R2R context is that the number of points used to build the surrogate model needs to be upper bounded. Otherwise, the model complexity would increase endlessly while the R2R search evolves in time. The criteria to select the points used to build the model can be based, e.g., on the order in which they have been evaluated or their distribution over the search space. In this thesis, Bayesian optimization is evaluated as an alternative to direct search methods in R2R control, in particular with the aim of improving the convergence of the algorithm. For more insight into the operations performed by Bayesian optimization methods, the reader is referred to any of the previously cited references.

The comparison between the direct search algorithm and the Bayesian search method is based on a Monte Carlo analysis. A hundred different searches, each starting from a random initial point, have been performed with the aim of minimizing the bouncing duration of the power relay. Thus, the costs of both methods in the two operations have been defined again as $J_m = \beta_m$ and $J_b = \beta_b$. For simplicity, all the experiments have been conducted using the Type A activation signal (see Fig. 7.5b) and the activation circuit in Configuration 1 (see Fig. 7.3). Consequently, the presented analysis should be interpreted as an illustrative example of the comparison methodology rather than a general study whose conclusions could be extrapolated to any other R2R situation. The results are presented in Figs. 7.15 and 7.16. On the one hand, Fig. 7.15 shows the evolution of \bar{J}_m and \bar{J}_b during the first 300 evaluations of the search when using each of the two methods. Since a hundred different searches have been conducted, the distribution of costs is represented using different colors and lines (see the figure caption for further details). On the other hand, Fig. 7.16 shows the percentage of searches in which the average cost of the Bayesian method is better than the average cost of the Direct search method. Hence, this figure can be used to determine which of the two search methods performs better for a given number of evaluations.

As expected, the behavior of the Bayesian method during the first evaluations is better. In fact, it only needs around 25 evaluations to reach an approximately steady state. On the other hand, the direct search method converges more slowly and, thus, its performance during the first evaluations is worse in the great majority of the searches. Despite that, the average bouncing duration using this latter method keeps going down as the search continues. As a consequence, there is a number of evaluations—around 75 in the making

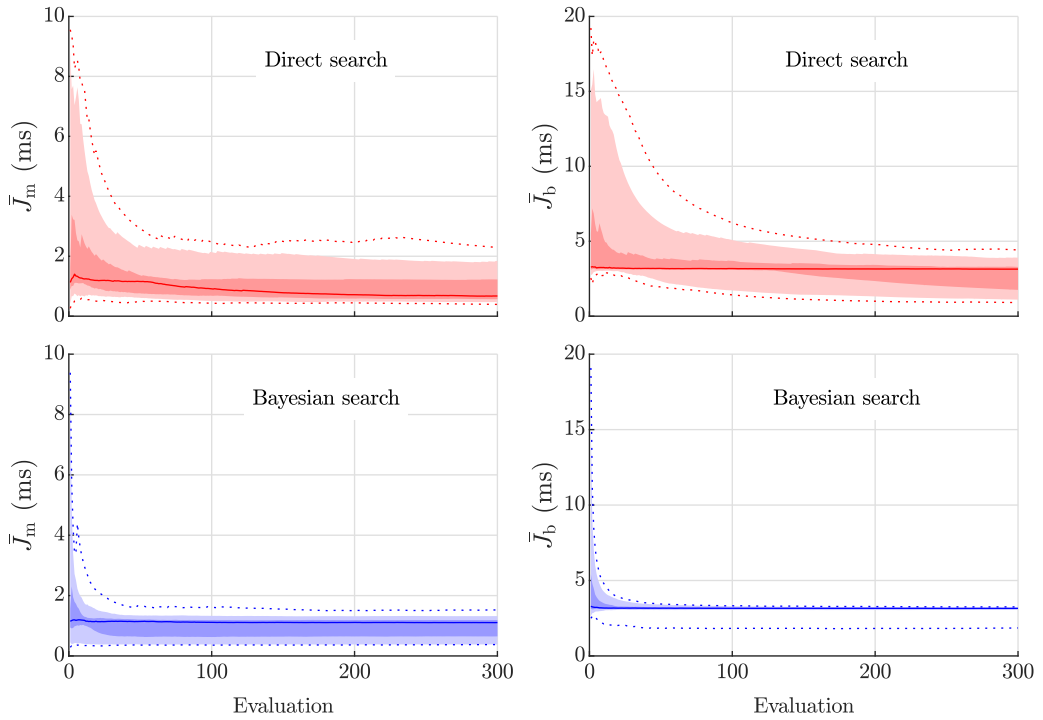


Figure 7.15: Comparison of search algorithms. Evolution of the average costs for the making (left) and breaking (right) operations. Results from 100 different searches. The dotted line represents the extreme values, the light shaded area is the 5-95 % range, the dark shaded area is the 25-75% range and the solid line is the median value.

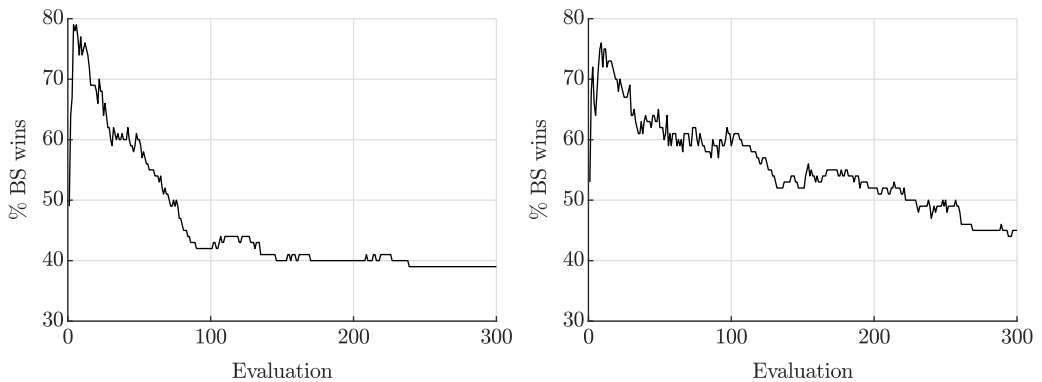


Figure 7.16: Comparison of search algorithms. Percentage of wins of the Bayesian method with respect to the number of evaluations. Results corresponding to the making (left) and breaking (right) operations. The performance of the Bayesian method is better during the first evaluations, but the direct search method starts to perform better after a given number of repetitions (see the 50% level).

search and around 225 in the breaking search—where the direct search method starts to perform better than the Bayesian algorithm. Hence, it can be concluded that, in this particular case and in terms of convergence, the best R2R policy would probably be to start the search with the Bayesian method and then, after a certain number of repetitions, switch to the direct search algorithm.

Chapter 8

Conclusions and Future Work

This thesis has been focused on several topics related to modeling and control of reluctance actuators. The dynamical modeling of this class of systems has been addressed in the first part of the document. Special emphasis has been given to the analysis of different electromagnetic phenomena that affect the behavior of these actuators and how to include them in the presented dynamical models. Then, the second part has been devoted to the proposal, analysis and validation of different estimation and control techniques. Run-to-Run control has been proposed as an alternative method to improve the performance of switch-type reluctance actuators. The main conclusions of the thesis are summarized in this last chapter. New research lines are also proposed based on the obtained results and the experience gained during the conduct of this research.

8.1 Conclusions

Compared to other alternatives, reluctance actuators feature high force density, fast response, low energy dissipation and reduced cost. These characteristics make them the best choice for small mass-market switch-type devices such as electromechanical relays and on-off valves. Since nothing comes for free, reluctance actuators also have certain disadvantages. In particular, the nonlinear nature of the magnetic force, which increases as the air gap decreases, is the origin of the impacts, the acoustic noise and the wear that the above-mentioned devices experience at the end of each switching process.

The work presented in this thesis has aimed to improve the understanding of the dynamic behavior of reluctance actuators and to propose solutions to their problems based on control systems theory. In this section, the main conclusions and contributions of the research are summarized. These are divided into four different categories that correspond to the proposed objectives of the research (see Section 1.3).

8.1.1 Dynamical modeling

The first objective pursued in the research has been the development of accurate control-oriented dynamical models for reluctance actuators. In this regard, the Magnetic Equivalent Circuit (MEC) has been the main methodology used to model the electromagnetic behavior of these devices. This approach results in fast transient simulations and it relies basically on two assumptions: The flux is confined in a region around the so-called main paths and it is uniform within the cross section of the circuit. On the other hand, models based on the Finite Element Method (FEM) can hardly be applied for estimation or control purposes due to their high computational requirements. However, they have been used in this research for some specific purposes, e.g., to analyze the validity of the approximations of the MEC method or to calculate the air gap reluctance of some devices for which there are no analytical solutions.

Special attention has been paid to the study of the electromagnetic phenomena—flux fringing, saturation, hysteresis and eddy currents—that occur in this class of actuators. Analytical formulations have been derived to include these phenomena in the proposed dynamical models. In particular, one of the contributions of the research is an explicit dynamical formulation of the Preisach model of hysteresis, which results in much faster simulations when compared to implicit solutions. In addition, a comparison between different functions to model magnetic saturation and an analytical solution for eddy currents in cylindrical cores have been also presented.

Reluctance actuators are generally characterized by a limited range of motion. Thus, the limits of the armature stroke need to be considered in order to accurately model the movement of these devices. The inclusion of these physical limits in the models leads to hybrid dynamics, i.e., a behavior that combines both continuous-time and discrete-time dynamics. For this reason, different hybrid automata have been proposed to model the movement of the actuator including the bouncing phenomenon.

In order to analyze the effects of the studied electromagnetic phenomena in reluctance actuators, five different hybrid dynamical models have been presented, ranging from a computationally inexpensive model to a comprehensive model that includes saturation, hysteresis, eddy currents and flux fringing. As expected, the results show that this latter model is the most accurate, but nevertheless it is hardly applicable to real-time implementations due to its internal structure and computational requirements. Despite that, it is still much less expensive than any FEM model, so it is the best choice for offline processes that require accurate transient simulations, such as the design and validation of control or estimation algorithms. The other four models are similar in terms of computational requirements and they are more precise the more phenomena they include. Thus, the best choice for real-time implementations is probably the model that includes saturation, flux fringing and eddy currents.

8.1.2 Measurement

The second objective of this thesis has been the evaluation of different measurement methodologies to improve the understanding of the dynamic behavior of reluctance actuators and, if possible, to be used as part of a controller. With regard to the position,

one of the main problems of mass-market devices like relays and valves is that these are usually encapsulated devices where the armature is not accessible. Assuming that the housing can be disassembled for experimental purposes, the measurement specifications are still very restrictive. Indeed, the motion of a short-stroke reluctance actuator is usually limited to less than one millimeter and it may last less than one millisecond. Three different optical instruments—a laser displacement sensor, a line scan camera and a high speed camera—have been evaluated in measuring the motion of an electromechanical relay. The results show that it is possible to record the trajectory of the armature and other components of the device if these are accessible, but all the studied techniques have some drawbacks. Overall, the main limitations of these instruments are the low flexibility—none is completely applicable to any reluctance actuator—and the high cost—they are thousands of times more expensive than standard relays and valves.

On the other hand, other variables that are much more easily obtainable in switch-type devices are the acoustic noise and, in the case of relays and contactors, the state of the electrical connections. It has been found that these variables have a direct relation to the motion of the armature and, thus, they can be used to evaluate the performance of the device. Contrary to the position, these variables can always be recorded using low-cost procedures and without need of disassembling the device. Hence, they are much better suited for practical implementations.

8.1.3 Estimation

The third objective pursued in this work has been the design and analysis of estimation algorithms. In particular, magnetic flux is one of the most relevant variables in reluctance actuators and it can only be measured using additional hardware. Thus, although secondary coils and Hall sensors have been already used to measure the flux in some high-precision actuators, there was a clear interest in the development of algorithms that could estimate this variable based only on measurements of the coil voltage and current. Two different algorithms have been presented for this purpose, both of which can be implemented in real time. Simulations and real experiments show that the estimators are accurate and robust against temperature variations. Besides, the algorithms also provide estimates of the resistance and the inductance of the actuator, which can be utilized for identification or further estimation purposes.

On the other hand, the armature position is probably the variable with the most interest when designing a soft-landing controller. Although different estimation methods have been proposed in the literature, the effect of magnetic hysteresis on the performance of these algorithms had never been studied. In this thesis, it has been shown that the estimation techniques that rely on inductance estimates are hardly applicable to actuators in which magnetic hysteresis plays an important role. The main reason is that inductance is not well defined when hysteresis is present because the relation between the current and the magnetic flux in those cases is not a bijection. Other estimation approaches have been also studied. The main conclusion is that the best estimation strategy, both in terms of accuracy and robustness, is to estimate the flux in a first step and then use the flux estimate as input of a secondary estimator that only includes a mechanical model of the actuator. In this way, given that the electromagnetic dynamics is not considered in the estimation model, the negative effects of magnetic hysteresis are considerably reduced.

8.1.4 Control

Finally, the fourth and last objective of this thesis has been the design and validation of control algorithms to achieve soft landing in switch-type reluctance actuators. First of all, the dynamical models developed in this work have been used to give a theoretical explanation for the switching behavior of this type of actuators, i.e., why they are not open-loop stable at any intermediate position between the stroke limits. In addition to that, analytical solutions have been also derived to express, as a function of the model parameters, the voltage values that produce the switching from the maximum to the minimum position and vice versa. These expressions could be used, e.g., in the design of a new actuator or to estimate the values of some of the parameters of an already existing device. Besides, the observability and controllability properties of these systems have been also studied for the first time.

Classical control techniques have been then used to design soft-landing controllers for reluctance actuators. Firstly, a trajectory tracking controller has been designed based on a feedback linearization scheme. It has been shown that, provided that accurate measurements or estimates of the position are available, the controller is able to achieve an almost perfect tracking of the designed trajectory. Nevertheless, in view of the results obtained in the measurement and estimation chapters, open-loop optimal control has been proposed as an alternative solution to achieve soft landing when the armature position cannot be measured or estimated. Since the main problem of open-loop strategies is the lack of robustness, the performance of the designed policies on perturbed systems has been studied by means of Monte Carlo simulations. The results show that, although soft landing is only achieved in some particular cases, the impact velocity of the armature is considerably reduced in the great majority of the cases.

In order to increase the robustness of the proposed solutions, Run-to-Run (R2R) control has been explored in the last chapter as an additional method to achieve soft landing. R2R techniques are specifically designed for systems that perform a repetitive operation and, thus, they are very well suited to being applied to switch-type devices. Considering the great flexibility of implicit R2R controllers, practical advice has been given on how to select and parameterize the input profile and how to use measurements such as the noise in order to evaluate the system performance. A direct search algorithm has been designed and presented, and the suitability of surrogate-based optimization methods to this problem has been also highlighted. The performed experiments show that the designed R2R controller is able to improve gradually the behavior of a switch-type device and that, after a few cycles, it outperforms other methodologies in the literature, at least with regard to bounce reduction. The main advantage of this technique is that, contrary to nominal open-loop solutions or estimation-based controllers, implicit R2R controllers do not rely on a dynamical model of the system and, hence, they are more robust and more versatile. Finally, given that convergence may be one of the biggest concerns when using these algorithms, a method to determine the best search algorithm for a given R2R controller has been also proposed.

8.2 Recommendations for future work

The research work performed during a doctoral investigation is just a modest contribution to the history of science. During the last four years, some problems have been solved, new ones have arisen and many questions have been left unanswered. Based on the obtained results and the experience gained during the conduct of this investigation, the following recommendations are given for future research:

- With regard to the dynamical modeling of reluctance actuators, the main recommendation is related to **magnetic hysteresis**. It has been shown that this phenomenon has a great effect on the dynamic behavior of these devices and, in the case that it is neglected, the accuracy of the models is considerably reduced. In this thesis, the Preisach model of hysteresis has been selected to describe this phenomenon because it is the most common approach in the literature. An explicit formulation of this model has been derived, which considerably reduces the computational requirements of the simulations and, thus, leads to much faster results than in the case of using an implicit version. Despite this significant improvement, the dynamical model for reluctance actuators that includes this formulation is still between ten and twenty times more expensive to evaluate than any of the models without hysteresis. Besides, it is hardly applicable to real-time estimation and control because of its internal structure, which depends on two sets of previous extrema values that are generally unknown. In view of the potential benefits, future research on this topic should explore other hysteresis models that may lead to simpler and computationally less expensive implementations. In particular, the discrete Preisach model and the positive feedback model [23] are good candidates for reducing the model complexity.
- **Open-loop optimal control** has the great advantage that it can be easily implemented in practice without need of measurements or estimation algorithms. Considering that electromechanical switches and solenoid valves are mass-market devices, this class of policies seems to be a suitable cost-effective approach to improve their performance. In this regard, different time-optimal and energy-optimal solutions have been described and evaluated in this thesis for a nominal system. Besides, further results not presented in this document [112] show that it is possible to include parameter uncertainty in the design of these policies so that they become more robust. Future researchers are encouraged to consider this promising approach as a practical way to control the dynamic behavior of switch-type devices with a very low cost of implementation.
- Concerning the **estimation of the armature position**, it is highly recommended to avoid the use of the inductance of the device as an intermediate variable in the estimation algorithm, specially if the core material is affected by magnetic hysteresis. As has been shown, this variable is not well defined when magnetic hysteresis is present and, thus, inductance-based methods generally result in great estimation errors. Future research on this field should mainly focus on improving the rate of convergence of the estimators so that they can be effectively used in an eventual feedback control loop. Adaptive estimation should also be considered as a method to improve the robustness of the estimators against parameter uncertainty.

- Last but not least, **Run-to-Run control** has been explored in this research work as a non-conventional method to control the dynamic behavior of switch-type devices. Although the obtained results are highly satisfactory, the possibilities to design a R2R algorithm are almost endless and, hence, further improvements could still be achieved. With regard to the input, the time-optimal policy has been selected in this thesis as the basic input profile, but several other alternatives may also be considered, e.g., energy-optimal profiles. Besides, given that the resistance of the device may change due to temperature variations, current-based R2R control—R2R control using the current as input instead of the voltage—should be also explored as a method to increase the convergence and robustness of the algorithms on reluctance actuators. The parameterization of the input profile is also a point that requires further research.

Regarding the output, two different signals—noise and electrical contacts—have been proposed in this thesis to evaluate the performance of a given operation using low-cost procedures. In addition to that, it has been shown that the electric current through the coil can also be easily measured and that it contains information about the armature trajectory. Consequently, it could be really useful to incorporate this variable to the evaluation step of the R2R controller, e.g., by comparing the current measurements with a reference profile.

Finally, another important focus for future research is the search algorithm of the R2R method. In this work, a direct search algorithm has been developed based on pattern search optimization methods. Besides, surrogate-based optimization has been highlighted as a promising approach to improve the convergence. The performance of the algorithm is nevertheless dependent on several factors—the design of the input profile, the stochastic nature of the output, the target of the search—so much research is still required to determine the best choice for each possible situation. In any case, it has been already found [115] that the advantages of Bayesian optimization are more evident when the search space has more dimensions, so this seems to be a good starting point for R2R controllers that consider more complex input profiles.

Bibliography

- [1] M. Faraday, “New Electro-Magnetic Apparatus,” *Quarterly Journal of Science, Literature and the Arts*, vol. 12, pp. 186–187, 1821.
- [2] M. Faraday, “Description of an Electro-magnetical Apparatus for the Exhibition of Rotatory Motion,” *Quarterly Journal of Science, Literature and the Arts*, vol. 12, pp. 283–285, 1821.
- [3] Ørsted, Hans Christian, “Experiments on the Effect of a Current of Electricity on the Magnetic Needle,” *Annals of Philosophy*, vol. 16, pp. 273–277, 1820.
- [4] Ampère, André-Marie, “Mémoire présenté à l’Académie royale des Sciences, le 2 octobre 1820, où se trouve compris le résumé de ce qui avait été lu à la même Académie les 18 et 25 septembre 1820, sur les effets des courans électriques,” in *Annales de Chimie et de Physique*, vol. 15, 1820, pp. 59–76.
- [5] M. Faraday, “V. experimental researches in electricity,” *Philosophical transactions of the Royal Society of London*, no. 122, pp. 125–162, 1832.
- [6] D. Marcsa and M. Kuczmann, “Design and control for torque ripple reduction of a 3-phase switched reluctance motor,” *Computers & Mathematics with Applications*, vol. 74, no. 1, pp. 89 – 95, Jul. 2017.
- [7] E. Richter, “High temperature, lightweight, switched reluctance motors and generators for future aircraft engine applications,” in *1988 American Control Conf. IEEE*, 1988, pp. 1846–1851.
- [8] C. A. Ferreira, S. R. Jones, B. T. Drager, and W. S. Heglund, “Design and implementation of a five-hp, switched reluctance, fuel-lube, pump motor drive for a gas turbine engine,” *IEEE Trans. Power Electron.*, vol. 10, no. 1, pp. 55–61, 1995.
- [9] K. M. Rahman, B. Fahimi, G. Suresh, A. V. Rajarathnam, and M. Ehsani, “Advantages of switched reluctance motor applications to ev and hev: Design and control issues,” *IEEE Trans. Ind. Appl.*, vol. 36, no. 1, pp. 111–121, Jan./Feb. 2000.
- [10] Z.-Q. Zhu and D. Howe, “Electrical machines and drives for electric, hybrid, and fuel cell vehicles,” *Proc. IEEE*, vol. 95, no. 4, pp. 746–765, 2007.

- [11] D. Matt, R. Goyet, J. Lucidarme, and C. Rioux, "Longitudinal-field multi-airgap linear reluctance actuator," *Electric machines and power systems*, vol. 13, no. 5, pp. 299–313, 1987.
- [12] J. Lucidarme, A. Amouri, and M. Poloujadoff, "Optimum design of longitudinal field variable reluctance motors-application to a high performance actuator," *IEEE Trans. Energy Conversion*, vol. 8, no. 3, pp. 357–361, Sep. 1993.
- [13] U. S. Deshpande, J. J. Cathey, and E. Richter, "High-force density linear switched reluctance machine," *IEEE Trans. Ind. Appl.*, vol. 31, no. 2, pp. 345–352, Mar./Apr. 1995.
- [14] D. B. Hiemstra, G. Parmar, and S. Awtar, "Performance tradeoffs posed by moving magnet actuators in flexure-based nanopositioning," *IEEE/ASME Trans. Mechatronics*, vol. 19, no. 1, pp. 201–212, Feb. 2012.
- [15] W.-C. Gan, N. C. Cheung, and L. Qiu, "Position control of linear switched reluctance motors for high-precision applications," *IEEE Trans. Ind. Appl.*, vol. 39, no. 5, pp. 1350–1362, Sep./Oct. 2003.
- [16] H. S. Lim and R. Krishnan, "Ropeless elevator with linear switched reluctance motor drive actuation systems," *IEEE Trans. Ind. Electron.*, vol. 54, no. 4, pp. 2209–2218, 2007.
- [17] X. Xue, K. W. E. Cheng, and Z. Zhang, "Model, analysis, and application of tubular linear switched reluctance actuator for linear compressors," *IEEE Trans. Ind. Electron.*, vol. 65, no. 12, pp. 9863–9872, Dec. 2018.
- [18] P. Enrici, F. Dumas, N. Ziegler, and D. Matt, "Design of a high-performance multi-air gap linear actuator for aeronautical applications," *IEEE Trans. Energy Convers.*, vol. 31, no. 3, pp. 896–905, Sep. 2016.
- [19] J.-F. Llibre, N. Martinez, B. Nogarède, and P. Leprince, "Linear tubular switched reluctance motor for heart assistance circulatory: Analytical and finite element modeling," in *10th Int. Workshop on Electron., Control, Measurement and Signals*. IEEE, 2011, pp. 1–6.
- [20] A. Katalenic, "Control of reluctance actuators for high-precision positioning," Ph.D. dissertation, Eindhoven Univ. of Technology, 2013.
- [21] A. Katalenic, H. Butler, and P. P. J. van den Bosch, "High-precision force control of short-stroke reluctance actuators with an air gap observer," *IEEE/ASME Trans. Mechatronics*, vol. 21, no. 5, pp. 2431–2439, 2016.
- [22] N. H. Vrijsen, J. W. Jansen, and E. A. Lomonova, "Prediction of magnetic hysteresis in the force of a prebiased e-core reluctance actuator," *IEEE Trans. Ind. Appl.*, vol. 50, no. 4, pp. 2476–2484, Jul. 2014.
- [23] N. Vrijsen, "Magnetic hysteresis phenomena in electromagnetic actuation systems," Ph.D. dissertation, Eindhoven Univ. of Technology, 2014.

- [24] I. MacKenzie and D. L. Trumper, "Real-time hysteresis modeling of a reluctance actuator using a sheared-hysteresis-model observer," *IEEE/ASME Trans. Mechatronics*, vol. 21, no. 1, pp. 4–16, Feb. 2016.
- [25] J. Bao, N. H. Vrijsen, B. L. J. Gysen, R. L. J. Sprangers, and E. A. Lomonova, "Optimization of the force density for medium-stroke reluctance actuators," *IEEE Trans. Ind. Appl.*, vol. 50, no. 5, pp. 3194–3202, Sep. 2014.
- [26] B. L. Gysen, S. Gibson, R. E. Clark, and G. W. Jewell, "High temperature permanent magnet actuator for fail-safe applications," *IEEEJ Trans. Ind Appl.*, vol. 128, no. 10, pp. 1198–1202, 2008.
- [27] S. Gibson, G. Jewell, and R. Clark, "Variable-airgap, cylindrical, linear variable reluctance actuators for high-force, medium-stroke applications," *IET electric power applications*, vol. 3, no. 4, pp. 352–362, Jul. 2009.
- [28] S. Haghbin, S. Lundmark, M. Alaküla, and O. Carlson, "Grid-connected integrated battery chargers in vehicle applications: Review and new solution," *IEEE Trans. Ind. Electron.*, vol. 60, no. 2, pp. 459–473, Feb. 2013.
- [29] S. Sadeghi, L. Guo, H. A. Toliyat, and L. Parsa, "Wide operational speed range of five-phase permanent magnet machines by using different stator winding configurations," *IEEE Trans. Ind. Electron.*, vol. 59, no. 6, pp. 2621–2631, Jun. 2012.
- [30] T. C. Beh, M. Kato, T. Imura, S. Oh, and Y. Hori, "Automated impedance matching system for robust wireless power transfer via magnetic resonance coupling," *IEEE Trans. Ind. Electron.*, vol. 60, no. 9, pp. 3689–3698, Sep. 2013.
- [31] M. Naidu, S. Gopalakrishnan, and T. Nehl, "Fault-tolerant permanent magnet motor drive topologies for automotive x-by-wire systems," *IEEE Trans. Ind. Appl.*, vol. 46, no. 2, pp. 841–848, Mar. 2010.
- [32] P. Sharma, S. P. Duttgupta, and V. Agarwal, "A novel approach for maximum power tracking from curved thin-film solar photovoltaic arrays under changing environmental conditions," *IEEE Trans. Ind. Appl.*, vol. 50, no. 6, pp. 4142–4151, Nov 2014.
- [33] J. Acero, J. Burdío, L. Barragan, D. Navarro, R. Alonso, J. Ramon, F. Monterde, P. Hernandez, S. Llorente, and I. Garde, "Domestic induction appliances," *IEEE Ind. Appl. Mag.*, vol. 2, no. 16, pp. 39–47, Mar./Apr. 2010.
- [34] P. Barkan, "A study of the contact bounce phenomenon," *IEEE Trans. Power App. Syst.*, no. 2, pp. 231–240, Feb. 1967.
- [35] R. C. Tung, A. Fruehling, D. Peroulis, and A. Raman, "Multiple timescales and modeling of dynamic bounce phenomena in rf mems switches," *J. Microelectromech. Syst.*, vol. 23, no. 1, pp. 137–146, Feb. 2014.
- [36] A. T. Van Zanten, "Evolution of electronic control systems for improving the vehicle dynamic behavior," in *Proc. 6th Int. Symp. Adv. Veh. Control*, vol. 2, no. 2, 2002, pp. 1–9.

- [37] M. Branciforte, A. Meli, G. Muscato, and D. Porto, "ANN and non-integer order modeling of abs solenoid valves," *IEEE Trans. Control Syst. Technol.*, vol. 19, no. 3, pp. 628–635, May 2011.
- [38] X. Zhao, L. Li, J. Song, C. Li, and X. Gao, "Linear control of switching valve in vehicle hydraulic control unit based on sensorless solenoid position estimation," *IEEE Trans. Ind. Electron.*, vol. 63, no. 7, pp. 4073–4085, Jul. 2016.
- [39] W. Hoffmann, K. Peterson, and A. G. Stefanopoulou, "Iterative learning control for soft landing of electromechanical valve actuator in camless engines," *IEEE Trans. Control Syst. Technol.*, vol. 11, no. 2, pp. 174–184, Mar. 2003.
- [40] J. Zhao and R. J. Seethaler, "Compensating combustion forces for automotive electromagnetic valves," *Mechatronics*, vol. 20, no. 4, pp. 433 – 441, Jun. 2010.
- [41] P. Mercorelli, "A hysteresis hybrid extended kalman filter as an observer for sensorless valve control in camless internal combustion engines," *IEEE Trans. Ind. Appl.*, vol. 48, no. 6, pp. 1940–1949, 2012.
- [42] Y. P. Yang, J. J. Liu, D. H. Ye, Y. R. Chen, and P. H. Lu, "Multiobjective optimal design and soft landing control of an electromagnetic valve actuator for a camless engine," *IEEE/ASME Trans. Mechatronics*, vol. 18, no. 3, pp. 963–972, Jun. 2013.
- [43] F. Malaguti, "Proportional control of on/off solenoid operated hydraulic valve by nonlinear robust controller," in *Proc. IEEE Int. Symp. Ind. Electron.*, vol. 2. IEEE, Jul. 2002, pp. 415–419.
- [44] J.-H. Lee, Y.-W. Yun, H.-W. Hong, and M.-K. Park, "Control of spool position of on/off solenoid operated hydraulic valve by sliding-mode controller," *J. Mech. Sci. Technol.*, vol. 29, no. 12, pp. 5395–5408, Dec. 2015.
- [45] J. W. McBride, "Electrical contact bounce in medium-duty contacts," *IEEE Trans. Compon. Hybrids, Manuf. Technol.*, vol. 12, no. 1, pp. 82–90, 1989.
- [46] J. McBride and S. Sharkh, "Electrical contact phenomena during impact," *IEEE Trans. Compon. Hybrids, Manuf. Technol.*, vol. 15, no. 2, pp. 184–192, 1992.
- [47] T. S. Davies, H. Nouri, and F. W. Britton, "Towards the control of contact bounce," *IEEE Trans. Compon. Packag. Manuf. Technol.*, vol. 19, no. 3, pp. 353–359, Oct. 1996.
- [48] M. T. Glinkowski and J. Esztergalyos, "Transient modeling of electromechanical relays. Part I: armature type overcurrent relay," *IEEE Trans. Power Delivery*, vol. 11, no. 2, pp. 763–770, Apr. 1996.
- [49] M. T. Glinkowski and J. Esztergalyos, "Transient modeling of electromechanical relays. Part II: armature type overcurrent relay," *IEEE Trans. Power Delivery*, vol. 11, no. 2, pp. 771–782, Apr. 1996.
- [50] H. Nouri, N. Larsen, and T. Davies, "Contact bounce simulation using matlab," in *Proc. 43rd IEEE Holm Conf. Elect. Contacts*. IEEE, Oct. 1997, pp. 284–288.

- [51] A. M. Pawlak and T. W. Nehl, "Transient finite element modeling of solenoid actuators: the coupled power electronics, mechanical, and magnetic field problem," *IEEE Trans. Magnetics*, vol. 24, no. 1, pp. 270–273, 1988.
- [52] C. Frangos and Y. Yavin, "Current controller design for an electromagnetic actuator using an online parameter optimization approach," *IEEE Trans. Ind. Electron.*, vol. 38, no. 1, pp. 48–50, 1991.
- [53] R. Rong and D. Lowther, "Storage and retrieval of solutions in the design of electromagnetic devices," *IEEE Trans. Magnetics*, vol. 30, no. 5, pp. 3648–3651, 1994.
- [54] M. Piron, P. Sangha, G. Reid, T. Miller, and D. M. Ionel, "Rapid computer-aided design method for fast-acting solenoid actuators," *IEEE Trans. Ind. Appl.*, vol. 35, no. 5, pp. 991–999, 1999.
- [55] N. Cheung, K. Lim, and M. Rahman, "Modelling a linear and limited travel solenoid," in *Proc. 19th Ann. Conf. IEEE Ind. Electron. (IECON)*. IEEE, 1993, pp. 1567–1572.
- [56] K. Lim, N. Cheung, and M. Rahman, "Proportional control of a solenoid actuator," in *Proc. 20th Annu. Conf. IEEE Ind. Electron. (IECON)*, vol. 3. IEEE, 1994, pp. 2045–2050.
- [57] M. F. Rahman, N. C. Cheung, and K. W. Lim, "Converting a switching solenoid to a proportional actuator," *IEEJ Trans. Ind. Appl.*, vol. 116, no. 5, pp. 531–537, 1996.
- [58] M. F. Rahman, N. C. Cheung, and K. W. Lim, "Position estimation in solenoid actuators," *IEEE Trans. Ind. Appl.*, vol. 32, no. 3, pp. 552–559, May/Jun. 1996.
- [59] N. Vaughan and J. Gamble, "The modeling and simulation of a proportional solenoid valve," *J. Dyn. Syst. Meas. Control*, vol. 118, pp. 120–125, Mar. 1996.
- [60] R. Rong, D. A. Lowther, Z. Malik, H. Su, J. Nelder, and R. Spence, "Applying response surface methodology in the design and optimization of electromagnetic devices," *IEEE Trans. Magnetics*, vol. 33, no. 2, pp. 1916–1919, 1997.
- [61] S. Wang and J. Kang, "Topology optimization of nonlinear magnetostatics," *IEEE Trans. Magnetics*, vol. 38, no. 2, pp. 1029–1032, 2002.
- [62] R. E. Clark, G. W. Jewell, S. J. Forrest, J. Rens, and C. Maerky, "Design features for enhancing the performance of electromagnetic valve actuation systems," *IEEE Trans. Magnetics*, vol. 41, no. 3, pp. 1163–1168, Mar. 2005.
- [63] T. Overboom, J. Jansen, and E. Lomonova, "Application of a permanent magnet biased e-core reluctance actuator in a magnetically suspended ceiling actuator," *IEEE Trans. Magnetics*, vol. 46, no. 6, pp. 2128–2131, 2010.
- [64] S. Park and S. Min, "Design of magnetic actuator with nonlinear ferromagnetic materials using level-set based topology optimization," *IEEE Trans. Magnetics*, vol. 46, no. 2, pp. 618–621, Feb. 2010.

- [65] S. Lim, T. Yamada, S. Min, and S. Nishiwaki, "Topology optimization of a magnetic actuator based on a level set and phase-field approach," *IEEE Trans. Magn.*, vol. 47, no. 5, pp. 1318–1321, 2011.
- [66] M. Amrhein and P. T. Krein, "3-d magnetic equivalent circuit framework for modeling electromechanical devices," *IEEE Trans. Energy Convers.*, vol. 24, no. 2, pp. 397–405, 2009.
- [67] J. R. Riba Ruiz and A. Garcia Espinosa, "A novel parametric model for ac contactors," *IEEE Trans. Magn.*, vol. 44, no. 9, pp. 2215–2218, 2008.
- [68] H. Lin, X. Wang, S. Fang, P. Jin, and S. Ho, "Design, optimization, and intelligent control of permanent-magnet contactor," *IEEE Trans. Ind. Electron.*, vol. 60, no. 11, pp. 5148–5159, Nov. 2013.
- [69] S. Fang, Q. Liu, H. Lin, and S. L. Ho, "A novel flux-weakening control strategy for permanent-magnet actuator of vacuum circuit breaker," *IEEE Trans. Ind. Electron.*, vol. 63, no. 4, pp. 2275–2283, Apr. 2016.
- [70] W. Kemmetmueller, D. Faustner, and A. Kugi, "Optimal torque control of permanent magnet synchronous machines using magnetic equivalent circuits," *Mechatronics*, vol. 32, pp. 22 – 33, Dec. 2015.
- [71] Z. Guofu, W. Qiya, Y. Wenying, and L. Huimin, "Permanent-magnet equivalent model of calculating relay's static attractive torque characteristics by finite element method," *IEEE Trans. Magn.*, vol. 48, no. 9, pp. 2467–2471, Sep. 2012.
- [72] B. Xu, R. Ding, J. Zhang, L. Sha, and M. Cheng, "Multiphysics-coupled modeling: Simulation of the hydraulic-operating mechanism for a sf6 high-voltage circuit breaker," *IEEE/ASME Trans. Mechatronics*, vol. 21, no. 1, pp. 379–393, Feb. 2016.
- [73] A. di Gaeta, U. Montanaro, and V. Giglio, "Experimental validation of a hybrid analytical-fem model of an electromagnetic engine valve actuator and its control application," *IEEE/ASME Trans. Mechatronics*, vol. 18, no. 2, pp. 807–812, Apr. 2013.
- [74] Z. Guofo, W. Qiya, and R. Wanbin, "An output space-mapping algorithm to optimize the dimensional parameter of electromagnetic relay," *IEEE Trans. Magn.*, vol. 47, no. 9, pp. 2194–2199, Sep. 2011.
- [75] D. Wattiaux and O. Verlinden, "Modelling of the dynamic behaviour of electromechanical relays for the analysis of sensitivity to shocks and vibrations," *Exp. Mech.*, vol. 51, no. 9, pp. 1459–1472, Nov. 2011.
- [76] B. L. J. Gysen, K. J. Meessen, J. J. H. Paulides, and E. A. Lomonova, "General formulation of the electromagnetic field distribution in machines and devices using fourier analysis," *IEEE Trans. Magn.*, vol. 46, no. 1, pp. 39–52, Jan. 2010.
- [77] T. Braun, J. Reuter, and J. Rudolph, "A novel observer approach for self sensing of single-coil digital valves," *IFAC-PapersOnLine*, vol. 50, no. 1, pp. 782 – 787, 2017, 20th IFAC World Congr.

- [78] F. Straußberger and J. Reuter, "Position estimation in electro-magnetic actuators taking into account hysteresis effects," *IFAC-PapersOnLine*, vol. 49, no. 21, pp. 206 – 212, 2016.
- [79] X. Jun, H. Jun-jia, and Z. Chun-yan, "A dynamic model of electromagnetic relay including contact bounce," in *2008 Int. Conf. Elect. Mach. and Syst.* IEEE, Oct. 2008, pp. 4144–4149.
- [80] A. García Espinosa, J. R. Riba Ruiz, and X. Alabern Morera, "A sensorless method for controlling the closure of a contactor," *IEEE Trans. Magn.*, vol. 43, no. 10, pp. 3896–3903, Oct. 2007.
- [81] J. R. M. van Dam, B. L. J. Gysen, E. A. Lomonova, and M. Dhaens, "Soft-landing control of low-energy solenoid valve actuators," in *13th Int. Conf. Ecological Vehicles and Renewable Energies*, Apr. 2018, pp. 1–5.
- [82] P. M. dos Santos Dias de Moraes and A. J. Perin, "An electronic control unit for reducing contact bounce in electromagnetic contactors," *IEEE Trans. Ind. Electron.*, vol. 55, no. 2, pp. 861–870, Feb. 2008.
- [83] B. Carse, N. Larsen, H. Nouri, and T. Davies, "An approach to the reduction of contact bounce using fuzzy control," in *Proc. IEEE Int. Symp. Ind. Electron.*, vol. 3. IEEE, Jul. 1999, pp. 1025–1029.
- [84] P. Eyabi and G. Washington, "Modeling and sensorless control of an electromagnetic valve actuator," *Mechatronics*, vol. 16, no. 3, pp. 159 – 175, Apr. 2006.
- [85] J. Tsai, C. R. Koch, and M. Saif, "Cycle adaptive feedforward approach controllers for an electromagnetic valve actuator," *IEEE Trans. Control Syst. Technol.*, vol. 20, no. 3, pp. 738–746, May 2012.
- [86] P. Mercorelli, "An antisaturating adaptive preaction and a slide surface to achieve soft landing control for electromagnetic actuators," *IEEE/ASME Trans. Mechatronics*, vol. 17, no. 1, pp. 76–85, Feb. 2012.
- [87] D. E. Kirk, *Optimal Control Theory - An Introduction*. Dover Publications, 2004.
- [88] M. Montanari, F. Ronchi, and C. Rossi, "Trajectory generation for camless internal combustion engine valve control," in *IEEE Int. Symp. Ind. Electron.*, vol. I, Jun. 2003, pp. 454–459.
- [89] C. R. Koch, A. F. Lynch, and S. K. Chung, "Flatness-based automotive solenoid valve control," *IFAC Proc. Volumes*, vol. 37, no. 13, pp. 817–822, sep 2004.
- [90] S. K. Chung, C. R. Koch, and A. F. Lynch, "Flatness-based feedback control of an automotive solenoid valve," *IEEE Trans. Control Syst. Technol.*, vol. 15, no. 2, pp. 394–401, Mar. 2007.
- [91] T. Glück, W. Kemmetmüller, and A. Kugi, "Trajectory optimization for soft landing of fast-switching electromagnetic valves," *IFAC Proc. Vol.*, vol. 44, no. 1, pp. 11 532–11 537, Jan. 2011.

- [92] A. Fabbri, A. Garulli, and P. Mercorelli, “A trajectory generation algorithm for optimal consumption in electromagnetic actuators,” *IEEE Trans. Control Syst. Technol.*, vol. 20, no. 4, pp. 1025–1032, Jul. 2012.
- [93] H. K. Khalil, *Nonlinear control*. Pearson, 2015.
- [94] P. Mercorelli, “Robust adaptive soft landing control of an electromagnetic valve actuator for camless engines,” *Asian J. Control*, vol. 18, no. 4, pp. 1299–1312, Nov. 2016.
- [95] T. Braun, J. Reuter, and J. Rudolph, “Observer design for self-sensing of solenoid actuators with application to soft landing,” *IEEE Trans. Control Syst. Technol.*, 2018.
- [96] R. R. Chladny and C. R. Koch, “Flatness-based tracking of an electromechanical variable valve timing actuator with disturbance observer feedforward compensation,” *IEEE Trans. Control Syst. Technol.*, vol. 16, no. 4, pp. 652–663, Jul. 2008.
- [97] A. García Espinosa, J. R. Riba Ruiz, J. Cusidó, and X. Alabern Morera, “Sensorless control and fault diagnosis of electromechanical contactors,” *IEEE Trans. Ind. Electron.*, vol. 55, no. 10, pp. 3742–3750, Oct. 2008.
- [98] X. Wang, H. Lin, S. Ho, S. Fang, and P. Jin, “Analysis of dynamic characteristics of permanent magnet contactor with sensorless displacement profile control,” *IEEE Trans. Magn.*, vol. 46, no. 6, pp. 1633–1636, Jun. 2010.
- [99] K. S. Peterson and A. G. Stefanopoulou, “Extremum seeking control for soft landing of an electromechanical valve actuator,” *Automatica*, vol. 40, no. 6, pp. 1063–1069, Jun. 2004.
- [100] M. Benosman and G. M. Atinç, “Extremum seeking-based adaptive control for electromagnetic actuators,” *Int. J. Control*, vol. 88, no. 3, pp. 517–530, 2015.
- [101] J. C. Blecke, D. S. Epp, H. Sumali, and G. G. Parker, “A simple learning control to eliminate rf-mems switch bounce,” *J. Microelectromech. Syst.*, vol. 18, no. 2, pp. 458–465, 2009.
- [102] Y. Kawakami, M. Takashima, M. Hasegawa, Y. Watanabe, and K. Sawa, “An evaluation method of the contact erosion based on the dc mode test of electromagnetic contactor,” in *Proc. 50th IEEE Holm Conf. Elect. Contacts and 22nd Int. Conf. Elect. Contacts*. IEEE, 2004, pp. 83–89.
- [103] H. Liang, W. Wang, and G. Zhai, “Thermal analysis of sealed electromagnetic relays using 3-d finite element method,” in *Proc. 53rd IEEE Holm Conf. Elect. contacts*. IEEE, 2007, pp. 262–268.
- [104] L. Li, D. Ma, and Z. Li, “Cox-proportional hazards modeling in reliability analysis—a study of electromagnetic relays data,” *IEEE Trans. Compon. Packag. Manuf. Technol.*, vol. 5, no. 11, pp. 1582–1589, 2015.
- [105] Z. Wu, G. Wu, H. Huang, and Y. You, “A novel residual electrical endurance prediction method for low-voltage electromagnetic alternating current contactors,” *IEEE Trans. Compon. Packag. Manuf. Technol.*, vol. 5, no. 4, pp. 465–473, 2015.

- [106] X. Ye, J. Deng, Y. Wang, and G. Zhai, "Quality analysis and consistency design of electromagnetic device based on approximation model," *IEEE Trans. Compon. Packag. Manuf. Technol.*, vol. 5, no. 1, pp. 99–107, 2015.
- [107] E. Ramirez-Laboreo, C. Sagues, and S. Llorente, "A new model of electromechanical relays for predicting the motion and electromagnetic dynamics," *IEEE Trans. Ind. Appl.*, vol. 52, no. 3, pp. 2545–2553, May/June. 2016.
- [108] E. Ramirez-Laboreo, C. Sagues, and S. Llorente, "A new run-to-run approach for reducing contact bounce in electromagnetic switches," *IEEE Trans. Ind. Electron.*, vol. 64, no. 1, pp. 535–543, Jan. 2017.
- [109] E. Ramirez-Laboreo and C. Sagues, "Reluctance actuator characterization via fem simulations and experimental tests," *Mechatronics*, vol. 56, pp. 58 – 66, Dec. 2018.
- [110] E. Ramirez-Laboreo, E. Moya-Lasheras, and C. Sagues, "Real-time electromagnetic estimation for reluctance actuators," *IEEE Trans. Ind. Electron.*, vol. 66, no. 3, pp. 1952–1961, Mar. 2019.
- [111] E. Ramirez-Laboreo, M. G. L. Roes, and C. Sagues, "Hybrid dynamical model for reluctance actuators including saturation, hysteresis and eddy currents," *IEEE/ASME Trans. Mechatronics*, vol. 24, no. 3, pp. 1396–1406, Jun. 2019.
- [112] E. Moya-Lasheras, E. Ramirez-Laboreo, and C. Sagues, "Probability-based optimal control design for soft landing of short-stroke actuators," *IEEE Trans. Control Syst. Technol.*, 2019.
- [113] E. Ramirez-Laboreo, C. Sagues, and S. Llorente, "A new model of electromechanical relays for predicting the motion and electromagnetic dynamics," in *Ind. Applicat. Soc. Annu. Meet.* IEEE, 2015, pp. 1–8.
- [114] E. Moya-Lasheras, C. Sagues, E. Ramirez-Laboreo, and S. Llorente, "Nonlinear bounded state estimation for sensorless control of an electromagnetic device," in *IEEE Conf. Decision and Control.* IEEE, Dec. 2017, pp. 5050–5055.
- [115] E. Moya-Lasheras, E. Ramirez-Laboreo, and C. Sagues, "A novel algorithm based on bayesian optimization for run-to-run control of short-stroke reluctance actuators," in *European Control Conf.* IEEE, Jun. 2019, pp. 1103–1109.
- [116] E. Ramirez-Laboreo, E. Moya-Lasheras, and C. Sagues, "Optimal open-loop control policies for a class of nonlinear actuators," in *European Control Conf.* IEEE, Jun. 2019, pp. 3261–3266.
- [117] D. Anton Falcon, S. Llorente Gil, D. Puyal Puente, E. Ramirez Laboreo, and C. Sagues, "A home appliance device and a method for operating a home appliance device," WO Patent 2017/163114 (A1). Filing Date: Nov. 28, 2016. Publication Date: Sept. 28, 2017.
- [118] J. C. Maxwell, "On Faraday's lines of force," *Trans. Cambridge Philos. Soc.*, vol. 10, 1855.

- [119] J. C. Maxwell, “On physical lines of force,” *The London, Edinburgh, and Dublin Philosoph. Mag. and J. Sci.*, Mar. 1861.
- [120] J. C. Maxwell, “A dynamical theory of the electromagnetic field,” *Philosop. Trans. Roy. Soc. London*, no. 155, pp. 459–512, 1865.
- [121] Z. Popovic and B. D. Popovic, *introductory Electromagnetics*. Prentice Hall, 2000.
- [122] D. J. Griffiths, *Introduction to electrodynamics*, 3rd ed. Prentice Hall, 1999.
- [123] J. D. Jackson, *Classical Electrodynamics*, 3rd ed. Wiley, 1998.
- [124] F. C. Moon, *Magneto-solid mechanics*. Wiley-Interscience, 1984.
- [125] E. C. Cherry, “The duality between interlinked electric and magnetic circuits and the formation of transformer equivalent circuits,” *Proc. Physical Soc. Section B*, vol. 62, no. 2, p. 101, 1949.
- [126] E. Lwithwaite, “Magnetic equivalent circuits for electrical machines,” in *Proc. IEE*, vol. 114, no. 11. IET, 1967, pp. 1805–1809.
- [127] J. J. Cathey, *Electric machines: analysis and design applying Matlab*. McGraw-Hill, 2001.
- [128] D. K. Cheng, *Field and wave electromagnetics*, 2nd ed. Pearson Education, 1989.
- [129] I. Lope, J. Acero, and C. Carretero, “Analysis and optimization of the efficiency of induction heating applications with litz-wire planar and solenoidal coils,” *IEEE Trans. Power Electron.*, vol. 31, no. 7, pp. 5089–5101, Jul. 2016.
- [130] C. W. T. McLyman, *Transformer and inductor design handbook*. CRC press, 2016.
- [131] J. M. Coey, *Magnetism and magnetic materials*. Cambridge University Press, 2010.
- [132] D. Jiles, *Introduction to magnetism and magnetic materials*. CRC press, 2015.
- [133] F. Preisach, “Über die magnetische nachwirkung,” *Zeitschrift für physik*, vol. 94, no. 5-6, pp. 277–302, May 1935.
- [134] I. Mayergoyz, “Mathematical models of hysteresis,” *IEEE Trans. Magn.*, vol. 22, no. 5, pp. 603–608, Sep. 1986.
- [135] L.-L. Rouve, T. Waeckerle, and A. Kedous-Lebouc, “Application of preisach model to grain oriented steels: comparison of different characterizations for the preisach function $p(\alpha, \beta)$,” *IEEE Trans. Magn.*, vol. 31, no. 6, pp. 3557–3559, Nov. 1995.
- [136] B. Azzerboni, E. Cardelli, G. Finocchio, and F. La Foresta, “Remarks about preisach function approximation using lorentzian function and its identification for nonoriented steels,” *IEEE Trans. Magn.*, vol. 39, no. 5, pp. 3028–3030, Sep. 2003.
- [137] P. Pruksanubal, A. Binner, and K. H. Gonschorek, “Determination of distribution functions and parameters for the preisach hysteresis model,” in *17th Int. Zurich Symp. Electromagnetic Compatibility*. IEEE, Feb. 2006, pp. 258–261.

- [138] I. Mayergoyz and G. Friedman, “Generalized preisach model of hysteresis,” *IEEE Trans. Magn.*, vol. 24, no. 1, pp. 212–217, Jan. 1988.
- [139] J. Lammeraner and M. Štafl, *Eddy currents*. Iliffe books Ltd. London, 1966.
- [140] L. Ljung and T. Glad, “On global identifiability for arbitrary model parametrizations,” *Automatica*, vol. 30, no. 2, pp. 265 – 276, 1994.
- [141] H. Wenzl, F. Straußberger, T. Braun, S. Wirtensohn, L. Kiltz, J. Reuter, and H. Aschemann, “Comparison and identifiability analysis of friction models for the dither motion of a solenoid,” in *23rd Int. Conf. Methods & Models in Automation & Robotics (MMAR)*. IEEE, 2018, pp. 321–326.
- [142] I. Newton, *Philosophiae Naturalis Principia Mathematica*, 1687.
- [143] R. Goebel, R. G. Sanfelice, and A. R. Teel, “Hybrid dynamical systems,” *IEEE Control Syst. Mag.*, vol. 29, no. 2, pp. 28–93, Apr. 2009.
- [144] E. Wiechert, “Ueber elastische nachwirkung,” Ph.D. dissertation, Königsberg University, 1889.
- [145] H. Goldstein, C. Poole, and J. Safko, *Classical mechanics*. AAPT, 2002.
- [146] W. Meissner and R. Ochsenfeld, “Ein neuer effekt bei eintritt der supraleitfähigkeit,” *Naturwissenschaften*, vol. 21, no. 44, pp. 787–788, 1933.
- [147] S. Bobbio, G. Milano, C. Serpico, and C. Visone, “Models of magnetic hysteresis based on play and stop hysterons,” *IEEE Trans. Magn.*, vol. 33, no. 6, pp. 4417–4426, Nov. 1997.
- [148] T. Matsuo, D. Shimode, Y. Terada, and M. Shimasaki, “Application of stop and play models to the representation of magnetic characteristics of silicon steel sheet,” *IEEE Trans. Magn.*, vol. 39, no. 3, pp. 1361–1364, May 2003.
- [149] E. Dlala, J. Saitz, and A. Arkkio, “Inverted and forward preisach models for numerical analysis of electromagnetic field problems,” *IEEE Trans. Magn.*, vol. 42, no. 8, pp. 1963–1973, 2006.
- [150] M. Hedegård, T. Wik, and C. Wallin, “Adaptive hysteresis compensation using reduced memory sequences,” *IEEE/ASME Trans. Mechatronics*, vol. 22, no. 5, pp. 2296–2307, Jun. 2017.
- [151] M. Montanari, F. Ronchi, C. Rossi, and A. Tonielli, “Control of a camless engine electromechanical actuator: Position reconstruction and dynamic performance analysis,” *IEEE Trans. Ind. Electron.*, vol. 51, no. 2, pp. 299–311, Apr. 2004.
- [152] E. H. Hall, “On a new action of the magnet on electric currents,” *Amer. J. Math.*, vol. 2, pp. 287–292, 1879.
- [153] A. Guillén, “Analysis of the motion of an electromechanical relay during switching,” Bachelor’s Thesis, Escuela de Ingeniería y Arquitectura, Universidad de Zaragoza, 2015, supervised by Edgar Ramírez Laboreo and Carlos Sagüés Blázquez.

- [154] J.-J. E. Slotine and W. Li, *Applied nonlinear control*. Prentice Hall, Englewood Cliffs, NJ, 1991.
- [155] R. E. Kalman, "On the general theory of control systems," *IFAC Proc. Volumes*, vol. 1, no. 1, pp. 491 – 502, 1960, 1st Int. IFAC Congr. Automat. Remote Control.
- [156] C. Chevalley, *Theory of Lie groups*. Princeton University Press, Princeton, New Jersey, 1946.
- [157] G. Haynes and H. Hermes, "Nonlinear controllability via Lie theory," *SIAM J. Control*, vol. 8, no. 4, pp. 450–460, 1970.
- [158] C. Lobry, "Contrôlabilité des systèmes non linéaires," *SIAM J. Control*, vol. 8, no. 4, pp. 573–605, 1970.
- [159] H. J. Sussmann and V. Jurdjevic, "Controllability of nonlinear systems." *J. Differential Equations*, vol. 12, pp. 95 – 116, 1972.
- [160] R. Hermann and A. Krener, "Nonlinear controllability and observability," *IEEE Trans. Autom. Control*, vol. 22, no. 5, pp. 728–740, 1977.
- [161] L. Hunt, "Sufficient conditions for controllability," *IEEE Trans. Circuits Syst.*, vol. 29, no. 5, pp. 285–288, May 1982.
- [162] Y. M. Kostyukovskii, "Simple conditions of observability of nonlinear controlled systems," *Automat. Remote Control*, vol. 10, pp. 1575–1584, 1968.
- [163] S. R. Kou, D. L. Elliott, and T. J. Tarn, "Observability of nonlinear systems," *Inform. Control*, vol. 22, no. 1, pp. 89–99, 1973.
- [164] K. Ogata, *Modern control engineering*, 5th ed. Prentice Hall, 2010.
- [165] K. J. Aström and R. M. Murray, *Feedback systems: an introduction for scientists and engineers*. Princeton university press, 2010.
- [166] D. S. Naidu, *Optimal Control Systems*, 1st ed., ser. Electrical Engineering Series. CRC Press, 2002.
- [167] D. E. Kirk, *Optimal Control Theory - An Introduction*. Dover Publications, 1998.
- [168] D. B. Roemer, M. M. Bech, P. Johansen, and H. C. Pedersen, "Optimum design of a moving coil actuator for fast-switching valves in digital hydraulic pumps and motors," *IEEE/ASME Trans. Mechatronics*, vol. 20, no. 6, pp. 2761–2770, Dec. 2015.
- [169] R. E. Kalman, "A new approach to linear filtering and prediction problems," *J. Basic Eng.*, vol. 82, no. 1, pp. 35–45, Mar. 1960.
- [170] B. D. Anderson and J. B. Moore, *Optimal Filtering*. Dover Publications, Mineola, New York, 2005.
- [171] C. K. Chui and G. Chen, *Kalman Filtering with Real-Time Applications*, 5th ed. Springer International Publishing, Cham, Switzerland, 2017.

- [172] B. D. O. Anderson and J. B. Moore, "Detectability and stabilizability of time-varying discrete-time linear systems," *SIAM J. Control Optim.*, vol. 19, no. 1, pp. 20–32, Jan. 1981.
- [173] J.-C. Renn and Y.-S. Chou, "Sensorless plunger position control for a switching solenoid," *JSME Int. J. C*, vol. 47, no. 2, pp. 637–645, 2004.
- [174] D. Pawelczak and H.-R. Trankler, "Sensorless position control of electromagnetic linear actuator," in *Proc. IEEE Instrum. Meas. Technol. Conf.*, vol. 1. IEEE, 2004, pp. 372–376.
- [175] I. Dülk and T. Kováčsházy, "Sensorless position estimation in solenoid actuators with load compensation," in *Proc. IEEE Instrum. Meas. Technol. Conf.* IEEE, 2012, pp. 268–273.
- [176] B. Srinivasan, S. Palanki, and D. Bonvin, "Dynamic optimization of batch processes: I. Characterization of the nominal solution," *Comput. Chem. Eng.*, vol. 27, no. 1, pp. 1–26, Jan. 2003.
- [177] B. Srinivasan, D. Bonvin, E. Visser, and S. Palanki, "Dynamic optimization of batch processes: II. Role of measurements in handling uncertainty," *Comput. Chem. Eng.*, vol. 27, no. 1, pp. 27–44, Jan. 2003.
- [178] Y. Wang, F. Gao, and F. J. Doyle, "Survey on iterative learning control, repetitive control, and run-to-run control," *J. Process Control*, vol. 19, no. 10, pp. 1589–1600, Dec. 2009.
- [179] E. Del Castillo and A. M. Hurwitz, "Run-to-run process control: literature review and extensions," *J. of Quality Technology*, vol. 29, no. 2, p. 184, Apr. 1997.
- [180] S. W. Butler and J. A. Stefani, "Supervisory run-to-run control of polysilicon gate etch using in situ ellipsometry," *IEEE Trans. Semicond. Manuf.*, vol. 7, no. 2, pp. 193–201, May 1994.
- [181] T. L. Clarke-Pringle and J. F. MacGregor, "Optimization of molecular-weight distribution using batch-to-batch adjustments," *Ind. Eng. Chem. Res.*, vol. 37, no. 9, pp. 3660–3669, Jul. 1998.
- [182] C. Owens, H. Zisser, L. Jovanovic, B. Srinivasan, D. Bonvin, and F. J. Doyle III, "Run-to-run control of blood glucose concentrations for people with type 1 diabetes mellitus," *IEEE Trans. Biomed. Eng.*, vol. 53, no. 6, pp. 996–1005, Jun. 2006.
- [183] R. Hooke and T. A. Jeeves, "Direct search solution of numerical and statistical problems," *J. ACM*, vol. 8, no. 2, pp. 212–229, 1961.
- [184] R. M. Lewis, V. Torczon, and M. W. Trosset, "Direct search methods: then and now," *J. Comput. Appl. Math.*, vol. 124, no. 1, pp. 191–207, 2000.
- [185] R. M. Lewis and V. Torczon, "Pattern search methods for linearly constrained minimization," *SIAM J. Optimization*, vol. 10, no. 3, pp. 917–941, 2000.
- [186] G. E. Box, "Evolutionary operation: A method for increasing industrial productivity," *J. R. Stat. Soc. Ser. C*, pp. 81–101, Jun. 1957.

- [187] C. Audet and J. E. Dennis Jr, “Mesh adaptive direct search algorithms for constrained optimization,” *SIAM J. Optimization*, vol. 17, no. 1, pp. 188–217, Jul. 2006.
- [188] L. M. Rios and N. V. Sahinidis, “Derivative-free optimization: a review of algorithms and comparison of software implementations,” *J. Global Optimization*, vol. 56, no. 3, pp. 1247–1293, Jul. 2013.
- [189] D. R. Jones, “A taxonomy of global optimization methods based on response surfaces,” *J. Global Optimization*, vol. 21, no. 4, pp. 345–383, Dec. 2001.
- [190] N. V. Queipo, R. T. Haftka, W. Shyy, T. Goel, R. Vaidyanathan, and P. K. Tucker, “Surrogate-based analysis and optimization,” *Progress in aerospace sciences*, vol. 41, no. 1, pp. 1–28, 2005.
- [191] J. Mockus, *Bayesian approach to global optimization: theory and applications*. Springer Science & Business Media, 2012, vol. 37.
- [192] E. Brochu, V. M. Cora, and N. De Freitas, “A tutorial on bayesian optimization of expensive cost functions, with application to active user modeling and hierarchical reinforcement learning,” *arXiv preprint arXiv:1012.2599*, 2010.
- [193] B. Shahriari, K. Swersky, Z. Wang, R. P. Adams, and N. De Freitas, “Taking the human out of the loop: A review of bayesian optimization,” *Proc. IEEE*, vol. 104, no. 1, pp. 148–175, 2015.

About the author

Édgar Ramírez Laboreo was born in Zaragoza, Spain, in 1990. He received the Industrial Engineer's degree and the MSc degree in Electronic Engineering from the University of Zaragoza, respectively in 2014 and 2015, both with honors. In 2015, he was awarded with the Academia General Militar Prize for being the highest ranking graduate of the School of Engineering and Architecture.



In 2013 he joined as a researcher the Aragon Institute for Engineering Research and the Department of Computer Science and Systems Engineering, University of Zaragoza. He was involved in several research projects, some of them in collaboration with BSH Home Appliances Spain. Then, in 2015, he started his PhD degree in Systems Engineering and Computer Science, the results of which are presented in this dissertation. His current research interests include electromechanics, magnetism, heat transfer, control systems and optimization.

Further and updated information about the author can be found on his personal pages on ResearchGate (www.researchgate.net/profile/Edgar_Ramirez-Laboreo) and LinkedIn (www.linkedin.com/in/ramirlab), or sending an email to ramirlab@gmail.com.

Reluctance actuators are characterized by having a high force density, good efficiency, high fault tolerance, and reduced cost. These features make them a promising alternative to other electromagnetic actuators for high-speed and high-precision applications. In addition, reluctance actuators are also ideal for small switching devices that require a modest performance because of their compactness, low cost, reduced mass, and low energy dissipation. In particular, electromechanical relays and solenoid valves are mass-market devices whose operation is based on a small reluctance actuator.

Despite their advantages, reluctance actuators are systems with highly nonlinear dynamics. One of their most distinctive features is the magnetic force that produces the motion, which is always attractive and varies greatly with the position of the armature. In essence, the nature of this force explains why relays and valves are subject to strong impacts and wear each time they are operated. Furthermore, electromagnetic phenomena such as magnetic hysteresis and eddy currents make the dynamic modeling of reluctance actuators even more complicated. The work of this thesis aims to investigate the capabilities of reluctance actuators and, in particular, to analyze the dynamic behavior and propose estimation and control algorithms for electromechanical switches and solenoid valves.



Universidad Zaragoza